Electron-Phonon Coupling in Quasi-Two-Dimensional Correlated Systems

by

Steven Sinclair Johnston

A thesis
presented to the University of Waterloo
in fulfillment of the
thesis requirement for the degree of
Doctor of Philosophy
in
Physics

Waterloo, Ontario, Canada, 2010

I hereby declare that I am the sole author of this thesis. This is a true copy of the thesis, including any required final revisions, as accepted by my examiners.

I understand that my thesis may be made electronically available to the public.

Abstract

Over the past 20 years a great deal of progress has been made towards understanding the physics of the high-temperature (high-T_c) cuprate superconductors. Much of the low-energy physics of these materials appears to be captured by two-dimensional Hubbard or t-J models which have provided significant insight into a number of properties such as the pseudogap, antiferromagnetism and superconductivity itself. However, intrinsically planar models are unable to account for the large variations in T_c observed across materials nor do they capture the electron-phonon (el-ph) interaction, the importance of which a number of experimental probes now indicate.

This thesis examines the el-ph interaction in cuprates using a combination of analytical and numerical techniques. Starting from the microscopic mechanism for coupling to in-plane and c-axis polarized oxygen phonons, the theory of el-ph coupling is presented. The el-ph self-energy is derived in the context of Migdal-Eliashberg theory and then applied to understanding the detailed temperature and doping dependence of the renormalizations observed by Angle-resolved photoemission spectroscopy. The qualitative signatures of el-boson coupling in the density of states of a d-wave superconductor are also examined on general grounds and a model calculation is presented for el-ph coupling signatures in the density of states. Following this, the theory is extended to include the effects of screening and the consequences of this theory are explored. Due to the quasi-2D nature of the cuprates, screening is found to anomalously enhance the el-ph contribution to d-wave pairing. This result is then considered in light of the material and doping dependence of T_c and a framework for understanding the materials variations in T_c is presented. From these studies, a detailed picture of the role of the el-ph interaction in the doped cuprates emerges where the interaction, working in conjunction with a dominant pairing interaction, provides much of the materials variations in T_c observed across the cuprate families.

Turning towards numerical techniques, small cluster calculations are presented which examine the effects of a local oxygen dopant in an otherwise ideal $Bi_2Sr_2CaCu_2O_{8+\delta}$ crystal. Here, it is demonstrated that the dopant locally enhances electronic properties such as the antiferromagnetic exchange energy J via local el-ph coupling to planar local oxygen vibrations. Finally, in an effort to extend the scope of this work to the underdoped region of the phase diagram, an examination of the properties of the single-band Hubbard and Hubbard-Holstein model is carried out using Determinant Quantum Monte Carlo. Here focus is placed on the spectral properties of the model as well as the competition between the the antiferromagnetic and charge-density-wave orders. As with the small cluster calculations, a strong interplay between the magnetic and lattice properties is observed.

Acknowledgements

Over the years I have had the opportunity to work with a number of talented and dedicated people. It therefore seems fitting to begin there. I would first like to thank my supervisor Tom Devereaux for his patience and guidance over the past five years. He has been a wonderful and supportive supervisor and I have really enjoyed my time working with him and his research group. (The extensive amounts of travel may have helped.)

Next, I would like to express my gratitude to Richard Scalettar for sharing his time and expertise with me while I was learning the ins and outs of Determinant Quantum Monte Carlo. Having access to his Hubbard model code helped quite a bit and I am sure this endeavour would have taken far longer without his help. I would also like to single out my experimental collaborators at Stanford University whom I have collaborated with on a number of occasions; Wei-Sheng Lee, Yulin Chen, Felix Schmitt and the other members of the Shen research group. Much of the experimental data shown in the later chapters of this work was taken by these people. The members of my own research group have also been wonderful to work with. Many thanks to Brian Moritz, Francois Vernay, Adam Sorini, Cheng-Chien Chen and Beth Nowadnick for sharing their expertise with me as well as providing a critical review of this manuscript.

During my time in graduate school I have made connections that I can only hope will be life long. I will always remember the time Ross and I spent in Vancouver bonding over what is now only referred to as *The Fenton Travers Experience*. Through that hardship I found a true friend who's companionship I will always value. And to my fellow graduate student Jeff Quilliam - we've been friends through the endeavour that is graduate school. I am so glad we met when we did and I can only hope we can find something to collaborate on in the future.

I would also like to thank Brian Corkum and his clan for their endless hospitality in Vancouver. You guys really made Vancouver into a second home for me and I look forward to returning for the long term at some point in the future. And from my first home I have a few more to thank by name. So to Wendy, James, Aden, Jakub, Marina (even though you are a "Vancouver" friend), Penny, Dylan, Frank, Christina, Leah and finally Aaron and Elizabeth - thank you for your tireless efforts in making life interesting. Without you guys I clearly would have lost my mind years ago. I would also like to extend a sincere thank you to Diane Walz and her extended family for opening their home to me during my stay in California. So to Diane, John, Rick, Jacki, Patty, James, Stacy, Guy, Jody, Casey, and of course the two kids Cannon and Jaxson, thank you so much for your hospitality.

And there is my eternal thanks to my family who have always been loving and supportive no matter what direction life takes. I could not have asked for anything more. I only wish my father could be here to see this moment. Early on in my high school career

he introduced me to calculus, a few years ahead of the curve. That was the point when I first started to take a serious interest in mathematics which ultimately lead me down this path. I miss you very much dad and will always be thankful for what you taught me.

This work was financed by generous financial support from the National Science and Engineering Research Council of Canada (NSERC) and Shared Hierarchical Academic Research Computing Network (SHARCNET). I would also like to thank the Stanford Institute for Materials and Energy Sciences (SIMES) for hosting me for a number of years in sunny California. Much of this work was completed during that time. Finally, a large component of this work required significant computational resources and I would like to acknowledge computational time provided by SHARCNET, SIMES, and the National Energy Research Scientific Computing Center (NERSC).

Dedication

This work is dedicated to my father James Gregory Johnston who passed away before it was completed.

Contents

List of Tables **xvii**

List of Figures **xxi**

1 Introduction **1**

1.1 High-Temperature Superconductivity 1

1.2 Properties of the High-T_c cuprates 3

1.2.1 Crystal Structure 3

1.2.2 Electronic Structure in the Normal State 4

1.2.3 The Zhang-Rice Singlet 6

1.3 Beyond the CuO_2 Plane 6

1.4 Phonons in HTSC 7

1.5 Scope and Organization 9

2 Experimental Evidence for Electron-Phonon Coupling **11**

2.1 Angle-Resolved Photoemission Spectroscopy 11

2.1.1 Experimental Setup 12

2.1.2 Energy and Momentum Distribution Curves 14

2.1.3 Nodal and Antinodal Regions of the Brillouin Zone 15

2.2 Dispersion Renormalizations in the Cuprates 15

2.2.1 The Kink Feature in the Nodal Region 16

2.2.2 Band Renormalizations in the Anti-Nodal Region 18

2.2.3 Evolution from the Nodal To Antinodal Region 19

2.3 Coupling to a Bosonic Mode . . . 21
2.3.1 Coupling to the Magnetic Resonance Mode . . . 21
2.3.2 Coupling to a Spectrum of Phonon Modes . . . 22
2.4 An Alternative Proposal: Hubbard Renormalizations . . . 24
2.5 Self-energy extraction from ARPES data: Coupling to Multiple Bosonic Modes . . . 25
2.6 Magnetic Resonance vs Phonon Modes: The Isotope Effect . . . 27
2.7 The High-Energy Anomaly . . . 27
2.8 Scanning Tunnelling Microscopy . . . 29
2.8.1 Local Inhomogeneity . . . 29
2.8.2 Bosonic Mode Coupling in STM . . . 30
2.9 Other Spectroscopies . . . 32

3 Theory of Electron-Phonon Coupling 35
3.1 Derivation of the Bare Coupling Constants . . . 36
3.2 Charge Transfer Coupling . . . 38
3.2.1 The A_{1g} and B_{1g} planar modes . . . 39
3.2.2 The Apical Oxygen Mode . . . 40
3.3 Deformation Coupling: Planar Breathing Modes . . . 41
3.4 Momentum Dependence of the Bare Vertices . . . 42
3.5 Coupling Strength $\lambda(\mathbf{k})$ on the Fermi Surface . . . 46
3.5.1 Total λ_z and λ_ϕ . . . 47
3.6 Weak Coupling Theory: Migdal-Eliashberg . . . 48
3.6.1 The Superconducting State . . . 49
3.6.2 The Normal State . . . 53
3.7 The Single-particle Spectral Function . . . 54
3.8 Summary . . . 56

4 Temperature, Doping and Materials Dependence of the ARPES Kinks 59

4.1 Temperature Dependence of the Kink 59

4.1.1 Temperature Dependence of the Peak-dip-hump 59

4.1.2 Temperature Evolution of the Nodal Kink 61

4.2 A Phenomenological Model for Doping Dependence of the Nodal Kink . . 65

4.3 The Materials Dependence of Coupling to c-axis Phonons 68

4.4 Summary 72

5 Phonon-Modulated Density of States 75

5.1 A Discrepancy of Energy Scales 76

5.2 Qualitative Signatures in the Density of States 77

5.2.1 Projected Electron-Boson Couplings 77

5.2.2 The Infinite Band Formalism 78

5.2.3 The Finite Band Formalism 82

5.3 A Model Calculation for Bi-2212 85

5.4 Summary 88

6 Theory of Screening in the Cuprates and Considerations for Phonon's Contribution to T_c 89

6.1 Formalism 90

6.1.1 The Two-Dimensional Coulomb Interaction 91

6.2 The Screened Electron-Phonon Vertex in $Bi_2Sr_2CaCu_2O_{8+\delta}$ 92

6.3 Anisotropy of the Screened Electron-Phonon Interaction 96

6.4 Phonon Contributions to T_c 98

6.5 Summary 103

7 The Impact of an Oxygen Dopant in $Bi_2Sr_2CaCu_2O_{8+\delta}$ 105

7.1 Dopant Atoms in the High-T_c Cuprates 105

7.2 Electrostatics 107

7.2.1 The Undoped Lattice 107

7.2.2 The Doped Lattice . . . 108
7.3 Small Cluster Calculations . . . 109
7.4 Local Electric Fields and Electron-Phonon Coupling . . . 111
7.5 Summary . . . 114

8 Determinant Quantum Monte Carlo 115
8.1 The General Methodology . . . 115
8.1.1 Sampling the Hubbard-Stratonovich Fields . . . 117
8.1.2 Unequal Time Green's Function . . . 119
8.2 The Fermion Sign Problem . . . 119
8.3 The Hubbard-Holstein Model . . . 121
8.4 Phonon Field Updates . . . 122
8.4.1 Single Site Updates . . . 122
8.4.2 Block Updates . . . 122
8.5 Measurements . . . 123
8.5.1 Autocorrelation and Equilibration Times . . . 124
8.5.2 Equilibration Time . . . 124
8.5.3 Autocorrelation Time . . . 125
8.6 Analytic Continuation: The Method of Maximum Entropy . . . 126
8.7 Summary . . . 128

9 DQMC Results for the Hubbard and Hubbard-Holstein Models 129
9.1 Electron-Phonon Coupling in Strongly Correlated Systems . . . 129
9.2 Spectral Properties of the Hubbard Model . . . 133
9.2.1 The Undoped Parent System . . . 134
9.2.2 Electron- and Hole-doped systems . . . 134
9.3 Results for the Hubbard-Holstein Model . . . 137
9.3.1 The Fermion Sign . . . 137
9.3.2 Filling vs Chemical Potential . . . 139
9.3.3 Susceptibilities for the Half-Filled Model . . . 140

9.4 Spectral Properties of Hubbard-Holstein Model 144
9.4.1 Discussion 147
9.5 Summary 148

10 Conclusions **151**

A Kramers-Kronig Relations for the Self-Energy **155**

B The Eliashberg Equations **157**

C Evaluation of the Trace over Fermion Degrees of Freedom **161**

D UDR Decomposition **165**

References **167**

List of Tables

3.1 Tabulated values of $\lambda_{z,\phi}$ for the four phonon branches considered in this work. 48

List of Figures

1.1 The generalized temperature-filling phase diagram of the high-T_c cuprates. . . 2

1.2 The crystal structure of the $HgBa_2Ca_{n-1}Cu_nO_{4n+\delta}$ ($n = 1-5$) family of high-T_c cuprates. 4

1.3 A schematic of the orbital energy levels and covalent binding in the CuO_2 plane. 5

1.4 A schematic picture of the Zhang-Rice Singlet (ZRS). 6

2.1 A cartoon picture of a typical ARPES setup. 12

2.2 A summary of the difference between MDCs and EDCs 14

2.3 Sample ARPES spectra taken along the nodal cut (0,0) - (π, π) in Bi-2212 16

2.4 MDC Linewidth of the Nodal Spectra of Bi-2212. 17

2.5 Peak-dip-hump structure in optimal doped Bi-2212 at $\mathbf{k} = (\pi, 0)$. 18

2.6 Representative EDCs near the antinodal region of the Bi- and Tl- families of cuprates 19

2.7 EDCs for Bi-2212 for various momentum points throughout the Brillouin Zone 20

2.8 A cartoon picture of the important phonon modes of the Cuprates 23

2.9 Temperature dependence of the Self-Energy of Bi-2212 in the nodal region 25

2.10 A comparison of the high-energy anomaly in NCCO and Bi-2201 28

2.11 A summary of the el-boson coupling inferred by STM 31

3.1 Phase convention of the five-band model. 37

3.2 The momentum structure of $g(\mathbf{q}, \mathbf{q})$ for the relevant phonon modes in the cuprates 45

3.3 λ in the Fermi surface for the phonon modes relevant to the cuprates. . . 46
3.4 The diagrams included in Migdal-Eliashberg theory. 49
3.5 $\Sigma(\mathbf{k}_{AN}, \omega)$ in the superconducting state. 52
3.6 A comparison of the el-ph self-energy in the normal and superconducting state of Bi-2212. 53
3.7 Simulated $A(\mathbf{k}, \omega)$ for Bi-2212. 55

4.1 The large scale temperature dependence of $\Sigma(\mathbf{k}, \omega)$ and $A(\mathbf{k}, \omega)$ in Bi-2212. 60
4.2 Experimental T-dependence of Σ in Bi-2212 and Bi-2201. 62
4.3 The T-dependence of the el-ph self-energy in Bi-2212. 63
4.4 The evolution of the nodal kink with doping in Bi-2212 66
4.5 The evolution of the energy scales in Bi-2212 as a function of doping . . 67
4.6 The local crystal field strength in the Hg-family of cuprates. 69
4.7 The materials dependence of $\lambda_{z,\phi}$ for the B_{1g} phonon. 71

5.1 $N(\omega)$ for an s- and d-wave superconductor coupled to a single boson mode. 79
5.2 $N(\omega)$ for a two-mode model where 1 mode renormalizes over a dominant high-energy mode. 80
5.3 Solutions to the Eliashberg equations when the full bandstructure is retained. 82
5.4 The effect of a finite boson spectral density on $N(\omega)$. 84
5.5 $N(\omega)$ obtained in a model calculation for Bi-2212. 86
5.6 The effects of damping on $N(\omega)$ in Bi-2212 87

6.1 The RPA diagrams for calculating the screened el-ph vertex. 90
6.2 The screened el-ph vertex for momentum transfer $\mathbf{q} = (q, 0)$ at $\mathbf{k} = (\pi, 0)$ 93
6.3 The screened electron-phonon interaction $\lambda_{\nu}(\mathbf{q}_{2D})$. 95
6.4 The screened electron-phonon interaction $\lambda_{\nu,d}(\mathbf{q}_{2D})$. 96
6.5 The screened values of λ for Bi-2212 97
6.6 Total $\lambda_{z,\phi}$ as a function of Ω_{pl}. 98
6.7 The double square-well model used to derive T_c. 100
6.8 T_c and the isotope exponent for multi-channel superconductivity. 102

7.1 A summary of the electrostatic results for the doped Bi2212 lattice. . . . 108
7.2 Diagrams of the doped Cu_2O_7 and Cu_2O_8 clusters. 110
7.3 Local Crystal fields in Bi-2212 near a dopant oxygen atom. 112
7.4 Electron addition and removal spectra for Bi-2212 near a dopant oxygen atom. 113

8.1 A summary of the value of the average fermion sign in DQMC simulations. 120
8.2 The average phonon field value at $\tau = 0$ as a function of warm up sweep. 124
8.3 Sample autocorrelation functions for the phonon displacement field. . . . 125

9.1 The spectral function for the Hubbard Model at half-filling. 135
9.2 $A(\mathbf{k}, \omega)$ for the doped single-band Hubbard model. 136
9.3 Summary of the average sign for the Hubbard-Holstein Model 138
9.4 $\langle n \rangle$ vs μ for the single-band Hubbard-Holstein model. 139
9.5 A summary of various susceptibilities for the Hubbard-Holstein model. . 142
9.6 A comparison between the Hubbard-Holstein model and an effective Hubbard model. 143
9.7 The single particle spectral function for the Hubbard-Holstein model. . . 144
9.8 $N(\omega)$ for the single-band Hubbard-Holstein model at half-filling. 145
9.9 Density of states for the Hubbard-Holstein model with $\Omega = 0.3t$. 146

Chapter 1

Introduction

1.1 High-Temperature Superconductivity

The pursuit of an understanding of high-temperature superconductivity (HTSC) in the copper oxide family of transition metal oxides is one of the most intriguing questions of modern condensed matter physics. However, despite more than 20 years of research since their initial discovery in 1986 by Bednorz and Müller [1], there is still no clear consensus on the underlying physics of these systems and no comprehensive microscopic theory exists. In fact, not only does the theory of Bardeen, Cooper and Schrieffer (BCS Theory) [2, 3, 4] fail to provide an accurate description of the superconducting state but even the traditional mechanism for electron pairing - a net attraction mediated by a phonon - is generally thought to be inappropriate. Furthermore, superconductivity aside, the cuprates still represent a serious challenge to the community in that even the normal state properties of these materials are not well understood.

It is generally accepted that the principle barrier to understanding the physics of the cuprates is due to the fact that they are members of a class of systems with strong electron-electron (el-el) interactions known collectively as "strongly correlated systems". In such systems the el-el interaction is strong enough that the traditional Fermi Liquid picture breaks down and the system can no longer be regarded as a sea of nearly free quasi-particles in a band. As a result, a number of new theoretical techniques such as Quantum Monte Carlo (QMC) methods, along with refinements in experimental techniques such as Angle-Resolved Photoemission Spectroscopy (ARPES), have been developed. Although understanding HTSC may open the door for manufacturing materials with still higher T_c's it is clear that the last 20 years of research have been fruitful if only for these advances.

One point of view regarding the cuprates is that their complexity is the result of a number of competing interactions, which are brought in and out of play by various factors

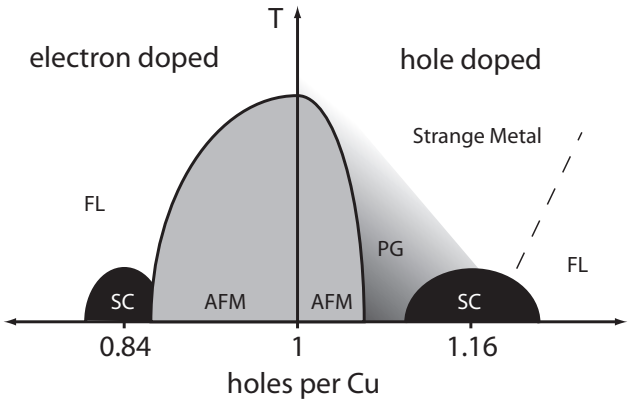

Figure 1.1: The generalized temperature-filling phase diagram of the high-T_c cuprates.

including doping, pressure and temperature. This is exemplified in the "universal" phase diagram for these materials. The now familiar temperature-doping phase diagram for the hole- and electron doped cuprates is shown in figure 1.1. The undoped parent compounds are charge transfer insulators displaying long range anti-ferromagnetic (AFM) order up to a rather high Néel temperature. As the system is doped with carriers the magnetic order is suppressed and superconductivity emerges at low carrier concentrations. With continued doping T_c continues to rise until an optimal doping of ~ 1.16 carriers/ Cu atom is reached. Beyond this point further doping only serves to suppress superconductivity.

The region between the AFM and superconducting dome is referred to as the pseudogap phase - an anomalous region where many properties, including portions of the Fermi surface are gapped out but superconducting order does not appear to be present. The presence of the pseudogap has been interpreted in one of two ways; 1) the pseudogap is a precursor to the full superconducting energy gap, where the system has a strong pairing interaction but lacks phase coherence [5] or 2) it is a distinct energy gap due to some sort of competing but presently hidden order such as a charge- or spin-density wave [6, 7]. At present, the debate over the one or two-gap issued is ongoing and serves as an example of the unusual normal state properties of the high-T_c cuprates.

Above the superconducting dome is a region where strange metallic behaviour begins to emerge which does not conform to the traditional Fermi liquid picture. For example, this region is characterized by a resistivity which famously varies linearly with temperature T [8] as opposed to the T^2 dependence predicted by Fermi liquid theory [9, 10]. For this reason this region is often referred to as a "marginal Fermi liquid". Finally, on the overdoped side of the phase diagram the cuprates begin to conform well to the Fermi-liquid description. Each of these regions of the phase diagram is an active field of research and the breadth of physics to be explored is large. In the case of electron doping,

the AFM phase extends far further and possibly makes contact with the superconducting phase. Furthermore, it is unclear if there is a corresponding pseudogap phase in the electron doped cuprates [11]. Finally, in the normal state, the electron- doped cuprates also appear to conform closer to the expectations of Fermi liquid theory as indicated in figure 1.1.

All of these areas of the phase diagram are being actively examined by various members of the community and understanding the physics of the cuprates is clearly an immense endeavour. This thesis will focus on a single aspect of the cuprate problem - that of the role of the electron-phonon interaction. In the early days of high-T_c a sort of consensus emerged in the community with the belief that phonons played a negligible role. However this conclusion may have been premature. Thanks to a number of experimental advances in the past 20 years a number of probes have uncovered evidence for a significant el-ph interaction across whole families of cuprates. As a result, a number of research groups have brought the question of phonons back to the forefront of high-T_c research. However, before proceeding to a review of the pertinent experiments and theoretical work, a more general review of the properties of the cuprates is in order.

1.2 Properties of the High-T_c cuprates

1.2.1 Crystal Structure

The crystal structure of the Hg-family of high-T_c cuprates $HgBa_2Ca_{n-1}Cu_nO_{4n+\delta}$ is shown in figure 1.2. This structure is representative of the other families of cuprates in that these are quasi-two dimensional materials consisting of one or more CuO_2 planes situated between rock salt layers (in this case the BaO/HgO layers). Traditionally these layers are thought of as charge reservoirs for accepting interstitial or substitutional dopant atoms. Such dopants donate or accept charge to the CuO_2 layers, where the low energy physics occurs, and it is through this doping process that a number of the interesting properties of the cuprates emerge. However, the introduction of these dopant atoms has additional effects, which will be discussed in greater detail later in this work.

In the normal state these materials exhibit a strong anisotropy in transport and are poor conductors along the *c*-axis perpendicular to the planes. Furthermore, experiments indicate that superconductivity is largely confined to the CuO_2 planes [12] and for this reason many theoretical models have focused on CuO_2 plane and neglected the remainder of the crystal. However, in recent years this picture has begun to change and there is an increasing amount of evidence pointing to the importance of the *c*-axis structures and other off-plane effects. This is perhaps unsurprising since the maximum T_c obtainable with doping varies dramatically from material to material. As the number of CuO_2 layers

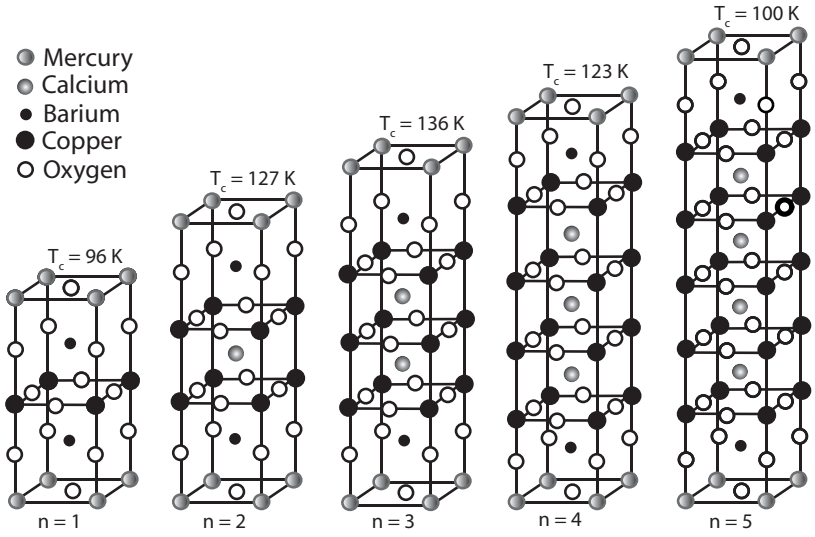

Figure 1.2: The crystal structure of the $HgBa_2Ca_{n-1}Cu_nO_{4n+\delta}$ ($n = 1 - 5$) family of high-T_c cuprates.

n is varied, T_cs at optimal doping increase until $n = 3$ and decrease beyond this point. Within a fixed number of layers, T_c can be varied quite substantially as the atoms in the charge reservoir layers are changed. In the single layer systems this effect can be quite dramatic where T_c varies by a factor of three. The role of off-plane effects will resurface as a recurring theme throughout this work.

1.2.2 Electronic Structure in the Normal State

Much of the low energy physics in the cuprates occurs within the CuO_2 planes in bands formed by the Cu and O atoms. Copper is a transition metal ion and, in the atomic limit, it has a partially filled $3d^9 4s^1$ valence state. In forming the solid the weakly bound Cu $4s$ electron is liberated leaving the partially filled $3d$ orbital to hybridize with the ligand oxygen atoms. Similarly, charge from the rock salt layers fills the O $2p$ orbitals leaving them with a $2p^6$ shell in the atomic limit. As shown in figure 1.2, the Cu atoms of the outermost layers occupy an octahedral environment centred between 6 ligand oxygen atoms (or 5 in multi layer systems). The crystal field generated by this ligand oxygen configuration lifts the five-fold degeneracy of the $3d$ orbitals separating them into the e_g doublet and t_{2g} triplet, as shown in figure 1.3.

The Cu^{2+} ion is a well known Jahn-Teller ion [13] and in the cuprates this leads to an elongation of the octahedron along the c-axis. The degree of elongation will vary

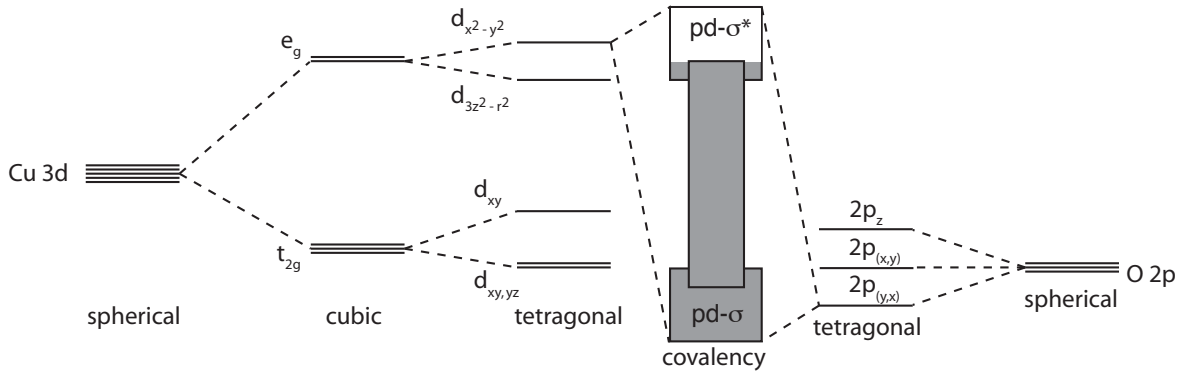

Figure 1.3: A schematic of the orbital energy levels and covalent bonding in the CuO_2 plane. Adapted from reference [13].

from material to material with the details of the environment, and it lifts the remaining degeneracy of the e_g, t_{2g} orbitals leaving the $3d_{x^2-y^2}$ orbital lying highest in energy. The crystal field of the tetragonal environment also lifts the degeneracy of the three O $2p$ orbitals. Covalency effects then hybridize the orbitals, forming bands. The highest lying partially filled band is the *pd-*σ^* band composed of the Cu $3d_{x^2-y^2}$ and the O $2p_{x,y}$ orbitals. These are the standard set of orbitals considered in multi-band tightbinding models for the cuprates. From the simple valence consideration given above, one expects that the undoped parent compounds of the cuprates will have a single hole per CuO_2 unit, leaving the *pd-*σ^* band half filled. For this reason, this electronic configuration is generically referred to as "half-filling".

Based on the considerations above, one would expect the half-filled case to be metallic. This expectation is confirmed by density functional theory (DFT) calculations using the local density approximation (LDA). However, the parent (half-filled) compounds are universally observed to be insulators displaying a long-range anti-ferromagnetic order. This is due to a strong el-el interaction present in transition metal ions which were neglected in the considerations thus far. Due to the electron's high angular momentum, the $3d$ wavefunction is spatially confining, and two electrons placed into these orbitals cannot separate far from each other. They therefore exert a strong Coulomb interaction upon one another and a large Coulomb energy must be paid to place two electrons into these orbitals. In the case of the half-filled cuprates the el-el interaction localizes the hole in the Cu $3d_{x^2-y^2}$ orbital, resulting in an insulating state. However, once the system is doped with additional holes/electrons this barrier is removed and properties illustrated in the phase diagram begin to emerge. The manner in which the cuprates are doped away from the half-filled parent insulator will be discussed in greater detail in chapter 9.

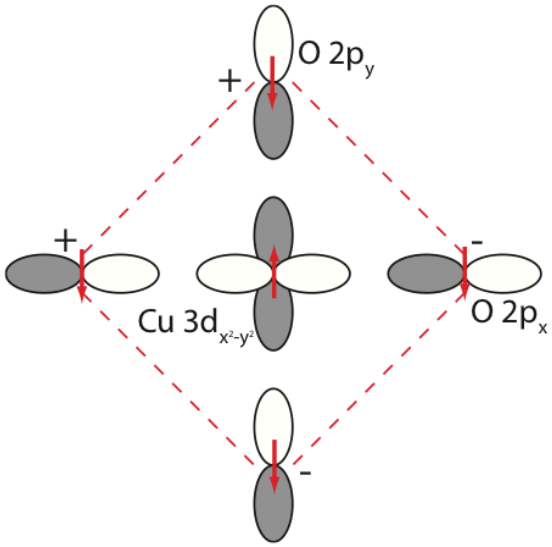

Figure 1.4: A schematic picture of the Zhang-Rice Singlet (ZRS).

1.2.3 The Zhang-Rice Singlet

The physics of the underdoped high-T_c cuprates is thought to be that of a doped Mott insulator [5]. Early on, Zhang and Rice showed a doped hole introduced to the antiferromagnetically ordered CuO_2 plane of the parent system will primarily form a superposition on the planar ligand oxygen sites [14]. The doped hole forms a local singlet with the localized hole on the Cu $3d_{x^2-y^2}$ site and the phase of the ligand hole alters, as shown in figure 1.4, in order to maximize its kinetic energy. This object is commonly referred to as the Zhang-Rice Singlet and is thought to be the basic building block of the low-energy excitations of the underdoped cuprates. Implicitly, when one works with down-folded single-band models such as the single-band Hubbard or t-J model, where the oxygen degrees of freedom have been integrated out, the carriers are thought to be ZRSs free to move on a reduced square lattice.

1.3 Beyond the CuO_2 Plane

As alluded to in section 1.2.1, there are increasing indications that c-axis structures and effects off of the CuO_2 plane are important to understanding the physics of the cuprates. The most obvious example of this is the variation of T_c with material composition which was previously discussed. It is also empirically known that the location of out-of-plane cation dopants with respect to the apical oxygen site can have a dramatic effect on how rapidly T_c is suppressed [15, 16, 17] and, in comparison, in-plane dopants have much less of an impact on T_c.

T_c has also been empirically linked to the Madelung energy difference between the apical and planar oxygen sites $\Delta\Phi_A$ (or the Cu-Apical O bond distance) [18]. This has been supported by the recent ARPES studies on the multi-layer $Ba_2Ca_3Cu_4O_8F_2$ systems, where the apical O has been replaced with F [19, 20, 21], resulting in a vastly different T_c than in its counterparts with apical oxygens. Theoretical work has linked $\Delta\Phi_A$ to the in-plane next nearest neighbour hopping of the ZRS t'. Pavarini *et al.* have shown that the maximal T_c in a given family scales with t' [22]. This is due to an increase in the apical $2p_z$-Cu $4s$ hybridization with smaller $\Delta\Phi_A$. A strong $2p_z$-$4s$ hybridization raises the energy of the Cu $4s$ orbital relative to the pd-σ^* band and reduces the effective O-O hopping via the $4s$ pathway. Therefore, the further away the apical sits from the CuO_2 plane, the higher the effective t'. T_c has also been linked to an increase in the overall magnitude of the coupling to the apical phonon mode which can be detrimental to d-wave pairing via the phonon's contribution to pairing in the s-wave channel [23].

Scanning Tunneling Microscopy has also linked in-plane electronic properties to off-plane structures and dopant atoms. For example, STM has mapped the location of out-of-plane oxygen dopants in $Bi_2Sr_2CaCu_2O_{8+\delta}$ (Bi-2212), and correlated these positions [24] with features in the local density of states. This has been interpreted as an increase in the local superconducting pairing potential by the dopant atom [25, 26, 27, 28]. Furthermore, real space modulations in the superconducting gap have been linked to supermodulation effects in Bi-2212 [29].

All of these observations are difficult to reconcile with intrinsically planar models and point to the need for considering off-plane effects. This need has been underscored by the growing recognition of the importance of c-axis polarized oxygen phonon modes in the cuprates [30, 31, 32, 33].

1.4 Phonons in HTSC

The original intuition by Bednorz and Müller was that HTSC would be caused by a strong el-ph interaction with modes associated with the Jahn-Teller distortion in transition metal oxides [1]. However, in the early days of high-T_c the idea of phonon mediated pairing was abandoned by many in favour of electronic pairing mechanisms. This is a possibility that has been pursued heavily by the community, be it in the form of a boson exchange analogous to phonons [34, 35], or an instantaneous mechanism associated with single formation in the doped AFM such as the Resonating Valence Bond scenario proposed by Anderson [36, 5].

In general, the role of phonons has been thought to be minimal. This is largely due to several early experiments suggesting weak el-ph coupling in the cuprates. These include the small isotope effect at optimal doping [37, 38, 39] and the apparent absence of

effects from phonons in the temperature dependence of the resistivity [40, 41]. However, continued isotope experiments have shown that a substantial isotope effect, even in excess of the $\alpha = 0.5$ value predicted by BSC theory, occurs in underdoped samples [42, 43]. This seems to indicate that phonons are playing a role of some kind in the cuprates, and this role is more pronounced in the underdoped region of the phase diagram.

It has also been argued that the d-wave nature of the superconducting gap does not support a phonon pairing mechanism, since all known phonon-mediated superconductors exhibit an s-wave energy gap. However this does not immediately preclude phonons in the cuprates. For example, it has been shown that the el-ph vertex for coupling to two c-axis oxygen phonon modes in the cuprates is attractive in the d-wave channel due to the charge-transfer nature of the coupling [30, 44]. Renormalization effects can enhance coupling in the d-wave channel if the remormalization enhances the forward scattering peak in the el-ph interaction over the interaction at large momentum transfers [45, 46]. Indeed, several works have shown that the effects of strong correlations will do just that, suppressing the backward scattering peak at a rate faster than the forward scattering peak [45, 47]. As will be demonstrated in chapter 6, the effects of poor screening in the cuprates can contribute to the d-wave channel of the el-ph vertex by a similar enhancement (suppression) of the small (large) $\mathbf{q}$ scattering. This renormalization may also explain why the el-ph coupling is absent from the transport measurements.

Additional compelling evidence for the importance of phonons in the high-T_c cuprates comes from angle-resolved photoemission (ARPES) experiments. ARPES has uncovered bandstructure renormalizations which have been interpreted as due to el-boson coupling, with phonons being a likely candidate. Similar signatures have been observed in scanning tunneling microscopy experiments in the form of modulations in the tunneling derived density of states. The tunneling experiment is analogous to the pioneering work by McMillian and Rowell [48, 49, 50] and the ARPES work has been considered as an angle resolved equivalent. Furthermore, workers in both fields have found that these signatures exhibit a clear ^{18}O isotope shift lending further support to the importance of the el-ph interaction. In addition to this, a recent ARPES study on the parent compound of the electron-doped cuprate $Ca_2CuO_2Cl_2$ uncovered broad spectral features at high binding energy, normally associated with the lower Hubbard Band. The shape of this lineshape does not conform to the expected Lortenzian form but rather is gaussian [51]. This has been interpreted as a Franck-Condon sideband due to the formation of small polarons.

Since many of these experimental observations are the focus of this work, a more detailed discussion of the evidence gathered by ARPES and STM will be given in the following chapter. However, for the reasons given here it is clear that the issue of the el-ph interaction in the cuprates is unresolved. Furthermore, due to the complex nature of the cuprates, understanding the exact role of phonons in these materials is a worthwhile undertaking as there is great potential for non-intuitive and interesting physics.

1.5 Scope and Organization

This thesis sets out to examine the role of el-ph interactions in the high-T_c cuprates using a combination of analytical and numerical techniques. The overall organization is as follows. In **chapter 1** (this chapter) focus is placed on introducing superconductivity in the cuprates and presenting some of their basic properties as well as a brief discussion of the general arguments for and against the consideration of the phonons in these materials.

In **chapter 2** a more comprehensive review of the literature will be conducted. This will begin with a review of experimental data pertinent to el-ph coupling in the cuprates. Here, focus will will be placed on data obtained from Angle-resolved photoemission spectroscopy and scanning tunneling microscopy, however neutron, infra-red and Raman spectroscopy results will also be briefly discussed.

Chapters 3 and 4 will present aspects of the theory of el-ph coupling in the high-T_c cuprates within the framework of Migdal-Eliashberg theory, which is generally applicable in the optimal and overdoped cuprates where the effects of correlations have been reduced by doping. Chapter 3 will focus on the derivations of the el-ph vertices for coupling to the relevant optical oxygen modes as well as the expressions for the self-energy. This formalism will then be applied to understanding the anisotropy of the couplings and the manifestation of this anisotropy in the single particle spectral function. In chapter 4 the finer details of the temperature, doping and materials dependence of the renormalizations observed in the high-T_c cuprates will be examined. This effort will provide a means to distinguish between the various proposed mechanisms for the band renormalizations. Here, it will be shown that the coupling to the spectrum of oxygen phonon modes is the most consistent interpretation given the available data.

In **Chapter 5** attention is turned to the role of el-ph coupling in modulating the density of states as probed by STM. Here, focus will be placed on understanding the difference in phonon mode estimates obtained by STM and ARPES experiments as well as what can be learned by the qualitative structure of these renormalizations in the density of states.

Chapter 6 will examine the role of poor screening in the cuprates with the goal of understanding how the quasi-2D nature of the cuprates directly affects the screening of the el-ph interaction as a function of doping. It will be shown that as the system is progressively overdoped the contribution to d-wave pairing provided by the phonons is enhanced. Following this, considerations of the phonon's role in d-wave pairing will be considered with a straight-forward multi-well model for T_c. In doing so, a framework for understanding the variations in T_c across the families of cuprates will be formulated.

In **Chapter 7** a departure from the analytical methods used up to this point will occur as the impact of local dopants is explored in an ideal Bi-2212 crystal. Here,

using exact diagonalization on small multi-band Hubbard clusters, it will be shown that oxygen dopants modify a number of properties of the cuprates and an entanglement of the lattice and magnetic degrees of freedom occurs, locally modifying the antiferromagnetic exchange energies J and J', as well as the mobility of the ZRS through the dopant's impact on the *lattice* degrees of freedom.

This focus on numerical results for el-ph coupling in strongly correlated systems will continue in **chapters 8 and 9** as attention is turned to Determinant Quantum Monte Carlo results on the Hubbard-Holstein model. The Hubbard-Holstein model is the simplest model which includes both el-el and el-ph interactions. Here, focus will be placed on the half-filled and nearly half-filled systems representative of the underdoped side of the phase diagram. Chapter 8 will present the details of the method while Chapter 9 will present the results of these calculations as well as provide a brief review of the literature on the subject of el-ph coupling in strongly correlated systems.

Finally, in **chapter 10**, conclusions will be presented as well as discussion of possible extensions of this work in the future.

Chapter 2

Experimental Evidence for Electron-Phonon Coupling

In recent years the role of electron-phonon (el-ph) coupling in the cuprates has returned to the forefront of active research. This is due to the growing pool of experimental evidence indicating the importance of the el-ph interaction. In this chapter the available data will be reviewed. This will motivate the study of the el-ph interaction in the cuprates and provide an experimental foundation in which the theories presented in this work can be cast. The primary experimental techniques discussed will be angle-resolved photoemission spectroscopy (ARPES) and scanning tunnelling microscopy (STM) due to the wealth of data currently available. However, in the final section of this chapter other probes such as neutron scattering, optical conductivity and Raman scattering will be briefly discussed.

2.1 Angle-Resolved Photoemission Spectroscopy

Angle-resolved Photoemission Spectroscopy (ARPES) has emerged as an invaluable tool for probing the electronic structure of materials [52]. In the field of high-T_c superconductivity ARPES has provided a number of key insights including the mapping of the Fermi surface [53], the determination of the d-wave gap structure in the superconducting state [54], the observation of the pseudogap [6, 7, 55] and, most recently, the observation of dispersion renormalizations throughout the Brillouin zone [21, 56, 57, 58, 59, 60, 61, 62, 63, 31, 64].

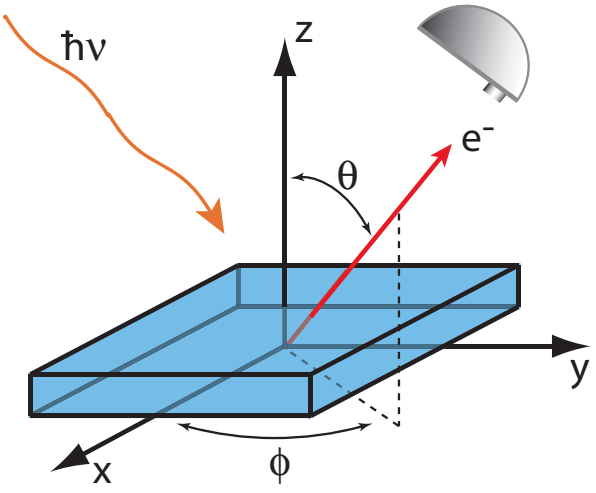

Figure 2.1: A cartoon picture of a typical ARPES setup.

2.1.1 Experimental Setup

ARPES is a photon-in electron-out spectroscopy which exploits the photoelectric effect to probe the electronic structure of a material. In an ARPES experiment, shown in figure 2.1, a photon is directed at the sample where it is absorbed by an electron in quasiparticle state $|\mathbf{k}, \omega\rangle$. If the electron is given sufficient energy to overcome the work function it is ejected and collected by a positionable detector at a solid angle (θ, ϕ). Energy and momentum conservation are then used to infer information about the electron's original state including its binding energy and crystal momentum. During the photoemission process only the component of the electron's momentum parallel to the surface of the sample is conserved [52, 32]. Therefore, ARPES is ideally suited for quasi-two dimensional materials such as the high-T_c cuprates.

The photoemission process is often thought about in terms of a "three step" model [32]: (1) the electron in the n-body state Ψ_i^n is first exited by the photon in the bulk of the material, (2) the electron then travels to the surface of the material where it is ejected paying an energy cost equal to the work function Φ of the material and (3) the electron travels to the detector where it is collected. A further conceptual simplification is often made, reducing this to a single step from excitation of the bound state to collection of the photoelectron. The photoelectron is assumed to have exited the sample quickly enough that the system does not relax (the so-called "sudden approximation" [52]) and the final state wavefunction can be written as $|\Psi_f\rangle = |\psi_p(\mathbf{k})\rangle|\Psi^{n-1}\rangle$ where $|\psi_p\rangle$ is the plane wave state of the photoelectron and $|\Psi^{n-1}\rangle$ is the final $n-1$ particle state left in the sample. In this framework, the magnitude of the photocurrent I is given by [52, 32]

$$I \propto A(\mathbf{k}, \omega)|M(\mathbf{k}, \omega)|^2 n_f(\omega) \tag{2.1}$$

where $|M(\mathbf{k}, \omega)|^2$ is the dipole matrix element for photoemission, n_f is the Fermi function

and $A(\mathbf{k},\omega)$ is the single-particle spectral function. $A(\mathbf{k},\omega)$ is a fundamental quantity in many-body theory and the utility of ARPES stems directly from its ability to probe this quantity.

Before proceeding to the experimental data it is useful to briefly review the Green's function formalism for a superconducting material[1]. In Nambu notation (with $\hat{\tau}_i$ the usual Pauli matrices), the Green's function is given by [9]

$$\hat{G}(\mathbf{k},\omega) = \hat{G}_0(\mathbf{k},\omega) - \hat{\Sigma}(\mathbf{k},\omega) \tag{2.2}$$

$$= \frac{\omega Z(\mathbf{k},\omega)\hat{\tau}_0 + [\epsilon(\mathbf{k}) + \chi(\mathbf{k},\omega)]\hat{\tau}_3 + \phi(\mathbf{k},\omega)\hat{\tau}_1}{[\omega Z(\mathbf{k},\omega)]^2 - [\epsilon(\mathbf{k}) + \chi(\mathbf{k},\omega)]^2 - \phi^2(\mathbf{k},\omega)}, \tag{2.3}$$

where $\hat{G}(\mathbf{k},\omega)$ and $\hat{G}_0(\mathbf{k},\omega) = [\omega\hat{\tau}_0 - \epsilon(\mathbf{k})\hat{\tau}_3]^{-1}$ denote the 2×2 matrix propagators for the dressed and bare electrons, respectively, $\epsilon(\mathbf{k})$ is the band dispersion of the non-interacting system, and $\hat{\Sigma}(\mathbf{k},\omega)$ is the self-energy written in the canonical form [9, 65]

$$\hat{\Sigma}(\mathbf{k},\omega) = \omega[1 - Z(\mathbf{k},\omega)]\hat{\tau}_0 + \chi(\mathbf{k},\omega)\hat{\tau}_3 + \phi(\mathbf{k},\omega)\hat{\tau}_1 \tag{2.4}$$

Here, $\omega[1 - Z(\mathbf{k},\omega)]$ and $\chi(\mathbf{k},\omega)$ the odd and even components of the single-particle self-energy and $\phi(\mathbf{k},\omega)$ is the anomalous self-energy of the Cooper pair. In the weak coupling limit $Z(\mathbf{k},\omega) = 1$, $\chi(\mathbf{k},\omega) = 0$ and $\phi(\mathbf{k},\omega) = \Delta(\mathbf{k})$, where $\Delta(\mathbf{k})$ gives the momentum structure of the superconducting gap with $\Delta(\mathbf{k}) = \Delta_0[\cos(k_x a) - \cos(k_y a)]/2$ in a d-wave superconductor [9]. In this limit $\hat{G}(\mathbf{k},\omega)$ is then given by

$$\hat{G}(\mathbf{k},\omega) = \frac{\omega\hat{\tau}_0 + \epsilon(\mathbf{k})\hat{\tau}_3 + \Delta(\mathbf{k})\hat{\tau}_1}{\omega^2 - E^2(\mathbf{k})} \tag{2.5}$$

where $E^2(\mathbf{k}) = \epsilon^2(\mathbf{k}) + \Delta^2(\mathbf{k})$ is the Bogoliubov quasiparticle energy. Finally, the spectral function, as probed by ARPES, is related to the single-particle Green's function $A(\mathbf{k},\omega) = -\frac{1}{\pi}\mathrm{Im}G_{11}(\mathbf{k},\omega)$.

This formalism can also be extended by setting the anomalous self-energy $\phi(\mathbf{k},\omega)$ to zero. In this case the spectral function reduces considerably

$$A(\mathbf{k},\omega) = -\frac{1}{\pi}\frac{\mathrm{Im}\Sigma(\mathbf{k},\omega)}{(\omega - \epsilon_{\mathbf{k}} - \mathrm{Re}\Sigma(\mathbf{k},\omega))^2 + (\mathrm{Im}\Sigma(\mathbf{k},\omega))^2}, \tag{2.6}$$

where $\Sigma(\mathbf{k},\omega) = \omega[1 - Z(\mathbf{k},\omega)] + \chi(\mathbf{k},\omega)$ is the self-energy in the normal state. For the non-interacting system $\Sigma(\mathbf{k},\omega)$ is zero and $A(\mathbf{k},\omega)$ reduces to a δ-function $A(\mathbf{k},\omega) = \delta(\epsilon_{\mathbf{k}} - \omega)$. In other words, the state $|\mathbf{k},\omega = \epsilon_{\mathbf{k}}\rangle$ is an eigenstate of the system. In the interacting case this is no longer so and $\Sigma(\mathbf{k},\omega)$ is non-zero. The state $|\mathbf{k},\omega\rangle$ becomes a

[1]This subject will be discussed in greater detail in the following chapter and an excellent review of the subject can be found in reference [65].

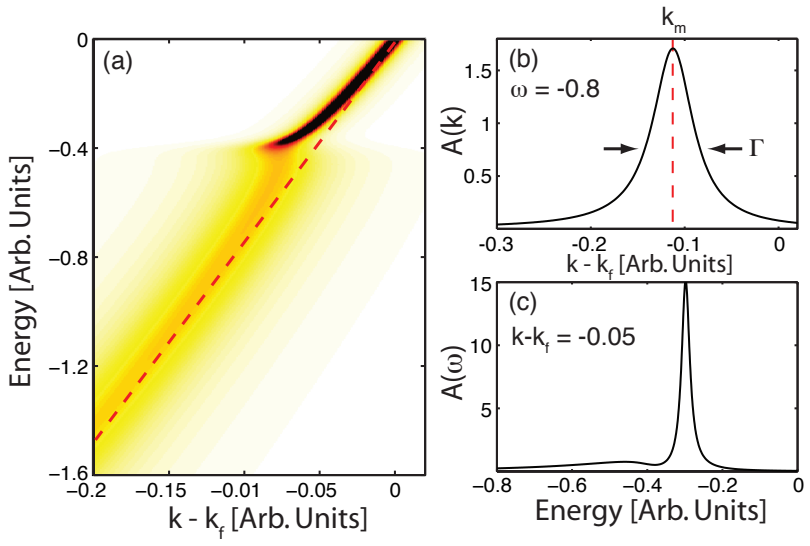

Figure 2.2: (a) A simulated ARPES spectra for an electron-phonon coupled system in the normal state. (b) A sample momentum distribution curve obtained by taking a slice of the spectra shown in at fixed energy. The red dashed line indicates the peak position of the MDC curve k_m used to define the MDC dispersion and the arrows indicate the width of the lineshape used to determine the MDC width. (c) An EDC curve obtained by taking a slice of the spectra at fixed momentum. The deviations from a lorentzian lineshape are clearly visible.

quasiparticle state with a lifetime characterized by $\mathrm{Im}\Sigma(\mathbf{k},\omega)$ and shifted in energy by $\mathrm{Re}\Sigma(\mathbf{k},\omega)$. It is through the self-energy that $A(\mathbf{k},\omega)$ encodes information about interactions in the system and by probing $A(\mathbf{k},\omega)$ one gains valuable information regarding the relevant physics of materials. This has been exemplified by the recent observation of dispersion renormalizations in the cuprates.

2.1.2 Energy and Momentum Distribution Curves

There are two common ways of performing data analysis on ARPES spectra, which are sketched in figure 2.2. The first is to examine the ARPES intensity at a fixed energy and as a function of momentum (Fig. 2.2b). This is commonly referred to as a Momentum Distribution Curve (MDC) analysis. Similarly, the momentum can be held fixed while the energy is varied (Fig. 2.2). This approach is referred to as an Energy Distribution Curve (EDC) analysis. Both techniques provide complementary information however, the MDC analysis can be used to obtain an estimate for the self-energy.

In an MDC analysis, the ARPES lineshape near the Fermi level can be fit by a

Lorentzian lineshape and the peak position k_m and linewidth Γ are obtained. The dispersion of k_m with binding energy is referred to as the MDC dispersion and it gives an approximation for the dispersion of the pole in the Green's function $\omega - \epsilon(\mathbf{k}) - Re\Sigma(\mathbf{k}, \omega)$ [52]. The MDC dispersion can therefore be used to extract an estimate for ReΣ. To do so, a form for the bare band $\epsilon(\mathbf{k})$ must be assumed. Typically this choice is taken to be a straight line connecting the Fermi level crossing to a point in the MDC dispersion at high binding energy. The difference between the assumed bare band and the MDC dispersion is then an estimate for ReΣ. An estimate for ImΣ can be obtained from the MDC line width with $\Sigma = v_k\Gamma/2$, where v_k is the band velocity.

2.1.3 Nodal and Antinodal Regions of the Brillouin Zone

In what follows references will be made to the "nodal" and "anti-nodal" regions of the Brillouin Zone. This nomenclature is common and is based on the momentum dependence of the superconducting gap. The nodal region refers to **k**-points in the vicinity of the lines $k_x = k_y$ where the superconducting gap is zero. The anti-nodal region refers to **k**-points near $(\pm\pi/a, 0)$ and $(0, \pm\pi/a)$ where the value of the superconducting gap is maximal. Here, a denotes the in-plane CuO_2 lattice spacing.

2.2 Dispersion Renormalizations in the Cuprates

Strong evidence for the importance of an electron-boson interaction in the high-$T_c$cuprates has been revealed by numerous ARPES experiments with the discovery of a "kink" in the nodal (0,0) - (π/a,π/a), dispersion and band renormalizations in the anti-nodal (0,π/a) - (π/a,π/a) dispersion of many of the cuprates [57, 31, 34, 58, 66, 67, 59, 60, 63, 68, 61, 69, 56, 70, 21, 64, 71, 72, 33, 73, 74, 75, 76, 77, 78, 62]. These band renormalizations represent an energy scale in the cuprates which has a direct impact on the low-energy physics and therefore may be related to superconductivity. It is therefore hoped that understanding the source of these renormalizations will provide important clues as to the identity of the underlying pairing mechanism in the cuprates. However, at present, the interpretation of these renormalizations is a subject of debate and a number of interpretations have been proposed. These include self-energy effects due to the Hubbard interaction [79], coupling to a magnetic excitation associated with a peak in the magnetic susceptibility at $(\pi/a, \pi/a)$ and/or a continuum of spin excitations [66, 67, 34, 75, 76] and renormalizations due to coupling to one or more phonon modes [80, 61, 30, 31, 72, 71, 33]. Each of these interpretations will be discussed in greater detail shortly, but first some of the salient experimental data is reviewed.

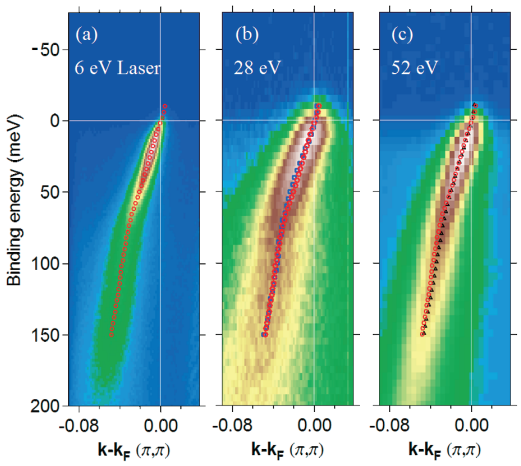

Figure 2.3: ARPES spectra along the node $(0,0)$ - (π,π) of optimally doped Bi-2212 in the superconducting state (T = 25, 26 and 16 K, respectively). The spectra were taken using different incoming photon energies: (a) 6 eV (laser system), (b) 28 eV and (c) 52 eV (both synchrotron sources). The red circles are the MDC derived dispersion for the laser data. The blue and black circles are the MDC derived dispersions obtained from the the synchrotron data. Reproduced from reference [64].

2.2.1 The Kink Feature in the Nodal Region

In the nodal region the band renormalizations take the form of a "kink" in the band dispersion, as shown in figure 2.3. In this case spectra are shown for data taken using a synchrotron light source (2.3b and 2.3c) as well as a laser source (2.3a) [64]. Superimposed on the ARPES false colour plots are the MDC derived dispersions. In all three sets of data an abrupt change in the dispersion is evident at a well defined energy scale $\sim 65-75$ meV. The first appearance of the nodal kink in the literature was in a report by Valla *et al.*, however the authors argued for a lack of a discrete energy scale and viewed the kink as a smooth curvature in the dispersion, interpreting the data as evidence for quantum criticality. The first linkage of the kink to an energy scale in the problem was later made by Bogdanov *et al.* [58].

The nodal kink is now known to be a universal feature of the high-T_c cuprates having been reported in nearly all of the hole-doped systems including $La_{2-x}Sr_xCuO_4$ (LSCO) [61, 62], $Bi_2Sr_2CuO_6$ (Bi-2201) [61, 74], Bi-2212 [57, 31, 58, 64, 61], $Bi_2Se_2Ca_2Cu_3O_{10}$ (Bi-2223) [81], $Tl_2Ba_2CuO_6$ (Tl-2201), $Tl_2Ba_2CaCu_2O_8$ (Tl-2212), $TlBa_2Ca_2Cu_3O_9$ (Tl-1223) [77], $YBa_2Cu_3O_{6+x}$ (YBCO) [67] and across the F-family, $Ba_2CaCu_2O_6(O,F)_2$ (F0223), $Ba_2Ca_3Cu_4O_8(O,F)_2$ (F0234) and $Ba_2Ca_4Cu_5O_{10}(O,F)_2$ (F0245) [21, 33]. In each case the energy scale of the kink occurs at approximately the same energy $\sim 65-75$ meV and it is now recognized as the lowest lying energy scale in the problem which has been observed universally in these systems. (Recently, a lower energy scale $\sim 8-10$ meV from the Fermi level, has been reported in optimal doped Bi-2212 but it remains to be seen if this will also be a universal feature in the dispersion of the cuprates. [82])

The typical metric for measuring the strength λ of the kink is to determine the ratio of the dispersion above and below the kink energy scale $1+\lambda = v_>/v_<$ where $v_<$ and $v_>$

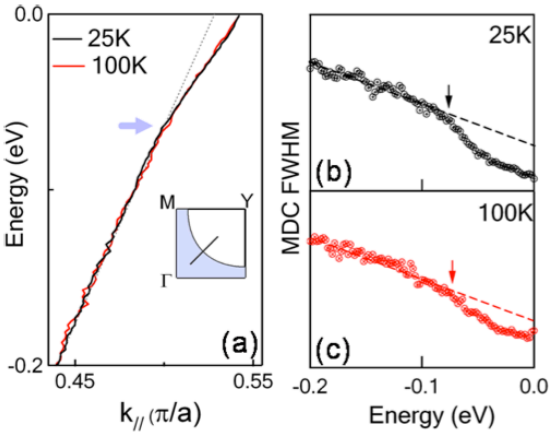

Figure 2.4: (a) MDC derived dispersions of Bi-2212, in the normal and superconducting state, observed along the nodal cut as indicated. (b) and (c) The MDC line width as a function of energy in the superconducting and normal state respectively. Reproduced from reference [83].

denote the velocity $d\epsilon/dk$ below and above the kink energy, respectively [2] [21, 61, 83]. Originally the nodal kink was only observed in the superconducting state [58] however, as instrument resolution improved it was later found to persist into the normal state albeit with a reduced strength [61, 31, 60]. Furthermore, the kink persists with progressive overdoping of the samples but the value of λ extracted from the overdoped samples is diminished with progressive overdoping [61, 62, 33].

In addition to the sudden increase in the rate of dispersion there is also an increase in the linewidth of the spectral function as the kink energy is crossed. This is not unexpected since any self-energy effects which affect the dispersion (ReΣ) must be Kramers-Kronig related to the linewidth (ImΣ). This is evident not only in the raw spectra shown in figure 2.3 but is also shown explicitly in figure 2.4 for the case of Bi-2212 in the normal and superconducting states [83]. In both cases, at the kink energy there is an increase in the linewidth of the spectral function, as indicated by the red and black arrows. The jump in the linewidth corresponds to an increase in ImΣ and is interpreted as a decrease in the quasiparticle lifetime due to the onset of a new scattering channel at this energy scale.

The temperature dependence of the nodal kink, also shown in figure 2.4, is also curious in that the position of the kink does not change with the opening of the superconducting gap [61, 31, 72, 71, 60, 83]. This is at odds with the expectations of coupling to a bosonic mode where the energy scale would be expected to shift from the boson frequency Ω in the normal state to $\Omega + \Delta_0$ in the superconducting state. Here, Δ_0 denotes the maximum value of the superconducting gap. Therefore, the observation of a constant kink energy seems to indicate that a single bosonic mode picture is inconsistent with the data. This point will be explored further in the following chapter.

[2] In the traditional framework of el-boson coupling one introduces a dimensionless coupling constant λ. The λ defined is a poor measure of this dimensionless coupling strength however it does allow one to identify trends in the coupling. This will be discussed in greater detail in chapter 3.

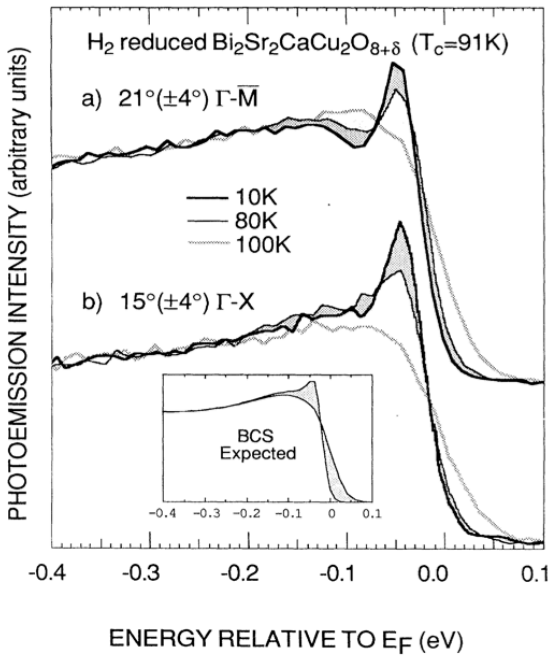

Figure 2.5: $A(\mathbf{k},\omega)$ at three different temperatures for $\mathbf{k}$ near the Fermi surface of optimal doped Bi-2212 ($T_c = 91$ K). (a) Spectra for a cut near the antinodal region. (b) Spectra for a cut near the nodal region. Each spectrum has been normalized to the intensity at $\omega = -200$ meV. Reproduced from reference [56].

2.2.2 Band Renormalizations in the Anti-Nodal Region

ARPES experiments have also observed renormalizations in the anti-nodal region of the Brillouin zone. These were first observed by Dessau *et al.* as the now famous peak-dip-hump (PDH) structure in the spectral function near $\mathbf{k} = (\pi, 0)$ in optimally doped Bi-2212, as shown in figure 2.5 [56]. In the normal state broad spectra, with no discernible peaks are observed. In the superconducting state this peak sharpens into a clear Bogoliubov quasiparticle peak. In the near nodal spectra (Fig. 2.5b) $A(\mathbf{k},\omega)$ falls monotonically at higher binding energies while in the near anti-nodal spectra a dip, followed by a hump, in $A(\mathbf{k},\omega)$ is observed. This PDH structure is reminiscent of the classic Engelsberg-Schrieffer signature of el-boson coupling to a discrete Einstein mode in a superconductor [80, 84]. In such a scenario the dip position should occur at $\Omega + \Delta_0$ and taking $\Delta_0 \sim 30$ meV, Norman *et al.* associated the PDH with a magnetic resonance mode $\Omega \sim 41$ meV which had been observed by Neutron scattering in some systems [85].

The interpretation of the PDH structure was initially complicated by the effects of bilayer splitting in the two layer system Bi-2212. However, resolution of the bilayer splitting has allowed for a separation of the two effects and the PDH structure has now been reported in a number of multilayer cuprates including Bi-2212 [31], Bi-2223, Tl-2212 and Tl-2223 [77, 33]. However, the PDH structure has not been observed in the single layer cuprates [77, 33, 86, 87, 88], as shown in figure 2.6. The absence of the PDH in the single layer systems implies that the origin for these renormalizations is constrained

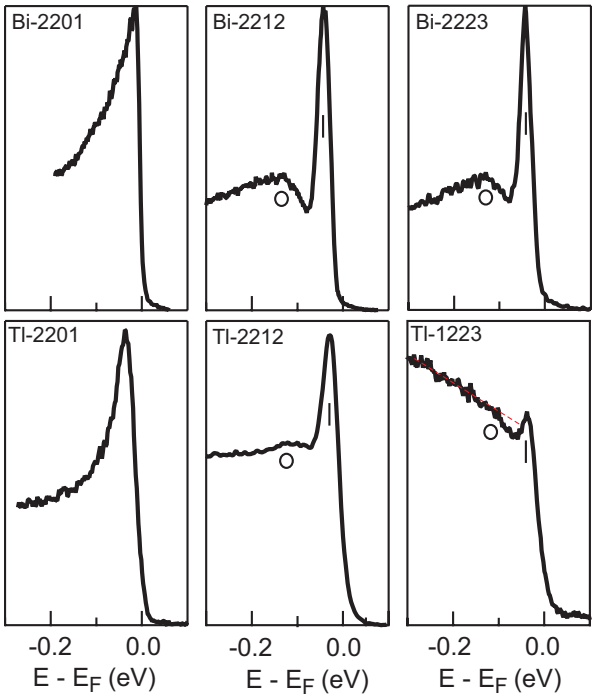

Figure 2.6: Representative EDCs near the antinodal region of the Bi- and Tl-families of cuprates, including the single-layer (Bi-2201, Tl-2201), bi-layer (Bi-2212, Tl-2212) and tri-layer (Bi-2223, Tl-1223) compounds. The high background in the data of Tl-1223 is likely due to the absence of a natural cleaving plane in the crystal structure. Nevertheless, a peak-dip-hump structure in the spectrum can still be discerned. The red dashed line is a guide-to-the-eye to make the "hump" more discernible. Reproduced from reference [33].

by the number of layers in the material. In an electron-boson scenario, this mode is either absent, or has a negligible coupling to the electrons in single layer compounds, but exhibits a prominent coupling in the multi-layer systems.

The manifestation of the PDH in the antinodal region in the raw spectra function differs qualitatively from the kink in the nodal region. Near $(0,\pi)$, the energy of the dip in the spectra, if interpreted as being due to el-boson coupling is the best measure of the energy scale of the renormalization [89, 30]. This region of suppressed weight divides the spectra into two regions, one at low binding energy, characterized by a sharp spectral function (the peak), which disperses asymptotically to the energy scale of the mode, and a broader peak at higher binding (the hump) with a weaker dispersion, as illustrated in figure 2.7.

2.2.3 Evolution from the Nodal To Antinodal Region

The kink in the nodal region and the PDH structure in the anti-nodal region indicate that the renormalizations observed by ARPES exhibit a large anisotropy. More recent studies have shown that these renormalizations are extended over large regions of the Brillouin zone and an evolution between the two regions occurs [60, 31, 69, 77]. In figure 2.7 EDCs are plotted for Bi-2212 in the superconducting state along cuts oriented parallel to the zone face and k_x fixed to values ranging from near the nodal region

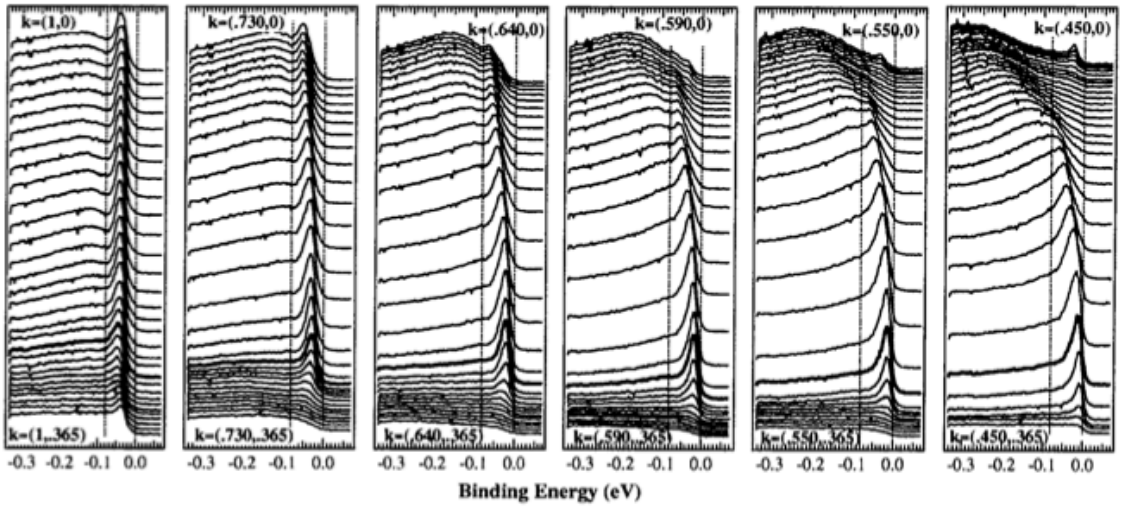

Figure 2.7: ARPES EDCs for optimal doped Bi-2212 at various points throughout the Brillouin zone. The thick black line corresponds to the Fermi momentum $\mathbf{k}_F$. Reproduced from reference [60].

to the anti-nodal region. Figure 2.7 also illustrates the extent of the renormalizations throughout the Brillouin zone. In the nodal region ($k_x = (0.45\pi/a, 0)$) the EDCs follow the trends already discussed - the peak in the EDC disperses until crossing the energy scale of the kink where it then broadens and disperses more rapidly at higher energy. This trend persists in the vicinity of the nodal cut as each cut is moved in the direction of the antinodal region. However, for intermediate points between the node and anti-node ($k_x = (0.59\pi/a, 0)$ and $k_x = (0.640\pi/a, 0)$) a crossover occurs. Here, the sharp low-energy peak begins to track asymptotically to the energy scale characterizing the kink, but with a trailing intensity, is observed. In conjunction, a broader dispersive hump structure forms at higher binding energy and the spectra begin to form the PDH structure. Moving still closer to the antinodal region, the dispersion of the sharp peak continues to flatten while the dispersion of the broader peak remains. However, despite the changes in the spectra the energy scale of the renormalization is constant throughout the zone in the superconducting state.

The first observation of deviations from the 70 meV energy scale was made by Gromko *et al.* who reported a kink in the antinodal region of overdoped Bi-2212 at an energy scale of 40 meV [63]. This lead the authors to link the anti-nodal kink to the magnetic spin resonance mode with a similar energy of $\Omega = 41$ meV in YBCO. Another important clue was reported by Cuk *et al.*, who also tracked the anisotropy of the renormalizations in optimal doped Bi-2212 and observed a change in the energy scale near the anti-node in the normal and superconducting states [31]. It was found that in the superconducting

state the 70 meV scale persisted throughout the zone but in the normal state this energy scale shifted to ~ 40 meV for the spectra near the anti-node but remained at ~ 70 meV near the node. This lead the authors to propose a scenario where two phonon modes with an anisotropic el-ph coupling interacted with electrons in different areas of the Brillouin zone [31, 30]. It is this proposal which is argued for and built upon in this work.

2.3 Coupling to a Bosonic Mode

A number of interpretations for these band renormalizations have been proposed. The most popular proposals involve coupling between the electrons of the CuO_2 planes and an underlying bosonic mode. These interpretations have attracted considerable interest in the hopes that the features seen in the ARPES spectra will act as an angle-resolved analog to the work of McMillian and Rowell on the tunnelling spectra of Pb [48, 65]. The implicit assumption here is that high-T_c superconducivity can be cast in terms of a pairing glue mediated by a bosonic mode(s). However, at this time there is considerable debate as to the identity of the bosonic mode, if it exists, and whether or not the mode(s) are relevant to superconductivity [36]. In this section the viable bosonic mode interpretations are presented and, in the following section, a purely electronic mechanism will be briefly discussed.

2.3.1 Coupling to the Magnetic Resonance Mode

The first proposal for these band renormalizations is coupling to a collective mode observed by neutron scattering near momentum transfers $\mathbf{q} = (\pi, \pi)$ [90, 59, 63, 68, 85, 91, 67, 34]. This mode is commonly referred to as the magnetic (or spin) resonance mode. It manifests itself as a peak in the magnetic susceptibility which emerges as the superconducting transition temperature is crossed [90, 92, 93, 94, 95]. The initial motivation for this proposal was the observation that both the mode and the nodal kink were originally only observed below T_c. However, since the initial proposal was made, instrument resolution has improved substantially and the kink is now known to exist in the normal state as well [31, 61, 60, 72, 71, 74].

In support of the magnetic resonance scenario, a quantitative comparison of ARPES and neutron measurements on $YBa_2Cu_3O_{6.6}$ has been made, and the overall strength of the coupling inferred from the data was indicated to be sufficient to account for HTSC [34]. However, it has been pointed out that a quantitative comparison between the spectroscopies is difficult due to the polar nature of the YBCO crystal structure (unlike the non-polar Bi- and Tl- families) which results in a heavy surface reconstruction when the sample is cleaved [33]. Such reconstructions have the potential to produce significant

differences between the bulk and surface layers of the material and can lead to inconsistencies where the Fermi surface revealed from ARPES matches that of an overdoped material, while the neutron scattering spectra used in the phenomenology was obtained on an underdoped material.

A number of other inconsistencies with the Neutron Resonance mode proposal have also been pointed out. The relatively narrow width of the mode in momentum space implies that the renormalizations should be relatively localized to impact electrons in a narrow region of the Fermi surface near the AF zone boundary. Given that renormalizations have been observed throughout the Brillouin zone it is unlikely that they are due to coupling with the magnetic resonance mode [69]. Furthermore, the appearance of the magnetic resonance mode is limited to a subset of the cuprates and is inconsistent with the materials in which renormalizations have been observed. For example, the resonance mode has not been observed in heavily overdoped Bi-2212 but has been observed in the single-layer Tl-2201 system [95]. This is at odds with the observation of the anti-nodal renormalizations in overdoped Bi-2212 [63] and the absence of the PDH in Tl-2201 [33] (Fig. 2.6).

2.3.2 Coupling to a Spectrum of Phonon Modes

An alternative proposal to coupling to the spin resonance mode is coupling to a spectrum of phonon modes [61, 31, 30, 69, 72, 71, 23, 77, 33, 74]. Here, the relevant modes are optical modes which involve the vibration of the lighter oxygen atoms and are therefore the highest lying phonon modes in energy and are sketched in figure 2.8.

Lanzara *et al.* [61] were the first to make this association linking the nodal kink to the an in-plane Cu-O bond stretching mode (figure 2.8d1,d2). These bond-stretching modes lie at an energy $\sim$ 65-75 meV at optimal doping as inferred from neutron scattering experiments [96]. Later, Cuk *et at.* [31] and Devereaux *et al.* [30] proposed a two-phonon mechanism to explain the nodal and antinodal renormalizations. In this scenario there is a conspiracy of energy scales, combined with an anisotropic el-ph coupling vertex, which results in an interplay between several phonon branches. In the normal state, the bond-stretching oxygen breathing mode is responsible for the nodal kink while the $\Omega \sim 36$ meV (determined from optical conductivity measurements [97]) bond buckling mode (figure 2.8a) is responsible for the anti-nodal PDH. With the opening of the superconducting gap ($\Delta_0 \sim 35$ meV) these modes shift to $\Omega+\Delta_0$ and the buckling mode dominates the spectra throughout the zone setting the uniform energy scale of 70 meV. The modes proposed here have been studied extensively in the context of Raman, infrared and neutron spectroscopy [98, 44, 99, 100, 92, 94]. Note that in figure 2.8 the A_{1g}/B_{1g} nomenclature of Raman spectroscopy is used for the planar c-axis modes. Strictly speaking this only holds at $\mathbf{q} = 0$, however, throughout this work the out-of-phase branch is denoted as B_{1g} and the

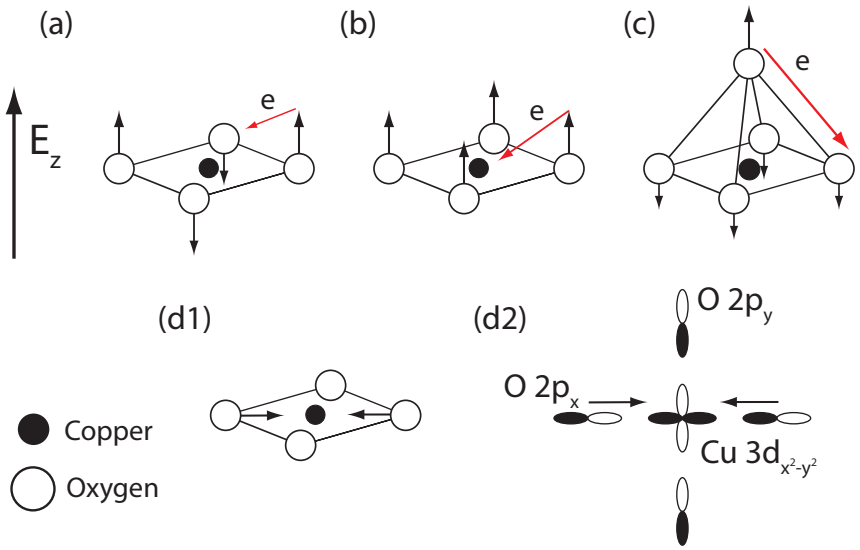

Figure 2.8: A sketch of the relevant oxygen phonon modes of the CuO_2 plane. (a) The out-of-phase planar oxygen vibration along the c-axis or B_{1g} mode. (b) The in-phase planar oxygen vibration along the c-axis or A_{1g} mode. (c) The c-axis apical oxygen vibration. (d) The in-plane oxygen vibration or half-breathing mode. A full breathing mode also occurs at $\mathbf{q} = (\pi, \pi)$ for this branch which involves displacements of the four ligand oxygens. The A_{1g}, B_{1g} and apical modes modulate the site energy of the oxygen as the atoms oscillate through a local crystal field. This results in a charge transfer coupling indicated by the red arrows. The half- and full- breathing modes are of a deformation type modulating the overlap between the Cu $3d_{x^2-y^2}$ and O $2p_{x,y}$ orbitals as shown in (d2).

in-phase branch is denoted as A_{1g}.

In the case of the c-axis modes el-ph coupling can arise due to the modulation of the atomic site energy as the ion oscillates through a local crystal field present in the system. These local fields arise due to breaking of mirror plane symmetry along the c-axis. For instance, in YBCO the Y^{3+} and Ba^{2+} ions on opposite sides of the CuO_2 plane produce a local field $\sim$ 0.8-2.1 eV/$\AA$ [101]. The motion through this field then drives the charge onto or off of the oxygen sites, as shown by the red arrows in figure 2.8. In the single layer systems, the planar oxygen atom sits in a mirror plane and the local crystal field is weak and the coupling must be of second order in ion displacement [98, 44, 102, 103]. Therefore, coupling to the c-axis planar modes such as the B_{1g} mode which is responsible for the antinodal renormalizations, is expected to be weak. This expectation is confirmed by the absence of the PHD structure in the antinodal region of the single-layer systems

(figure 2.6).

The phonon scenario has been criticized using evidence based on density functional theory (DFT), within the local density approximation (LDA). These calculations have provided evidence for a weak el-ph coupling in YBCO and LSCO [104, 105, 106, 107]. LDA predicts the total coupling of all the modes to be less than one, and when self-energies are calculated within the weak coupling limit it is found that the coupling to all modes is too small to account for the nodal kink by a factor of 3-5 [105, 106]. However, while DFT has been able to accurately predict phonon dispersions, the width of the phonon lineshapes are underestimated in most cases in comparison with experiment, sometimes by an order of magnitude [108]. This is perhaps not unexpected given that DFT predicts metallic behaviour for the undoped cuprates and over predicts the bandwidth of the *pd*-σ^* by a factor of five in optimally doped Bi-2212 [109]. These observations seem to indicate that that LDA may be the wrong formalism for describing the cuprates and therefore it is unclear that these findings explicitly rule out lattice phonons.

2.4 An Alternative Proposal: Hubbard Renormalizations

An alternative proposal has recently been made by Byczuk *et al.* based on a purely electronic origin for the kinks [79]. In this scenario, self-energy effects due to the strong el-el interactions produce changes in the quasiparticle weight at an energy scale ω^*. This in turn produces a change in width of $A(\mathbf{k}, \omega)$ and therefore the real part of the self-energy, due to its Kramer-Kronig relation to the imaginary part, develops a peak at the same energy scale, producing a kink in the bare dispersion. Since these features are due to correlation physics the kinks would be expected in any strongly correlated system and do not require the invocation of a bosonic mode. Furthermore, in this scenario the kink would be expected in both the normal and superconducting states, as observed in experiment. However, since the correlation strength is set by the charge transfer energy to move a hole from copper to oxygen sites, one would naively expect the strength and position of the renormalization to be constant throughout the zone and independent of temperature. It is therefore difficult to reconcile this proposal with the nodal/antinodal dichotomy of the band renormalizations and their temperature dependence. Furthermore, since the charge transfer energy is roughly constant across the cuprate families, this proposal does not predict a significant materials dependence to the renormalization features. This too is at odds with current experimental observations and the absence of the PDH in the single layer systems.

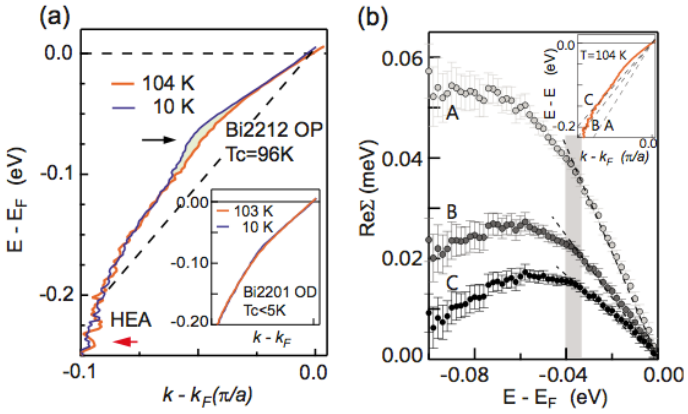

Figure 2.9: (a) The MDC-derived band dispersions of optimally doped Bi-2212 at temperatures above and below T_c. The apparent kink and the onset of the HEA are approximately indicated by the black and red arrows, respectively. The shaded area highlights the difference between the band dispersion at these temperatures. The dashed line indicates the "bare band" assumed for extracting the the ReΣ as described in the text. The inset shows the MDC derived dispersions in the case of non-superconducting Bi-2201. (b) ReΣ, extracted from the normal state MDC dispersion, using different choices for the bare band as plotted and labeled in the inset. The shaded area indicates the energy of the subkink feature associated with the second boson mode. Reproduced from reference [71].

2.5 Self-energy extraction from ARPES data: Coupling to Multiple Bosonic Modes

One aspect which distinguishes the phonon coupling scenario from the other proposals is the possibility for coupling to multiple phonon modes. If the system is coupled to more than one phonon mode then features should appear in $A(\mathbf{k},\omega)$ and $\Sigma(\mathbf{k},\omega)$ at each of the mode energies $\Omega_\nu + \Delta_0$. Indeed, there have been a number of studies indicating multiple features in estimates for ReΣ extracted from ARPES spectra in the nodal region. Zhou *et al.* were the first to report such features in optimally doped LSCO [73]. This was later confirmed in optimal and overdoped LSCO by Meevasana *et al.* when they examined the doping dependence of the self-energy in the same material [74]. A similar report of a secondary feature in the temperature-dependent nodal self-energy of Bi-2212 was later made by Lee *et al.* [71].

In order to extract ReΣ from ARPES spectra a standard procedure is applied. This procedure is illustrated in figure 2.9 for the case of optimally doped Bi-2212. First, the MDC dispersion is obtained from the raw data. These are shown as the solid lines in

figure 2.9a. Next, an underlying bare band is assumed, as indicated by the dashed lines, and the difference between the MDC dispersion and bare band is taken as an estimate for ReΣ. The choice of bare band will effect the overall magnitude of the extracted estimate for ReΣ, however the position of peaks or changes in slope in ReΣ is relatively immune to this choice, as shown in figure 2.9b. It should also be noted that the choice of bare band is complicated by the recent observation of a second band renormalization at high binding energy ~ 300 meV, commonly referred to as the high-energy anomaly (HEA, see below) or "waterfall". The presence of the HEA results in changes to the band structure and care must be taken to ensure that the choice in bare band isolates the self-energy of the low-energy kink from the self-energy effects of the HEA. Therefore, as was done in figure 2.9, the bare band is typically assumed to be a linear band connecting the Fermi surface crossing with the MDC dispersion at an energy well below the low energy kink (for example, at a binding energy of $\sim 150 - 200$ meV) but higher than the onset of the HEA ($\sim 250 - 300$ meV). With this choice, the extracted ReΣ can be viewed as an estimate for the self-energy contribution of the low-energy mode superimposed over the physics responsible for the HEA.

As shown in figure 2.9b, multiple features can be seen in the extracted self-energy in the normal state. There is the main peak responsible for the 70 meV kink as well as a "subkink", indicated by the grey box, where the slope of the extracted ReΣ shows a prominent change. Since the energy of this subkink in the normal state is $\sim 35 - 40$ meV this feature was interpreted as self-energy contribution from the lower energy B_{1g} mode. Furthermore, the temperature dependence of the subkink was found to shift with the opening of the superconducting gap as one would expect in the traditional el-boson coupling framework. This will be discussed in greater detail in chapter 4 when the temperature dependence of the el-ph self-energy is presented.

In the work of Zhou *et al.*, the ReΣ was extracted in a similar manner while a second estimate was obtained by calculating the self-energy using the standard Eliashberg formalism for el-ph coupling (see Chapters 3 and 4). Zhou *et al.* then assumed a spectrum of boson modes with spectral density $\alpha^2F(\nu)$ which was used as input to the Eliashberg formalism. An optimization procedure, based on the method of maximum entropy, was then used to generate the $\alpha^2F(\nu)$ which optimized the agreement between the calculated and extracted ReΣ [73]. This procedure produced a spectral density whose peaks had a one-to-one correspondence with peaks in the phonon density of states obtained from neutron scattering on the same material. This provided strong evidence for coupling to multiple oxygen phonons in LSCO.

Meevasana *et al.* applied a similar procedure to the doping-dependent extracted ReΣ and found that a single phonon spectral density could account for the observed ReΣ provided a filter function was applied to the strength of the low energy modes. This function $\propto \omega^2/(\omega^2 + \omega_{SC}^2)$, was chosen to simulate the decreased coupling to low-energy

modes which is expected from the increase in the material's ability to more effectively screen perturbations due to increased carrier concentrations [74]. Here, the filter function had a single adjustable parameter, the characteristic screening frequency ω_{SC}, and this simple model produced excellent agreement between the phonon density of states and the ARPES extracted ReΣ. Each of these observations supports the picture of multiple bosonic modes and directly connects these modes to the oxygen phonons in LSCO and Bi-2212.

2.6 Magnetic Resonance vs Phonon Modes: The Isotope Effect

In order to distinguish between the magnetic resonance and phonon scenarios, several oxygen isotope experiments have been carried out on Bi-2212. The first of these was reported by Gweon *et al.* who observed large shifts $\sim$ 30 meV in the nodal state spectra at high binding energies upon ^{18}O substitution [110]. Although the largest effect was observed at high binding energy, the kink position was also observed to shift by $\sim$ 3 meV as one would expect for an oxygen mode. It should be noted however that the large changes at high binding energy are in dispute and have not been reproduced by another group [111, 112] and, if the high energy isotope effect is robust then it is very sensitive to doping. Despite the dispute over the changes at high binding energy the changes in the kink position are robust and the shift in the kink position with ^{18}O substitution has been confirmed in a recent high resolution laser ARPES study [113]. The clear observation of an isotope shift in the nodal region is compelling evidence for the el-ph coupling scenario and with these observations even some of the original advocates of the spin resonance mode now conclude that the nodal kink must be due to el-ph coupling [114].

2.7 The High-Energy Anomaly

Recently, a series of high-resolution ARPES experiments, extending up to $\sim$ 1-1.5 eV in energy, have uncovered a high-energy anomaly (HEA) in the dispersion of the hole- [115, 116, 117, 118, 119, 120, 121, 122] and electron-doped [123, 124, 125, 126] cuprates. Like the low-energy kinks already discussed, the HEA has attracted considerable interest and a number of theoretical proposals have already been made. These include spin-charge separation [115], spin polarons [127], in-gap band-tails [128], coupling to a collective mode such as phonons [118], plasmons [129], or paramagnons [119, 130, 129, 131], photoemission matrix elements [120] and strong correlation or "Mott" physics [116, 79, 132, 133, 134]. Furthermore, there have also been assertions that the HEA should not be found [133] in

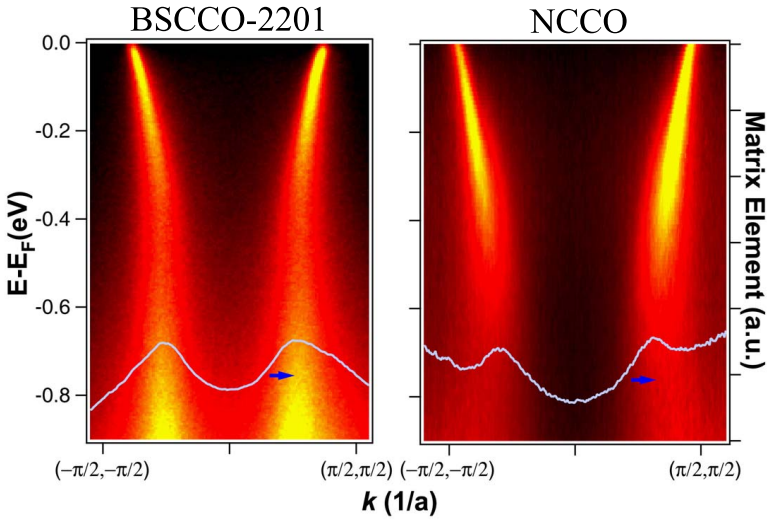

Figure 2.10: A comparison of the HEA in hole- and electron-doped systems. The left panel shows the nodal ARPES data for Bi-2201. while the right panel shows the nodal data for NCCO. The matrix element profile is shown in each panel as the blue line (see reference [136]). Although the appearance of the HEA is affected by changes in the photoelectric matrix elements, they cannot account for the strong band renormalizations.

the electron-doped cuprates. This assertion has been supported by one study [135] but is contrary to other experimental findings [123, 124, 125, 126].

False colour plots of ARPES spectra in optimal doped Bi-2201 and nearly-optimal doped $Nd_{1.83}Ce_{0.17}CuO_4$ (NCCO) are shown in figure 2.10 The HEA renormalization manifests itself as a kink or "waterfall" in the band dispersion and occurs at ~ 300 meV in the hole-doped cuprates and $\sim 500 - 600$ meV in the electron-doped cuprates. At low energies, the electronic dispersion tracks downward in energy following a band which appears to be shallower than that predicted by LDA [84, 109]. Extracted EDC dispersions follow this shallow band, tracking to the Γ-point as weight is reduced by matrix elements and self-energy effects [116, 126]. (Estimates for the value of the photoemission matrix element [136] are shown as the blue line in in figure 2.10.) At the energy scale of the HEA the false colour spectra undergo a sudden vertical drop while the width of the spectra significantly broadens. This gives rise to the "waterfall" appearance in the dispersion, shown in figure 2.10. MDC derived dispersions track this waterfall feature in the band dispersion and show that the lower, incoherent portion of the band lies at an energy greater than that predicted by LDA, as one would expect for a strongly correlated system. Finally, the degree to which the shallow, low-energy band can be seen in the data can be altered through the use of different photon energies [120, 126] or by probing the spectra

in the second Brillouin zone [120].

Coupling to phonons can be ruled out based on the relatively high energy scale of the HEA. Coupling to spin fluctuations or magnons is generally consistent with the energy scale of the HEA based on antiferromagnetic exchange energy $J \sim$ 100-150 meV. However, this interpretation is unable to account for the difference in the energy scale in the hole- and electron-doped cuprates. Recent quantum Monte Carlo calculations have shown that the HEA can be thought of a crossover point between the coherent quasiparticle band formed by doping the Mott insulator and the incoherent lower Hubbard band which is present due to strong correlations [126, 121, 123]. This proposal is able to account for the dichotomy in the electron- and hole-doped materials and will be discussed in further detail in chapter 8, when the spectral properties of the Hubbard and Hubbard-Holstein models are presented.

2.8 Scanning Tunnelling Microscopy

Scanning Tunnelling Microscopy (STM) is a complementary probe to ARPES in that it provides real space information about the electronic structure at the surface of a sample. In an STM experiment, a metallic tip is held at a distance (typically $\sim 1-2$ $\mathring{A}$) above the sample and a bias voltage is applied across the tip-vacuum-sample interface resulting in a tunnelling current. For a fixed distance between the tip and the sample, and an applied bias voltage V, the tunnelling current is given by [9]

$$I = 2e \sum_{\mathbf{p},\mathbf{k}} |T_{\mathbf{p},\mathbf{k},V}|^2 \int_{-\infty}^{\infty} \frac{d\epsilon}{2\pi} A_{\text{tip}}(\mathbf{k},\epsilon) A_{\text{sample}}(\mathbf{p},\epsilon+eV) \left[n_f(\epsilon) - n_f(\epsilon+eV)\right] \tag{2.7}$$

where e is the fundamental unit of charge, $A(\mathbf{k},\epsilon)$ is the spectral function and $T_{\mathbf{k},\mathbf{p}}$ is the matrix element for tunnelling through the vacuum interface. The details of the tunnelling matrix element $T(\mathbf{k},\mathbf{p},V)$ will depend on the details of the tip and sample as well as the distance between the two, however, it is typically modelled as having a weak momentum dependence. With this assumption it can be shown that the derivative of the induced tunnelling current is proportional to the density of states $dI/dV \propto N(\mathbf{r},\omega)$ of the underlying sample in the vicinity of the tip $\mathbf{r}$. A state of the art STM setup is equipped with tips which terminate at a point no more than a few atoms across. This allows most modern tunnelling microscopes to achieve a spatial resolution of less than the lattice spacing in most materials.

2.8.1 Local Inhomogeneity

STM experiments on the cuprates have indicated that these systems show a large degree of electronic inhomogeneity. This inhomogeneity occurs both in the normal and super-

conducting states and has been observed in Bi-2201 [137, 138], Bi-2212 [139, 140, 24, 141, 142], Bi-2223 [143]. Maps of the local value of the superconducting gap, obtained from the peak-to-peak distance in dI/dV spectra, show patchwork regions with varying gap magnitudes. Furthermore, the size of the local superconducting gap is also correlated with the shape of the superconducting coherence peaks; large gap regions tend to have muted coherence peaks while regions with a small gap tend to have sharp coherence peaks [24]. Furthermore, in the case of $Bi_2Sr_2CaCu_2O_{8+\delta}$, the size of the local superconducting gap has been correlated with the location of interstitial oxygen dopants [24]. Despite this correlation, however, the source of the electronic inhomogeneity is still unknown but the fact that the correlation exists again ties the local electronic properties of the CuO_2 plane to off-plane dopant atoms. This will be explored in greater detail in chapter 6 when the interplay of local oxygen dopants with local el-ph coupling is explored.

2.8.2 Bosonic Mode Coupling in STM

The dispersion renormalizations observed by ARPES in the cuprates should also be manifest in the density of states, which can näively be thought of as a sum over the ARPES spectra. Indeed, recent STM studies have found modulations in the tunnelling derived DOS of a number of cuprates. The first of these reports was made by Lee *et al.* in Bi-2212 [144]. Similar modulations have also been observed in Bi-2223 [143], which have been interpreted as being due to the spin-resonance mode. Tunnelling experiments have also been conducted on Bi-2201 and, in analogy to the ARPES studies, no clear modulation of the DOS has been seen in the data [137, 138]. In conventional superconductors, such as lead, similar modulations of the DOS have been shown to correspond to peaks in the phonon density of states and thus provided the most compelling evidence for phonon mediated pairing [65, 48]. Therefore, as with the kinks discussed previously, these modulations are expected to carry information about the underlying pairing mechanism in the cuprates.

Figure 2.11a shows a set of typical spectra reported in reference [144]. One clearly sees the progressive muting of the coherence peak in the large gap spectra, which is typical of the local inhomogeneity. A second feature can also be seen which is similar to the peak-dip-hump structure observed in the anti-nodal region by ARPES. To the right of the spectra d^2I/dV^2 is also plotted in order to highlight this feature. In analogy to the PDH structure as well as the DOS modulations in conventional superconductors, this feature was originally interpreted as due to coupling to a bosonic mode, and perhaps the same mode responsible for the ARPES observed renormalizations. In reference [144] the shoulder on the high-energy side of the dip (the maxima in the d^2I/dV^2, indicated by the black arrows) was taken as the energy scale of the bosonic mode. Taking this energy relative to the local value of the superconducting gap produces a distribution of mode energies as shown in figures 2.11b and 2.11c.

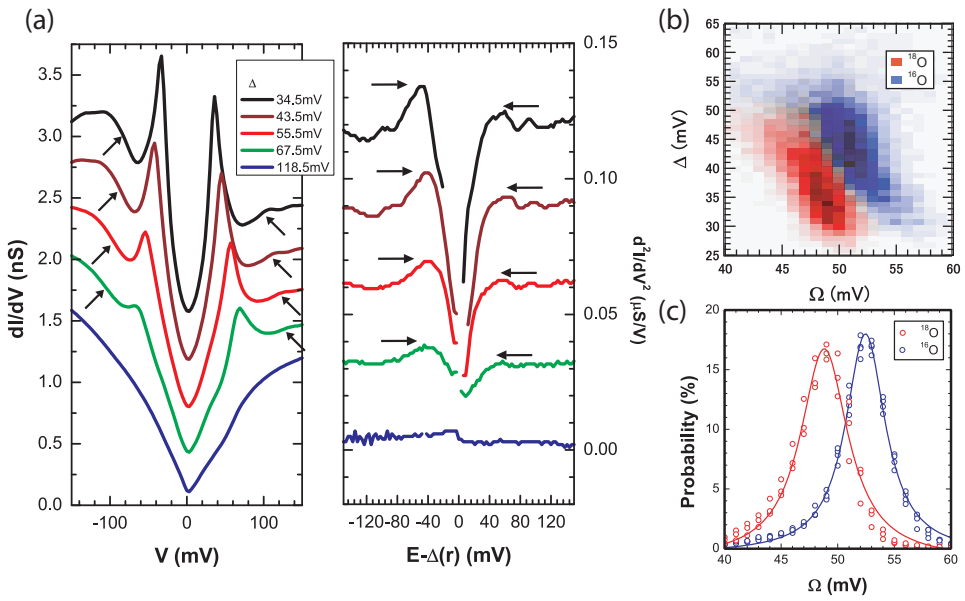

Figure 2.11: (a) Left: The STM derived DOS dI/dV for Bi-2212. Each spectra has been spatially averaged over spectra with comparable gap sizes. Right: the corresponding d^2I/dV^2 highlighting the presence of modulations in the DOS. The black arrows indicate the feature used to determine the energy of the bosonic mode. (b) The distribution of bosonic mode energies versus the corresponding gap size. (c) The probability distribution of bosonic mode energies as a function of energy. Adapted from reference [144].

There are a number of interesting observations about the extracted mode estimates, which bear directly on identification of the responsible mode. First, the distribution of mode energies is inversely correlated with the local gap size. Large gap regions tend to have smaller mode estimates, which is opposite to the expectations of BCS theory if the mode responsible for the modulations is also responsible for pairing. Second, the average mode energy is ~ 55 meV which is inconsistent with the energy scale extracted by ARPES. Jenkins *et al.*, in reference [143], have asserted that the correct feature from which the boson mode energy can be extracted is the local minima in $dI/dV \propto N(\omega)$. Once this correction is made the mode estimate falls to $\sim 35-45$ in both Bi-2212 and Bi-2223 [143, 145]. In chapter 4 the manifestation of the boson in the single-particle density of states will be examined in greater detail. It will be shown that the assertion of reference [143] is in agreement with the el-ph coupling scenario. However, it will also be shown that this observation has implications extending beyond a simple correction in the mode energy estimate. Finally, the distribution of mode estimates exhibits a clear oxygen isotope shift similar to that observed in ARPES and size of the frequency shift

is consistent with that expected for O^{18} substitution. This isotope effect is again a clear indication of a lattice origin for the renormalizations however, there is some debate as to whether this lattice effect is intrinsic to the CuO_2 plane or is arising due to cotunneling through the apical oxygen [146, 147].

Similar structures in the DOS have been reported in a number of other cuprates. Bicrystal grain boundary SIS junction measurements on optimally doped LSCO thin films observe modulations in the DOS at energy scales which correspond directly to peaks in the neutron derived phonon spectra [148]. The presence of multiple features in the DOS of LSCO is consistent with multiple energy scales observed by ARPES discussed previously [73]. Furthermore, examinations of tunneling data on YBCO and the electron doped cuprate $Pr_{0.88}LaCe_{0.12}CuO_4$ have also produced a similar correspondence between the structure in the DOS and phonon density of states in these materials [149, 150] The observation of multiple mode coupling, as well as the fact that the spin resonance mode is well separated from the phonon energies in the electron-doped systems, provides further evidence that the spin resonance mode is unlikely to be the source of these features.

2.9 Other Spectroscopies

A number of other spectroscopies have also observed evidence for strong el-ph coupling in the cuprates. Inelastic neutron scattering, a natural probe for measuring phonon dispersions and linewidths, has made a number of interesting observations [151]. For example, an anomalous softening of the in-plane bond-stretching modes as a function of doping has been reported in LSCO [96]. At optimal doping a discontinuity in the dispersion of the in-plane modes has also been reported at low temperature [152]. Furthermore, the phonon linewidths observed by neutron scattering are consistently larger, by as much as an order of magnitude, than those predicted by density functional theory in the local density approximation (LDA) [108]. Finally, in YBCO, the B_{1g} phonon has been observed to soften at the normal-to-superconducting phase transition [153].

A number of the phonon modes examined in this work are Raman active and, as one might expect, Raman spectroscopy experiments performed on the cuprates also indicate coupling to these modes. Raman experiments in YBCO show that the out-of-phase c-axis oxygen vibration exhibits a Fano lineshape, which is indicative of a coupling to electrons. Furthermore, the softening observed in neutron scattering is also observed [99, 154, 100]. The in-phase c-axis buckling and apical modes in a number of systems soften by as much as 20 cm^{-1} (a 5%-10% change) with doping as well as with temperature or as the normal-to-superconducting phase transition is crossed. This has been observed in many systems including the Hg-family $HgBa_2Ca_{n-1}Cu_nO_{4n+\delta}$ $(n = 1 - 4)$ [155, 156, 157] and $Bi_2Sr_2Ca_2Cu_3O_{10+\delta}$ [158].

The phonon renormalizations reported in these neutron and Raman studies would not be expected unless the lattice degrees of freedom were directly coupled to the electronic degrees of freedom. We have now seen that multiple probes indicate that there is a strong el-ph interaction in the cuprates. In the next chapter the theory of el-ph coupling will be presented in the framework of Migdal-Eliashberg theory. This coupling theory has been remarkably successful in accounting for the el-ph interaction in good metals and conventional superconductors. In recent years a number of workers have applied the theory to the high-T_c cuprates in the optimal and overdoped regions of the phase diagrams [30, 33, 72, 71, 23]. In the coming chapters this theory will be applied to understanding the doping and temperature dependence of the ARPES kinks. The theory will also be extended to include the effects of screening.

Chapter 3

Theory of Electron-Phonon Coupling

In this chapter the theory of electron-phonon (el-ph) coupling in the cuprates is presented. The cuprate unit cell contains many atoms and therefore a number of phonon modes are present in these materials. However, in this work, focus is placed on four optical phonon branches of the CuO_2 plane. They are the c-axis in-phase and out-of-phase planar oxygen modes (denoted A_{1g} and B_{1g}, respectively [1]), the in-plane Cu-O bond stretching modes (the half- and full-breathing), and finally the c-axis apical oxygen modes. These modes, which are sketched in figure 2.8, primarily involve the motion of the lighter oxygen atoms and therefore have the highest lying energies in the phonon spectrum. This makes them ideal candidates for the modes responsible for the dispersion renormalizations discussed in the previous chapter. Furthermore, a number of studies have indicated that these modes have a particularly strong coupling to the CuO_2 electrons. For example, the A_{1g} and B_{1g} modes have been studied extensively in the context of Raman, infrared and neutron spectroscopies [99, 100, 92, 94, 98, 44, 97] and are known to exhibit strong el-ph coupling. The apical mode shows strong renormalizations across the superconducting transition [155, 159, 157, 158], while the breathing modes exhibit a large degree softening with doping [96]. These renormalizations indicate that these phonons interact with the electrons of the system and provide direct experimental evidence for el-ph coupling to these modes.

[1] This nomenclature is due to the Raman spectroscopy and the symmetry of the modes at $\mathbf{q} = 0$ notation. For the sake of brevity, these modes will be denoted as "A_{1g}" and "B_{1g}" throughout this work.

3.1 Derivation of the Bare Coupling Constants

In general, coupling between electrons and the lattice can occur through a number of microscopic mechanisms. The first is via a deformation coupling where the atomic vibration modulates the overlap of the atomic orbitals of neighbouring atoms. This is the primary coupling pathway for the half- and full breathing modes [30, 23, 160]. A second mechanism is a charge transfer coupling. This occurs when the lattice site oscillates through a local crystal field arising from an asymmetry in the local crystal environment. In this case, the lattice vibration modulates the on-site energy of the atomic orbitals and drives charge on or off of the site. In the cuprates, the coupling to the c-axis modes is largely of this type [44, 98] however, this does not preclude a second pathway of a deformation type. If the oxygen ion sites in a plane of mirror symmetry, such as in the case of the CuO_2 planes in an ideal single layer cuprate, the Madelung energy of the site is at a local minima. The modulation of the Madelung energy energy and therefore the resulting coupling via the charge transfer channel must be of second order in displacement [44, 30, 33, 98, 102, 103]. However, steric forces may force the CuO_2 plane to buckle along the c-axis which then creates a deformation coupling to linear order in the displacement that was previously forbidden by symmetry [161]. It should also be noted that these possibilities do not exhaust the list of possible coupling mechanisms. For example, in semiconductors the piezoelectric coupling, where the atomic vibrations induce changes in the polarization of the atomic orbitals, is important [9]. However, for the purpose of this work only the deformation and charge transfer coupling mechanisms will be considered.

The first step in modelling the el-ph interaction is the derivation of the form of the matrix element $g(\mathbf{k}, \mathbf{q})$ for quasiparticle scattering from state $\mathbf{k}$ to $\mathbf{p} = \mathbf{k} - \mathbf{q}$ where $\mathbf{q}$ is the momenta transferred to the lattice. In metallic systems $g(\mathbf{k}, \mathbf{q})$ is usually momentum independent or purely a function of momentum transfer $g(\mathbf{q})$ [9]. However, in the cuprates, the form of $g(\mathbf{k}, \mathbf{q})$ depends on the details of the underlying bandstructure, the symmetry of the phonon modes and the microscopic mechanism for coupling. Once the el-ph vertex is known, the general form of the el-ph Hamiltonian can be cast in the form [9]

$$H_{el-ph} = \frac{1}{\sqrt{N}} \sum_{\mathbf{k},\mathbf{q},\sigma} g(\mathbf{k}, \mathbf{q}) c^{\dagger}_{\mathbf{k}-\mathbf{q},\sigma} c_{\mathbf{k},\sigma} (b^{\dagger}_{\mathbf{q}} + b_{-\mathbf{q}}) \tag{3.1}$$

where $c^{\dagger}_{\mathbf{k},\sigma}$ ($c_{\mathbf{k},\sigma}$) and $b^{\dagger}_{\mathbf{q}}$ ($b_{\mathbf{q}}$) are the electron and boson creation (annihilation) operators, respectively.

The starting point for deriving the form of $g(\mathbf{k}, \mathbf{q})$ is a multi-band tightbinding model for the CuO_2 plane. For coupling to the modes involving the planar oxygen atoms a three band model, including the Cu $3d_{x^2-y^2}$ and O $2p_{x,y}$ orbitals, is sufficient [44, 30, 23]. However, to derive the coupling to the apical mode the model must be extended to include

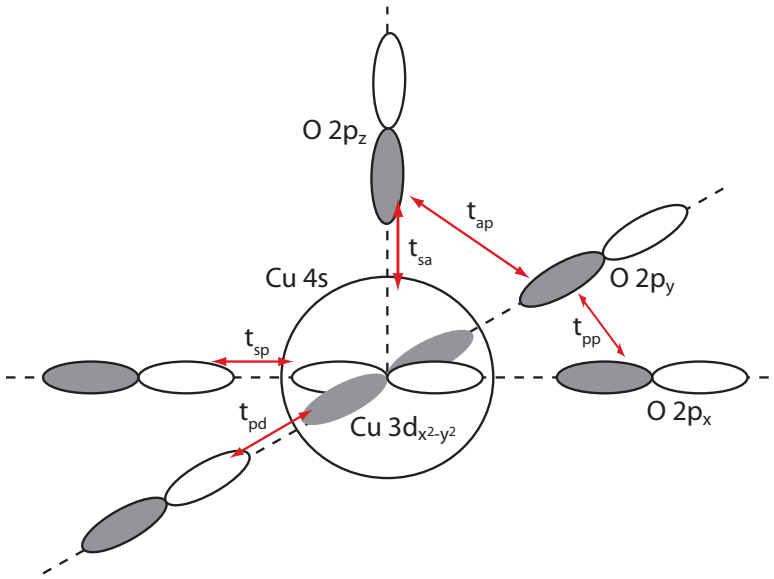

Figure 3.1: A sketch of the orbitals included in the five-band model used to derive the el-ph coupling constants $g(\mathbf{k}, \mathbf{q})$. The white and grey colours denote lobes of differing sign.

the Cu $4s$ and apical O $2p_z$ orbitals. This extended five band model is shown in figure 3.1. The corresponding Hamiltonian is $H = H_{\text{site}} + H_{\text{kin}}$ where

$$H_{\text{site}} = \sum_{\mathbf{n},\sigma} \epsilon_d d^\dagger_{\mathbf{n},\sigma} d_{\mathbf{n},\sigma} + \sum_{\mathbf{n},\delta,\sigma} \epsilon_p p^\dagger_{\mathbf{n},\delta,\sigma} p_{\mathbf{n},\delta,\sigma} + \epsilon_a \sum_{\mathbf{n},\sigma} a^\dagger_{\mathbf{n},\sigma} a_{\mathbf{n},\sigma} + \epsilon_s \sum_{\mathbf{n},\sigma} s^\dagger_{\mathbf{n},\sigma} s_{\mathbf{n},\sigma} \tag{3.2}$$

and

$$\begin{aligned} H_{\text{kin}} \;=\; & \sum_{\mathbf{n},\delta,\sigma} P_\delta t_{pd} [d^\dagger_{\mathbf{n},\sigma} p_{\mathbf{n},\delta,\sigma} + h.c.] + \sum_{\mathbf{n},\delta,\delta',\sigma} P_{\delta,\delta'} t_{pp} p^\dagger_{\mathbf{n},\delta,\sigma} p_{\mathbf{n},\delta',\sigma} + \sum_{\mathbf{n},\delta,\sigma} P'_\delta t_{sp} [s^\dagger_{\mathbf{n},\sigma} p_{\mathbf{n},\delta,\sigma} + h.c.] \\ & - \sum_{\mathbf{n},\delta,\sigma} P'_\delta t_{ap} [a^\dagger_{\mathbf{n},\sigma} p_{\mathbf{n},\delta,\sigma} + h.c.] - t_{sa} \sum_{\mathbf{n},\sigma} [s^\dagger_{i,\sigma} a_{i,\sigma} + h.c.] \end{aligned} \tag{3.3}$$

Here, $\delta = \pm\hat{x}, \pm\hat{y}$ denotes the planar oxygen basis and the operators $d^\dagger_{\mathbf{n},\sigma}$ ($d_{\mathbf{n},\sigma}$), $p^\dagger_{\mathbf{n},\delta,\sigma}$ ($p_{\mathbf{n},\delta,\sigma}$), $a^\dagger_{\mathbf{n},\sigma}$ ($a_{\mathbf{n},\sigma}$) and $s^\dagger_{\mathbf{n},\sigma}$ ($s_{\mathbf{n},\sigma}$) are the creation (annihilation) operators for electrons of spin σ on the Cu $3d_{x^2-y^2}$, planar O $2p_\delta$, apical O $2p_z$ and Cu $4s$ orbitals, respectively. The overlap integrals and site energies are denoted as indicated in figure 3.1. Finally, the assumed phase convention is $-P_{\pm x} = P_{\pm y} = \pm 1$, $P_{\pm x,\pm y} = -P_{\pm x,\mp y} = \pm 1$ and $P'_{\pm x} = P'_{\pm y} = \mp 1$. In order to reduce this to the three band model used in previous works [23, 30, 44, 102] the hoppings t_{sp} and t_{ap} are set to zero.

One now invokes translational invariance and consequently, Fourier transforms the fermion operators. Furthermore, following Ref. [162], one defines canonical fermions α, β from combinations of the ligand oxygen orbitals via the Wannier transformation

$$\alpha_{\mathbf{k},\sigma}, \beta_{\mathbf{k},\sigma} = \pm i \frac{\sin(k_{x,y}a/2)p_{\mathbf{k},x,\sigma} \mp \sin(k_{y,x}a/2)p_{\mathbf{k},y,\sigma}}{\mu_{\mathbf{k}}} \tag{3.4}$$

where $\mu_{\mathbf{k}}^2 = \sin^2(k_x a/2) + \sin^2(k_y a/2)$. The five band Hamiltonian is then $H = \sum_{\mathbf{k},\sigma} H_{\mathbf{k},\sigma}$ where

$$\begin{aligned} H_{\mathbf{k},\sigma} &= H_{\text{site}} + 2t_{pp}[\alpha^\dagger_{\mathbf{k},\sigma}\alpha_{\mathbf{k},\sigma} - \beta^\dagger_{\mathbf{k},\sigma}\beta_{\mathbf{k},\sigma}] + 2\big[t_{pd}\mu_{\mathbf{k}} d^\dagger_{\mathbf{k},\sigma}\alpha_{\mathbf{k},\sigma} + t_{pp}\chi_{\mathbf{k}}\alpha^\dagger_{\mathbf{k},\sigma}\beta_{\mathbf{k},\sigma} \\ &+ t_{ps}\kappa_{\mathbf{k}} s^\dagger_{\mathbf{k},\sigma}\alpha_{\mathbf{k},\sigma} - t_{ps}\lambda_{\mathbf{k}} s^\dagger_{\mathbf{k},\sigma}\beta_{\mathbf{k},\sigma} - \frac{t_{sa}}{2} s^\dagger_{\mathbf{k},\sigma}a_{\mathbf{k},\sigma} - t_{pa}\kappa_{\mathbf{k}} a^\dagger_{\mathbf{k},\sigma}\alpha_{\mathbf{k},\sigma} + t_{pa}\lambda_{\mathbf{k}} a^\dagger_{\mathbf{k},\sigma}\beta_{\mathbf{k},\sigma} + h.c.\big] \end{aligned} \tag{3.5}$$

and

$$\nu_{\mathbf{k}} = 4\frac{\sin^2(k_x a/2)\sin^2(k_y a/2)}{\mu_{\mathbf{k}}^2} \qquad \kappa_{\mathbf{k}} = \frac{\sin^2(k_x a/2) - \sin^2(k_y a/2)}{\mu_{\mathbf{k}}}$$
$$\lambda_{\mathbf{k}} = 2\frac{\sin(k_x a/2)\sin(k_y a/2}{\mu_{\mathbf{k}}} \qquad \chi_{\mathbf{k}} = \lambda_{\mathbf{k}}\kappa_{\mathbf{k}}.$$

The Hamiltonian is bilinear in fermion operators and is easily diagonalized. For the sake of simplicity, the diagonalization is performed numerically using a linear algebra package such as LaPack or Matlab. In what follows, the band eigenfunctions defining the orthogonal transformation to the band basis are denoted as $\phi_b(\mathbf{k})$, $\phi_s(\mathbf{k})$, $\phi_{x,y}(\mathbf{k})$ and $\phi_a(\mathbf{k})$ for the Cu $3d$ and Cu $4s$, planar O $2p_{x,y}$ and apical O $2p_z$ orbitals, respectively. In the case of the three band model the basis functions for the Cu and planar oxygen orbitals reduce to a simple compact analytic form [30, 23]:

$$\begin{aligned} \phi_b &= \frac{1}{N(\mathbf{k})}\left[\epsilon^2(\mathbf{k}) - t'^2(\mathbf{k})\right] \\ \phi_{x,y} &= \mp\frac{i}{N(\mathbf{k})}\left[\epsilon(\mathbf{k})t_{x,y}(\mathbf{k}) - t_{y,x}t'(\mathbf{k})\right] \\ N(\mathbf{k})^2 &= [\epsilon^2(\mathbf{k}) + t'^2(\mathbf{k})]^2 + [\epsilon(\mathbf{k})t_x(\mathbf{k}) - t_y(\mathbf{k})t'(\mathbf{k})]^2 + [\epsilon(\mathbf{k})t_y(\mathbf{k}) - t_x(\mathbf{k})t'(\mathbf{k})]^2 \end{aligned}$$

where $t'(\mathbf{k}) = -4t_{pp}\sin(k_x a/2)\sin(k_y a/2)$, $t_\alpha(\mathbf{k}) = 2t_{pd}\sin(k_\alpha a/2)$ and $\epsilon(\mathbf{k})$ is the anti-bonding solution to the reduced three band Hamiltonian.

3.2 Charge Transfer Coupling

To derive the electrostatic coupling to c-axis phonons a modulation of the electrostatic coupling between the charge density at the oxygen site and the electrostatic potential at

that site Φ_{ext} is introduced. The Hamiltonian is of the form:

$$H'_{\text{site}} = -e \sum_{n,\sigma} p^{\dagger}_{\mathbf{n},\sigma} p_{\mathbf{n},\sigma} \Phi_{\text{e}xt}(R_{\mathbf{n}}) \tag{3.6}$$

where $\mathbf{n}$ is a site index, $p^{\dagger}_{\mathbf{n},\sigma}$ ($p_{\mathbf{n},\sigma}$) are the creation (annihilation) operator at the oxygen site, e is the electron charge, and $R_{\mathbf{n}}$ denotes the atomic positions in the crystal. Expanding for small displacements about the equilibrium position equation 3.6 is rewritten as $H' = H_{site} + H_{\text{el-ph}}$ where

$$H_{\text{el-ph}} = e \sum_{\mathbf{n},\sigma} p^{\dagger}_{\mathbf{n},\sigma} p_{\mathbf{n},\sigma} \vec{E}_{\mathbf{n}} \cdot \vec{U}_{\mathbf{n}} \tag{3.7}$$

and $\vec{E}_{\mathbf{n}}$ is the local crystal field given by the gradient of the Madelung potential $\nabla \cdot \Phi_{\text{ext}}$ at site $\mathbf{n}$ and $\vec{U}_{\mathbf{n}}$ is the displacement of the oxygen atom from its equilibrium position.

The magnitude of the local crystal fields at the oxygen sites will depend on the structural details as well as the chemical composition of the unit cell and will therefore vary from system to system. If the oxygen atom sits in a mirror plane of the crystal, as is the case of the CuO_2 planes in an ideal single layer systems then, by symmetry, the Madelung potential landscape is at a local minimum and $\vec{E} = \nabla \cdot \Phi$ is zero (small fields can be developed in the real undoped system due to defects which break translational symmetry). This is in contrast with the multi-layer cuprates where the CuO_2 plane does not occupy a mirror plane and a sizeable electric field can be generated across the plane. However, in the case of the field strength at the apical site, the apical oxygen atom occupies a position between the CuO_2 plane and the charge reservoir layer. As such, even in the single layer systems, coupling to the apical branch can occur. From these considerations, coupling to the c-axis modes can develop a materials dependence[2] and this observation will be explored further in chapter 6.

3.2.1 The A_{1g} and B_{1g} planar modes

For coupling to the A_{1g} and B_{1g} modes one then has

$$H_{el-ph} = eE_{z,p} \sum_{\mathbf{n},\delta,\sigma} U_{\mathbf{n},\delta} p^{\dagger}_{\mathbf{n},\delta,\sigma} p_{\mathbf{n},\delta,\sigma} \tag{3.8}$$

where $U_{\mathbf{n},\delta}$ denotes the displacement of the planar oxygen atom along the c-axis and $E_{z,p}$ is the component of the electric field along the c-axis at the planar oxygen site.

[2]Estimates for the local field strength as a function of material have been calculated by the author in a previous work [23].

Performing the usual Fourier transform and applying the transformation to the band representation yields ($\mathbf{p} = \mathbf{k} - \mathbf{q}$)

$$H_{el-ph} = \frac{eE_{z,p}}{\sqrt{N}} \sum_{\mathbf{k},\mathbf{q},\sigma} \left[U_x(\mathbf{q})\phi_x(\mathbf{k})\phi_x(\mathbf{p}) + U_y(\mathbf{q})\phi_y(\mathbf{k})\phi_y(\mathbf{p}) \right]. \tag{3.9}$$

Finally, the oxygen displacement is expanded in terms of normal modes

$$U_\alpha(\mathbf{q}) = \sqrt{\frac{\hbar}{2M_o\Omega(\mathbf{q})}} \epsilon^\alpha(\mathbf{q})[b_\mathbf{q} + b^\dagger_{-\mathbf{q}}] \tag{3.10}$$

where M_o is the mass of the oxygen atom, $\Omega(\mathbf{q})$ is the dispersion of the phonon branch and $\hat{\epsilon}^\alpha(\mathbf{q})$ is the phonon eigenvector. For the A_{1g} and B_{1g} modes the eigenvectors are [44, 30, 23]

$$\hat{\epsilon}^{x,y}(\mathbf{q}) = S_{x,y} \frac{\hat{z}}{N(\mathbf{q})} e^{-iq_{(x,y)}a/2} \left(1 + e^{-iq_{(y,x)}}\right) \tag{3.11}$$

where $N^2(\mathbf{q}) = 4[\cos^2(q_x a/2) + \cos^2(q_y a/2)]$ is a normalization factor and $S_{x,y} = \pm 1$ for the B_{1g} branch and $S_{x,y} = 1$ for the A_{1g} branch. The interaction Hamiltonian is now cast in the form of equation 3.1 with the el-ph coupling constant for the A_{1g} and B_{1g} branches given by

$$g(\mathbf{k},\mathbf{q}) = \frac{g_0^{A1g,B1g}}{N(\mathbf{q})} \left[\phi_x(\mathbf{k})\phi_x(\mathbf{p}) e^{-iq_x a/2}(1 + e^{-iq_y a/2}) \pm \phi_y(\mathbf{k})\phi_y(\mathbf{p}) e^{-iq_y a/2}(1 + e^{-iq_x a/2})) \right] \tag{3.12}$$

with $g_0^{A1g,B1g} = eE_{z,p}\sqrt{\hbar/2M_O\Omega(\mathbf{q})}$ and the $\pm$ corresponding to the A_{1g} and B_{1g} modes, respectively.

3.2.2 The Apical Oxygen Mode

To obtain the coupling to the apical mode a similar consideration for the modulation of the apical site energy is undertaken

$$H_{el-ph} = eE_{z,a} \sum_{\mathbf{n},\sigma} a^\dagger_{\mathbf{n},\sigma} a_{\mathbf{n},\sigma} U^a_\mathbf{n} = \frac{eE_{z,a}}{\sqrt{N}} \sum_{\mathbf{q},\mathbf{k},\sigma} a^\dagger_{\mathbf{k},\sigma} a_{\mathbf{p},\sigma} U^a(\mathbf{q}). \tag{3.13}$$

As with the coupling to the planar oxygen branches, the band eigenfunctions are introduced and the oxygen displacement is expanded in terms of normal modes. In this case, the momentum dependence of the apical phonon is neglected and $\epsilon^a(\mathbf{q}) = \hat{z}$. The

interaction Hamiltonian is again in the form of equation 3.1 and the generic form of the apical vertex is

$$g(\mathbf{k},\mathbf{q}) = g_0^{apex}\phi_a^\dagger(\mathbf{k})\phi_a(\mathbf{p}) \tag{3.14}$$

with $g_0^{apex} = eE_{z,a}\sqrt{\hbar/2M_o\Omega_{apex}(\mathbf{q})}$. More complicated motion of the apical oxygen atom, involving the motion of the planar oxygen atoms, can be treated accordingly.

To obtain the leading order momentum dependence of the apical coupling a downfolding procedure [163] is applied to equation 3.5 in order to determine the amount of apical character of the band crossing the Fermi level. The resulting downfolded apical eigenfunction $\phi'_a(\mathbf{k})$ is then

$$\phi'_a = 2t_{ap}\frac{\kappa_\mathbf{k}}{\epsilon_\mathbf{k} - \epsilon_a}. \tag{3.15}$$

The leading order momentum dependence of the apical coupling is then $g(\mathbf{k},\mathbf{q}) \sim d_\mathbf{k}d_\mathbf{p}$ where $d_\mathbf{k} = [\cos(k_x a) - \cos(k_y a)]/2$ is the d-wave form factor. The coupling is strongest for electrons in the antinodal region and the momentum structure of the form factor is similar to the c-axis hopping term between CuO_2 layers $t_\perp(\mathbf{k})$ [164]. Furthermore, this coupling has an anisotropy similar in form to that of the B_{1g} mode, however it does not contribute to d-wave pairing due to its momentum dependence at large $\mathbf{q}$.

3.3 Deformation Coupling: Planar Breathing Modes

The in-plane vibrations of the oxygen atoms produces a modulation of the Cu-O overlap and the integral t_{pd} is now taken to be site dependent $t_{pd}^\mathbf{n}$. It is assumed that displacement of the Cu and O atoms, $U_\mathbf{n}^{Cu}$ and $U_\mathbf{n}^{O}$, about their equilibrium position $R_\mathbf{n}$ is small and the overlap integral is expanded, keeping only terms to linear order in displacement

$$t_{pd}^\mathbf{n} = t_{pd} + \left.\frac{\partial t_{pd}}{\partial r}\right|_{r=R} \cdot [U_\mathbf{n}^{Cu} - U_\mathbf{n}^{O}] = t_{pd} + g_{pd}[U_\mathbf{n}^{Cu} - U_\mathbf{n}^{O}]\hat{\delta} \tag{3.16}$$

where $\hat{\delta} = \hat{x}$, $\hat{y}$ is the unit basis vector between the Cu and planar oxygen site. The first term in equation 3.16 is the Co-O overlap term appearing in the original Hamiltonian while the second term provides the el-ph coupling. At this point the motion of the heavier Cu atom is neglected leaving

$$H_{el-ph} = \sum_{\mathbf{n},\delta,\sigma}\frac{\partial t_{pd}}{\partial U}[d^\dagger_{\mathbf{n},\sigma}p_{\mathbf{n},\delta,\sigma} + h.c.]U_{\mathbf{n},\delta}\cdot. \tag{3.17}$$

As with the previous two cases, equation 3.17 is Fourier transformed and the normal mode expansion for the in-plane vibration is introduced. For the breathing modes the phonon eigenvectors are taken to be $\epsilon^\alpha(\mathbf{q}) = \sin(q_\alpha)\hat{\delta}/N(\mathbf{q})$ with $N^2(\mathbf{q}) = \sin^2(\mathbf{q}_x a/2) +$

$\sin^2(\mathbf{q}_y a/2)$ and $\hat{\delta} = \hat{x}$,$\hat{y}$ for the motion of the x and y oxygen atoms, respectively [23]. The final form for the coupling to the breathing mode is:

$$g_{br}(\mathbf{k},\mathbf{q}) = g_0^{br} \sum_{\alpha=x,y} P_\alpha \epsilon_\alpha(\mathbf{q}) \left[\cos(p_\alpha a/2)\phi_b(\mathbf{p})\phi_\alpha(\mathbf{k}) - \cos(k_\alpha a/2)\phi_\alpha(\mathbf{p})\phi_b(\mathbf{k})\right] \quad (3.18)$$

where $g_0^{br} = g_{pd}\sqrt{\hbar/2M_o\hbar\Omega_{br}(\mathbf{q})}$ and $P_{x,y} = \pm 1$. The Cu $3d_{x^2-y^2}$ and O $2p_{x,y}$ orbital overlap scales as $t_{pd}(d) \sim d^{-\beta}$ with $\beta = 3.5$ [165] and an overall estimate for the strength of the coupling to the breathing branches is $g_{pd} \sim 2$ eV/$\mathring{A}$ for $t_{pd} = 1.1$ eV, $d = 1.92$ $\mathring{A}$ and $\Omega_{br}(\mathbf{q}) = \Omega_{br} = 70$ meV, which results in $g_0^{br} = 86$ meV.

3.4 Momentum Dependence of the Bare Vertices

In the previous section it was shown how the explicit form for the el-ph coupling to oxygen modes is determined by the nature of the coupling (charge transfer or deformation), the local environment surrounding the CuO_2 plane, and the orbital content of the band crossing the Fermi level. The relevant parameters - the magnitude of the orbital hybridization, the local crystal field, the charge- transfer energy, the shape of the Fermi surface, and the density of states at the Fermi level - all control the overall magnitude of the coupling as well as the full fermionic $\mathbf{k}$ and bosonic $\mathbf{q}$ momentum dependence of the coupling $g(\mathbf{k},\mathbf{q})$. The band character enters through the band eigenvectors ϕ, which depend on the complexity of the unit cell. At the Brillouin zone center the wavefunctions are atomic in character and the band is unique. Large momentum variations of the band character then occur for increasing momentum and a very strong momentum dependence of the overall el-ph coupling can occur, as has been observed in recent LDA treatments [105].

One now wishes to estimate the magnitude and anisotropy of the bare couplings in the absence of charge screening in order to determine the possible discrepancies with LDA treatments, which treat correlations on the mean field level and includes 3D metallic screening. In order to estimate general tendencies, both in momentum dependence as well as magnitudes, some simplifications are now introduced. First it is assumed that $2t_{pd}$ is much greater than any relevant energy scale in the system, keeping in mind that the charge transfer energy $\Delta = \epsilon_p - \epsilon_d \sim 0.8$ eV when treating correlations at the mean field level as is done in approaches such as LDA [161]. In this limit the ϕ functions can be represented as

$$\phi_{x,y} = \pm i \frac{\sin(k_{x,y}a/2)}{\sqrt{\sin^2(k_x a/2) + \sin^2(k_y a/2)}} + O(\Delta/2t_{pd})^2 \quad (3.19)$$

and

$$\phi_{Cu} = \frac{\Delta/t_{pd}}{\sqrt{\sin^2(k_x a/2) + \sin^2(k_y a/2)}} + O(\Delta/2t_{pd})^2. \quad (3.20)$$

To the same order, the denominators in these expressions are constant over constant energy contours. Therefore, since one is interested in states near the Fermi surface the band eigenfunctions are represented by $\phi_{x,y}(\mathbf{k}) = A_O \sin(k_{x,y}a/2)$, $\phi_b(\mathbf{k}) = A_{Cu}$ and $\phi_a(\mathbf{k}) = A_a[\cos(k_x a) - \cos(k_y a)]/2$, with coefficients determined by $A_O^2 = \langle \phi_{x,y}^2(\mathbf{k}) \rangle / \langle \sin^2(k_{x,y}a/2) \rangle$, $A_{Cu}^2 = \langle \phi_b^2(\mathbf{k}) \rangle$, and $A_a = \langle \phi_a^2(\mathbf{k}) \rangle / \langle ((\cos(k_x a) - \cos(k_y a))^2/4) \rangle$. Here, $\langle \dots \rangle$ denotes a Fermi surface average: $\langle A \rangle = \sum_{\mathbf{k}} A_{\mathbf{k}} \delta(\epsilon_{\mathbf{k}}) / \sum_{\mathbf{k}} \delta(\epsilon_{\mathbf{k}})$. With this approach, the overall coupling anisotropy can be simplified without loss of generality. In what follows, the Fermi surface averages are evaluated using the full five band model, defined by Eq. 3.5.

As a consequence of this simplification, the coupling to the breathing branches loses its fermionic momentum dependence:

$$\begin{aligned} g_{br}(\mathbf{k}, \mathbf{q}) &= g_0^{br} A_{Cu} A_O \sum_{\alpha = x,y} P_\alpha \epsilon_\alpha \sin(q_\alpha a/2) \\ &= g_0^{br} A_{Cu} A_O \sqrt{\sin^2(q_x a/2) + \sin^2(q_y a/2)}. \end{aligned} \tag{3.21}$$

This form for the coupling has also been obtained in a t-J model approach [160], but in this case the degree of oxygen and copper character of the band has been explicitly retained through the coefficients A_{Cu} and A_O, respectively. Furthermore, in this form, the fermionic $\mathbf{k}$-dependence vanishes and the overall coupling of electrons to the breathing branch is determined by spanning conditions across the Fermi surface and is governed solely by the $\mathbf{q}$-dependence of the coupling.

The coupling to the A_{1g} and B_{1g} modes can be likewise simplified

$$\begin{aligned} g_{B1g,A1g}(\mathbf{k}, \mathbf{q}) &= eE_{z,p} \sqrt{\frac{2\hbar}{M_O N(\mathbf{q}) \Omega_{B1g,A1g}}} A_O^2 e^{-i(q_x + q_y)a/2} \times \\ &\quad [\sin(k_x a/2) \sin(p_x a/2) \cos(q_y a/2) \pm \sin(k_y a/2) \sin(p_y a/2) \cos(q_x q/2)] \end{aligned} \tag{3.22}$$

These expressions recover the Raman form factor in the limit $\mathbf{q} \to 0$ for each mode, and they obey the symmetry conditions for momentum reflections about $\pi/2$ as discussed previously. The fermionic dependence cannot be neglected for either of these branches.

Lastly, the momentum structure of the coupling to the apical branch simplifies considerably

$$g_{apex}(\mathbf{k}, \mathbf{q}) = g_0^{apex} A_a^2 \left[\cos(k_x a) - \cos(k_y a)\right] \left[\cos(p_x a) - \cos(p_y a)\right] / 4. \tag{3.23}$$

Once again, a substantial fermionic dependence emerges from the c-axis charge transfer pathways and the apical character of the band crossing the Fermi level.

Before proceeding further a few comments are in order. In using equations 3.21 - 3.23 the form of the el-ph coupling has been simplified while explicitly retaining the role

of the band character in determining the overall strength of the couplings. Since the eigenfunctions enter to the fourth power for $g^2(\mathbf{k},\mathbf{q})$, the total coupling strength determined in this approach may change considerably when adjusting multi-band parameters. However, this method has the advantage that the materials dependence of the coupling, parameterized by A_O, A_{Cu}, and A_a can be calculated using a variety of methods such as exact diagonalization, quantum Monte Carlo, tight-binding models or LDA. It is also emphasized that the total coupling strengths (calculated in the next section) that are obtained in this formalism are similar to those obtained from LDA treatments, even though the latter includes the effects of screening [166, 167, 105, 104].

Another advantage of this approach is that it allows for the use of a renormalized bandstructure while retaining the explicit band character of the original five-band model. This is important since the overall strength of the el-ph couplings scales with the density of states at the Fermi level N_F; narrow bandwidth systems will exhibit larger couplings in comparison to large bandwidth systems with the same vertex $g(\mathbf{k},\mathbf{q})$ and quasiparticle weight. With an appropriate choice in parameters, the five-band model in section 3.1 reasonably reproduces the bandwidth (and N_F) determined by LDA calculations [109]. However, as has been noted in reference [108], LDA over-predicts the total bandwidth (and consequently N_F is under-predicted) in comparison with experiment. Therefore it is expected that the total couplings will be underestimated if the five-band model with parameters tuned to match LDA is used. A simple rescaling of the bandstructure in conjunction with the full form of the ϕ functions is insufficient to correct this since such a procedure would generate incorrect values for the ϕ-functions and produce errors in the band character as a function of $\mathbf{k}$. The use of the el-ph couplings defined by equations 3.21 - 3.23 allows for a resolution of this issue. Here, the correct band character is captured by calculating A_O, A_a and A_{Cu} using the five-band model but the Fermi surface and bandstructure can be obtained from a tightbinding model derived from fits to ARPES data [168]. This approach allows one to capture the increased value of N_F while simultaneously retaining estimates for the correct band character.

In order to visualize the $\mathbf{k}$-dependence of the coupling constants in more detail $g(\mathbf{k},\mathbf{q})$ is plotted in figure 3.2 for momentum points on the Fermi surface in Bi-2212. The coupling constants are plotted as a function of momentum transfer $\mathbf{q}$ starting from $\mathbf{k}$-points on the Fermi surface. The specific shape of the Fermi surface is not crucial to the overall anisotropy of the coupling (but it does affect the overall magnitude of the coupling) and so the Fermi surface is obtained from a 5-parameter tightbinding model with parameters obtained from fits to ARPES data [168]. The dependency on transferred momenta arises from the nature of the charge-transfer coupling of the different modes. The c-axis modes (Figs. 3.2a1-2,4 and 3.2b1-2,4), being electrostatic in nature, translate into stronger coupling for small momentum transfers, while the deformation-type coupling of the breathing branches gives stronger coupling at large $\mathbf{q}$, and vanishes in the limit $\mathbf{q} \to 0$ (Figs. 3.21a3 and 3.21b3).

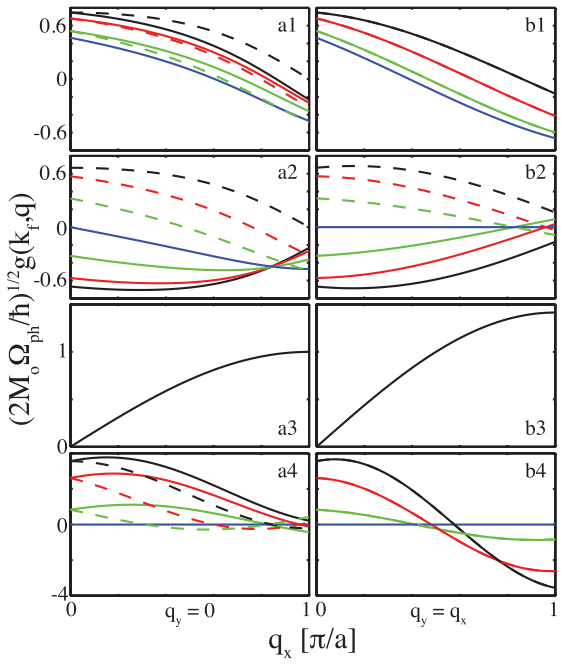

Figure 3.2: Plots of the el-ph coupling constant $g(\mathbf{k}_F, \mathbf{q})$ for fermionic momentum on the Fermi surface as a function of transferred momentum $(q_x, 0)$ (a1-a4) and $(q_x = q_y)$ (b1-b4), respectively. a1,b1 (a2,b2) plot coupling to the A_{1g} (B_{1g}) branches, respectively, a3,b3 plot coupling to the breathing branch, and a4,b4 plot coupling to the apical branch. The colours denote angles from the corner of the Brillouin zone (shown in the inset of Fig. 3.3) with black - 0°, solid red = 15°, solid green - 30°, solid blue - 45° (or the nodal point), dashed green - 60°, dashed red - 75° and dashed black - 90°.

Apart from the breathing modes, an appreciable fermionic momentum dependence of the couplings to the c-axis modes is found, which is a consequence of the symmetry of the underlying phonon eigenvectors. For the case of the A_{1g} and apical modes, for $\mathbf{q}$ along the zone diagonal (Figs. 3.2a1 and b4, respectively), the fermionic momentum dependence is symmetric with respect to reflections about $\pi/4$ while the B_{1g} coupling (Fig. 3.2b2) changes sign. Momentum transfers along the zone face (Figs 3.2a1, 3.2a2, 3.2a4) do not obey any set selection rule, although the symmetric- or anti-symmetric-like character of the coupling is evident in the form of the coupling $g(\mathbf{k}, \mathbf{q})$. Finally, the strong momentum dependence of the charge transfer along the c-axis dictates that the apical coupling vanishes for any fermion momentum along the zone diagonal (3.2b4).

The strong dependence of the coupling on $\mathbf{k}$ and $\mathbf{q}$ leads to anisotropic coupling between electrons and phonons as has been pointed out in previous work [30, 23]. As the most relevant scattering processes involve states near the Fermi level, the explicit momentum dependence, as seen in ARPES, is most clearly envisioned by calculating $\mathbf{k}$-dependent self-energies, in terms of the dimensionless momentum-resolved el-ph coupling $\lambda(\mathbf{k})$.

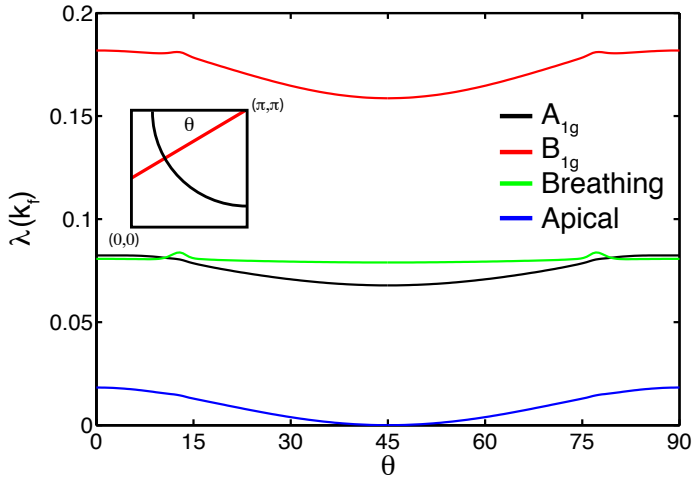

Figure 3.3: Plots of $\lambda_\nu(\mathbf{k})$ for momentum points along the Fermi surface. Inset: The definition of θ. Parameters used are defined in the text.

3.5 Coupling Strength $\lambda(\mathbf{k})$ on the Fermi Surface

In this section, the momentum dependence of the overall magnitude and anisotropy of the bare el-ph coupling λ is presented for the four phonon branches. Here, the effects of screening, which are discussed in chapter 6, are neglected. The contribution of a dispersionless mode with energy Ω_ν to the electron self-energy $\lambda_\nu(\mathbf{k})$ is defined as [9]:

$$\lambda_\nu(\mathbf{k}) = \frac{2}{N\Omega_\nu} \sum_{\mathbf{p}} |g(\mathbf{k},\mathbf{q})|^2 \delta(\xi_{\mathbf{k}}) \tag{3.24}$$

with $\xi(\mathbf{k}) = \epsilon_{\mathbf{k}} - \mu$. The δ-function restricts the sum to initial and final fermion states $\mathbf{k}$, $\mathbf{p}$, on the Fermi surface, with scattering between them governed by the transferred phonon momentum $\mathbf{q}$.

The resulting $\lambda_\nu(\mathbf{k}_F)$ for the four modes are shown in figure 3.3. By using this bandstructure, the impact of the high-energy anomaly on the low energy bandstructure are accounted for in an approximate manner. The el-ph vertices are evaluated using Eqs. 3.21 - 3.23 along with the conventional parameter set (in eV): $t_{pd} = 1.1$, $t_{pp} = 0.5$, $t_{ap} = 0.29$, $t_{sp} = 2.0$, $t_{sa} = 1.5$, $\epsilon_d = 0$, $\epsilon_p = -0.8$, $\epsilon_a = -1$ and $\epsilon_s = 7$ [161, 18]. For this choice of parameters $A_o^2 = 0.446$, $A_b^2 = 0.592$ and $A_a^2 = 4.52 \times 10^{-2}$. Additionally, estimates of the local field strength at the planar and apical oxygen sites for Bi-2212 are used $E^z_{\mathrm{z,p}} = 3.56$, $E^z_{\mathrm{z,a}} = 16.33$ eV/$\mathring{A}$, respectively.

A strongly varying $\lambda(\mathbf{k})$ is obtained for the c-axis modes, largely weighting antinodal fermion states. This arises from both the fermion dependence of the bare couplings as well as the small momentum transfers connecting antinodal points on the Fermi surface. This dependence has been noted in prior treatments of these modes [30, 23]. In the case of the breathing modes, a weaker anisotropy is produced along the Fermi surface due to large momentum transfers (π, π) connecting antinodal portions of the Fermi surface, as well as $(\pi, 0)$ and $(0, \pi)$ transfers connecting nodal points. The inclusion of a variation of the copper character of the band across the Fermi surface yields a more anisotropic coupling [30, 23]. However, this anisotropy is not as strong as that reported in a recent LDA study [105], where the breathing branches couple more strongly to antinodal states.

3.5.1 Total λ_z and λ_ϕ

The full coupling λ_z, which renormalizes the single particle self-energy, is given by a sum over the contributions of each mode averaged over the Fermi surface, $\lambda_z = \sum_\mu \langle \lambda(\mathbf{k}) \rangle$. This can be visualized as averaging over the curves of figure 3.3. A similar coupling strength λ_ϕ can be defined for the phonon's contribution to the anomalous self-energy of the Cooper pair by projecting onto the momentum channel of the superconducting gap. For a $d_{x^2-y^2}$ gap the d-wave projected λ_ϕ is

$$\lambda_\phi = \frac{2}{N\Omega_\mu} \sum_\mu \frac{\sum_{\mathbf{k},\mathbf{p}} d_\mathbf{k} d_\mathbf{p} |g_\mu(\mathbf{k}, \mathbf{q})|^2 \delta(\epsilon_\mathbf{k}) \delta(\epsilon_\mathbf{p})}{\sum_\mathbf{k} d_\mathbf{k}^2 \delta(\epsilon_\mathbf{k})} \tag{3.25}$$

with $d_\mathbf{k} = [\cos(k_x a) - \cos(k_y a)]/2$. A positive (negative) λ_ϕ denotes an attractive (repulsive) interaction in the ϕ ($d_{x^2-y^2}$) momentum channel. The value of $\lambda_{z,\phi}$ for the modes discussed here are listed in table 3.1. Both the A_{1g} and B_{1g} modes enhance d-wave pairing while the breathing mode suppresses pairing and the apical mode gives no contribution. The total value of λ_ϕ is far too small to account for the experimental value of T_c. (In order to reproduce the experimentally observed gap size $\lambda_{z,\phi}$ of order one are required. A more thorough discussion of this is presented in chapter 5.) However, the sizeable contribution from the B_{1g} mode can work in conjunction with another pairing mechanism. This will be discussed in further detail in chapters 4 and 6.

The strength of the overall coupling depends on the planar oxygen character of the band. Since the eigenfunctions enter to the fourth power in $|g_\nu(\mathbf{k}, \mathbf{q})|^2$ through the projections A_O, A_{br} and A_a, λ values may change considerably when adjusting the parameters of the multi-band model. Likewise, these numbers will be increased if the bandwidth is renormalized in accordance with experiment [109]. The values obtained here are similar to those obtained from LDA treatments, even though LDA includes the effects of screening [104, 105, 106, 167, 166]. These effects will be incorporated in chapter 6.

Total $\lambda_{z,\phi}$		
Branch	λ_z	λ_ϕ
A_{1g}	7.74×10^{-2}	4.42×10^{-2}
B_{1g}	0.17	0.12
Apical	8.27×10^{-2}	-4.75×10^{-2}
Breathing	1.11×10^{-2}	0
Total	0.341	0.1149

Table 3.1: Tabulated values of $\lambda_{z,\phi}$ for the four phonon branches considered in this work.

3.6 Weak Coupling Theory: Migdal-Eliashberg

The self-energy arising due to the el-ph interaction can be derived from the generic form of the interaction Hamiltonian Eq. 3.1. In the usual treatment of el-ph coupling, the so-called Migdal approximation, only the subset of rainbow diagrams shown in figure 3.4a are considered in calculating the electron self-energy. This approximation neglects higher order diagrams such as the crossing diagrams shown in 3.4b. These diagrams give a contribution to the self-energy of order $(m^*/M)^{1/2} \sim \Omega/\epsilon_F$, where Ω is the phonon frequency and ϵ_F is the Fermi energy [169]. In good metals this approximation provides accurate results and the extension of this theory to the superconducting state by Eliashberg, known as Migdal-Eliashberg theory [170, 9], provides an extremely powerful framework for understanding conventional superconductivity. It has also been shown that this approximation can account for much of the experimental data pertaining to el-ph coupling in the optimal and overdoped high-T_c cuprates [30] and, due to its previous success, this model will be further applied towards understanding the finer details of the el-ph renormalizations in chapter 4. The el-ph interaction will also have an affect on the phonons, renormalizing their dispersions and imparting a finite lifetime. However, typical approaches based on Migdal-Eliashberg incorporate the phonon self-energy in an ad-hoc manner by using experimentally determined phonon dispersions [171]. This is the approach adopted here.

The class of diagrams neglected in the Migdal approximation (Fig. 3.4b) become critical when the strength of the el-ph interaction is large. In this limit the electron becomes increasingly dressed by a cloud of phonons and the electron and surrounding lattice distortion become closely coupled. This results in an increase in the electron's effective mass as the lattice distortion must be moved in conjunction with the electron. The new quasiparticle comprised of the electron plus the phonon cloud is a polaron. At moderate el-ph coupling large polarons are formed where the lattice distortions extend over a large volume with relatively small ion displacements. However, at a critical coupling strength $\lambda \sim 1$, a crossover occurs to a small polaron where the electron is heavily dressed and

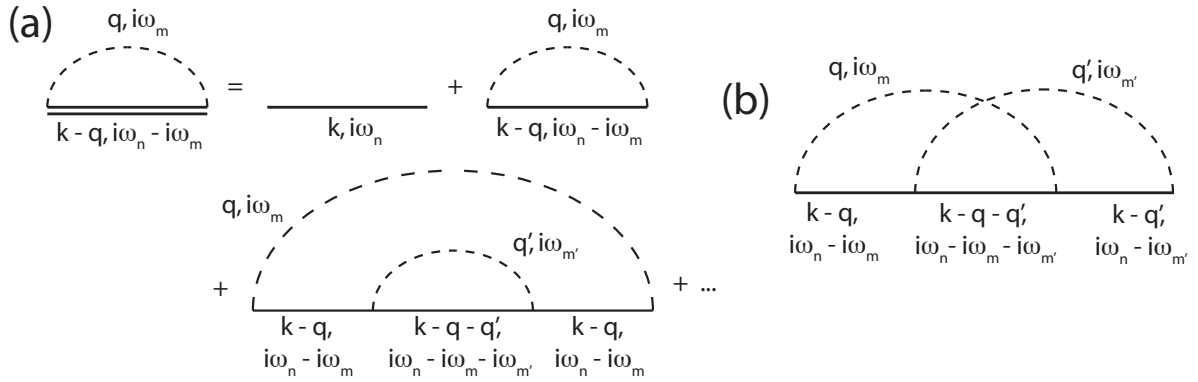

Figure 3.4: (a) The series of rainbow diagrams usually retained in calculating the el-ph self-energy. (b) An example of the crossing diagram neglected in Migdal theory. Such terms give corrections to the self-energy of order $(m^*/M)^{1/2}$ where m^* is the effective mass of the electron and M is the ion mass.

has a very large effective mass. There is a large body of work examining el-ph coupling in this limit and a review of this work will be given chapter 9, where numerical work on the Hubbard-Holstein model is presented.

3.6.1 The Superconducting State

In the superconducting state, the self-energy $\Sigma(\mathbf{k}, i\omega_n)$ on the imaginary frequency axis, obtained from summing the infinite series of rainbow diagrams, is given by (in Nambu notation, $\mathbf{p} = \mathbf{k} - \mathbf{q}$)

$$\hat{\Sigma}(\mathbf{k}, i\omega_n) = \frac{1}{N\beta} \int_0^\infty d\nu \frac{2\nu\alpha^2 F(\mathbf{k}, \mathbf{q}, \nu)}{\nu^2 + (\omega_m - \omega_n)^2} \hat{\tau}_3 \hat{G}(\mathbf{p}, i\omega_m) \hat{\tau}_3 \tag{3.26}$$

where $\omega_{n,m}$ are Fermion frequencies, $\hat{\tau}_3$ is the usual Pauli matrix and $\alpha^2 F(\mathbf{k}, \mathbf{q}, \nu) = -|g(\mathbf{k}, \mathbf{q})|^2 \mathrm{Im} D(\mathbf{q}, \nu)$ is the effective el-boson spectral function. Here, $D(\mathbf{q}, \nu)$ is the boson propagator and $\hat{G}(\mathbf{k}, i\omega_n)$ is the electron propagator given by:

$$\hat{G}(\mathbf{k}, i\omega_n) = \frac{i\omega_n Z(\mathbf{k}, i\omega_n)\hat{\tau}_0 + [\epsilon_\mathbf{k} + \chi(\mathbf{k}, i\omega_n)]\hat{\tau}_3 + \phi(\mathbf{k}, i\omega_n)\hat{\tau}_1}{[i\omega_n Z(\mathbf{k}, i\omega_n)]^2 - [\epsilon_\mathbf{k} + \chi(\mathbf{k}, i\omega_n)]^2 - \phi^2(\mathbf{k}, i\omega_n)}. \tag{3.27}$$

The self-energy can also be written in the canonical form [65]

$$\hat{\Sigma}(\mathbf{k}, i\omega_n) = i\omega_n[1 - Z(\mathbf{k}, i\omega_n)]\hat{\tau}_0 + \chi(\mathbf{k}, i\omega_n)\hat{\tau}_3 + \phi(\mathbf{k}, i\omega_n)\hat{\tau}_1 \tag{3.28}$$

where $i\omega_n[1 - Z(\mathbf{k}, i\omega_n)]$ and $\chi(\mathbf{k}, i\omega_n)$ are the odd and even pieces of the single-particle self-energy and $\phi(\mathbf{k}, i\omega_n)$ is the anomalous self-energy. The el-ph coupling strength λ_z

characterizes the contribution to $Z(\mathbf{k},\omega)$ and $\chi(\mathbf{k},\omega)$ while λ_ϕ characterizes the contribution to $\phi(\mathbf{k},\omega)$. Equations 3.26-3.28 are solved self-consistently on the Matsubara frequency axis. The self-energy on the real axis can then obtained by performing the usual analytic continuation $i\omega_n \rightarrow \omega + i\delta$ where $\delta > 0$ is a real, infinitesimal number.

In general, a full analytic expression for the self-energy on the real axis cannot be obtained if equation 3.26 is solved self-consistently. However, analytic expressions can be obtained in the limit of large bandwidth, where the band dispersion at the Fermi level is well approximated by a linear dispersion. A full derivation of the self-energy in this limit is presented in appendix B. In systems with a narrow bandwidth, where the curvature near the Fermi level is important, Eq. 3.28 must be evaluated numerically and Marsiglio *et al.* [172] have developed an efficient iterative method for doing so. With this method, $\hat{\Sigma}(\mathbf{k},\omega)$ is obtained by iteratively solving [172, 171]

$$\begin{aligned}\hat{\Sigma}(\mathbf{k},\omega) &= \frac{1}{N\beta}\sum_{\mathbf{p}}\sum_{m=0}^{\infty}\lambda_0(\mathbf{k},\mathbf{q},\omega - i\omega_m)\hat{\tau}_3\hat{G}(\mathbf{k},i\omega_m)\hat{\tau}_3 \\ &+ \frac{1}{N}\sum_{\mathbf{k}}\int_{-\infty}^{\infty}d\nu\alpha^2F(\mathbf{k},\mathbf{q},\nu)[n_b(\nu)+n_f(\nu-\omega)]\hat{\tau}_3\hat{G}(\mathbf{k},\omega-\nu)\hat{\tau}_3\end{aligned} \tag{3.29}$$

using the solution obtained on the imaginary axis as input. Here, n_b and n_f are the usual Bose and Fermi factors and

$$\lambda_0(\mathbf{k},\mathbf{q},\omega) = \int_0^\infty d\nu\alpha^2F(\mathbf{k},\mathbf{q},\nu)\frac{2\nu}{\omega^2-\nu^2}. \tag{3.30}$$

Note that the second term of equation 3.29 is identically zero when $\omega = i\omega_n$ and reduces to Eq. 3.26. The self-energies calculated using this formalism have been examined in a previous work [23] and it was found that, for coupling strengths similar to those given in table 3.1, the effects of the multi-phonon rainbow diagrams give a small contribution to the el-ph self-energy. Therefore, in examining phonon features in the ARPES spectra due to el-ph coupling, it is sufficient to consider only a single iteration of the Eliashberg equations, where simple closed form expressions for $\hat{\Sigma}(\mathbf{k},\omega)$ can be obtained. However, if one wishes to calculate the self-energy for boson modes which significantly contribute to pairing then the full solution to equation 3.29 is required. This will be the case in chapter 4, when the generic signatures of bosonic modulations in the density of states are considered.

In order to derive the simplified single-iteration expressions, the electron bare propagator in the superconducting state is introduced

$$\hat{G}^{-1}(\mathbf{k},i\omega_n) = i\omega_n\hat{\tau}_0 + \epsilon_{\mathbf{k}}\hat{\tau}_3 + \Delta(\mathbf{k})\hat{\tau}_1. \tag{3.31}$$

The optical oxygen modes, indexed by ν, are modelled with dispersionless Einstein modes of frequency Ω_ν and their bare phonon propagator

$$D_\nu(\mathbf{q}, i\omega_m) = -\frac{2\Omega_\nu}{\omega_m^2 + \Omega_\nu^2}. \tag{3.32}$$

Substituting equations 3.32 and 3.31 into equation 3.26 and analytically continuing to the real axis produces a simple form for the el-ph self-energy. The final form for the imaginary part of the three self-energy components are [3]

$$\begin{aligned}\omega Z_2(\mathbf{k},\omega) &= \frac{\pi}{2N}\sum_{\mathbf{p},\nu}|g_\nu(\mathbf{k},\mathbf{q})|^2\big([n_b(\Omega_\nu)+n_f(E_\mathbf{p})][\delta(\omega+\Omega_\nu-E_\mathbf{p})+\delta(\omega-\Omega_\nu+E_\mathbf{p})] \\ &\quad +[n_b(\Omega_\nu)+n_f(-E_\mathbf{p})][\delta(\omega-\Omega_\nu-E_\mathbf{p})+\delta(\omega+\Omega_\nu+E_\mathbf{p})]\big) \end{aligned}\tag{3.33}$$

$$\begin{aligned}\chi_2(\mathbf{k},\omega) &= -\frac{\pi}{2N}\sum_{\mathbf{p},\nu}|g_\nu(\mathbf{k},\mathbf{q})|^2\frac{\epsilon_\mathbf{p}}{E_\mathbf{p}}\big([n_b(\Omega_\nu)+n_f(E_\mathbf{p})][\delta(\omega+\Omega_\nu-E_\mathbf{p})-\delta(\omega-\Omega_\nu+E_\mathbf{p})] \\ &\quad +[n_b(\Omega_\nu)+n_f(-E_\mathbf{p})][\delta(\omega-\Omega_\nu-E_\mathbf{p})-\delta(\omega+\Omega_\nu+E_\mathbf{p})]\big) \end{aligned}\tag{3.34}$$

$$\begin{aligned}\phi_2(\mathbf{k},\omega) &= \frac{\pi}{2N}\sum_{\mathbf{p},\nu}|g_\nu(\mathbf{k},\mathbf{q})|^2\frac{\Delta_\mathbf{p}}{E_\mathbf{p}}\big([n_b(\Omega_\nu)+n_f(E_\mathbf{p})][\delta(\omega+\Omega_\nu-E_\mathbf{p})-\delta(\omega-\Omega_\nu+E_\mathbf{p})] \\ &\quad +[n_b(\Omega_\nu)+n_f(-E_\mathbf{p})][\delta(\omega-\Omega_\nu-E_\mathbf{p})-\delta(\omega+\Omega_\nu+E_\mathbf{p})]\big) \end{aligned}\tag{3.35}$$

where $E_\mathbf{p}^2 = \epsilon_\mathbf{p}^2 + \Delta_\mathbf{p}^2$ defines the quasi-particle energy in the superconducting state. Finally, the real parts of the self-energy are obtained using the Kramers-Kronig relations (See Appendix A).

To illustrate the energy structure of the self-energies the real and imaginary parts of Z, χ and ϕ are plotted in figure 3.5 for a momentum point on the Fermi surface in the antinodal region ($\mathbf{k} = (\pi/a, 0.18\pi/a)$) of Bi-2212. Here, the self-energies are evaluated using the same parameters used for Fig. 3.3, and assuming a d-wave superconductor at $T = 25$ K with $\Delta_0 = 35$ meV. The structure of the self-energies for other modes is similar apart from the overall magnitude of the self-energy, reflecting the momentum structure of $g(\mathbf{k}, \mathbf{q})$.

The imaginary parts of the self-energy Z_2, χ_2 and ϕ_2 all show an onset at the energy of the bosonic mode Ω_ν. This is due to energy conservation considerations which prevent fermions within Ω_ν of Fermi surface from coupling to the optical phonon modes at low T [9]. At higher energies peaks in the three self-energies occur at two energy scales. The first of these is set by $\Omega_\nu + \Delta_0$ where Δ_0 is the maximum value of the superconducting gap

[3] A full derivation of the self-energy has been presented in previous works by the author[23, 72].

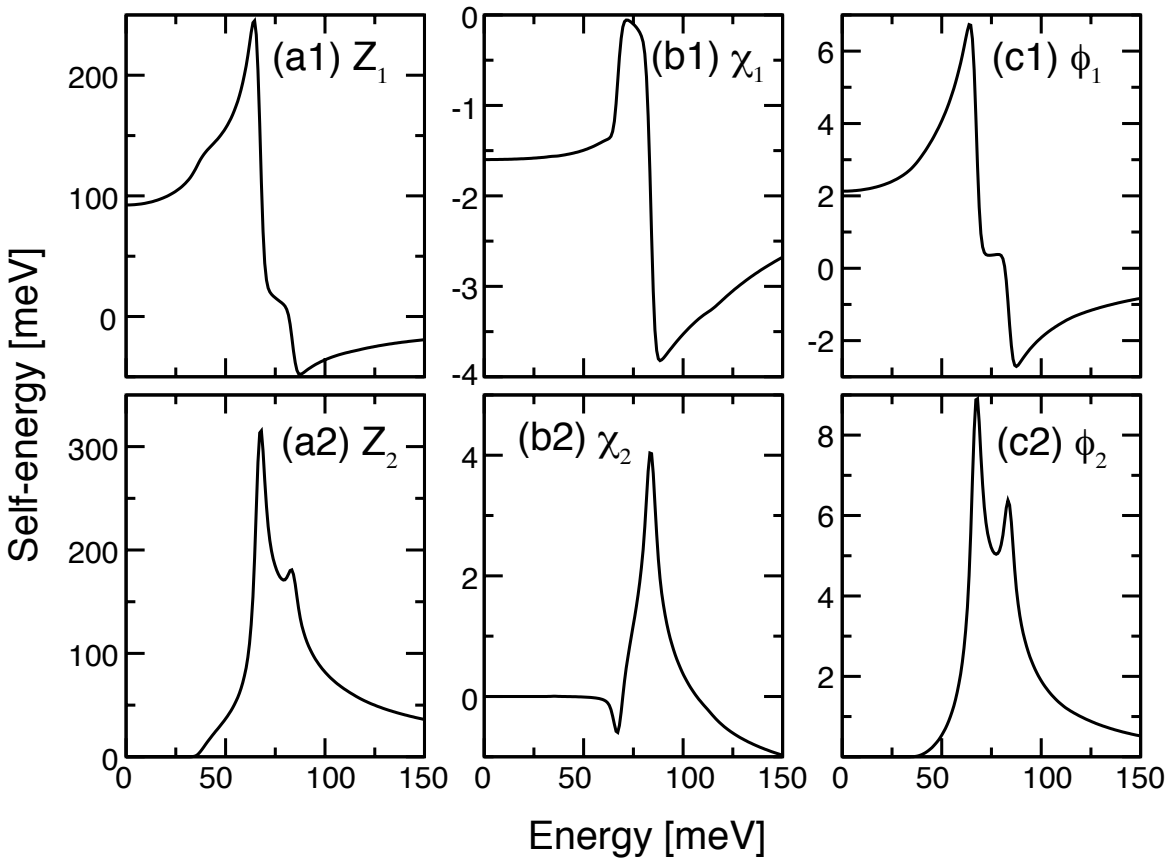

Figure 3.5: The electron-phonon self-energies calculated for coupling to the 36 meV B_{1g} branch in the superconducting state (25 K) of Bi-2212. Here, the self-energy has been calculated for a point on the Fermi surface in the antinodal region with $\mathbf{k} = (\pi/a, 0.18\pi/a)$.

on the Fermi surface. The second peak is set by the van Hove singularity and occurs at $\Omega_\nu + E(0,\pi)$. This feature can be muted with the inclusion of k_z dispersion. In addition, χ has structure at higher energies associated with the van Hove singularities at the top and bottom of the band. The real parts of the self-energies also develop peak structure, which gives way to a step-down at $\Omega_\nu + \Delta_0$ and $\Omega_\nu + E(0,\pi)$ due to their Kramers-Kronig relation to the imaginary parts. From the magnitudes of the self-energies shown in figure 3.5 it is also apparent that the self-energies are dominated by the renormalization parameter $Z(\mathbf{k},\omega)$. Based on the overall magnitude of the anomalous self-energy it is clear that the phonons alone cannot account for the high T_c observed in the cuprates.

The real and imaginary parts of single-particle self-energy $-\omega Z(\mathbf{k},\omega)+\chi(\mathbf{k},\omega)$, which determines the renormalization of the single particle spectral function $A(\mathbf{k},\omega)$, are shown

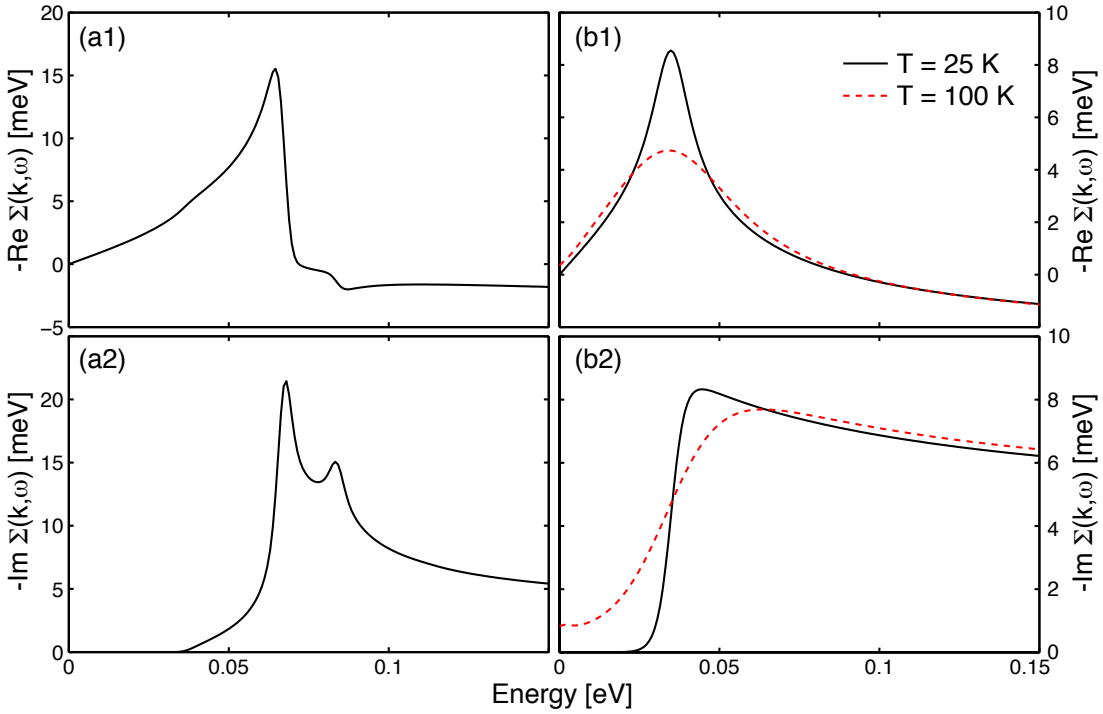

Figure 3.6: The single-particle self-energy $\Sigma(\mathbf{k},\omega) = -\omega Z(\mathbf{k},\omega) + \chi(\mathbf{k},\omega)$ evaluated at a point on the Fermi surface $\mathbf{k} = (\pi/a, 0.18\pi/a)$. (a1),(a2) The self-energy in the superconducting state (25 K) with $\Delta_0 = 35$ meV. (b1),(b2) the self-energy in the normal state (25 K, black and 100 K, red dashed). In both cases, the chemical potential shift determined by $\mathrm{Re}\chi(\mathbf{k},0)$ (at 25 K) has been subtracted from the real part of the self-energy.

in figures 3.7a1, and 3.7a2, respectively. Following the structure in Z and χ, the imaginary part of the self-energy has an onset at Ω_ν and peaks at $\Delta_0 + \Omega_\nu$. It is this increase in the $\mathrm{Im}\Sigma$ which produces the lineshape broadening in $A(\mathbf{k},\omega)$ below the kink energy. The real part, again due to Kramers-Kronig consistency, has a peak at an energy just below this energy scale, which gives way to a step down at $\Delta_0 + \Omega_\nu$. It is this peak which produces the kink feature in $A(\mathbf{k},\omega)$.

3.6.2 The Normal State

The formalism given in the previous section can be extended to the normal state by setting $\phi = \Delta_\mathbf{k} = 0$ and replacing the quasi-particle energy with the band dispersion

$E_{\mathbf{k}} = \epsilon_{\mathbf{k}}$. The self-energy in the normal state then reduces to

$$\begin{aligned}\Sigma_2(\mathbf{k},\omega) &= -\omega Z_2(\mathbf{k},\omega) + \chi_2(\mathbf{k},\omega) \\ &= -\frac{\pi}{N}\sum_{\mathbf{p}} |g(\mathbf{k},\mathbf{q})|^2 \big[(n_f(\omega_0-\omega)+n_b(\Omega_0))\delta(\omega-\Omega_0-\epsilon_{\mathbf{p}}) \\ &\qquad +[n_f(\Omega_0+\omega)+n_b(\Omega_0)]\delta(\omega+\Omega_0-\epsilon_{\mathbf{p}})\big] \qquad (3.36)\end{aligned}$$

which recovers the standard result [9]. The real part of the self-energy is again obtained from the Kramers-Kronig relations. The real and imaginary parts of $\Sigma(\mathbf{k},\omega)$ in the normal state are plotted in figure 3.6b1 and 3.6b2, respectively. In order to highlight the position of the peaks in the self-energy Σ is plotted for $T = 25$ and 100 K. In the low temperature plot a clear peak is found in ReΣ at the energy of the phonon mode Ω_ν. At this same energy scale ImΣ has an onset similar to that observed in the superconducting state. In the 100 K spectra the self-energy is significantly broadened due to thermal effects. As a result, the onset in ImΣ is rounded and the peak in ReΣ is broadened and reduced in intensity.

3.7 The Single-particle Spectral Function

The single-particle spectral function is related to the imaginary part of the dressed electron Green's function $A(\mathbf{k},\omega) = -\frac{1}{\pi}\mathrm{Im}G_{11}(\mathbf{k},\omega)$. In the superconducting state the dressed Green's function is given by

$$\hat{G}(\mathbf{k},\omega) = \frac{\omega Z(\mathbf{k},\omega)\hat{\tau}_0 + [\epsilon_{\mathbf{k}} + \chi(\mathbf{k},\omega)]\hat{\tau}_3 - \phi(\mathbf{k},\omega)\hat{\tau}_1}{[\omega Z(\mathbf{k},\omega)]^2 - [\epsilon_{\mathbf{k}} + \chi(\mathbf{k},\omega)]^2 - \phi^2(\mathbf{k},\omega)}. \qquad (3.37)$$

while in the normal state the Green's function reduces to the usual form

$$G(\mathbf{k},\omega) = \frac{1}{\omega - \epsilon_{\mathbf{k}} - \Sigma(\mathbf{k},\omega) + i\delta}. \qquad (3.38)$$

The spectral function is shown in figure 3.7 for Bi-2212 in the normal (100 K, upper panels) and superconducting (25 K, lower panels) states. Here, coupling to the 36 meV B_{1g} and 70 meV breathing branches have been included. The form of the el-ph vertices are defined by equations 3.21 and 3.22 with the overall strength of the el-ph coupling is determined using the same parameters used in 3.3. Since the el-ph interaction is insufficient to produce the full magnitude of the superconducting gap, a small piece is added to the real part of ϕ in order to maintain the value of the gap function $\Delta(\mathbf{k},\omega) = \phi(\mathbf{k},\omega)/Z(\mathbf{k},\omega)$ at the gap edge $\omega = \Delta_0$, where Δ_0 is the maximum value of the superconducting gap. This procedure is consistent with the idea of the phonons

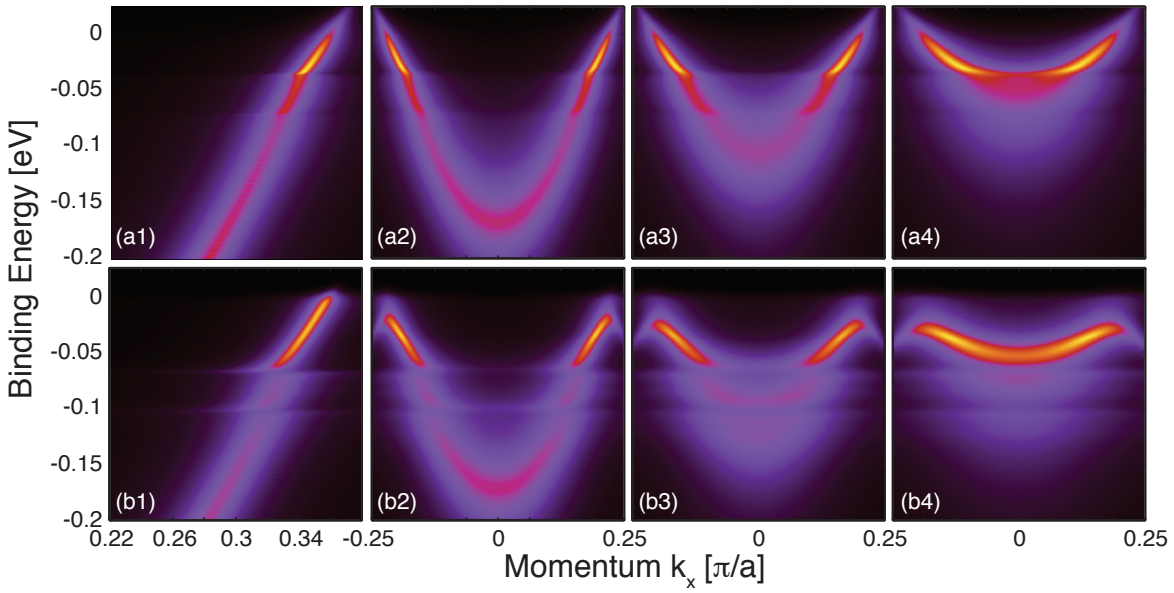

Figure 3.7: The single-particle spectral function $A(\mathbf{k},\omega)$ in (a) the normal (100 K) and (b) superconducting (25 K) states. Here, $A(\mathbf{k},\omega)$ is calculated for el-ph coupling to the 36 meV B_{1g} bond-buckling and 70 meV bond-stretching modes as was considered in reference [30]. The cuts in momentum space are taken along (a1,b1) the zone diagonal ($k_x = k_y$) and along cuts parallel to the zone face; (a2,b2) $k_y = 0.65$, (a3,b3) $k_y = 0.75$ and (a4,b4) $k_y = 0.85$ (in units of π/a).

modulating the electronic properties of the system over another dominant pairing mechanism [89]. Panels 3.7a1 and 3.7b1 correspond to a cut taken along the nodal direction (0,0) - (π/a,π/a). Panels 3.7a2-a4 (and 3.7b2-b4) correspond to cuts taken parallel to the zone face (0,π/a) - (π/a,π/a) for $k_y = 0.65$, 0.75 and 0.85 π/a, respectively. These results reproduce the trends observed in previous works [23, 30].

In the normal state (Fig. 3.7a1-a4) kinks occur in the spectral function at the energy of the phonon branches Ω_ν (36 and 70 meV, respectively), corresponding to the peak in the self-energy shown in figure 3.6. At this energy scale the width of $A(\mathbf{k},\omega)$ grows considerably due to the onset of phonon scattering channel, signified by the slow rise in ImΣ (Fig. 3.6b2). In the superconducting state the energies of these features shift by the maximum value of the superconducting gap on the Fermi surface, following the shift in peak position of the self-energies. This occurs throughout the zone, even for cuts in the nodal region where $\Delta_\mathbf{k}$ is vanishing. This is due to the fact that the el-ph scattering process links states from $\mathbf{k}$ to $\mathbf{p}$ located throughout the zone and thus the scattered electrons feel the full gap. Furthermore, scattering to the antinodal states,

where the gap is largest, is favoured by the B_{1g} branch's coupling. This further enhances the sampling of the large gap in this region. The strength of the kink renormalizations in the superconducting state are also increased in comparison with the corresponding cut in the normal state, in agreement with experiment [31, 71]. This is due to the enhancement of the density of states in the antinodal region, which accompanies the opening of the d-wave gap. (This point will be discussed further in the next chapter when the temperature dependence of the renormalizations is examined in greater detail.) The anisotropy of the coupling is also clearly reflected in the evolution of renormalizations through momentum space. In the antinodal region the strength of the coupling to the B_{1g} branch is largest, following the structure of $\lambda(\mathbf{k}_F)$ shown in figure 3.3, which results in more pronounced el-ph features.

Another notable feature of the near anti-nodal cuts is the trailing intensity asymptotically approaching the phonon energy Ω_ν (or $\Delta_0 + \Omega_\nu$ in the superconducting state). At the kink energy the coupling between the electronic and phononic states has mixed the character of these states and the trailing intensity represents the electron states which have developed significant phonon character and now track the dispersion of the phonon (in this case a dispersionless phonon). If the band is shallow enough along a particular cut in momentum space (for example panels a4, b4) then this trailing intensity can merge with the other side of the band. This produces a sharp quasiprticle band above the phonon energy and a broader incoherent band at higher binding energies where the electron is dressed by phonon scattering. These two regions are separated by a region of low intensity and this is the origin of the peak-dip-hump structure in the anti-nodal region. This also highlights an important kinematic constraint that governs which fermion states can couple to each mode. The spectra will show a mixing of electron and phonon states if the band energy along a particular cut crosses the phonon mode energy. However, if the band along a particular cut lies above the mode energy then the spectra will show a level repulsion in the form of a flattened band bottom along that cut. In the cuprates, the shallow band in the vicinity of the antinodal region of the Brillouin zone limits the coupling to those states to modes with energies less than $\epsilon(0, \pi)$. Thus, one expects coupling to the modes to disappear from the spectra when $\Omega_\nu < \epsilon(\mathbf{k})$ along the entire cut. In the case of the apical mode, although coupling may be largest in the antinodal region, a kink effect is prevented kinematically. Moreover, the breathing modes will be observable only for near-nodal cuts and disappears in the antinodal region once the bottom of the bare band rises above the phonon energy, as shown in figure 3.7a4.

3.8 Summary

This chapter presented the theory of el-ph coupling within the framework of the Migdal approximation, which is generally valid in the limit of weak el-ph coupling. Attention was

placed on a number of optical phonon branches in the cuprates which involve the planar and apical oxygen atoms. In terms of the microscopic mechanisms for coupling, the c-axis modes couple to the electrons via the modulation of the atomic site energy, arising due to presence of a local crystal field generated by the surrounding environment. Since the magnitude of the crystal field is determined by the structure and composition of the unit cell the coupling to the c-axis modes will naturally have a materials dependence. In contrast, the in-plane breathing modes couple via a deformation coupling, which depends on the in-plane lattice constant. Since the latter only varies by only a few percent between the cuprates, the coupling to the breathing branch should be relatively independent of the material.

The observation of this materials dependence provides one pathway for distinguishing between the phonon and magnetic resonance scenarios that have been proposed for the "kinks". In the single-layer cuprates, the peak-dip-hump structure is absent indicating that either the coupling to the mode responsible is extremely weak in these systems or that the mode is absent in these materials. In the phonon scenario, where the c-axis B_{1g} mode is responsible for the antinodal peak-dip-hump, this can be naturally accounted for since the electric field strength, and therefore total coupling to this mode, is expected to be small. The spin resonance mode has been observed in some single layer systems [95] and therefore a peak-dip-hump structure would be expected if the spin resonance mode where responsible for this feature. These material dependent aspects of the coupling to the c-axis modes will be discussed further in chapter 6 when considerations for the phonon's contribution to T_c are presented.

With the microscopic mechanism for el-ph coupling identified, expressions for the el-ph coupling constants $g(\mathbf{k}, \mathbf{q})$ were then derived. Due to the underlying symmetries of the phonon eigenvectors, as well as the symmetries of the atomic orbitals, the momentum structure of $g(\mathbf{k}, \mathbf{q})$ was found to be anisotropic in $\mathbf{k}$ around the Fermi level. In general, the c-axis modes couple strongly in the anti-nodal region while the in-plane modes couple strongly for large momentum transfers $\mathbf{q}$. As a consequence of this anisotropic coupling, momentum dependent renormalizations then naturally arises.

Finally, the structure of the self-energies and single-particle spectral functions were also examined. In agreement with prior work, the formalism presented here captures the observed anisotropy of the coupling in both the normal and superconducting states, as well as the increased coupling strength in the superconducting state. Furthermore, the cross over from a kink in the nodal region to a peak-dip-hump structure and band breakup in the antinodal region was also captured. From these observations it is clear that the gross features observed in ARPES experiments are present in this model. Investigation will continue down this path in the following chapter and the model presented here will be used to further examine the agreement between theory and experiment. In this case, the details of the temperature and doping dependence of these renormalizations will be

presented. Furthermore, there still remains the open question of how these dispersion renormalizations observed by ARPES are related to the density of states modulations observed by scanning tunneling microscopy. This question will also be addressed.

Chapter 4

Temperature, Doping and Materials Dependence of the ARPES Kinks

The Migdal-Eliashberg formalism presented in the previous chapter has been successfully applied to understanding the anisotropy of the renormalizations observed in the high-T_c cuprates [23, 30]. In this chapter this work is extended and focus is placed on the details of the temperature, doping and materials dependence of these renormalizations. Some of the results presented in this chapter have appeared in references [71, 72, 33].

4.1 Temperature Dependence of the Kink

4.1.1 Temperature Dependence of the Peak-dip-hump

In the standard treatment of el-ph coupling effects, the Debye temperature sets a characteristic temperature scale which is well above T_c in conventional materials. However, in the cuprates and other systems with small Fermi energies, these energy scales can be comparable. As a result, the temperature dependence of the phonon induced self-energies can be very different from that of conventional superconductors. According to the ARPES measurements on the Bi-2212 system, the band renormalization in the antinodal region (the PDH structure) shows a dramatic superconductivity-induced enhancement when the system undergoes the normal to superconducting phase transition. As discussed in chapter 2, it has been argued that only a mode that emerges in the superconducting state can explain this temperature-dependent effect [60, 66, 68, 70] and phonons are thereby excluded.

The sharpness of the el-ph self-energy is strongly temperature dependent due to the fact that T_c of optimally doped Bi-2212 is close to 100 K. To demonstrate this temper-

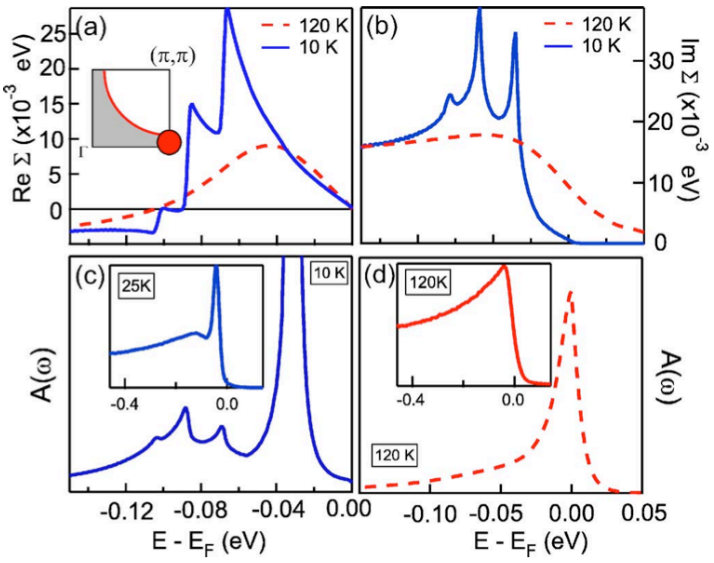

Figure 4.1: The calculated (a) real part ReΣ, (b) imaginary part ImΣ of the self-energy and the corresponding spectral functions $A(\mathbf{k},\omega)$ in (c) the normal state and (d) the superconducting state. An extra 5 meV is added to the imaginary part of the self-energy to provide a small additional broadening below the phonon frequency. The location for this calculation is indicated in the inset of (a) by a red dot with the red curve representing the FS. Insets (c) and (d) are the data of optimally doped Bi-2223 systems (T_c = 110 K) taken in the superconducting (25 K) and normal states (120 K) [81], respectively.

ature dependence, the self-energy in the normal (120 K) and superconducting states (25 K) is presented for a *d*-wave superconductor coupled to the 36 meV B_{1g}, 55 meV A_{1g} and 70 meV breathing modes. The el-ph coupling for the B_{1g} and breathing modes are those given by Eqs. 3.12 and 3.18. Here, for simplicity, the A_{1g} coupling is treated as a constant in the calculations presented in this section. The motivation for the three-mode treatment here is the success of the two-mode calculation [30] as well as the recent discovery of multiple mode coupling in LSCO [74, 73]. For this calculation, the tight-binding band structure given in reference [66] has been used and the superconducting gap size has been set to $\Delta_0 = 35$ meV. The real and imaginary parts of the single-particle self-energy $\Sigma(\mathbf{k},\omega) = \omega[1 - Z(\mathbf{k},\omega)] + \chi(\mathbf{k},\omega)$ and the spectral function $A(\mathbf{k},\omega)$ at $\mathbf{k} = (0,\pi)$ are determined using equations 3.33 - 3.35. The results are shown in figure 4.1. For reference, the corresponding experimental EDCs are plotted in the insets of panels 4.1c and 4.1d.

At high temperature, both $\mathrm{Re}\Sigma(\mathbf{k},\omega)$ and $\mathrm{Im}\Sigma(\mathbf{k},\omega)$ do not exhibit sharp features, as shown by the dashed curve in Fig. 4.1a and 4.1b, respectively. This demonstrates that thermal broadening at high temperature smears out the peak structure of the self-

energy. In addition, broadening due to other many-body effects would further smear any features in $\Sigma(\mathbf{k},\omega)$ and subsequently $A(\mathbf{k},\omega)$. Thus, one should not expect to observe any sharp renormalizations from el-ph coupling at $\mathbf{k} = (0,\pi)$ in the normal state. In the superconducting state, the peaks in the self-energy sharpen significantly. This is due to two effects; the reduction of thermal broadening at low temperature and the opening of the superconducting gap, which increases the density of states in the vicinity of the phonon energies. As a result, the PDH structure of the spectral function at $\mathbf{k} = (0,\pi)$ emerges at low temperature but disappears at high-temperature, as illustrated in Figs. 4.1c and 4.1d, respectively. This is in agreement with ARPES experiments on optimally doped Bi-2212 and Bi-2223 [60, 31, 70, 81]. While this behaviour is expected for any phonon, it should be noted that the self-energies from coupling to modes that involve momentum transfers within and between antinodal regions of the FS, such as the A_{1g} and B_{1g} modes, are greately enhanced for all $\mathbf{k}$ due to the large DOS enhancements in these regions via the opening of a d-wave gap.

4.1.2 Temperature Evolution of the Nodal Kink

As shown in chapter 3, in the Eliashberg formalism, coupling to a sharp bosonic mode in a d-wave superconductor yields a dispersion kink in the nodal region at an energy of $\Delta_0 + \Omega_0$. Above T_c, this energy scale appears at the boson energy Ω_0 due to the closing of the gap. However, as was noted in chapter 2, this is not observed experimentally and the apparent kink energy in the nodal region remains at ~ 70 meV in both the normal and superconducting state. This lack of energy shift has been a long standing puzzle, which seems to contradict theoretical predictions and has been cited as a reason to doubt the el-ph interpretation for the band renormalizations [79].

In the previous chapter it was proposed that energy scales of the B_{1g} and breathing modes as well as the gap size conspired to produce similar kink energies in the normal and superconducting states. In this section, this claim will be examined in greater detail by examining the temperature dependent shifts in spectral weight and it will be shown that the experimental data is consistent with this proposal. In order to address this issue focus is placed on the temperature dependence of the band dispersion in Bi-2212 along the nodal cut (0,0) - (π,π). Compared to other cuprates with lower T_c's, the large gap size $\Delta_0 \sim 40$ meV in optimal doped Bi-2212 provides a better opportunity to resolve the superconductivity-induced shifts of the renormalizations.

Experimental estimates for ReΣ, obtained from optimal doped Bi-2212 using the procedure outlined in chapter 2, are presented in figure 4.2a. Data taken from above and below T_c are shown. At both temperatures, the maximum in ReΣ, which determines the kink position, occurs at ~ 70 meV. This coincidence of the positions verifies the previous observations of the absent shift of the kink position. In addition, the data below T_c

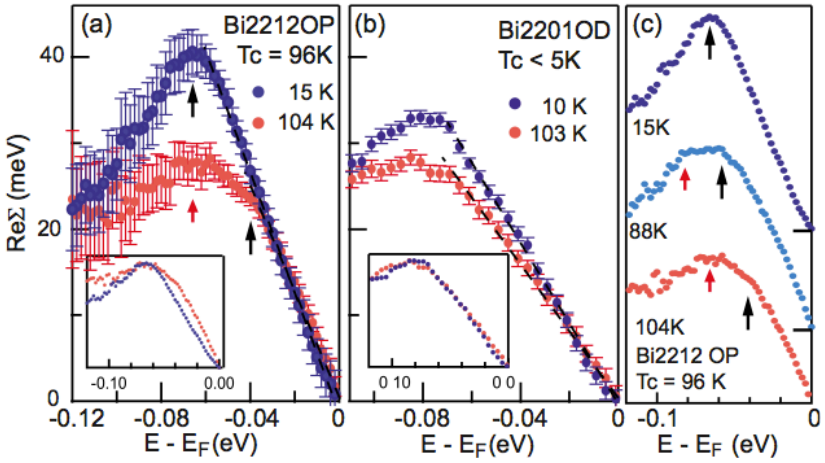

Figure 4.2: (a) ReΣ in the normal and superconducting state for optimally doped Bi-2212. (b) Non-superconducting heavily overdoped Bi-2201. The insets plot ReΣ with their maximum normalized to illustrate the difference of the self-energy profile. The arrows indicate the energy positions of the kink and subkink. The error bars were estimated from the 99.7% confidence interval of the fitted MDC peak positions. (c) The evolution of ReΣ across the superconducting phase transition. Reproduced from reference [71].

has a much stronger peak in ReΣ, reflecting the increase in the kink strength in the superconducting state. An additional feature can be seen in the normal state data - a shoulder or "subkink" at about $\sim 34 \pm 4$ meV, where the slope of ReΣ abruptly changes. Furthermore, this feature is is not present in the data below T_c.

In figure 4.2b similar estimates for ReΣ are shown for a Bi-2201 sample. The data was obtained at similar temperatures but both were taken above the T_c of the sample (< 5 K). In comparison to the Bi-2212 data there are two key differences. First, the overall magnitude of ReΣ is comparable at the two temperatures, and second, no change in slope occurs between the maximum in ReΣ and the Fermi level. This difference between the two samples indicates that thermal effects alone cannot account for the temperature dependent changes in Bi-2212. For Bi-2212 in the normal state, the 70 meV peak is assigned to the in-plane breathing branch while the 34 meV feature is assigned to the bond-buckling B_{1g} mode. The absence of the subkink feature in the Bi-2201 data is interpreted as due to the weak coupling to the B_{1g} mode in the single layer cuprates where the CuO_2 plane sits in a plane of mirror symmetry.

The temperature evolution of ReΣ in the Bi-2212 sample, from above T_c to below T_c, is shown in figure 4.2c. The data at 88 K provides important information that was not available in earlier experiments and two processes can be seen. First, both the maximum

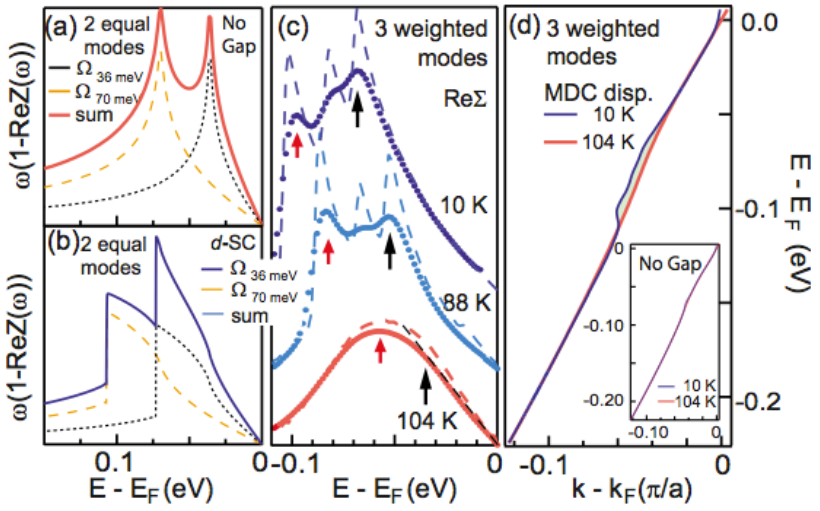

Figure 4.3: The self-energy $Z(\omega)$ for two equally strong Einstein modes in the case of (a) a normal state and (b) a d-wave superconductor with $\Delta_0 = 37$ meV. (c) The extracted ReΣ by applying the MDC analysis to the spectral functions calculated with three weighted Einstein modes in a tight-binding band structure at different temperatures ranging from a normal state (104 K) to a superconducting state (88 K with $\Delta_0 = 20$ meV, and 10 K with $\Delta_0 = 37$ meV). The arrows indicate the energy positions of the kink and subkink. (d) The band dispersion along the nodal direction extracted from the spectral functions calculated using the same parameters as (c). The shaded area highlights the difference between the band dispersions at these two temperatures. The inset plots the MDC dispersions at 104 and 10 K extracted for the case of a non-superconductor.

(shorter arrow) and the subkink (longer arrow) shift towards higher binding energy with the opening of the superconducting gap. This energy shift is expected in the Eliashberg formalism, lending further support for interpreting the fine structures in ReΣ as coupling to the B_{1g} and breathing phonon branches. Second, a non-trivial redistribution of the relative weight between the two features occurs as the gap opens. The feature occurring lower in energy gradually grows until, at a temperature well below T_c (15 K), the lower energy feature dominates and sets the maximum of ReΣ. As a result, the higher energy feature, associated with the breathing mode, is unresolvable. This gives an impression that there is a superconductivity-induced change of mode coupling, favouring the lower energy B_{1g} branch at the expense of coupling to the higher energy breathing branch as T_c is crossed.

To qualitatively understand the spectral weight redistribution of the features in ReΣ it is sufficient to consider a simple bosonic spectrum consisting of two Einstein modes with

energies $\Omega = 36$ and 70 meV, respectively. These energies correspond to the energies of the subkink and maximum in the ReΣ data. To simplify matters, the momentum dependence of $g(\mathbf{k}, \mathbf{q})$ can be neglected since focus is placed on a specific cut in momentum space and therefore the relative anisotropy is irrelevant. The single particle self-energy $\omega[1 - Z(\omega)]$, calculated using the formalism presented in the previous chapter, is plotted in figure 4.3a and 4.3b for the normal state (no gap) and a d-wave superconductor with $\Delta_0 = 37$ meV, respectively. Here, the self-energy was calculated at $T = 0$ K and assuming a parabolic band structure and a circular Fermi surface. In both cases the strength of the coupling to the two modes are identical with $\Omega\lambda_z = 52$ meV. The total self-energy is then given by the sum of the contributions from both modes shown in the figures.

When the superconducting gap is absent the two peaks of the total self-energy are equally strong. However, in the superconducting state the lower energy peak appears to be stronger than the high energy peak despite the fact that the two modes have an equal coupling strength. This enhancement is in agreement with the experimental data shown in figure 4.2. According to the model, this enhancement is primarily due to the highly asymmetric shape of $\omega[1 - Z(\omega)]$ near the singularity for each mode in the superconducting state; it increases monotonically from E_f up to the singularity at $\Omega_0 + \Delta_0$, then drops suddenly to a value near zero (Fig. 4.3b). Thus, when summing the contributions from the two modes, the self-energy peak induced by the lower energy mode "sits" on the rising slope of the self-energy of the higher energy mode. As a consequence the low energy peak appears to be enhanced. Meanwhile, the self-energy peak of the higher energy mode sits on the tail of the self-energy of the lower energy mode and no significant enhancement occurs for this mode in the total self-energy. The normal state case is qualitatively different - the self-energy peaks are more or less symmetric with respect to the logarithmic divergence (Fig. 4.3a). Thus, in the normal state, the high energy mode peak acquires an enhancement from the tail of the low energy mode's peak.

The key features demonstrated in Figures 4.3a and 4.3b remain valid for bosonic spectrums of more than one mode as well as for band structures representative of the cuprates at finite temperatures. In figure 4.3c self-energies from coupling to three phonon modes, with energies of 36, 50 and 70 meV, are plotted at finite temperatures. The relative strength of each mode has been adjusted such that the shape of ReΣ resembles that of the 104 K data in figure 4.2a; the coupling strength then remains unchanged for the superconducting state calculations (d-wave gap, at 88 K with $\Delta_0 = 20$ meV, 10 K with $\Delta_0 = 37$ meV). The spectral functions along the nodal direction were calculated and the convolved with a two- dimensional Gaussian response function with a 10 meV energy resolution and a $0.012\pi/a$ momentum resolution. This allows for a simulation of a finite instrument resolution. The MDC analysis used for actual ARPES data was then applied to the simulated data in order to extract the renormalized band dispersions. As shown in figure 4.3d, the difference between the MDC dispersions at these two temperatures (shaded area) is significantly larger than that caused by thermal broadening (the inset).

Furthermore, the calculated self-energies reproduces the experimental data on optimally doped Bi-2212 as well as the reference experiment on non- superconducting, heavily overdoped Bi-2201 (Fig. 4.2).

The temperature dependent evolution of the calculated self-energy extracted from MDC dispersions is shown in Fig. 4.3c. As expected, the peaks in the ReΣ corresponding to each of the individual modes, are less resolvable due to the superposition of the modes and the smearing produced by the limited instrument resolution. This effect produces subkinks in the ReΣ, which is reminiscent of the data shown in figure 4.2 and the extracted ReΣ obtained from other cuprates [31, 73]. The calculations also demonstrate that the multimodes nature can still survive at temperatures of 104 K and manifests itself in the profile of the self-energy. Furthermore, the two-process evolution of the ReΣ observed in the data is qualitatively reproduced. Again, it is emphasized that the apparent kink (the broad maximum of ReΣ) in the band dispersion at 15 and 104 K is caused by different modes - at 104 K the 70 meV kink is produced by coupling to the breathing branch while at 15 meV the kink is produced by coupling to the B_{1g} mode. However, in the case of non-superconducting Bi-2201, the apparent kink in the dispersion is caused by the same mode (the breathing mode), since no temperature dependent energy shift of ReΣ is observed (Fig. 4.2). These results also indicate that the apparent kink position alone does not tell a complete story of the renormalizations observed in the cuprate families.

4.2 A Phenomenological Model for Doping Dependence of the Nodal Kink

One of the criticisms often levelled against the el-ph scenario for the dispersion kink is the strong doping dependence of the kink's position and strength. Based on wisdom gained from studying conventional metals, phonons are not expected to have a strong doping dependence in either their dispersions or coupling strength. However, these considerations are not necessarily valid for layered, doped Mott/charge-transfer insulators where doping dramatically changes the metallicity and the ability of the electrons to screen charge fluctuations. Many experiments on various cuprates report strongly doping-dependent el-ph coupling for the modes considered here. For example, inelastic neutron- scattering measurements show that the half- and full-breathing modes exhibit prominent softening of their dispersions as the systems are doped away from half-filling [96, 173]. In Raman and infrared spectroscopies the Fano line shapes of phonon modes with B_{1g} and B_{1u} symmetries show strong doping dependences [103, 174]. Furthermore, the strength of the phonon energy shift and line width variation across T_c also changes strongly with doping [100, 175].

Recent ARPES studies have also uncovered a sophisticated doping dependence of the

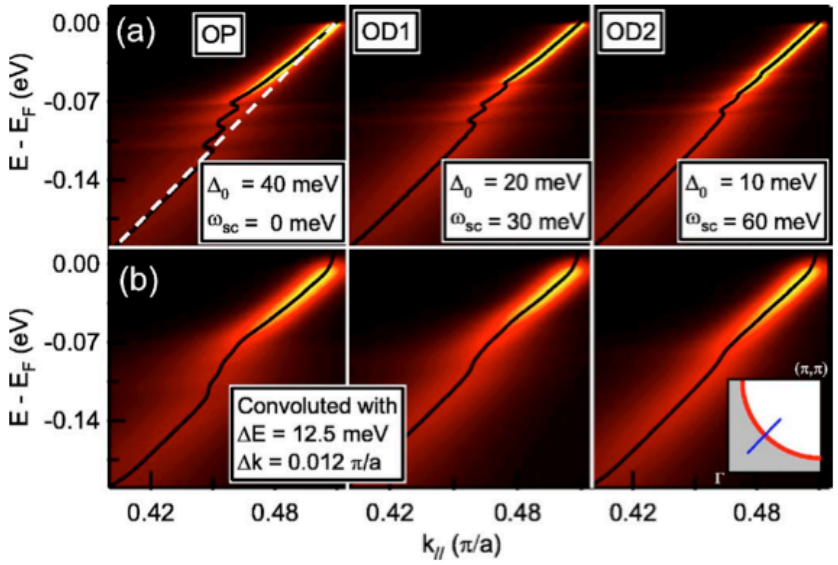

Figure 4.4: False color plots of the spectral function in the superconducting state (a) without resolution convolution and (b) with resolution convolution. The cuts are taken along the nodal direction, as indicated by the blue line of the inset. The black curves are the band dispersion extracted from the maximum position of the momentum distribution curves, which cut the spectral function at fixed energy. The MDC-derived dispersions in (a) exhibit three sharp "subkinks" due to the coupling to the three phonon modes used in the model, while in (b) the subkinks are washed out by the finite instrument resolution effect leaving an apparent single kink in the band dispersion. The white dashed line shown in panel (a) illustrates the bare band for extracting ReΣ.

electronic self-energy. One is the observation of coupling to multiple bosonic modes along the nodal direction [73]. The other is the doping dependent c-axis screening of the el-ph interaction [74]. In chapter 6 the full description of screening in the cuprates will be presented. In short, for el-ph coupling at long wavelengths, the screening becomes more effective at reducing the coupling strength when the c-axis conductivity becomes more metallic. These two results, plus the variation of the superconducting gap with doping, implies a highly convoluted doping dependence for the kink energy in the cuprates. This section examines these issues in the case of the nodal kink in the superconducting state of Bi-2212.

In figure 4.4 false colour plots of the calculated spectral functions are shown, including coupling to the B_{1g}, A_{1g} and breathing phonon branches. Here, the superconducting gap sizes were set to be 40, 20 and 10 meV for the optimal (OP) and more overdoped (OD1, OD2) systems, respectively. At this level the effects of doping and screening are treated

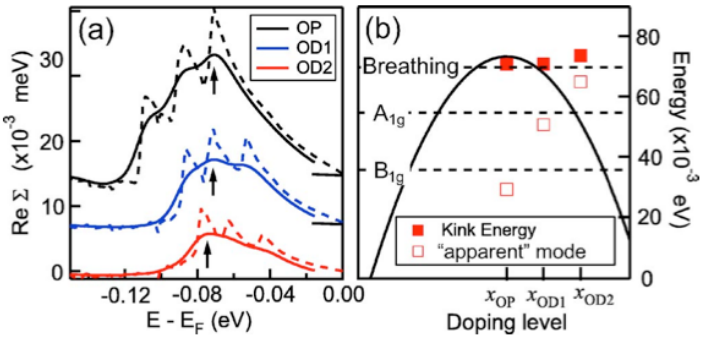

Figure 4.5: (a) The ReΣ extracted from Fig. 4.4a (dashed lines and 4.4b (solid lines) by subtracting a linear bare band (dashed line in Fig. 4.4a) from the band dispersion. The arrows indicate the maximum positions of the ReΣ where the "single" apparent kink in the band dispersion is usually defined. (b) A summary of the doping dependence of the apparent kink energy and the apparent mode energy extracted by assuming a single mode scenario.

phenomenologically [74, 176], leaving the full treatment of screening for chapter 6. In this approach, the coupling strength of the breathing mode, whose appreciable coupling occurs only for short wavelengths and large momentum transfers, remains unchanged as a function of doping. For the c-axis phonons (A_{1g} and B_{1g}), a filter function $\omega^2/(\omega^2+\omega_{sc}^2)$, with different values of the c-axis screening frequency ω_{sc} is applied in order to simulate the doping-dependent coupling strength which arises due to the change in the material's ability to screen effectively along the c-axis [176]. Although this is a simplification of the screening effects, it represents the general behaviour of screening considerations for phonons involving small in-plane momentum transfers. In addition, a component $\delta+\omega^2$ eV, with $\delta = 5$ meV, is added to the imaginary part of the self-energy to mimic the quasiparticle lifetime broadening due to electron- electron interactions.

As shown in figure 4.4a, the coupling to multiple phonon modes induces several "subkinks" in the dispersion. The positions of these subkinks mostly corresponds to the energies of the phonons plus the maximum value of the gap Δ_0. In figure 4.5a ReΣ, extracted by subtracting an assumed linear bare band, is plotted (dashed lines) for the three cases considered. The dominant feature in ReΣ for the OP case is induced by the 36 meV B_{1g} mode, while for the OD1 and OD2 cases, the features of the 55 meV A_{1g} and 70 meV breathing mode begin to out weigh the contribution from the B_{1g} mode. This demonstrates that the change of the SC gap magnitude and the effect of increased screening of the c-axis modes with increasing doping alters the relative strength of each phonon's contribution to $\Sigma(\mathbf{k},\omega)$.

To simulate the resolution limitation of experiment, the calculated spectral functions

are convolved with a 2D Gaussian distribution characterized by a typical ARPES instrumental resolution: 12.5 meV in energy resolution and 0.012 π/a in momentum resolution. The resolution broadened spectra are shown in figure 4.4b and the extracted ReΣ are shown in figure 4.5a (solid lines). As illustrated, the subkinks are less pronounced and become broadened into a "single" kink in the dispersion which is located at roughly the energy of the dominant phonon. This position is reflected in the maximum position in ReΣ, indicated by the black arrows in figure 4.5a and the solid red squares in figure 4.5b. If one assumes a single mode is responsible for the band renormalizations, and then extracts the doping dependence of the mode by subtracting the value of the superconducting gap, then a doping dependence of the mode energy is obtained. The energy scale obtained from this procedure is shown by the clear squares in figure 4.5b. It is important to note that the apparent energy scale obtained from this procedure does not correspond to any of the phonons used in the model; instead it is an average between the dominant features. Clearly the kink energy should not be taken as a precise measurement of the energy of any particular bosonic mode.

The calculations presented in this section cast doubt on the analysis of the doping dependent properties of the kink in the nodal band dispersion based on a single mode coupling scenario [67, 75]. More importantly, these calculations also serve to illustrate the complex nature of lattice effects in the cuprates which can develop a complicated temperature and doping dependence due to the interplay of a number of factors.

4.3 The Materials Dependence of Coupling to c-axis Phonons

Having examined the temperature and doping dependence of the band renormalizations attention is now turned to the materials dependence. As noted earlier, the coupling to c-axis phonons is expected to have a strong materials dependence due to the electrostatic environment generated by the structure and composition of the unit cell. In a previous work by the author [23] variations in the Madelung potential and local electric fields were calculated for the Bi-, Tl- and Hg-families of cuprates using the Ewald summation technique [177]. In this study a point charge model was assumed for each cuprate and formal valences were assigned to each atom in the unit cell. Structural data obtained from x-ray diffraction experiments was used to determine the structure of the unit cell. The results for the E-field strength at the planar oxygen site of the outermost CuO_2 layer in the Hg-family are reproduced in figure 4.6. (Similar trends were obtained for the Tl- (n = 1-4 layers) and Bi- (n = 1-3 layers) families.)

As discussed in chapter 3, the crystal field in the single layer system is identically zero (absent any static buckling which may occur within the CuO_2 plane) since the

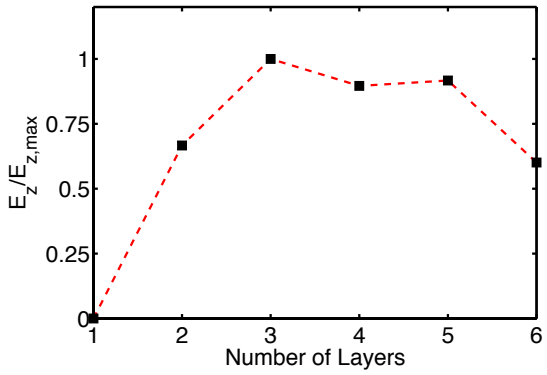

Figure 4.6: The local crystal field strength at the planar oxygen site of the outermost CuO_2 plane of the Hg-family of cuprates. All results have been normalized by the maximum field ~ 1.8 eV/$\mathring{A}$, which occurs in the $n = 3$ layer system.

CuO_2 plane lies in a mirror plane of the crystal. However, as the number of layers n is increased the outermost CuO_2 plane is moved away from this mirror plane and the field strength increases until reaching a maximum in the $n = 3$ layer system. The variation of the crystal field strength with the number of layers can be understood in terms of the spatial variation of the Madelung potential. The gradient of the Madelung potential, which determines the E-field, is identically zero at the mirror planes of the crystal. Such mirror planes generally lie at the middle and edges of the unit cell. Since the crystal is periodic, a point of steepest decent for the Madelung energy must exist at a location between these mirror planes. (The trivial solution of a uniform Madelung potential is also admitted, as is the case with $CaCuO_2$ [161].) Empirically, the Ewald calculations for the Madelung potential [23] indicate that for $n = 1 - 3$ the outermost plane approaches this point and therefore experiences a larger field due to the increased gradient. For $n > 3$ the outermost layer passes this point and the field is reduced. Finally, as the number of layers continues to increase there is an overall reduction in the amplitude of the Madelung potential variations such that a uniform profile occurs in the limit of the infinite layer compound $CaCuO_2$. The strength of the coupling to c-axis modes scales as E_z^2 and therefore the coupling to the planar c-axis modes will exhibit a similar materials dependence. Indeed, such a variation has been reported in the $Ba_2Ca_{n-1}Cu_nO_{2n}(O,F)_2$ family of cuprates, where the strength of the nodal kink in the hole-doped band diminishs monotonically from the $n = 3$ system to the $n = 5$ system [33].

The variations in the crystal fields are not the only way in which the composition of the unit cell will affect el-ph coupling. Changes in structure can also affect the planar oxygen content of the pd-σ^* band at the Fermi level through modifications of the atomic overlap integrals with changing interatomic distances. This will be reflected in a materials dependent variation in the oxygen content of the band crossing the Fermi level and is parameterized by A_o^2. As discussed previously, there is an empirical relationship between T_c and the distance of the apical oxygen from the CuO_2 plane. This relationship has generally been tied to the effective increase in the next nearest neighbour hopping of the

Zhang-Rice Singlet t' due to hybridization effects between the apical O $2p_z$ and Cu $4s$ orbital [18] via the effective planar O-O hopping. Such hybridization effects also have a direct impact on the coupling to the planar c-axis oxygen modes by lowering the value of A_o with decreasing apical distance. Since A_o enters $\lambda_{z,\phi}$ to the fourth power, the apical position can therefore exert a significant influence on the strength of the coupling to the planar c-axis modes. It should also be noted that the coupling to the breathing branch is not largely affected by this despite the fact that A_o also enters into the coupling for this mode. This is due to the fact that the breathing coupling also involves the copper character and the total coupling to the breathing branches scales as $A_o^2 A_{cu}^2$. As the planar oxygen character varies with apical distance, so does the copper character but in the opposite direction due to normalization requirements. Therefore as A_o is increased A_{cu} is decreased and the total coupling to the breathing mode is left relatively unchanged.

In figure 4.7 a systematic examination of the variation of the local E-field and planar oxygen character A_o is presented as a function of the material's T_c at optimal doping. To obtain A_o the five band model presented in chapter 3 is used but with site energies assigned using the energy level model of reference [18]. Using hole language, the on-site energies are set to $\epsilon_d = 0$, $\epsilon_p = \Delta$, $\epsilon_a = \Delta + \Delta\Phi_A/\epsilon(\infty)$ and $\epsilon_s = \epsilon_d - 7$. Here, Δ is the charge transfer energy associated with moving a hole from the oxygen site to the copper site. Δ is related to the difference in the Madelung energies $\Delta\Phi = \Phi_O - \Phi_{Cu}$ on the two sites and is given by

$$\Delta = \frac{\Delta\Phi_M}{\epsilon(\infty)} - I_{Cu}(2) + A_O(2) - \frac{e^2}{d_p} \tag{4.1}$$

where $I_{Cu}(2)$ and $A_O(2)$ are the second ionization and electron affinity energies for the Cu and O sites, respectively [18]. The factor e^2/d_p represents the contribution of the Coulomb interaction between the introduced electron-hole pair and d_p is the in-plane Cu-O bond distance. Following Ref. [18], the values $\epsilon(\infty) = 3.5$ and $I_{Cu} + A_O(2) + e^2/d_p = 10.9$ eV are assumed. In determining ϵ_a, $\Delta\Phi_A = \Phi_A - \Phi_O$ denotes the Madelung energy difference between the apical and planar oxygen sites. The Madelung energies of the individual sites are obtained from the electrostatic calculations of Ref. [23] in order to account for the material dependent crystal environment of the CuO_2 plane. In terms of the orbital overlaps, the apical distance also alters the overlap integrals t_{ap} and t_{sa}, which are adjusted using the scheme of reference [165]. The remaining overlap integrals, t_{pd}, t_{pp} and t_{sp}, which are a function of the in-plane bond distances are held fixed throughout the calculation. Finally, the electron correlations are handled at the mean field level by including $U_{dd} = 8$, $U_{pp} = 4$ and $U_{pd} = 1$ (in units of eV) [160]. The overall effect of the mean-field corrections is to shift the site energies

$$\begin{aligned}
\tilde{\epsilon}_d &= U_{dd}\langle n_i^d\rangle/2 + 4U_{pd}\langle n_i^p\rangle + U_{pd}\langle n_i^a\rangle \\
\tilde{\epsilon}_p &= \epsilon_p + U_{pp}\langle n_i^p\rangle/2 + 2U_{pd}\langle n_i^d\rangle \\
\tilde{\epsilon}_a &= \epsilon_a + U_{pp}\langle n_i^a\rangle/2 + U_{pd}\langle n_i^d\rangle
\end{aligned} \tag{4.2}$$

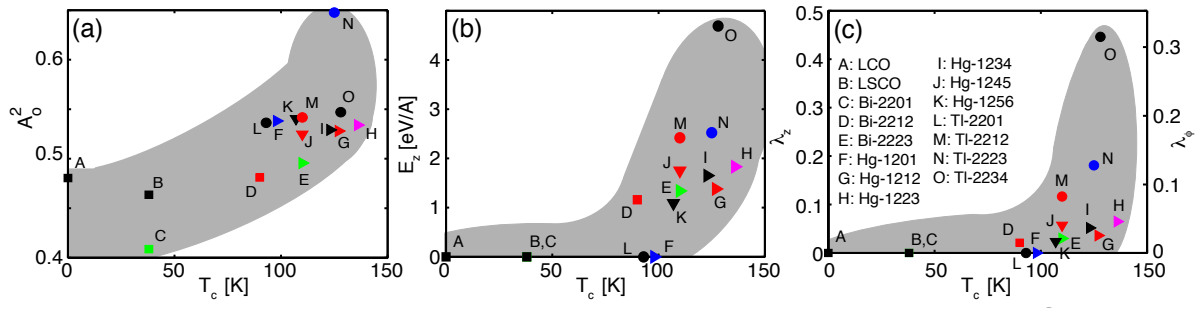

Figure 4.7: (a) The planar oxygen character at the Fermi surface A_o^2 as a function of the material's T_c. (b) The corresponding local E-field at the planar oxygen site of the outermost CuO_2 plane in the parent compound. (c) The value of λ_z for the B_{1g} branch of the outermost plane of the material.

while the value of $\tilde{\epsilon}_s$ is adjusted to maintain the difference $\tilde{\epsilon}_s - \tilde{\epsilon}_d = 7$ eV. In equation 4.2 n_i^α is the total number operator for orbital α at site i and the paramagnetic solution for $\langle n_i^\alpha \rangle$ has been assumed.

The results for A_o, E_z and the resulting $\lambda_{z,\phi}$ are shown in figure 4.7. Due to the increased hybridization of the Cu $4s$ and apical O $2p_z$ orbitals with decreasing apical distance there is a direct correlation between T_c (longer apical distance) and A_o, as shown in figure 4.7a. In figure 4.7b the E_z field at the planar oxygen site in the parent compounds are shown, reproduced from reference [23]. Here, a similar correlation between E_z and T_c is found for the reasons previously discussed. Finally, in figure 4.7c, the total coupling λ_z (λ_ϕ) $\propto E_z^2 A_o^4$ for the B_{1g} branch is given and, following the trends in A_o and E_z, a clear correlation between the total coupling and the T_c of the material develops. Here, focus has placed on the B_{1g} branch since it provides the largest contribution to pairing of the modes considered here.

The correlation between the material's T_c and the strength of the B_{1g} coupling is quite suggestive and provides a natural framework for understanding the large variations in T_c observed from material to material. Once again, the overall values of $\lambda_{z,\phi}$ shown in figure 4.7c are far too small to account for HTSC. However, this does not preclude phonons from playing some role, perhaps by contributing to pairing and enhancing the pairing correlations provided by another dominant interaction. Such a possibility has been considered in previous works which have examined the contribution from el-ph coupling in conjunction with antiferromagnetic spin fluctuations [178, 179]. In this scenario, a baseline T_c is set by the spin fluctuations. This interaction is governed by the properties of the CuO_2 plane, such as the charge transfer energy Δ or antiferromagnetic exchange energy J, and therefore the strength of this interaction is likely to be independent of the material (unless interlayer coupling plays some role in the interaction). T_c is then further

enhanced by the weaker contribution from the el-ph interaction which, as shown in figure 4.7, is strongly materials dependent. This picture naturally explains the variations in T_c with composition and changes in the number of layers. It also provides direct microscopic connection between the structure of the unit call and the T_c of the material. However, the question remains as to how enhancement is expected for the el-ph coupling strengths reported here. This will be addressed in greater detail in chapter 6, when a calculation for T_c is presented for a multi-channel model for pairing mediated by bosonic exchange.

4.4 Summary

This chapter has examined the temperature, doping and materials dependence of el-ph coupling within the weak-coupling framework of Migdal-Eliashberg theory. Overall, the details were well accounted for in the framework of the el-ph scenario. On the other hand, scenarios based on a single electronic mechanism or the spin resonance mode are unable to account for these details. The key difficulties are: (1) the nearly constant energy scale in the nodal kink as a function of doping in the small gap systems[72, 61], (2) the presence of multiple energy scales in the nodal spectra, (3) the clear kink in the normal state data, (4) the detailed agreement between the B_{1g} phonon mode and the momentum dependence of the renormalization features [30, 31], and (5) the tiny spectral weight ($\sim 2\%$) associated with the spin resonance mode, which is unlikely to give sufficient strength to produce the observed renormalizations. These weaknesses of the spin resonance mode, and the agreement between the phonon models and the data demonstrated here, provide further support to the interpretation of the band renormalizations as being due to coupling to a spectrum of bosonic modes.

The expected materials dependence of the coupling to the B_{1g} branch was also presented and a clear correlation between the strength of the coupling and T_c was demonstrated. In light of this observation, a multi-channel scenario for pairing was proposed to account for the materials variation in T_c. In the following chapters this idea will be explored in further detail. In chapter 5 attention will be turned to the el-ph coupling induced modulations in the density of states as probed by scanning tunneling microscopy experiments. Here, it will be argued that the qualitative signatures in the tunneling data are consistent with the idea of such a multi-channel pairing scenario and a reconciliation of the different energies scales extracted from the tunneling and photoemission data can be achieved if such a scenario is adopted.

In assessing the materials dependence of el-ph coupling focus was placed on coupling to the B_{1g} branch. However, the ARPES data shows clear signatures of coupling to the breathing branch and the shape of the ReΣ indicated that coupling to the 55 meV A_{1g} branch is also present. These modes will also contribute to the total values of $\lambda_{z,\phi}$

and, in the case of the breathing mode this coupling is detrimental to pairing. Therefore one might naively expect the contributions from the breathing branch might cancel the contribution from the B_{1g} branch. However, at this point the effects of screening have only been included at a phenomenological level. In chapter 6 a microscopy theory of screening is derived. There it is shown that the quasi-2D nature of the cuprates results in incomplete screening of the coupling to c-axis modes in comparison to the screening of the in-plane breathing modes. This reduces the pair-breaking contribution from the breathing branch and enhances the total coupling in the $d_{x^2-y^2}$ channel provided by the c-axis modes. With this observation, T_c calculations are then presented in order to further assess the degree to which phonons can enhance the overall value of T_c. In this case, a sizeable enhancement of T_c is produced despite the small overall el-ph coupling strengths presented here.

Chapter 5

Phonon-Modulated Density of States

In conventional superconductors, the role of electron-phonon (el-ph) interactions as the pairing "glue" was ultimately confirmed by McMillan and Rowell with their work on the tunnelling spectrum of lead [49, 50, 48]. In this work, McMillan and Rowell used the tunnelling-derived density of states (DOS) proportional to the derivative of the tunnelling current's I-V characteristics $N(\omega) \propto dI/dV$, as input to invert the strong-coupling Eliashberg equations and obtained the effective boson spectrum responsible for superconductivity [48, 65]. The extracted boson spectrum α^2F accurately reproduced the phonon spectrum measured independently by neutron scattering and a one-to-one correspondence was found between peaks in α^2F and minima in d^2I/dV^2. This result was a striking confirmation of both Eliashberg theory and the phonon mediated pairing mechanism of BSC theory.

Due to the success of McMillan and Rowell's work, a great deal of effort has been expended in search of similar signatures of bosonic structures in the cuprates. In the previous chapters such structures as observed by angle-resolved photoemission spectroscopy (ARPES) have been discussed in the context of coupling to a spectrum of phonons involving oxygen vibrations. Formally, the DOS is given by a sum over the spectral function $N(\omega) = \sum_{\mathbf{k}} A(\mathbf{k}, \omega)$. Therefore, if one neglects matrix elements, the tunnelling spectra can be thought of as a sum over ARPES spectra and renormalizations observed in one probe should also be present in the other. Indeed, as discussed briefly in chapter 2, evidence for coupling to a bosonic mode(s) has also been reported in scanning tunnelling microscopy (STM) [144, 145, 143] and superconducting-insulating-superconducting (SIS) junction tunnelling experiments [148, 149, 150] where the el-boson coupling appears as modulations in the DOS in analogy to the structures observed in lead. The manifestation of el-ph coupling in the high-T_c cuprates is the topic of this chapter and the major results presented here have appeared in reference [180].

5.1 A Discrepancy of Energy Scales

Despite the appearance of el-boson coupling in ARPES and STM experiments, a direct reconciliation of the renormalizations observed by the two probes has been difficult. This is due not only to complications arising from matrix elements but also the fact that inconsistent methods for extracting mode energies from tunnelling data have appeared in the literature. For example, in Bi-2212 [144], estimates for the local gap size are determined from the peak-to-peak distance of the coherence peaks while the energy of the bosonic mode is identified as the energy position of a peak in d^2I/dV^2, measured relative to the energy of the superconducting gap. While the positions of the superconducting coherence peaks vary at different tip locations, estimates for the mode energy are inversely correlated with the local gap size and a distribution of mode estimates is obtained, centred at 52 meV. Furthermore, this distribution shows a clear ^{18}O isotope shift [144]. The energy of the bosonic mode also appears to be immune to doping while the tunneling spectra change qualitatively. These observations rule out coupling to the spin resonance mode and point to a lattice origin for the mode involving oxygen vibrations, similar to those invoked to explain the band renormalizations observed by ARPES. However, the 52 meV mode energy is inconsistent with the energies of the dominant phonon modes used to interpret ARPES data for the same material (the 36 meV B_{1g} and 70 meV breathing modes) [30, 31]. This discrepancy raises questions regarding the identity of the mode observed by STM. Is it one of the modes observed in ARPES? If so, why does it manifest at a different energy scale in each of the probes? Or, if it does reflect a different bosonic mode, why is it only manifested in the tunnelling experiments?

The interpretation of the STM data has been further complicated by two additional studies: one the tri-layer system $Bi_2Sr_2Ca_2Cu_3O_{10+\delta}$ (Bi-2223) [143] and a second study on the bi-layer Bi-2212 [145]. In these works a mode energy $\Omega_0 \sim$ 35-45 meV was obtained by identifying a local minima in $N(\omega)$ (a root in d^2I/dV^2) with the mode energy. Although this energy scale is consistent with both the B_{1g} phonon and the magnetic resonance modes, both works interpreted the data in terms of coupling to the latter.

In the case of the SIS junction tunnelling experiments, multiple features have been reported in the density of states of optimal doped $La_{1.84}Sr_{0.16}CuO_4$ (LSCO) thin films [148]. Similar features have also been reported in $YBa_2Cu_3O_{7-\delta}$ [149], as well as the electron-doped system $Pr_{0.88}LaCe_{0.12}CuO_4$ [150]. In analogy to the traditional signatures of el-ph coupling in lead [48, 65, 49, 50, 181], these works associated minima in d^2I/dV^2 with the boson energy scale and found a direct correspondence between features in the DOS and the phonon density of states obtained from neutron scattering.

The observation of multiple modes in the tunneling spectrum of LSCO, as well as the fact that the spin resonance mode is well separated in energy from the low-lying phonon

modes in the electron-doped systems, indicates the spin-resonance mode is unlikely to be the source of these modulations. However, the question remains whether coupling to the mode can be cast in the usual form of el-ph coupling to oxygen modes developed in this work, or whether the structure in the DOS could be due to phonon-assisted co-tunneling from the STM tip via the apical atoms as proposed by Pilgram *et al.* [147]. Co-tunneling via a strong local apical coupling of electrons in the STM tip to the apical atom imparts structure in the form of a peak in the DOS at an energy scale of $\Delta_0 + \Omega$ and multiples of the phonon frequency $\Delta_0 + 2\Omega$, $\Delta_0 + 3\Omega$, ..., even though the coupling between the planar superconducting electrons and the apical atom may be weak [146, 147].

From these examples it is clear that a well defined procedure for extracting bosonic mode energies from d-wave superconductors is lacking. Therefore, before turning to a model calculation, the qualitative signatures of el-boson coupling in a d-wave superconductor will be examined in order to explicitly determine how bosonic mode couplings are expected to appear in the DOS. Furthermore, by examining the qualitative structure of the mode couplings, a means of differentiating between the extrinsic co-tunneling proposal [147] or intrinsic el-ph coupling [30, 23, 182] will also be obtained.

5.2 Qualitative Signatures in the Density of States

5.2.1 Projected Electron-Boson Couplings

In order to examine the signatures of el-boson coupling in a d-wave superconductor it is important to consider the coupling of each mode projected onto the relevant momentum channels. To this end, the el-boson coupling constant can be expanded in terms of Brillouin zone harmonics

$$|g(\mathbf{k},\mathbf{q})|^2 = \sum_{J,J'} Y_J(\mathbf{k}) |g_{J,J'}|^2 Y_{J'}(\mathbf{k}-\mathbf{q}) \tag{5.1}$$

where the sum J runs over the irreducible representations of the point group of the crystal. For the purpose of discussion, assume that $g_{J,J'}$ is diagonal in this basis and identify $J = 0$ and $J = 2$ with the s and $d_{x^2-y^2}$ symmetries, respectively.

The overall strength of the el-boson coupling in momentum channel J is parameterized by the dimensionless constant λ_J

$$\lambda_J = \int_0^\infty \frac{2d\nu}{\nu} \frac{\sum_{\mathbf{k},\mathbf{q}} \alpha^2F(\mathbf{k},\mathbf{q},\nu) Y_J(\mathbf{k}) Y_J(\mathbf{p}) \delta(\epsilon_\mathbf{k}) \delta(\epsilon_\mathbf{p})}{\sum_\mathbf{k} Y_J(\mathbf{k})^2 \delta(\epsilon_\mathbf{k})}. \tag{5.2}$$

For an Einstein mode $\alpha^2F(\mathbf{k},\mathbf{q},\nu) = |g(\mathbf{k},\mathbf{q})|^2\delta(\nu - \Omega_0)$ and equation 5.2 reduces to equation 3.25. In a d-wave superconductor $\lambda_{J=0} = \lambda_z$ ($Y_0(\mathbf{k}) = 1$) characterizes the

contribution to the el-boson self-energies $Z(\mathbf{k},\omega)$ and $\chi(\mathbf{k},\omega)$ while $\lambda_{J=2} = \lambda_\phi$ ($Y_2(\mathbf{k}) = [\cos(k_x a) - \cos(k_y a)]/2$) characterizes the contribution to $\phi(\mathbf{k},\omega)$. The relative values of $\lambda_{z,\phi}$ also determine the transition temperature T_c, which, in the weak coupling limit, is given by [181, 183]

$$k_b T_c = 1.13\hbar\Omega_0 \exp\left[-\frac{1+\lambda_z}{\lambda_\phi}\right]. \tag{5.3}$$

As can be seen from equation 5.3, a large λ_z relative to λ_ϕ results in a lower T_c. In general, $\lambda_z > \lambda_\phi$ and, as will shown here, the relative magnitudes of $\lambda_{z,\phi}$ can affect the qualitative signatures of the boson modulations in the density of states.

5.2.2 The Infinite Band Formalism

In order to calculate the boson-modulated density of states one must solve the Eliashberg equations for a given boson spectral density. These equations will be solved using the method of Marsiglio *et al.* [172], with the self-energy obtained by self-consistently solving equation 3.29. As a starting point, a set of approximations are made which are commonly used in Eliashberg treatments of the cuprates [114, 184, 185, 186]. Essentially, the role of band structure is neglected by replacing the sum over $\mathbf{k}$ with an integral over the normal state DOS $N_n(\omega)$. $N_n(\omega)$ is then replaced by its value at the Fermi level and the limits if the energy integral are extended to infinity. For brevity, the resulting form of the Eliashberg equations due to this approximation will be referred to as the *infinite band* formalism. For further details the reader is referred to appendix B.

Once the underlying structure of the band has been neglected the DOS $N_s(\omega)$ in the superconducting state can be written as

$$\frac{N_s(\omega)}{N_F} = \mathrm{Re}\left\langle \frac{\omega}{\sqrt{\omega^2 - \Delta^2(\mathbf{k},\omega)}} \right\rangle \tag{5.4}$$

where N_F is the density of states at the Fermi level and $\Delta(\mathbf{k},\omega) = \phi(\mathbf{k},\omega)/Z(\mathbf{k},\omega) = \Delta_1(\mathbf{k},\omega) + i\Delta_2(\mathbf{k},\omega)$ is the complex momentum-dependent gap function and $\langle ... \rangle$ denotes an average over the Fermi surface [65]. It is convenient to introduce the notation Δ_0 for the maximum value of the superconducting gap on the Fermi surface, which is given by the value of the gap function at the gap edge $\Delta_0 = \Delta(k_f^{AN}, \omega = \Delta_0)$, where $\mathbf{k}_f^{AN}$ denotes the Fermi momentum point closest to $(\pi/a, 0)$. For $\omega \gg \Delta_0$, Eq. 5.4 can be expanded yielding

$$\frac{N_s(\omega)}{N_F} = 1 + \frac{1}{2\omega^2}\langle \Delta_1^2(\mathbf{k},\omega) - \Delta_2^2(\mathbf{k},\omega)\rangle. \tag{5.5}$$

From Eq. 5.5 it is clear that the phononic substructure in $N_s(\omega)$ is given by the frequency dependence of the $\langle \Delta(\mathbf{k},\omega)\rangle$.

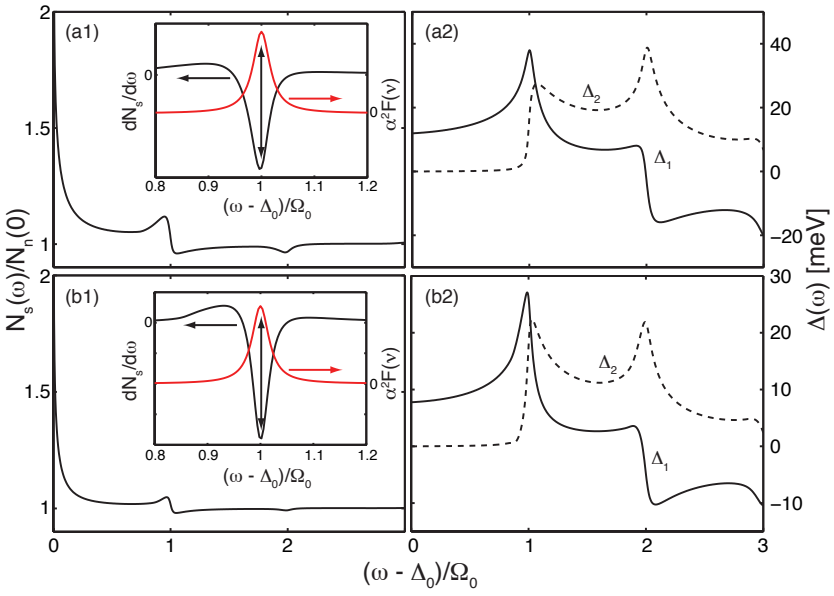

Figure 5.1: (a1), (a2) $N_s(\omega)$ and corresponding real $\Delta_1(\omega)$ and imaginary parts $\Delta_2(\omega)$ of the gap function $\Delta(\omega)$, respectively, for an s-wave superconductor coupled to a single boson mode with $\lambda = 0.8$. (b1), (b2) $N_s(\omega)$ and $\Delta(\omega)$ for a d-wave superconductor with $\lambda_z = 1.6$ and $\lambda_\phi = 0.8$. The insets of panels (a1),(b1), show $dN_s/d\omega$ and $\alpha^2F(\nu + \Delta_0)$ in order to highlight the correspondence between features in the DOS and peaks in the boson spectrum.

For an isotropic s-wave superconductor, the momentum dependence of the gap function vanishes $\Delta(\mathbf{k}, \omega) = \Delta(\omega)$ and $\lambda_z = \lambda_\phi$. In Figs. 5.1a1, 5.1a2, $N_s(\omega)$ and the corresponding $\Delta(\omega)$ are plotted, respectively, for this case. Here, the boson spectral density α^2F was modelled using a single Lorentzian distribution centred at $\Omega_0 = 52$ meV and the half-width at half-maximum (HWHM) $\Gamma_b = 1$ meV. Finally, the overall coupling strength of the coupling has been set such that $\lambda = 0.8$. As $\omega \to \Delta_0 + \Omega_0$, the real part of $\Delta(\omega)$ begins to rise producing an enhancement in the DOS for $\omega \lesssim \Delta_0 + \Omega_0$. At $\Delta_0 + \Omega_0$ the real part begins to drop while the imaginary part experiences a sudden rise due to Kramers-Kronig consistency. This results in a rapid suppression in weight at this energy scale, driving $N_s(\omega)$ below its bare value. As a result, the energy scale $\Delta_0 + \Omega_0$ manifests as a shoulder in the DOS or a minimum in $dN_s/d\omega$, as shown in the inset of Fig. 5.1a1. This is the classic McMillan-Rowell signature of el-boson coupling, similar to that observed in Pb where phonons are solely responsible for pairing. [48, 65, 181]

In the case of a d-wave superconductor the situation is nearly identical when $\lambda_z = \lambda_\phi = 0.8$, and the magnitude of the gap function is comparable to that obtained for the s-wave case with the same value of λ (not shown). Since the boson contributes equally

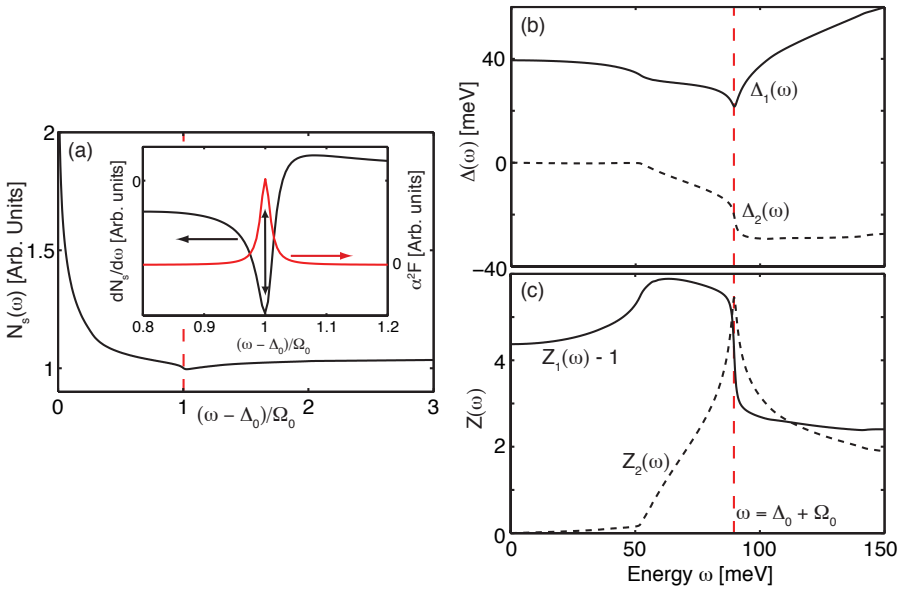

Figure 5.2: (a) $N_s(\omega)$ for a d-wave superconductor where the $\Omega \sim 52$ meV mode renormalizes over a dominant mode associated with spin fluctuations with $\Omega_{sf} = 260$ meV. Inset: $dN_s/d\omega$ and $\alpha^2F(\nu - \Delta_0)$ highlighting the correspondence between the low-energy mode and structure in $N_s(\omega)$. (b), (c) $\Delta(\omega) = \Delta_1(\omega) + i\Delta_2(\omega)$ and $Z(\omega) = Z_1(\omega) + iZ_2(\omega)$ for this case. The red dashed lines indicate the energy of $\Delta_0 + \Omega_0$ where Ω_0 is the energy of the centre of the low-energy spectra density (inset, panel (a)).

to the two momentum channels, the boson energy scale manifests as a shoulder on the low-energy side of the modulations. The structure of the modulation is qualitatively unchanged when $\lambda_z > \lambda_\phi$, as shown in figure 5.1b1,5.1b2 for $\lambda_z = 2\lambda_\phi = 1.6$. The only discernible difference is the overall magnitude of $\Delta(\omega)$ which is reduced by a factor of 2. This illustrates the importance of the relative magnitude of λ_z and λ_ϕ in determining the magnitude of the gap and T_c.

The next case considered is one of a low-energy boson that renormalizes over a second mode, which is higher in energy and dominant in its contribution to pairing. This high-energy mode is associated with spin fluctuations and is characterized by a broad Lorentzian spectral density with $\Gamma_{sf} = 30$ meV and centred at $\Omega_{sf} \sim 2J = 260$ meV. The total coupling to the spin fluctuation mode is set such that $\lambda_{sf,z} = \lambda_{sz,\phi} = 1.6$. For the low-energy boson, a sharp spectral distribution with $\Gamma_b = 0.5$ meV while still centred at $\Omega_0 = 52$ meV is assumed and the overall strength is set such that $\lambda_{b,z} = 1.6$ and $\lambda_{b,\phi} = 0$. In this case the sharper spectral density and increased coupling strength are required in order to accentuate the weak low-energy feature.

The results for $N_s(\omega)$, $\Delta(\omega)$ and $Z(\omega)$ obtained from this model are shown in Fig. 5.2. The structure of the renormalizations in this case differs considerably and the shoulder on the low energy side of the renormalization is significantly less pronounced than in figure 5.1. In the Eliashberg formalism, a high energy boson produces a gap function whose real part is relatively frequency independent for energies on the order of lower energy mode Ω_b while an instantaneous pairing interaction produces a frequency-independent gap function up to an energy scale set by the Coulomb interaction [187]. Therefore, assuming a frequency independent pair field ϕ_0, modulated by el-boson coupling, the gap function can be written as

$$\frac{\phi(\omega)}{Z(\omega)} = \frac{\phi_0 + \delta\phi(\omega)}{Z_0 + \delta Z(\omega)} = \frac{\phi_0}{Z_0}\left(\frac{1 + \delta\phi/\phi_0}{1 + \delta Z/Z_0}\right)$$

where $\delta\phi$ and δZ are the el-boson contributions to the self-energy. The DOS (for $\omega \gg \Delta_0$) can then be written as

$$\frac{N_s(\omega)}{N_f} = 1 + \frac{\Delta_0^2}{2\omega^2}\left(1 - \frac{\delta\phi(\omega)}{\phi_0} - \frac{\delta Z(\omega)}{Z_0}\right). \tag{5.6}$$

To evaluate the structure in this case it is again noted that for any bosonic mode, including phonons, $\lambda_\phi \leq \lambda_z$. Furthermore, if the el-boson contribution to pairing is small (as is the case in figure 5.2) $\delta\phi$ can be neglected and one sees that the fine structure tracks the structure of $\delta Z(\omega)$ (Fig. 5.2c) and $\Delta_1(\omega)$ (Fig. 5.2b) is suppressed as $\omega \to \Delta_0 + \Omega_0$. This behaviour produces a dip structure in $N_s(\omega)$ (Fig. 5.2a) with no pronounced shoulder on the low-energy side of the renormalization. Finally, in this case energy scale of the boson still appears as a minima in $dN_s/d\omega$ (inset of Fig. 5.2a).

Experimentally, the modulations in the tunneling spectra appear as a dip-hump structure with no pronounced shoulder on the low-energy side of the modulations [143, 144, 145]. It can therefore be concluded that, within the validity of Eliashberg theory, the bosonic mode responsible for the DOS renormalizations cannot be the dominant contributor to pairing in the cuprates. If this were the case then the low-energy shoulder should be present in the STM data. More likely, the low-energy boson modulates the electronic structure over, or in conjunction with, the dominant pairing mechanism.

The two-mode scenario has already been invoked in the treatment of the ARPES data presented in chapters 3 and 4. There it was demonstrated that relatively small values of $\lambda_z \sim 0.3$-0.5 are needed to reproduce the dispersion kinks. Since such coupling strengths are far too small to account for high T_c the superconducting gap was added by hand, consistent with the idea of a dominant pairing interaction which is weakly modified by the el-boson interaction [89]. Furthermore, the calculations presented here demonstrate that such a two-mode model produces a dip in $N(\omega)$ with no pronounced shoulder, consistent with the shape of the spectra observed experimentally. However, although the two-mode

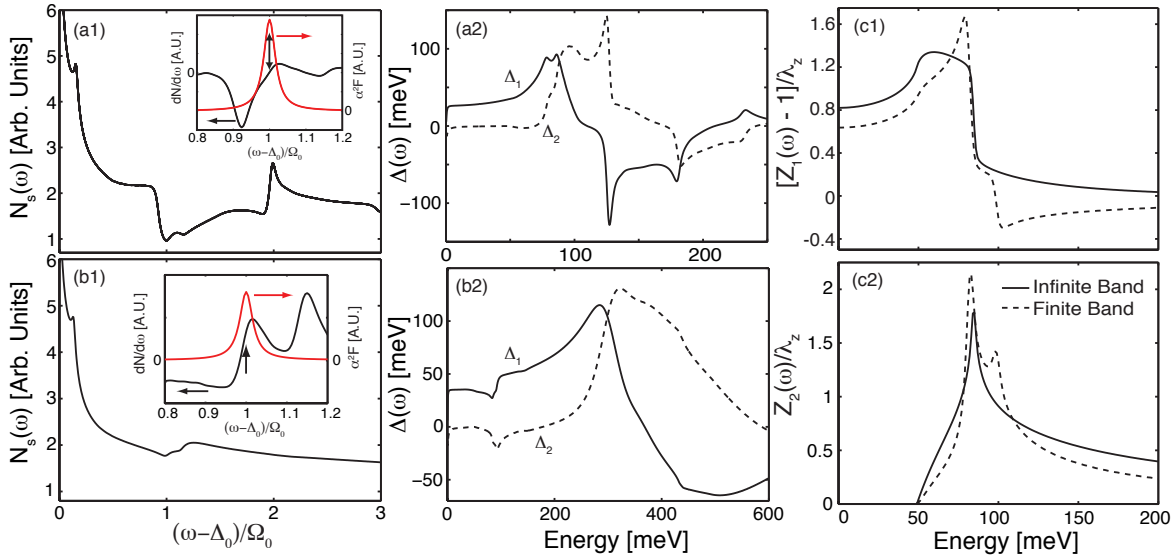

Figure 5.3: The solutions to the finite band Eliashberg equations for the single- and two-mode models. (a1),(a2) $N(\omega)$ and $\Delta(\omega)$, respectively, for a d-wave superconductor coupled to a single low-energy mode which is the sole contributor to pairing. (b1),(b2) $N(\omega)$ and $\Delta(\omega)$ for the two mode case analogous to the case shown in Figs. 5.1c1,c2. The insets of panels (a1) and (b1) show $dN/d\omega$ and the low energy component of $\alpha^2F(\nu + \Delta_0)$. (c1), (c2) The real and imaginary parts of $Z(\omega)$ calculated in the infinite- (solid) and finite-band (dashed) Eliashberg formalisms. Here, a single iteration of the Eliashberg equations has been assumed with coupling to an Einstein mode centred at $\Omega = 50$ meV and assuming a d-wave gap of 35 meV.

model is able to account for the lack of shoulder feature in the DOS, the hump structure on the high-energy side of the boson energy scale is absent in the model calculation. This is due to the fact that the structure of the band has been neglected, as will be demonstrated in the next section.

5.2.3 The Finite Band Formalism

The calculations presented in the previous section are now repeated, but this time equation 3.29 is solved while retaining the full **k**-dependence of the band structure. In figure 5.3 the solutions to these *finite band* Eliashberg equations are shown. As with the infinite band calculations two cases are considered: a single mode with $\lambda_z = 1.9 = \lambda_\phi$, $\Gamma = 1$ meV, and $\Omega_0 = 52$ meV, and a case with two modes parameterized by $\Omega_{b,sf} = 52$, 300 meV $\Gamma_{b,sf} = 1$, 30 meV, $\lambda_{z,sf} = \lambda_{\phi,sf} = 1.7$, $\lambda_{z,b} = 0.52$ and $\lambda_{\phi,b} = 0$. In order to model the low energy dispersion the same 5-parameter tight-binding model used in the previous

chapters has been used [168].

Fig. 5.3a1, a2, show $N(\omega)$ and $\Delta(\omega)$, respectively, for the single low-energy mode which acts as the sole source of pairing, and in analogy to Fig. 5.1b1,b2 and Fig. 5.3b1,b2 shows the results for the two mode calculation, in analogy to Fig. 5.2. The first observation is that the shoulder feature remains when the mode contributes significantly to pairing, while a pronounced dip-hump structure is produced when the mode renormalizes over another dominant mechanism. In the latter case the hump is more pronounced due to the structure in the underlying band. In the cuprates the energy of the phonons (and spin resonance mode) lie at an energy similar to that of the superconducting gap Δ_0 and van Hove singularity $\epsilon(0, \pi/a)$. Therefore, there is an overall enhancement of the self-energy due to the increased density of states to which the bosons can couple in the anti-nodal region. This degeneracy of energy scales has already been noted in studies on the temperature dependence of the el-ph self-energy observed by ARPES [30, 72] (also see chapter 4). To further illustrate this point Fig. 5.3c1,c2 compares the real and imaginary parts of $Z(\omega)$ in the two formalisms. In order to compare comparable cases $Z(\omega)$ has been calculated assuming a single iteration of the Eliashberg equations and the results have been normalized by the value of λ_z. When the full bandstructure is retained $Z(\omega)$ (as well as χ and ϕ) develops additional structure not present in the infinite band case. A sharper peak at $\Delta_0 + \Omega_0$ appears and an additional feature is produced at the energy of the van Hove. As a result of this secondary feature $Z_1(\omega)$ drops more rapidly at $\Delta_0 + \Omega_0$ and becomes negative at energies larger than $\Delta_0 + E(0, \pi)$. It is this sharper drop and sign change which results in the prominent hump observed in $N(\omega)$. However, if the underlying bandstructure is neglected $Z_1(\omega)$ remains positive and smoothly approaches zero as $\omega \to \infty$ and hence no hump is produced in the DOS. From these considerations it is clear that the structure in the underlying band can contribute to the structure of the self-energy and should therefore be retained in realistic treatments of narrow bandwidth systems such as the cuprates.

The second observation is that the correspondence between the minima in $dN/d\omega$ and peaks in α^2F no longer holds (insets of Figs. 5.3a1 and b1). For the single-mode model the peak in $\alpha^2F(\nu)$ corresponds to the minimum in $N(\omega)$ or the root in $dN/d\omega$ while for the two-mode model this energy scale does not correspond to any feature in $dN/d\omega$. For the choice of α^2F and $\epsilon_{\mathbf{k}}$ used here, the energy scale $\Delta_0 + \Omega_0$ is located between the root and maximum in $dN/d\omega$ and either energy scale gives a reasonable estimate for the mode energy. However, if broader phonon spectral densities are used, or additional broadening mechanisms are introduced, then the two features will begin to merge and a single maxima in $dN/d\omega$ will occur at an energy set by the relative energy of these two features. In figure 5.4 $N(\omega)$ and $dN/d\omega$ are plotted for the two-mode model, calculated for varying values of the low-energy mode's spectral width Γ_b. Here, the parameters of the high-energy mode are the same as those used to generate figure 5.2 and the coupling to the low-energy mode has been adjusted such that the total value of $\lambda_{z,\phi}$ is fixed for

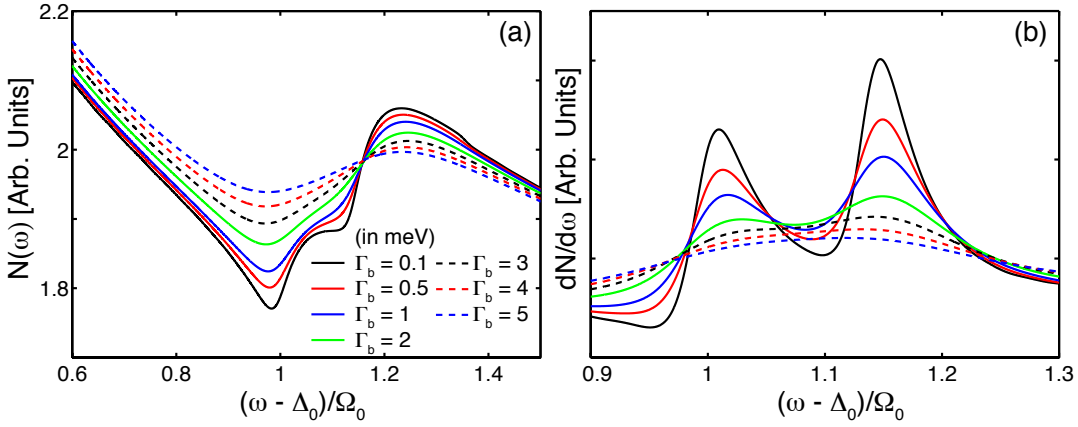

Figure 5.4: (a) $N(\omega)$ and (b) $dN/d\omega$ for energies in the neighbourhood of the low-energy boson's renormalizations for various values of the low-energy mode's spectral width Γ_b (in meV, see text).

each Γ_b.

The qualitative change in the phonon fine-structure is the central result of this chapter. It reconciles the discrepancy in the ~ 52 meV scale observed in STM [144] and the ~ 70 meV "kink" observed by photoemission in Bi-2212.[30] In Ref. [144] the maxima in $d^2I/dV^2 \propto dN/d\omega$ was taken for the mode estimate, corresponding to the shoulder of the dip-hump structure of the DOS. However, as shown above, the energy scale of the mode is more accurately given by the minimum in $N(\omega)$ (root in d^2I/dV^2), Therefore, by choosing the maxima in d^2I/dV^2 as the energy scale of the boson mode an overestimate for the mode energy is likely to be obtained. A closer examination of Fig. 1 of Ref. [144] (reproduced in figure 2.11) reveals that the minima in the DOS is $\sim$ 15-20 meV lower in energy. This brings the mode estimate in line with the energy of the B_{1g} phonon invoked to explain the kink in the nodal region of superconducting Bi-2212. Indeed, Ref. [145] has tracked the minimum in the related Bi-2223 system, which also has strong coupling to the B_{1g} phonon, and obtained a mode energy of 35 meV, consistent with our findings. This is in agreement with Ref. [143] who used a similar procedure on Bi-2212 and also obtained a mode estimate of 35 meV. The qualitative difference in structure also provides a pathway to experimentally distinguish between fine structure due to co-tunnelling effects, where a maximum in $N(\Omega_0+\Delta_0) \propto dI/dV|_{\omega=\Omega_0+\Delta_0}$ occurs, and intrinsic el-boson coupling where a minimum is expected if the mode is not dominating pairing, or a shoulder is expected if the mode is contributing significantly to pairing.

5.3 A Model Calculation for Bi-2212

Attention is now turned to a model calculation for Bi-2212 including coupling to the out-of-phase Cu-O bond buckling B_{1g} phonon mode. Based on the arguments developed in the previous section this phonon is assumed to renormalize over a dominant interaction. It is therefore sufficient to consider el-ph self-energy in the same manner that was adopted for the ARPES calculations of the previous chapters. Namely, only a single iteration of the Eliashberg equations is considered and the phonon mode is modelled as a dispersionless Einstein mode with $\Omega_0 = 36$ meV. For simplicity, the coupling constant is expanded as $|g(\mathbf{k},\mathbf{q})|^2 = g_z^2 + g_\phi^2 Y_d(\mathbf{k}) Y_d(\mathbf{p})$ and $g_{z,\phi}$ are set such that $\lambda_{z,\phi} = 0.31,\ 0.1$. These values are comparable to the values obtained in chapter 3. The zero-temperature expressions for the imaginary parts of the self-energies are

$$\begin{aligned}
\omega Z_2(\mathbf{k},\omega) &= \frac{\pi}{2N}\sum_{\mathbf{p}} |g(\mathbf{k},\mathbf{q})|^2 [\delta(E_{\mathbf{p}} + \Omega_0 - \omega) + \delta(E_{\mathbf{p}} + \Omega_0 + \omega)] \\
\chi_2(\mathbf{k},\omega) &= -\frac{\pi}{2N}\sum_{\mathbf{p}} |g(\mathbf{k},\mathbf{q})|^2 \frac{\epsilon_{\mathbf{p}}}{E_{\mathbf{p}}} [\delta(E_{\mathbf{p}} + \Omega_0 - \omega) + \delta(E_{\mathbf{p}} + \Omega_0 + \omega)] \qquad (5.7) \\
\phi_2(\mathbf{k},\omega) &= \frac{\pi}{2N}\sum_{\mathbf{p}} |g(\mathbf{k},\mathbf{q})|^2 \frac{\Delta_{\mathbf{p}}}{E_{\mathbf{p}}} [\delta(E_{\mathbf{p}} + \Omega_0 - \omega) + \delta(E_{\mathbf{p}} + \Omega_0 - \omega)]
\end{aligned}$$

where $E(\mathbf{k}) = \sqrt{\epsilon^2(\mathbf{k}) + \Delta^2(\mathbf{k})}$ and the real-part of the self-energies are obtained via the Kramers-Kronig relations. In these calculations the superconducting gap Δ_0 is taken as an input parameter and, as in previous chapters, the real part of ϕ is supplemented in order to maintain the value of the gap at the gap edge [89, 72]. Finally, an intrinsic damping $\Gamma = 5$ meV, independent of ω and $\mathbf{k}$, is added to the imaginary part of $Z(\mathbf{k},\omega)$ and the band structure is taken from the usual 5-parameter tightbinding model [168].

The DOS results are presented in figure 5.5, where three different values of Δ_0 have been chosen to mimic the variation in the LDOS observed in different regions of an optimally doped sample. Note that in this case the DOS modulations are more pronounced due to the δ-function used to model the phonon spectral density. The calculated DOS for the three gap values all show a clear dip in the spectra around $\Delta_0 + \Omega_0$. The calculations also show a secondary structure at $E(0,\pi) + \Omega_0$ due to the van Hove singularity at $\mathbf{k} = (0,\pi)$. Estimates are obtained empirically for the mode energy and gap size from the calculated DOS via the gap referencing procedure used in Ref. [24] on the hole side ($\omega > 0$) of the spectra, in order to avoid complications associated with the van Hove singularity.

When the gap referencing procedure is applied to the data, the resulting gap estimate is equal to the quadrature addition of the maximum value of the superconducting gap on the Fermi surface Δ_0 and the damping term Γ. The empirically determined mode energy

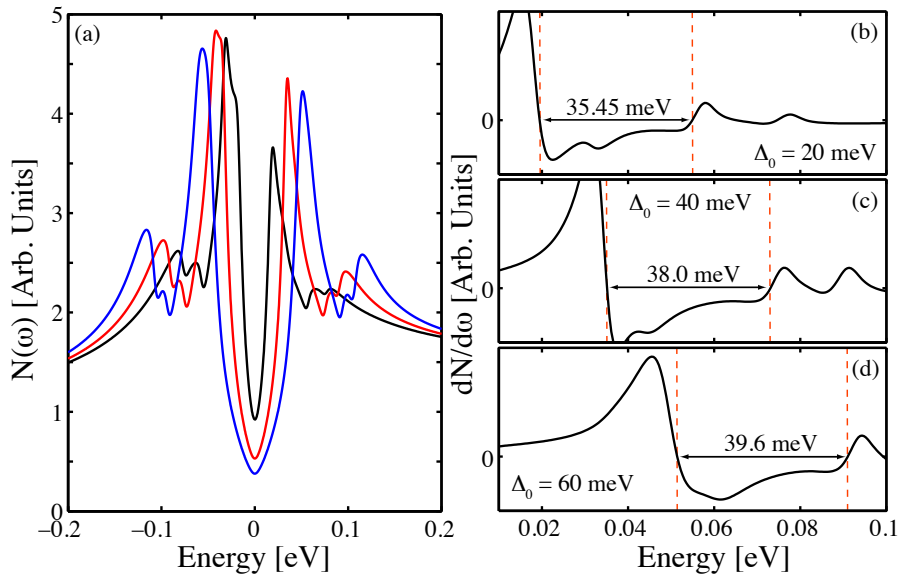

Figure 5.5: (a) The density of states calculated for coupling to the B_{1g} phonon branch at $T = 0$. Each spectra is calculated using a 5-parameter tight-binding bandstucture and a d-wave gap with $\Delta_0 = 20$ (black), 40 (red) and 60 (blue) meV. (b)-(d) $dN/d\omega$ for the indicated gap size. The red dashed lines indicate the position of the roots corresponding to estimates for Δ_0 and $\Delta_0 + \Omega_0$, respectively.

is therefore underestimated since the effective mode position is $\Omega_0 + \Delta_0 - \sqrt{\Delta_M^2 + \Gamma^2}$. Since a constant value of Γ has been used for each value of Δ_0, the small gap data has a larger ratio of Γ/Δ_0, and thus the extracted mode energy systematically deviated from Ω_0.

The constant value of Γ used in figure 5.5 does not capture the local inhomogeneity of the parameters entering into the DOS itself. In order to correct this the magnitude of the el-ph coupling and inelastic damping Γ included in both the spectral function and evaluation of the self-energy are now modified as a function of gap size. The larger gap values are naively associated with "underdoped" regions which, due to the reduction in screening of the el-ph interaction, leads to an increase in the relative strength of the coupling with gap size. At the same time, damping effects are taken to increase together with the gap size to mimic the crossover to smeared gap structures in the large gap regions. This is modelled as an increasing ratio of Γ/Δ_0 in the large gap region. The DOS was then recalculated for input gap values ranging from 15 to 60 meV.

The new DOS spectra obtained are presented in Fig. 5.6a. For small gap inputs sharp coherence peaks can be seen, followed by a defined dip-hump structure associated

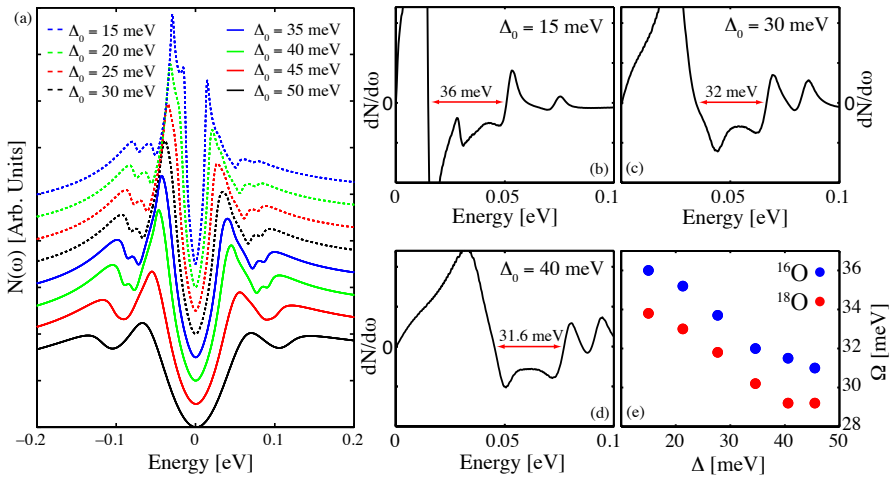

Figure 5.6: A waterfall plot of $N(\omega)$ calculated for doping values spanning the large gap to small gap regions. Each DOS was calculated for coupling the same mode used in figure 5.5. The gap values indicated in the legend denote the input values of Δ_0. (b),(c) $dN/d\omega$ for selected DOS presented in panel (a) for the hole side ($\omega > 0$) of the spectrum. The red arrows indicate the roots used to estimate the energies Δ_0 and $\Delta_0 + \Omega_0$. (e) The mode energy estimate obtained from the position of the local minima relative to the coherence peak. The blue data points correspond to data for ^{16}O simulations while the red data points correspond to ^{18}O simulations.

with the el-ph coupling. For larger gaps, the associated increased damping smears the coherence peaks and they are washed away for $\Delta_0 = 60$ meV. The gap and phonon energy scales can now be extracted from $dN/d\omega$, which are shown for selected spectra in Figs. 5.6b-d. The resulting correlation between the extracted Δ_0 and Ω_0 are shown in Fig. 5.6e (blue dots). The anti-correlation which emerges between the two energies stems from the progressive underestimation of the mode energy as the gap size and Γ are increased.

In order to model the isotope effect, these calculations were repeated with adjustments appropriate for the replacement of ^{16}O with ^{18}O. Specifically, this includes a shift in the phonon frequency by a factor of $\sqrt{M_{16}/M_{18}}$ and a decrease in the overall coupling by a factor $(M_{16}/M_{18})^{1/4}$. (This substitution leaves the value of λ unchanged.) The red data points of Fig. 5.6e show the correlation between the estimate for Ω and Δ_0 obtained for ^{18}O upon repetition of the previous calculations. In both cases, the anti-correlation persists and a clear isotope shift can be seen, which is on the order of that observed and that one would expect based on the known shift in the phonon energy. The overall agreement with the experiments is good, and the anti-correlation can be accounted for

relatively well by incorporating damping effects into a simple el-ph picture.

5.4 Summary

In this chapter the details of DOS renormalizations due to el-boson coupling in a d-wave superconductor were examined. It was found that the appearance of el-boson coupling in s-wave superconductors can be qualitatively different than superconductors whose gap symmetry lies in a higher momentum channel. In general, the el-boson vertex $g(\mathbf{k}, \mathbf{q})$ is projected onto the various momentum channels and the relative weight of the s-wave projected coupling λ_z and the gap-symmetry (d-wave in the case of the cuprates) projected coupling affects not only T_c but also the qualitative structure of the el-boson renormalizations in the single-particle density of states. As a consequence of this, the general structure of the modulations can be used to infer information about the pairing nature of a particular bosonic mode; if the mode contributes significantly to pairing then a pronounced shoulder is expected to form on the low-energy side of the DOS modulations. However, if the mode does not contribute significantly to pairing (its $\lambda_\phi \ll \lambda_\phi^{\text{tot}}$) then the renormalizations should appear as a dip-hump structure with a hump appearing in the high-energy side of the renormalizations. In STM experiments a clear dip-hump renormalization has been observed, which lacks the classic McMillian-Rowell signature [144, 145, 143]. Therefore, one can conclude that the low-energy mode is not the primary source of pairing in the high-T_c cuprates.

This conclusion is also consistent with the el-ph model used to interpret the ARPES experiments. In chapters 3 and 4 it was shown that relatively weak el-ph couplings with $\lambda_z \sim$ 0.3-0.5 ($\lambda_\phi < \lambda_z$) are required to accurately account for the kinks in the band dispersion. Such el-ph coupling strengths are far to small to account for the high value of T_c in these systems and in the ARPES calculations it was assumed that the phonon modes renormalize over a gap produced by some other coupling mechanism. The Bi-2212 model calculations presented in this chapter demonstrate that this model is also able to reproduce the renormalizations in the DOS. Furthermore, using simple considerations for additional local dampening, this model is able to reproduce the observed anti-correlation and oxygen isotope shift. Although the arguments for the local dampening will also hold for the coupling to spin-resonance mode, the isotope shift cannot be explained using such models. From the combined ARPES and STM results a consistent picture emerges - that of el-ph coupling renormalizing the low-energy electronic structure and acting in conjunction with a dominant pairing interaction which acts at a higher energy scale.

Chapter 6

Theory of Screening in the Cuprates and Considerations for Phonon's Contribution to T_C

The phenomenological treatment of the doping dependence of the nodal kink presented in chapter 4 has highlighted the importance of screening effects. In this chapter a microscopic theory for screening in the cuprates is presented in order to determine the effects of screening in a more rigorous manner. In conventional metals, lattice vibrations are well screened and the overall strength of the electron-phonon (el-ph) interaction is reduced [9, 188]. However, the situation is quite different in the cuprates due to the quasi-2D nature of the crystal structure. For example, in LSCO the ratio of the c-axis and in-plane resistivities ρ_c/ρ_{ab} range from 8×10^3 for lightly underdoped samples to 1×10^3 at optimal doping [189]. As a result, doped carriers have a greatly reduced conductivity along the c-axis and are thus unable to effectively screen perturbations oriented along this direction. This means that the screening of the c-axis phonons is incomplete and this has a number of important consequences for the physics of the high-T_c cuprates.

The role of screening in the cuprates has been examined in previous works in the context of the anomalous softening of the in-plane bond stretching modes [190, 191, 192, 193]. In these works it was found that screening and charge fluctuation effects, which are reduced along the c-direction, are needed in order to accurately reproduce the anomalous softening of the half- and full- breathing branches with doping. Since the previous works have focused largely on the role of screening in determining phonon self-energies, this chapter will focus on the role of screening in renormalizing the electron self-energies, which are reflected in experimental probes such as angle-resolved photoemission spectroscopy (ARPES) and scanning tunneling microscopy (STM).

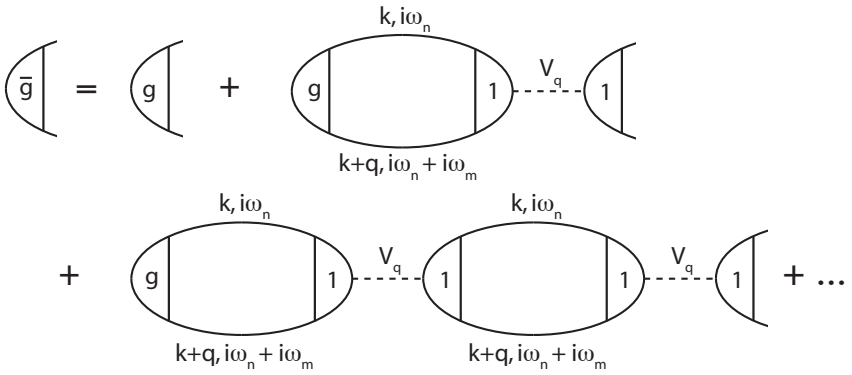

Figure 6.1: The diagrams retained in calculating the screened el-ph vertex within the random phase approximation. Here, $\bar{g}$ and g denote the renormalized and bare el-ph vertices, respectively, and $V_{\mathbf{q}}$ is the Coulomb interaction.

6.1 Formalism

In the standard treatment of screening the renormalized el-ph vertex is calculated within the random phase approximation [194]. The subset of diagrams considered in this approach are shown in figure 6.1. By summing these diagrams the screened el-ph vertex is given by

$$\begin{aligned}\bar{g}(\mathbf{k},\mathbf{q}) &= g(\mathbf{k},\mathbf{q}) + \Pi_{g,1}(\mathbf{q})v_{\mathbf{q}} + \Pi_{g,1}(\mathbf{q})v_{\mathbf{q}}\Pi_{1,1}(\mathbf{q})v_{\mathbf{q}} + \Pi_{g,1}(\mathbf{q})v_{\mathbf{q}}[\Pi_{1,1}(\mathbf{q})v_{\mathbf{q}}]^2 + \dots \\ &= g(\mathbf{k},\mathbf{q}) + \frac{\Pi_{g,1}(\mathbf{q})v_{\mathbf{q}}}{1-\Pi_{1,1}(\mathbf{q})v_{\mathbf{q}}} \end{aligned} \tag{6.1}$$

where $V_{\mathbf{q}} = 4\pi e^2/q^2$ is the 3D Coulomb interaction and $\Pi_{a,b}(q,\Omega_{ph})$ is the frequency-dependent polarizability calculated with vertices a,b respectively. The polarizabilities are obtained by evaluating the electron-hole bubble yielding

$$\Pi_{g,1}(\mathbf{q}, i\Omega) = \frac{1}{N\beta}\sum_{m}\sum_{\mathbf{k},\sigma} g(\mathbf{k},\mathbf{q})G(\mathbf{k}, i\omega_n)G(\mathbf{k}+\mathbf{q}, i\omega_n + i\Omega). \tag{6.2}$$

for the mixed polarizability $\Pi_{g,1}$ and an analogous expression for the pure polarizability $\Pi_{1,1}$ with $g(\mathbf{k},\mathbf{q}) = 1$. To evaluate the polarizabilities, attention is restricted to the normal state and the bare electron propagator $G^{-1}(\mathbf{k}, i\omega_n) = i\omega_n - \epsilon(\mathbf{k})$ is introduced, resulting in the standard Lindhard expression [9]

$$\Pi_{g,1}(\mathbf{q},\Omega_{ph}) = \frac{2}{V_{cell}}\sum_{\mathbf{k}} g(\mathbf{k},\mathbf{q})\frac{f(\epsilon_{\mathbf{k}}) - f(\epsilon_{\mathbf{k}+\mathbf{q}})}{\epsilon_{\mathbf{k}} - \epsilon_{\mathbf{k}+\mathbf{q}} + \hbar\Omega_{ph} + i\delta} \tag{6.3}$$

where $\delta > 0$ is an infinitesimal real number.

In good three-dimensional metallic systems the plasma frequency Ω_{pl} is usually much larger than the phonon frequencies. In the limit $\mathbf{q} \to 0$ the effective coupling is $\bar{g}(\mathbf{k}, \mathbf{q} \to 0) - \delta g$ with δg denoting the average value of $g(\mathbf{k}, \mathbf{q} \to 0)$ on the Fermi surface. The bare el-ph coupling is therefore well screened in this case. Turning to the cuprates, from the point of view of the Coulomb interaction, the materials are 3D with $\mathbf{q}^2 = \mathbf{q}_{2D}^2 + q_z^2$ and $\mathbf{q}_{2D} = (q_x, q_y)$. However, due to the largely incoherent c-axis transport observed across the under- and optimal-doped regions of the phase diagram, the polarizabilities are largely determined by the planar conduction electrons. Therefore, the polarizabilities are evaluated by restricting the momentum sum to the in-plane wavevectors and $\Pi_{a,b}(\mathbf{q}, \Omega) = \Pi_{a,b}^{2D}(\mathbf{q}_{2D}, \Omega)$. This results in a number of important changes to screening for small in-plane momentum transfers $\mathbf{q}_{2D} \ll \mathbf{q}$.

A qualitative feel for the effects of poor screening can be obtained by considering the case of a Holstein or $\mathbf{q}$-dependent coupling $g(\mathbf{k}, \mathbf{q}) = g(\mathbf{q})$. For this case, in the limit of small in-plane momentum transfers, where $v_F q_{2D} \ll \Omega_{pl}$, the polarizabilities simplify to

$$\Pi_{1,1}(\mathbf{q}, \Omega_{ph}) = \frac{n q_{2D}^2}{m \Omega_{ph}^2} \qquad \frac{n}{m} = \frac{1}{V_{\text{cell}}} \sum_{\mathbf{k}} f(\epsilon_{\mathbf{k}}) \left[\frac{\partial^2 \epsilon_{\mathbf{k}}}{\partial k_x^2} + \frac{\partial^2 \epsilon_{\mathbf{k}}}{\partial k_y^2} \right] \tag{6.4}$$

and

$$\Pi_{g,1}(\mathbf{q}, \Omega_{ph}) = \frac{n q_{2D}^2}{m_g(q) \Omega_{ph}^2} \qquad \frac{n}{m_g(q)} = \frac{g(q)}{V_{\text{cell}}} \sum_{\mathbf{k}} f(\epsilon_{\mathbf{k}}) \left[\frac{\partial^2 \epsilon_{\mathbf{k}}}{\partial k_x^2} + \frac{\partial^2 \epsilon_{\mathbf{k}}}{\partial k_y^2} \right] \tag{6.5}$$

where V_{cell} is the unit cell volume and f is the Fermi distribution. The screened el-ph interaction is then

$$\bar{g}(\mathbf{q} \to 0) = g(\mathbf{q}) - \frac{m}{m_g(\mathbf{q})} \frac{\Omega_{pl}^2(q)}{\Omega_{pl}^2(q) - \Omega_{ph}^2} = g(\mathbf{q}) \left[1 - \frac{\Omega_{pl}^2(q)}{\Omega_{pl}^2(q) - \Omega_{ph}^2} \right] \tag{6.6}$$

with $\Omega_{pl}^2(q) = \Omega_{pl}^2 (q_{2D}/q)^2$. The effects of poor screening are clear; for small in-plane momentum transfers $\mathbf{q}_{2D} \ll \mathbf{q}$ the screening correction in equation 6.6 is small and the bare el-ph vertex is recovered. As the q_z component of the phonon momenta grows, the region of small $\mathbf{q}_{2D}$ for which the correction is small also grows and a cone of momentum transfers is produced where screening is inoperable. Thus, the c-axis Raman active phonons, whose couplings are strongest for small momentum transfer $\mathbf{q}$ and $\Omega_{pl}(q) < \Omega_{ph}$, will survive the effects of screening in the cuprates. These conclusions will also hold for any quasi-2D layered system with poor conductivity along the c-axis.

6.1.1 The Two-Dimensional Coulomb Interaction

Due to the quasi-2D nature of the cuprates the full 3D form for the Coulomb interaction is inappropriate for evaluating the screened el-ph vertex. Instead, a form for Coulomb

interaction for a layered system with charge density confined to the layers but Coulombically coupled across the planes is used [195, 196]

$$V(q_{ab}, q_z) = \frac{V}{q_{ab} a \tanh(q_{ab}/q_0)} \frac{1}{1 + F_z}. \tag{6.7}$$

Here, $V = 2\pi e^2/a\sqrt{\epsilon_{ab}\epsilon_c}$, $q_0 = (4/c)\sqrt{\epsilon_c/\epsilon_{ab}}$, with ϵ_{ab} and ϵ_c the in-plane and out-of-plane dielectric constants, respectively. The c-axis lattice constant sets the in-plane momentum scale beyond which the planes become effectively decoupled. This leads to an interpolation between the 2D and 3D forms for the Coulomb interaction where $F_z = \sin(q_z c/4)/\sinh(q_{ab}/q_0)$ provides the q_z dispersion of the interaction.

6.2 The Screened Electron-Phonon Vertex in $Bi_2Sr_2CaCu_2O_{8+\delta}$

In this section the screened el-ph vertices for the case of Bi-2212 are presented. In figure 6.2 the pure charge polarizability $\Pi_{1,1}$ and the screened vertices $\bar{g}(\mathbf{k}, \mathbf{q})$ for the various modes considered in chapter 3 are presented. The results are plotted for momentum transfer along the zone face $\mathbf{q}_{2D} = (q, 0)$ and the momentum axis has been plotted on a logarithmic scale in order to highlight the behaviour at small $\mathbf{q}_{2D}$. Here, $\Pi_{1,1}$ has been calculated assuming an $\Omega_{ph} = 60$ meV Einstein phonon. For the screened vertices the parameters and bare vertices $g(\mathbf{k}, \mathbf{q})$ given in chapter 3 have been used. In addition, an artificial broadening $\delta = 5$ meV has been introduced in order to smooth the singularities and $\epsilon_{\mathbf{k}}$ was obtained from a tight binding fit for optimal doped Bi-2212 [168]. The lattice parameters were obtained from structural data with $a = b = 3.8$ $\mathring{A}$ and $c = 30.52$ $\mathring{A}$ [97]. The high-frequency dielectric constants, which determine the plasma frequency, were obtained from optical conductivity data with $\epsilon_{ab}(\infty) = \epsilon_c(\infty) \sim 4.8$ [97]. For this choice in parameters $\Omega_{pl} = 0.914$ eV at optimal doping, which is consistent with experiment [197]. In order to calculate the screened el-ph vertex the static dielectric constants are also needed. Here, $\epsilon_c(0) = 10$, again obtained from optics measurements [97], while the ratio $\epsilon_{ab}(0)/\epsilon_c(0) = 4$ is assumed. This ratio produces a factor two reduction of the breathing vertex at $\mathbf{q} = (0, \pi)$, shown in figure 6.2f, in agreement with reference [160].

Turning now to the results for the pure charge polarizability, which are plotted in figure 6.2a. The real part of $\Pi_{1,1}$ rises as q^2 before abruptly falling when the condition $v_F q = \Omega_{ph}$ is satisfied. At this point the imaginary part experiences a rise due to its Kramers-Kronig relation to the real part. At higher momentum transfers the structure in $\Pi_{1,1}$ is determined by the details of the band structure. These kinematic considerations give rise to similar forms for the mixed polarizabilities $\Pi_{g,1}$, although the detailed q-dependence is different due to the different momentum dependence of the bare el-ph

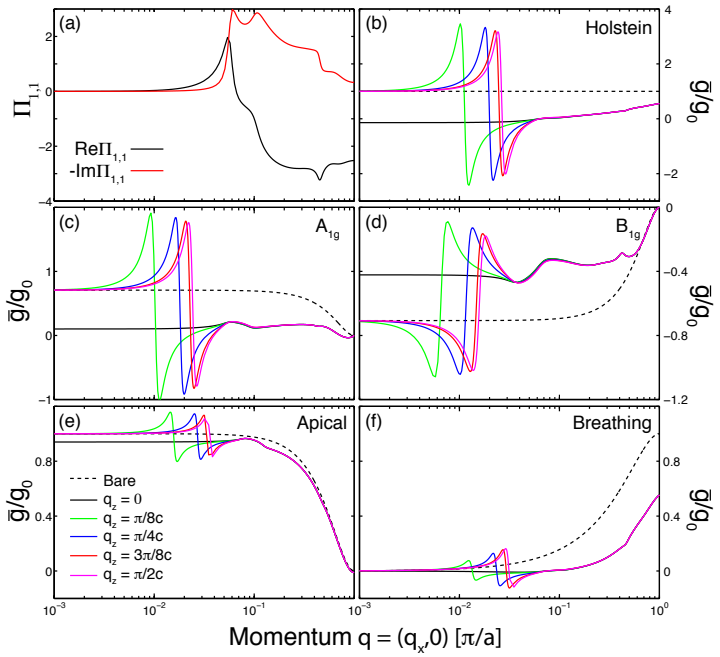

Figure 6.2: (a) Plots of the real (black) and imaginary ($-1\times$, red) parts of the charge susceptibility $\Pi_{1,1}$ and (b-f) the renormalized electron-phonon coupling $\bar{g}(\mathbf{k},\mathbf{q})$ in arb. units for $\mathbf{k}=(0,\pi)$ and different values of q_z, as a function of in-plane momentum transfers $\mathbf{q}=(q,0)$. In the case of the bond-stretching mode, a small q_y component has been added in order to better visualize the effects of screening on the breathing branches at small $\mathbf{q}_{2D}$. The plasma frequency in this case is $\Omega_{pl}=0.914$ eV which corresponds to optimal doping.

vertices. For example, in the case of the breathing branches $\Pi_{g,1}$ is largest at large $\mathbf{q}$ due to the increased coupling associated with the deformation coupling mechanism.

In Fig. 6.2b-f the screened el-ph vertices for scattering from $\mathbf{k}=(0,\pi)$ with momentum transfers along the zone face $\mathbf{q}=(q_x,0)$ are plotted for various values of q_z. The corresponding bare vertex ($q_z=0$) is shown as the dashed black lines in each of the panels. To illustrate the effects of poor screening on the long-range Coulomb interaction, a momentum independent coupling $g=1$ has also been included (Fig. 6.2b). For a momentum-independent vertex $\Pi_{g,1}=g\Pi_{1,1}$ and, for $\Omega\ll\Omega_{pl}(q)$ screening is perfect, leaving only a small el-ph interaction which survives at large in-plane momentum transfer. This is shown as the black line in panel 6.2b, which corresponds to $q_z=0$. For finite q_z the cone of small momentum transfers forms where screening is inoperable. This region of unscreened coupling occurs over a small range of q-vectors until $\mathbf{q}=(\mathbf{q}_{2D},q_z)$ satisfies $\Omega_{pl}(q)=\Omega_{ph}$. At this point a logarithmic divergence occurs, which is cut off by

the damping introduced by a finite value of δ. For increasing q_z this condition moves to progressively larger $\mathbf{q}_{2D}$ and a window of momentum points opens where the vertex can be well represented by its bare value.

Likewise, figures 3c-f plot the renormalized vertices for the A_{1g}, B_{1g}, apical and breathing branches, respectively. Here, the renormalized vertices have been determined using the simplified forms for the el-ph vertices, defined by equations 3.21 - 3.23, and using the same parameter set used to produce figure 3.3. For large $\mathbf{q}_{2D}$ the c-axis couplings are largely unaffected by screening due to the fall-off of the polarizabilities at large $\mathbf{q}_{2D}$. However, for the breathing branch, where the bare coupling weights large momentum transfers, the growth of the mixed polarizability leads to an overall suppression of the screened vertex at large $\mathbf{q}_{2D}$. For small in-plane momentum transfer - relevant for c-axis Raman active phonons considered here - screening is ineffective and the coupling is enhanced over the large $\mathbf{q}$ coupling. Again, for the breathing branch only small effects are noticed at small $\mathbf{q}_{2D}$ due to the nature of the deformation-type coupling. Furthermore, since any fermionic dependence of the bare breathing couplings has been neglected, the mixed polarizability $\Pi_{g,1}$ is proportional to the pure charge polarizability $\Pi_{1,1}$ in this case.

The renormalized momentum-dependent coupling strength $\lambda_\nu(\mathbf{q}_{2D})$ is defined by substituting the screened el-ph vertex into Eq. 3.24 and summing over c-axis momenta

$$\lambda_\nu(\mathbf{q}_{2D}) = \frac{2N_F}{N_c\Omega_\nu}\sum_{\mathbf{k},q_z}\langle|\bar{g}(\mathbf{k},\mathbf{q},\Omega_{pl})|^2\rangle_{FS}. \tag{6.8}$$

This function is plotted in figure 6.3 for the A_{1g}, B_{1g}, apical and breathing branches in panels (a)-(d), respectively. When summed over out-of-plane momentum transfers q_z, the net coupling is on the order of the bare coupling for small $\mathbf{q}_{2D}$. The fermionic momentum dependence of the bare vertices for the B_{1g} case noticeably alters $\lambda(\mathbf{q}_{2D})$ for momentum transfers along the zone diagonal, which are largely projected out, while also preserving the small $\mathbf{q}_{2D}$ form of the interaction. The A_{1g} and apical cases are similar to one another even though the anisotropy of the bare couplings for each mode are substantially different and weight out different regions of the Brillouin zone. For all of the c-axis modes, coupling is small for $\mathbf{q}_{2D} = \mathbf{Q}_{AF} = (\pi/a, \pi/a)$. The addition of strong correlations are expected to further suppress the el-ph vertex for large $\mathbf{q}$ since both Monte Carlo and slave-boson studies have shown that the Hubbard short-range term of the Coulomb repulsion further suppresses coupling at large $\mathbf{q}$ [45, 47]. Therefore, with the suppression of large $\mathbf{q}$ scattering, the Raman-active c-axis modes are not expected to appear in transport measurements. Likewise, the breathing modes are altered at small $\mathbf{q}_{2D}$ but the overall coupling does not give substantial weight at these momentum transfers.

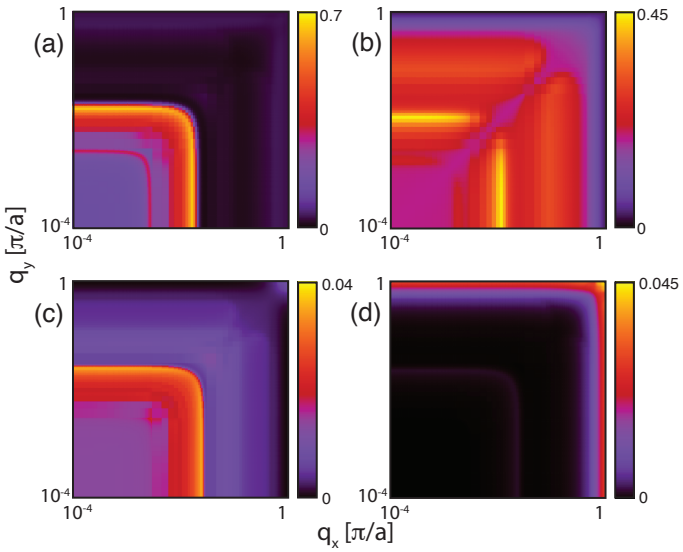

Figure 6.3: Plots of the renormalized momentum-dependent couplings $\lambda_\nu(\mathbf{q}_{2D})$ for the (a) A_{1g}, (b) B_{1g}, (c) apical and (d) breathing modes. The momentum axis are plotted on a logarithmic scale in order to highlight the region of poor screening at small $\mathbf{q}_{2D}$.

The $\mathbf{q}$-dependence also has a strong effect on the d-wave projected pair interaction. In figure 6.4 the d-wave projected coupling

$$\lambda_{\nu,d} = \frac{2N^d}{N_c\Omega_\nu}\sum_{q_z}\langle|\bar{g}(\mathbf{k},\mathbf{q},\Omega_{pl})|^2 d_{\mathbf{k}} d_{\mathbf{k}-\mathbf{q}}\rangle^d_{\mathbf{k}_{FS}} \tag{6.9}$$

for the four branches is plotted as a function of $\mathbf{q}_{2D}$. The phonons that strongly favour small $\mathbf{q}$ scattering (the c-axis modes) promote d-wave pairing while the phonons that favour large $\mathbf{q}$-scattering (the bond-stretching modes) are detrimental. For the bond-stretching modes, while a large region of q-space supports pairing, the large weight near $\mathbf{q} = \mathbf{Q}$ dominates the coupling and results in an overall suppression of the branch's contribution to d-wave pairing. The consequence of poor screening for finite q_z, which accentuates small $\mathbf{q}$ couplings is twofold: it enhances the overall d-wave coupling compared to the coupling at $q_z = 0$ and it diminishes the repulsive contribution from the bond-stretching modes. Therefore, as the effects of screening become more prominent with doping it is expected that the total contribution to pairing mediated by these optical oxygen branches will increase.

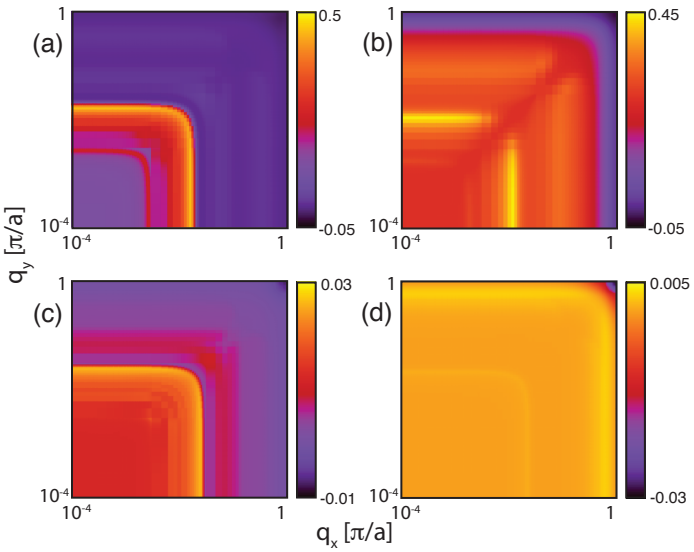

Figure 6.4: Plots of the renormalized momentum-dependent couplings projected onto the d-wave channel $\lambda_{\nu,d}(\mathbf{q}_{2D})$ for the (a) A_{1g}, (b) B_{1g}, (c) apical and (d) breathing modes. The momentum axis are plotted on a logarithmic scale in order to highlight the region at small $\mathbf{q}_{2D}$.

6.3 Anisotropy of the Screened Electron-Phonon Interaction

The poor screening of the c-axis modes will also affect the overall anisotropy and magnitude of the el-ph coupling. Using the renormalized vertices, defined by Eq. 6.1, $\lambda_\nu(\mathbf{k}_F)$ defined by Eq. 3.24, is plotted in figure 6.5. In order to mimic the effects of doping, the plasma frequency has been varied from 0.289 - 0.914 eV, in accordance with experiment and reflecting the increased metallic behaviour that occurs as the system is doped. This is accomplished by rescaling the product $\epsilon_{ab}\epsilon_c$ while maintaining the ratio ϵ_{ab}/ϵ_c. The values of $\lambda_z(\mathbf{k}_F)$ are plotted in figure 6.5. The black lines correspond to $\Omega_{pl} = 0.289$ eV (underdoping) and the purple dashed lines correspond to $\Omega_{pl} = 0.914$ eV (Optimal doping). The intermediate curves correspond to the values of Ω_{pl}, smoothly varying between the under- and optimal-doped values.

Screening causes several noticeable effects compared to the unscreened case presented in chapter 3. As the plasma frequency is increased the A_{1g}, apical and breathing branches are screened more effectively and the overall vertex is lowered for all $\mathbf{k}$ around the Fermi surface. In the case of the A_{1g} and apical branches, the largest effect occurs in the antinodal region where the bare vertex is largest. However, in the case of the B_{1g} branch

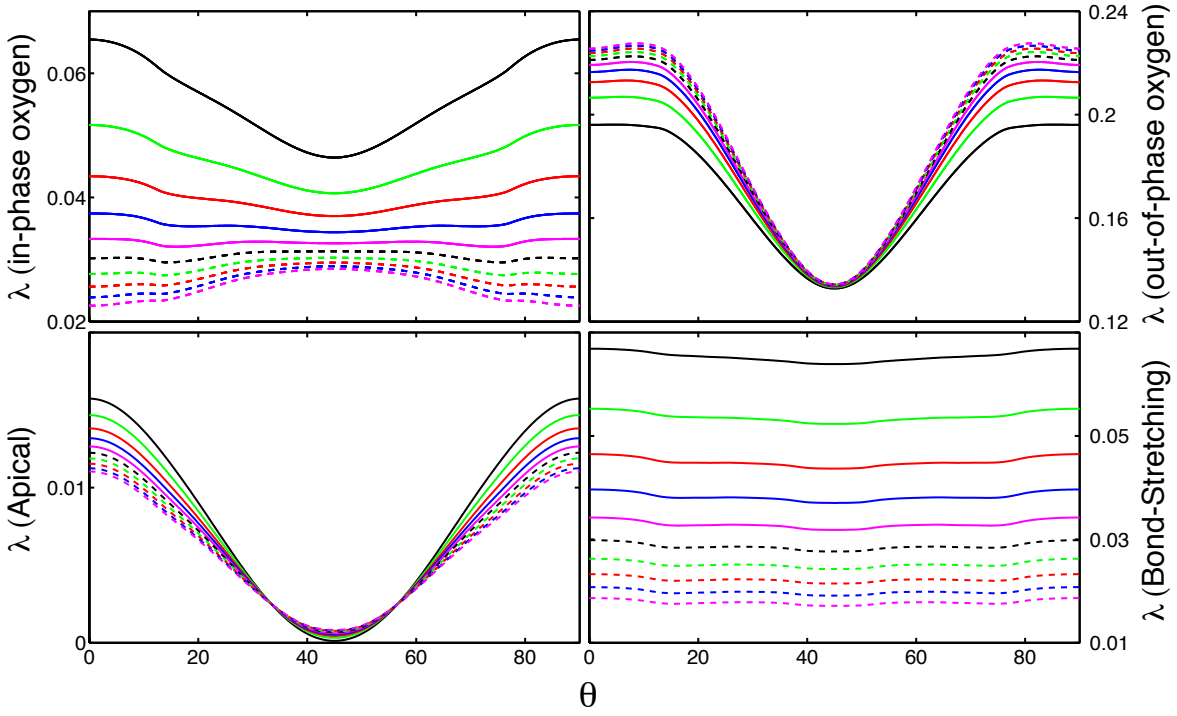

Figure 6.5: Plots of the screened el-ph $\lambda(\mathbf{k}_F)$ for fermions at the Fermi level as a function of Fermi surface angle θ for several different values of the plasma frequency. The plasma frequency used varies from 0.914 eV (purple dashed) to 0.289 eV (solid black).

there is an anomalous anti-screening which occurs and the B_{1g} vertex in the antinodal region is enhanced with increasing Ω_{pl}. This non-intuitive result is due to the out-of-phase motion of the oxygen atoms since the only difference in the form of the bare vertices for the A_{1g} and B_{1g} branches is the phase of the phonon eigenvectors. It is also evident that the self-energy due to coupling to c-axis phonons should redistribute weight around the Fermi surface as the number of doped holes varies. Such a redistribution of weight could be directly probed in ARPES studies, providing a means to experimentally verify these predictions. From these results it is inferred that in the cuprates a window in $\mathbf{q}$-space at small $\mathbf{q}_{2D}$ opens in which the c-axis el-ph interaction can be quite large and avoid screening. This would vanish if the material were fully conducting along the c-axis. Furthermore, this effect will become more pronounced in the underdoped systems as Ω_{pl} is reduced with decreasing hole concentration and the system becomes more ionic in character.

In contrast to the c-axis modes, since poor screening does not affect large momentum transfers, the strength of the coupling to the breathing branches dramatically increases

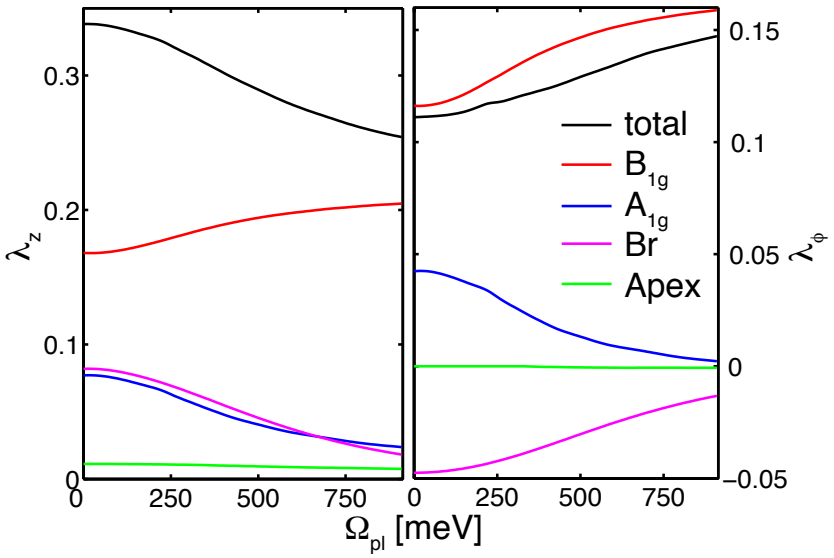

Figure 6.6: Plots of the total λ_z (left) and λ_ϕ (right) as a function of the plasma frequency Ω_{pl}. The parameters used are defined in the text.

for smaller Ω_{pl}. This implies that the electron self-energy contribution from the breathing branches should grow with underdoping. However, this finding must be viewed with a degree of caution since the large **q**- behaviour is also strongly renormalized by Coulomb interactions which have been neglected in this treatment.

Finally, in figure 6.6 the total coupling $\lambda_{z,\phi}$ resulting from the screened el-ph vertex is plotted as a function of Ω_{pl}. Following the trends in figure 6.5, the total coupling in both channels for the A_{1g}, apical, and breathing branches decreases with increasing Ω_{pl}. However, for the B_{1g} branch the couplings in both channels increases due to the anti-screening effect and enhanced el-ph coupling a small $\mathbf{q}_{2D}$. In the case of the projected d-wave coupling, the attractive interaction of the A_{1g} branch is largely cancelled by the repulsive interaction of the breathing branch. Therefore, the total *attractive* d-wave interaction mediated by phonons, which is primarily provided by the B_{1g} branch, is enhanced with progressive doping.

6.4 Phonon Contributions to T_c

In chapter 4 it was shown that the strength of a material's coupling to the B_{1g} branch is correlated with the material's T_c at optimal doping. Based on this observation it was argued that phonons could provide a pathway to understanding the material variations in

T_c. In such a picture, a two-channel model is invoked where phonons contribute to pairing in conjunction with a dominant d-wave pairing mechanism. The effects of screening presented in this chapter indicate that this proposal may also be able to account for the doping dependence of T_c. In this section such a proposal will be examined further using a simple multi-channel model for superconductivity in the cuprates based on Eliashberg theory. The primary goal is to determine the degree to which phonons can be expected to modify T_c and the implicit assumption here is that superconductivity can be described in the usual bosonic exchange framework.

The starting point for calculating T_c is the generalized d-wave Eliashberg equations for coupling to a spectrum of Einstein modes characterized by frequency Ω_μ and spectral density $B_\mu(\nu) = \delta(\nu - \Omega_\mu)$. The expressions are

$$\begin{aligned}
\Delta(\omega)Z(\omega) &= \sum_\mu \lambda_{\phi,\mu}\frac{\Omega_\mu}{2}\int_0^\infty dz Re\left\langle \frac{\Delta(\omega)\cos^2(\theta)}{\sqrt{z^2-\Delta^2(\omega)\cos^2(\theta)}}\right\rangle K_-(\omega,z,\nu) \\
\omega[1-Z(\omega)] &= \sum_\mu \lambda_{z,\mu}\frac{\Omega_\mu}{2}\int_0^\infty dz Re\left\langle \frac{z}{\sqrt{z^2-\Delta^2(\omega)\cos^2(\theta)}}\right\rangle K_+(\omega,z,\nu)
\end{aligned} \tag{6.10}$$

with kernals

$$\begin{aligned}
K_\pm(\omega,z,\Omega) &= [n_b(x)+n_f(-z)]\left[\frac{1}{\omega+\Omega+z+i\delta}\pm\frac{1}{\omega-\Omega-z+i\delta}\right] \\
&+ [n_b(x)+n_f(z)]\left[\frac{1}{\omega-\Omega+z+i\delta}\pm\frac{1}{\omega+\Omega-z+i\delta}\right].
\end{aligned}$$

Here, the role of bandstructure has been neglected in order to allow for a simple analytic solution for T_c. The full derivation of these expressions is given in appendix B. Attention is now restricted to the two mode case with $\mu = 1, 2$ corresponding to the B_{1g} phonon and an antiferromagnetic spin fluctuation, respectively. Each mode is characterized by couplings $\lambda_{z,\mu}$ and $\lambda_{\phi,\mu}$. In this calculation only the B_{1g} phonon branch is considered since this mode gives the largest contribution to d-wave pairing and the antiferromagnetic spin fluctuation is considered to be the dominant pairing interaction.

In order to obtain an expression for T_c, a standard set of approximations [181] are now made. First, the imaginary parts of $\Delta(\omega)$ and $Z(\omega)$ are neglected. Next, it is noted that in the vicinity of the superconducting transition $T \to T_c$ the value of the gap is small with $\Delta(\omega) \to 0$ for all ω. Therefore $\Delta(\omega)$ appearing in the denominators of Eqs. 6.10 can be neglected and $\Delta(\omega)$ can be replaced by its value at $\omega = 0$ on the right hand side of Eq. 6.10. Finally, since the frequency of the boson modes is large, thermal bosons can be neglected and $n_b(\Omega_\nu) = 0$. With these approximations the Eliashberg equations

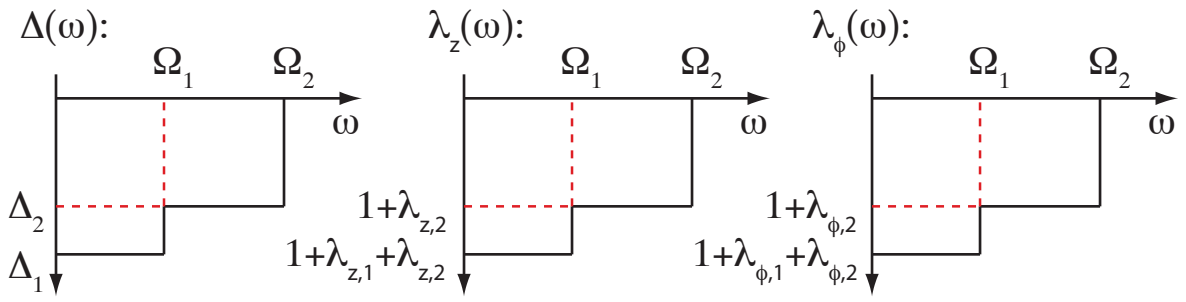

Figure 6.7: The double square-well model used to derive T_c.

simplify to

$$\begin{aligned}\Delta(0)Z(\omega) &= \sum_\mu \lambda_{\phi,\mu}\Omega_\mu \int_0^\infty dz Re\left\langle \frac{\Delta(z)\cos^2(\theta)}{z}\right\rangle \left[\frac{n_f(-z)}{z+\Omega_\mu} - \frac{n_f(z)}{z-\Omega_\mu}\right] \\ [1-Z(\omega)] &= \sum_\mu \lambda_{z,\mu}\Omega_\mu \int_0^\infty dz \left[\frac{n_f(-z)}{\omega^2-(z+\Omega_\mu)^2} + \frac{n_f(z)}{\omega^2-(z-\Omega_\mu)^2}\right].\end{aligned}$$

At this level, the value of the mass renormalization parameter $Z(\omega)$ is replaced with its zero frequency and zero temperature value

$$Z(0) = 1 + \sum_\mu \lambda_{z,\mu}\Omega_\mu \int_0^\infty dz \frac{1}{(z+\Omega_\mu)^2} = 1 + \sum_\mu \lambda_{z,\mu} \tag{6.11}$$

which is then substituted into the expression for the gap function. Lastly, z appearing in the denominator of the terms inside the square bracket of Δ are neglected leaving the final expression for the gap function

$$\Delta(\omega)Z(0) = \sum_\mu \lambda_{\phi,\mu} \int_0^\infty dz \frac{\Delta(z)}{z} \tanh\left(\frac{z}{2T_c}\right). \tag{6.12}$$

A double square-well model for the frequency dependence of $\Delta(\omega)$ [183], as shown in figure 6.7, is now introduced. This approximation produces the set of coupled equations

$$\begin{aligned}\Delta_1(1+\lambda_{z,1}+\lambda_{z,2}) &= (\lambda_{\phi,1}+\lambda_{\phi,2})\int_0^{\Omega_1} dz \frac{\Delta_1 \tanh(\frac{z}{2T_c})}{z} + (\lambda_{\phi,1}+\lambda_{\phi,2})\int_{\Omega_1}^{\Omega_2} dz \frac{\Delta_2 \tanh(\frac{z}{2T_c})}{z} \\ \Delta_2(1+\lambda_{z,2}) &= \lambda_{\phi,2}\int_0^{\Omega_1} dz \frac{\Delta_1 \tanh(\frac{z}{2T_c})}{z} + \lambda_{\phi,2}\int_{\Omega_1}^{\Omega_2} dz \frac{\Delta_2 \tanh(\frac{z}{2T_c})}{z}\end{aligned} \tag{6.13}$$

which are solved for the non-zero solution for Δ_1 and Δ_2. For $\Omega_1 \sim 35$ meV and $T_c \leq 100$ K the integrals can be replaced by their asymptotic value as $z \to \infty$ [181, 183]

$$\int_0^{\Omega/2T_c} dz \frac{\tanh(z)}{z} \sim \frac{1.134\Omega}{T_c}. \tag{6.14}$$

This asymptotic form is substituted into equations (6.13) and the system then solved for T_c. The final expression for, valid in the regime of weak coupling is (explicitly inserting the k_b factor):

$$k_b T_c = 1.134\Omega_1 \exp\left[-\frac{1+\lambda_{z,1}+\lambda_{z,2}}{\lambda_{\phi,1}+\lambda_{\phi,2}} \frac{1+\lambda_{z,2}-\lambda_{\phi,2}\log(\Omega_2/\Omega_1)}{1+\lambda_{z,2}}\right]. \tag{6.15}$$

This expression recovers the McMillan result [48, 181] (μ^* has been neglected here) for the single-well case in the limits of $\lambda_{1,z}$, $\lambda_{1,\phi} \to 0$ or $\lambda_{2,z}$, $\lambda_{2,\phi} \to 0$. This expression differs from that reported previously [178] due to the assumed frequency dependence of Z.

The result for the two-channel model is plotted in figure 6.8a (solid curve) as a function of the phonon's projected d-wave coupling $\lambda_{1,\phi}$. Here, the phonon is associated with the $\Omega_1 = 36$ meV B_{1g} branch with the ratio $\lambda_{1,z}/\lambda_{1,\phi} = 3$ held fixed. The strength of the $\Omega_2 = 260$ meV spin fluctuation is also held fixed with $\lambda_{2,z} = 2\lambda_{2,\phi}$, $\lambda_{\phi,2} = 1$, which produces a baseline $T_c = 62$ K without the contribution from the B_{1g} branch. The value of T_c obtained for phonon only mediated pairing is also shown (dashed curve), multiplied by a factor of 10. For the double well model, the resulting T_c is not a simple addition of the T_c obtained from each mode individually and even small el-ph couplings can produce a sizeable enhancement of T_c.

The isotope exponent $\alpha = -\partial \log T_c / \partial \log M$ defines the power law of the shift in T_c with respect to changes of oxygen ion mass M. In conventional phonon-mediated superconductors $\alpha = 1/2$ (with some notable deviations in systems with strong coupling or large Coulomb pseudopotentials μ^* such as Pb or Nb),[9, 181] and the existence of an isotope effect is unambiguous evidence for a phonon mediated pairing mechanism [2, 3, 4]. In the two-well model used here $\alpha = [1 - \delta\alpha]/2$ where

$$\delta\alpha = \frac{1+\lambda_{z,1}+\lambda_{z,2}}{\lambda_{\phi,1}+\lambda_{\phi,2}} \frac{\lambda_{\phi,2}}{1+\lambda_{z,2}} \tag{6.16}$$

reduces the overall magnitude of α from the value of $1/2$ that would occur for a purely phonon-mediated pairing. Without el-ph coupling ($\lambda_{z,1} = \lambda_{\phi,1} = 0$) α is identically zero. Furthermore, if the spin fluctuation mode is turned off ($\lambda_{z,2} = \lambda_{\phi,2} = 0$) then $\alpha = 1/2$ as expected. A similar reduction in α and enhancement of T_c has been reported when the phonon contribution to pairing is taken to be attractive in the $d_{x^2-y^2}$ channel [179]. Figure 6.8b shows the resulting value of α and demonstrates that a small isotope exponent is possible despite large contributions to pairing provided by phonons.

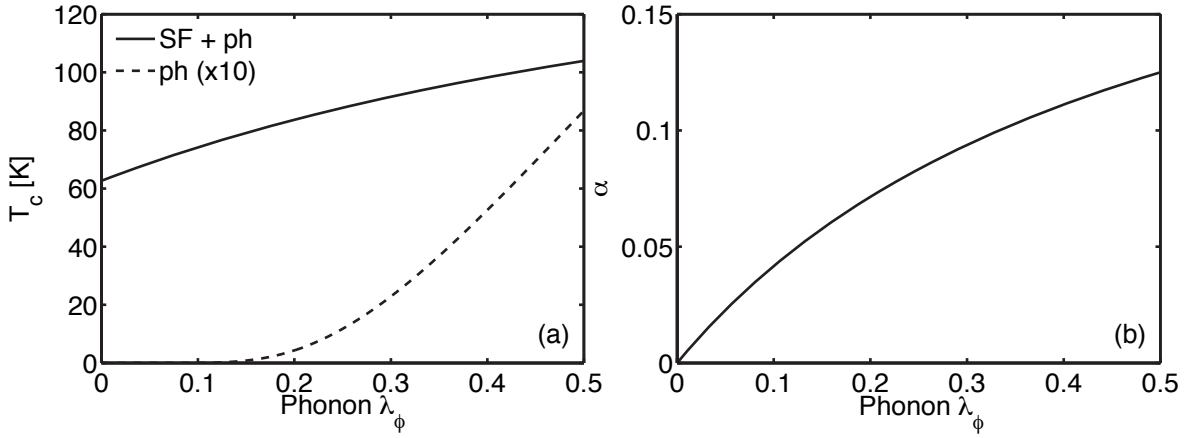

Figure 6.8: (a) T_c for a d-wave superconductor with contributions from two channels, a 260 meV mode associated with spin-fluctuations and a 35 meV phonon as a function of the phonon modes contribution to superconductivity. The dashed line shows the T_c one would expect from the phonon alone (multiplied by a factor of 10). (b) The corresponding isotope exponent.

In comparing the results of figure 6.8b to experiment a degree of caution is warranted. Experimentally, the isotope exponent at optimal doping is small ($\sim 0.0 - 0.2$) and increases with underdoping [32, 37, 38]. However, the screening results of the previous section indicate that the overall contribution to d-wave pairing mediated by el-ph coupling increases with doping due to screening effects. Therefore, one might naturally expect that the isotope exponent would increase with doping, contrary to experimental observations. However, doping dependent changes are also expected for the spin-fluctuation mediated pairing. Since it is the relative contributions from each channel that sets the value of the isotope exponent, a direct calculation of α expected experimentally is not possible until the details of the dominant pairing interaction are understood. Nevertheless, these calculations show that phonons with relatively small coupling strengths can play a substantial role in determining T_c while producing small signatures in traditional metrics such as the isotope effect. It is also important to note that these results are limited by the applicability of Migdal-Eliashberg theory and the fact that T_c is difficult to calculate correctly and is therefore generally a poor metric to compare with experiment. However, this enhancement is generic to multi-channel superconductors and this result serves as a guide for understanding the material dependence of T_c.

6.5 Summary

In this chapter the theory of poor screening in the cuprates was formulated. It was shown that due to the quasi-2D nature of the cuprate unit cell, and poor conductivity along the c-axis, a window of small in-plane momentum transfers $\mathbf{q}_{2D}$ opens where screening becomes inoperable. As a consequence of this, coupling to c-axis phonon modes can survive the effects of screening at small $\mathbf{q}_{2D}$ and the contribution to d-wave pairing mediated by these modes is enhanced. Such effects are also expected in any quasi-2D system with phonon modes polarized perpendicular to the plane and these effects are entirely absent in good 3D metals.

Poor screening, when combined with the materials dependence of the el-ph coupling presented in chapter 4, provides a natural means for addressing the doping and material's dependence of T_c. In order to qualitatively assess the phonon-mediated contribution to pairing a simple model calculation for T_c was also presented. Using a simple two-well model it was demonstrated that although the total values of $\lambda_{z,\phi}$ are small for el-ph coupling, the inclusion of this pairing channel can give sizeable enhancements to T_c. This multichannel scenario is also consistent with both the ARPES and STM results discussed in chapters 4 and 5, respectively, where only moderate values of $\lambda_{z,\phi}$ where required to reproduce the renormalizations observed by these probes. This model for high-temperature superconductivity is also supported by the observation that such a two-channel model is required in order to reproduce the qualitative structures in the tunnelling-derived density of states. From these results a consistent picture of high-temperature superconductivity emerges where many factors cooperate in order to produce the large observed value of T_c.

Chapter 7

The Impact of an Oxygen Dopant in $Bi_2Sr_2CaCu_2O_{8+\delta}$

In this chapter the interplay between electron-phonon coupling and strong correlations will be examined via exact diagonalization (ED) of small cluster Hamiltonians. This treatment has the advantage of being exact but is limited in the size of problem that can be handled due to the exponential growth of the Hilbert space with cluster size. Due to this size limitation small cluster ED calculations are particularly well suited for capturing local physics. Therefore, we consider el-ph coupling in the context of local oxygen dopants interstitially placed in an otherwise perfect crystal of $Bi_2Sr_2CaCu_2O_8$. The key results presented in this chapter have appeared in ref. [198].

7.1 Dopant Atoms in the High-T_c Cuprates

The precise role of atoms lying off the CuO_2 planes has been an intriguing puzzle in the study of the high-T_c cuprates. Traditionally such dopants are thought to provide a charge reservoir to dope holes into the CuO_2 plane. However, it has become clear that an understanding of the pairing mechanism will require addressing the large variations in T_c arising from the local environment surrounding the CuO_2 planes [16]. Empirically, the role of the apical or axial orbitals has been a vehicle linking T_c either to an effective electron hopping t' along diagonal Cu-Cu bonds [22] or to the stability of the Zhang-Rice singlet (ZRS) [18]. However, to date these arguments have pointed out possible links but offer little microscopic reason for the impact on T_c itself.

Scanning tunneling microscopy (STM) in $Bi_2Sr_2CaCu_2O_{8+\delta}$ (Bi-2212) has revealed that nanoscale inhomogeneity is correlated with the location of interstitial oxygen dopant atoms [24] or the superlattice modulation [199, 29]. The location of dopants has been

correlated with suppressed peak features with larger gap energies in the observed local density of states (LDOS), and has been associated with local modification of superconducting pairing [25, 200]. This suggests a non-trivial link between the dopant atoms and the electronic properties of the material on a local level.

In metallic systems defects can be effectively screened and have little impact on the electrostatics of the material. This is in contrast to the cuprates, which have poor screening along the c-axis and are unable to effectively screen the dopant's impurity charge. As a result, these dopants and accompanying structural changes may have a substantial impact on the electrostatic properties of the material. This may be reflected in quantities such as the charge transfer energy Δ, effective hoppings t, t', magnetic exchange interaction J, or electron- phonon (el-ph) coupling strength λ.

From t-J studies [201, 202], it has been argued that dopants give an enhancement of J and thus larger superconducting gap energies if one assumes a dominant spin-fluctuation-based pairing mechanism. While the overall pairing mechanism - Coulomb repulsion, magnons, phonons, or some combination - is still a subject of debate, the overall shape of the observed LDOS suggests that incoherence, giving broad spectral features, is an important ingredient to the understanding of local pairing modifications.

In order to quantitatively address these issues, electrostatic Ewald calculations are performed for Bi-2212 supercells to determine the spatial dependence of the Madelung energies around atomic sites in the crystal. It is found that while Madelung energies on O and Cu are spatially varied on the scale of eVs, these changes largely cancel and Δ is slightly increased near the dopant, yielding an overall suppression locally to J. This information is then combined into exact diagonalization (ED) cluster studies, yielding effective parameters t, t', J and J'. Large $O(1)$ changes are found in both t' and c-axis el-ph coupling λ, quantities known to strongly modify a $d_{x^2-y^2}$ pairing interaction. Finally, ED cluster studies including c-axis phonons are shown to produce a broadened spectra, a reduced charge gap, in agreement with experiments [24]. As a consequence, a sizeable local increase of J results due to reduced gap *via* a gain in lattice energy. While a unique pairing mechanism cannot be determined in this approach, the results imply a strong interplay and entanglement between el-ph coupling, local superconducting pairing and antiferromagnetic correlations.

7.2 Electrostatics

7.2.1 The Undoped Lattice

The Ewald summation technique [177] is a powerful method for evaluating sums of long-ranged electrostatic interactions. In essence, it breaks the summation into two pieces; a

well-behaved short-range piece plus the problematic long-range piece. The short range piece is easily evaluated in real space, while the long range piece is evaluated in reciprocal space where it becomes short ranged and rapidly convergent. Electrostatic calculations using Ewald's method are performed on supercell consisting of $3 \times 3 \times 1$ Bi-2212 unit cells for a total of 270 atoms. Supercells up to four times this size have been examined and it was found that the results are not qualitatively different. Each unit cell contains two primitive cells stacked along the c-axis for a total of four CuO_2 planes, as shown in fig. 7.1a. Using formal valence for the atoms, along with the known structural data [97], the Madelung energies Φ obtained are $\Phi_{apex,plane} = 18.48$, 10.16 eV, for the apical, planar oxygen sites respectively, and $\Phi_{Cu} = -38.22$ eV for the copper site, consistent with the values reported previously [18].

The in-plane charge transfer energy Δ is related to the difference in the Madelung energies for the Cu and O sites $\Delta\Phi_M = \Phi_O - \Phi_{Cu}$ and is given by

$$\Delta = \frac{\Delta\Phi_M}{\epsilon(\infty)} - I_{Cu}(2) + A_O(2) - \frac{e^2}{d_p} \tag{7.1}$$

where $I_{Cu}(2)$ and $A_O(2)$ are the second ionization and electron affinity energies for the Cu and O sites, respectively. The factor of e^2/d_p represents the contribution of the Coulomb interaction between the electron-hole pair introduced in the charge-transfer process (this term is not included in the Ewald summation used to determine $\Delta\Phi_M$). In this work, following reference[18], we take the dielectric constant $\epsilon(\infty) = 3.5$ and $I_{Cu}(2) - A_O(2) + e^2/d_p = 10.9$ eV, yielding $\Delta = 2.92$ eV in the ideal lattice. Besides setting the scale for gap excitations, Δ largely governs the magnetic exchange energy J. In the limit of small hole hopping J is given by[203]:

$$J = \frac{4t_{pd}^4}{(\Delta + U_{pd})^2}\left[\frac{1}{U_d} + \frac{2}{2\Delta + U_p}\right]. \tag{7.2}$$

Using a canonical standard set of parameters[1], an exchange energy $J \sim 147$ meV is obtained, in rough agreement with experiments[151].

7.2.2 The Doped Lattice

To model the doped lattice the Ewald calculation was repeated with a single oxygen dopant atom inserted in the unit cell, shown schematically in fig. 7.1a, and the neighbouring atoms displaced as indicated by a recent LDA study [204]. The oxygen dopant was assigned formal valence, with surplus charge distributed equally among orbitals in the CuO_2 planes.

[1](In eV): $U_d = 8.8$, $U_p = 4.1$, $t_{pd} = 1.0$, $t_{pp} = 0.5$, $\epsilon_d = 0$ and $\epsilon_p = 2.92$ where U_p and U_d are the on-site Coulomb repulsion for the O $2p$ and Cu $3d_{x^2-y^2}$ orbitals, t_{pd} their overlap and t_{pp} is the O $2p$-$2p$ overlap integral.

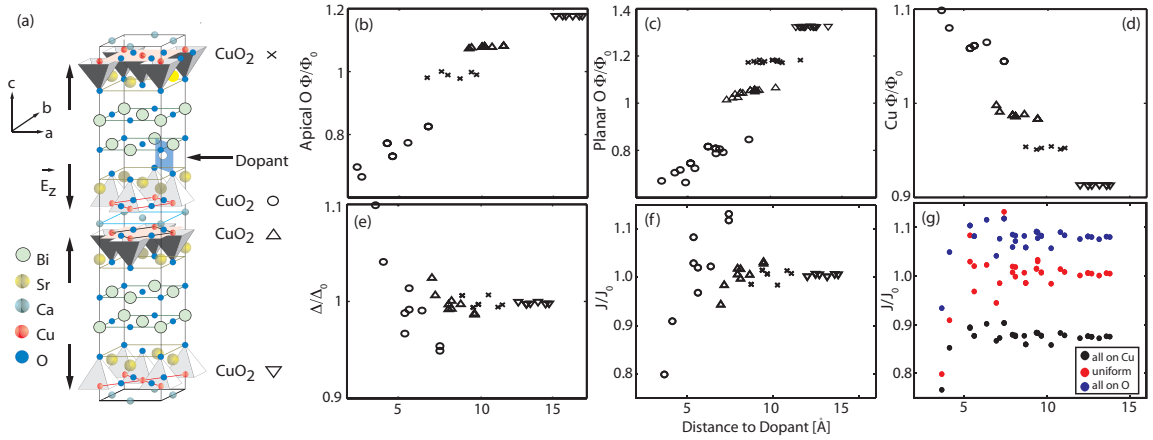

Figure 7.1: (a) Schematic location of the dopant oxygen in the Bi-2212 unit cell. Individual CuO_2 planes are labeled by the symbols shown. The arrows on the left indicate the orientation of the local crystal field at the oxygen site in the undoped lattice. (b-d) Madelung energies of the apical O, planar O and Cu sites, respectively, in the doped lattice. The local value of the charge transfer energy Δ (e) and derived exchange interaction J (f), obtained by averaging $\Delta\Phi_M$ between Cu and its four neighbouring O sites. (g) Resulting J for different distributions of charges. All values have been normalized to the undoped lattice values. The distance to the dopant is defined as the distance to the closest dopant, accounting for the periodicity of the superlattice.

The site-dependent Madelung energies are presented in fig. 7.1a-d, showing large scale variations for sites closest to the dopant atom. Suppressions/enhancements of O/Cu Madelung energies are observed, respectively, rising/falling to bulk values, shifted by the presence of the doped holes, further away from the dopant. However, since the relative sign of the Madelung energies for Cu and O are negative, these changes largely cancel for $\Delta\Phi_M$ and thus Δ (fig. 7.1e) is largely unaffected.

Modifications in Δ allow us to examine the effect of the dopant on the exchange energy J (fig. 7.1f, equation 7.2). Reflecting the spatial variations of Δ, J is suppressed by up to 20% near the dopant. Allocating the dopant's excess charge on either Cu or O, or distributed on both result in slightly different values of J (fig. 7.1g) but the overall suppression seems rather immune to the way in which charge is distributed.

7.3 Small Cluster Calculations

Equation 7.2 for J is based on a perturbative treatment in the limit of small hopping. One would like to test the prediction of a suppression in J in a non-perturbative way. To

do so, exact diagonalization (ED) studies of three-hole Cu_2O_7 and Cu_2O_8 clusters were employed to determine the changes to the Zhang-Rice singlet parameters [203]. The clusters are shown schematically in fig. 7.2a-c. The ED calculations involve a three-band model which includes the Cu $3d_{x^2-y^2}$, O $2p_x$ and $2p_y$ orbitals. The Hamiltonian is $H = \sum_{i,\sigma} H_{i,\sigma}$, with

$$\begin{aligned} H_{i,\sigma} &= \epsilon_d^i d_{i,\sigma}^\dagger d_{i,\sigma} + \sum_\delta \epsilon_p^{i,\delta} p_{i,\delta,\sigma}^\dagger p_{i,\sigma,\delta} + \sum_\delta t_{pd}^{i,\delta}[d_{i,\delta}^\dagger p_{i,\delta,\sigma} + h.c.] + \sum_{\delta\neq\delta'} t_{pp}^{\delta,\delta'} p_{i,\delta,\sigma}^\dagger p_{i,\delta',\sigma} \\ &+ U_d \hat{n}_{i,\uparrow}\hat{n}_{i,\downarrow} + U_p \sum_\delta \hat{n}_{i,\delta,\uparrow}\hat{n}_{i,\delta,\downarrow} \end{aligned} \tag{7.3}$$

where δ denotes the Cu-O basis vectors and $\hat{n}_{i,\sigma}$ is the number operator. From this three-band model, an effective singleband Hubbard or t-J model is derived, with effective nearest $2t$ and next-nearest $2t'$ neighbour hopping determined from the bonding-antibonding splitting of the ZRS in the three-hole sector and J derived from the singlet-triplet splitting in the two-hole sector. In terms of clusters, Cu_2O_7 determines t and J as the ZRS involves a common bridging oxygen while Cu_2O_8 clusters yield t', J', via O-O hopping [203]. For the undoped lattice we obtain $t = 330$, $t' = -140$ meV and antiferromagnetic exchange couplings of $J = 158$, $J' = 14.4$ meV. Note that J may be further fine-tuned by adjusting t_{pd} and t_{pp}.

The dopant is included by locally varying the on-site Cu and O energies ϵ_d and ϵ_p, respectively, as shown in figure 7.2. Here, two $Cu_2O_{7,(8)}$ clusters are used which differ with respect to the location of the dopant, and the site energies have been determined from site modified Madelung Energies (Fig. 7.1), according to eq. 7.1. For the Cu_2O_7 cluster $t = 336$ and $J = 155$ meV are obtained. For the Cu_2O_8 clusters the values $t' = -187(-237)$ and $J' = 15(15)$ are obtained, respectively. Electrostatic modulations to J and J' are slightly suppressed over the undoped cluster values, in general agreement with the Madelung energy estimates, although the magnitude is smaller. Importantly, it is noted that the symmetric placement of the dopant for the Cu_2O_7 cluster gives only small changes to t, while for the Cu_2O_8 cluster the increase is noticeably larger, particularly for the geometry in fig. 7.2c. The asymmetric location of the dopant favours occupation of the oxygen ligand orbitals in the plaquette containing the dopant, giving larger modifications of t'.

These cluster calculations have been repeated including the modulations in t_{pd} induced by the structural distortions, according to the displacements of the Cu-O bond distances predicted by LDA [204, 165], as shown in fig. 7.2d. Here, the values $t = 324$, $J = 142$, $t' = -180(-234)$ and $J' = 17(19)$ meV. This tends to further suppress J. Thus, the oxygen dopant's net effect is to mildly suppress J and increase t', indicating that the dopant cannot be viewed as only modifying site energies and increasing J in downfolded single-band models [201, 202]. This is also supported by recent perturbation examinations of J due to local variations in band structure [205].

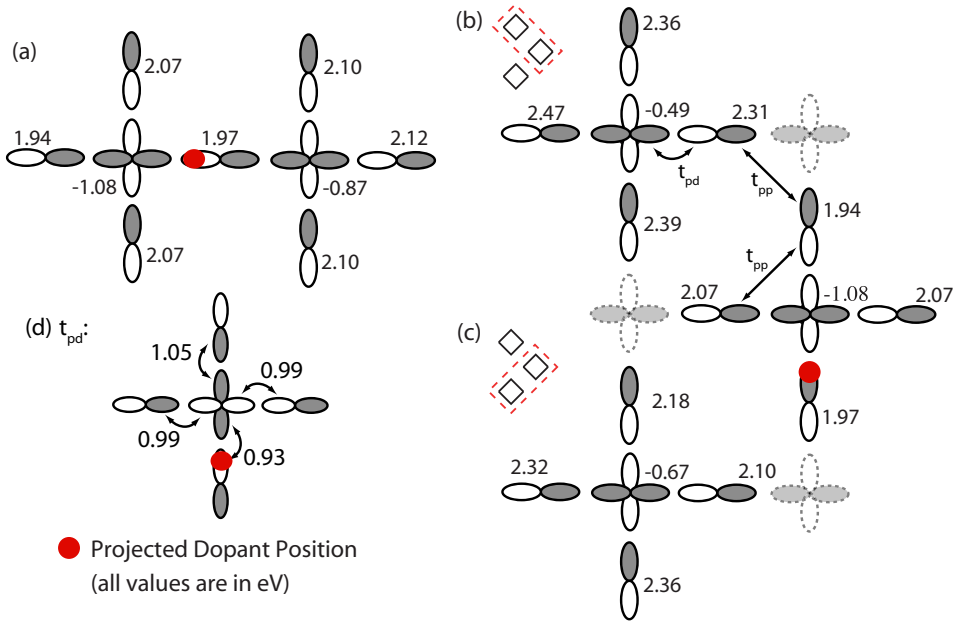

Figure 7.2: (a) Cu_2O_7 cluster used to extract t and J. (b,c) Two Cu_2O_8 clusters, outlined in red, used to extract t' and J'. The values for $\epsilon_{p,d}$ are indicated. (d) Modifications to t_{pd} due to the dopant induced displacements of the nearby sites.

In addition, the attractive or repulsive effect of the dopant on the local ZRS binding energy has been investigated. When examining the ground state energy of the three hole cluster in the presence of the dopant, the ground state is lowered in energy on these small clusters and therefore the dopant may attract local hole charge density. It was found that the dopant alters the ZRS density for the Cu_2O_7 cluster, attracting 10% more weight in the plaquette nearest to the dopant. Part of this charge reorganization will of course be screened by the long-range Coulomb interaction and carrier metallicity which will tend to minimize charge density variations, and will also be compensated by changes in the overall chemical potential in the grand canonical ensemble. Thus, while this would be better suited in larger clusters, it is inferred that the changes by the dopant to the local ZRS properties t, J, t' and J' seem to represent the most dominant effects on the local bandstructure.

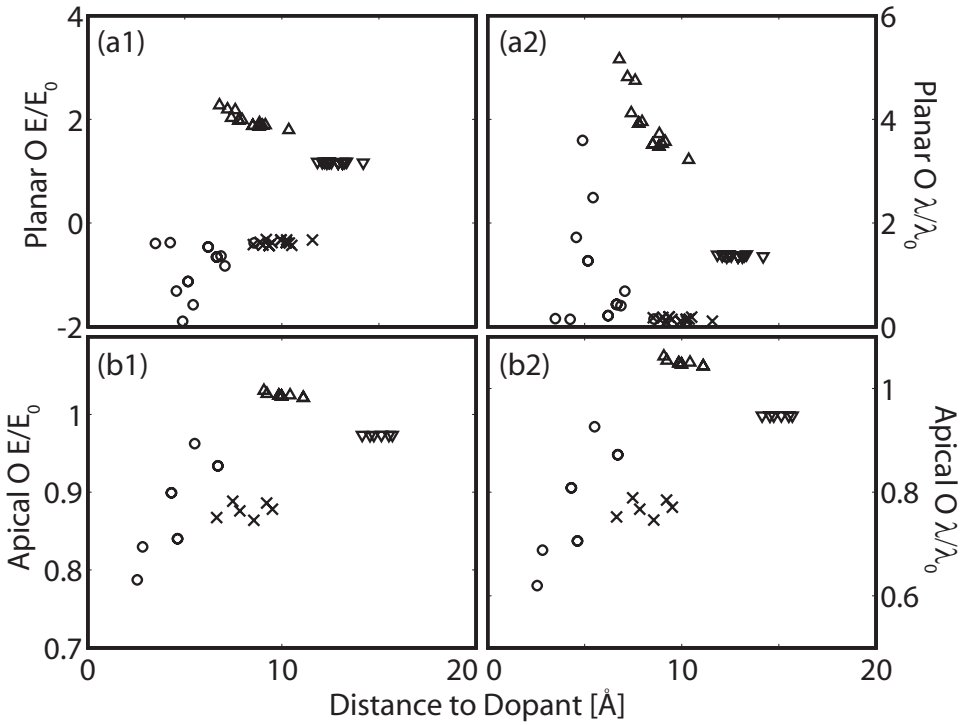

Figure 7.3: (a1),(b1) Normalized local crystal fields at the planar and apical oxygen sites of the doped lattice. (a2),(b2) The corresponding electron-phonon coupling strength $\lambda \propto E^2$. The data points follow the same key as Fig. 7.1.

7.4 Local Electric Fields and Electron-Phonon Coupling

Since the Madelung energies are locally modified on the eV scale, real space modifications may result in substantial changes to the local crystal fields. Ions vibrating along the c-axis are sensitive to the spatial gradients of the Madelung energies and Devereaux *et al.* [44] have shown that these values of the local field determine the overall strength of el-ph coupling at the oxygen sites. This in turn controls the coupling to Raman active A_{1g} planar and apical vibrations, and out-of-phase planar B_{1g} vibrations. While these couplings themselves are not sufficiently strong to give high T_c's, local changes of el-ph coupling due to eV scale changes in Madelung energies, in principle, can have a strong impact on local bosonic pairing[182, 27, 206, 144], polaron formation, as well as magnetic based pairing *via* modifications of the overall properties of the ZRS. Therefore, the dopant's effect on the crystal field in connection to local changes in el-ph coupling will be examined.

For the undoped crystal, c-axis crystal fields are $E_{apex,plane} = 18.74,\ 1.16\ \mathrm{eV}/\mathring{A}$ for the apical and planar sites, respectively, oriented as indicated in fig. 7.1. For the doped lattice, in fig. 7.3a1 and b1 we plot the local c-axis electric field strength at the planar and apical sites, respectively, and the corresponding el-ph coupling strength $\lambda \propto E^2$ in fig. 7.3a2 and b2 [44]. One can see that the E-field strength is very sensitive to the local symmetry breaking introduced by the dopant, especially in the case of the planar oxygen atoms. The presence of the dopant's bare charge in the otherwise positively charged SrO/BiO structure suppresses the field in the closest lying plane, and the structural changes further modify the local fields. The largest changes to the E-field occur in the plane whose field is oriented towards the dopant. In this case, the geometry is such that the dopant's bare charge increases the strength of the original field, driving λ for the c-axis planar oxygen modes up by a factor of 5. As it is well known that the c-axis phonons give an attractive interaction in the $d_{x^2-y^2}$ channel, this suggests that superconductivity may be locally promoted by the dopant, in agreement with the assessment of ref. [25, 200]. The enhanced el-ph coupling may on the other hand drive a tendency to locally bind a hole to the lattice near the dopant location. This raises the possibility that LDOS modifications could be related to local polarons rather than pairing.

To address this issue, ED was employed for Cu_2O_7 Hubbard clusters coupled to c-axis oxygen vibrations. The Hamiltonian for the cluster is $H = H_{el} + H_{lat} + H_{el-ph}$ where H_{el} is defined in eq. 7.3, and

$$H_{lat} = \sum_{\nu} \Omega_\nu \hat{n}^\nu \qquad\qquad H_{el-ph} = \sum_{\nu,i,\delta,\sigma} g_\nu (b_\nu^\dagger + b_\nu) e_\nu^\delta p_{i,\delta,\sigma}^\dagger p_{i,\delta,\sigma}. \tag{7.4}$$

Here, $\hat{n}^\nu$ is the phonon number operator for branch ν, e_ν^δ is the polarization of the ν-th quantized local displacement, and $g_\nu = eE\sqrt{\hbar/2M_O\Omega_\nu}$ sets the el-ph coupling strength for mode ν. Here coupling to uniform out-of-phase B_{1g} and in-phase A_{1g} c-axis modes ($\Omega = 36$ and 55 meV, respectively) coupled to the oxygen hole density by local field eE is considered. Local modifications to the phonon mode energies compared to the bulk have not been included. All ED calculations were performed for a truncated phonon Hilbert space retaining only 6 quanta for each mode. The calculation has been checked for a larger Hilbert space and the results are unchanged for a greater number of quanta for the parameter range investigated here.

In order to make contact to STM LDOS measurements, the electron addition and removal spectra $A_\pm$, defined as

$$A_\pm(\omega) = \sum_i |\langle \Psi_i^{1,3} | c, c^\dagger | \Psi_{GS}^2 \rangle|^2 \delta(\omega - E_i^{1,3} + E_{gs}^2), \tag{7.5}$$

where Ψ_i^n denotes the n-hole eigenstate with energy E_i^n, are plotted in fig. 7.4a and b for different values of el-ph coupling $g_{B1g} = \sqrt{55/36} g_{A1g}$. As the coupling is increased,

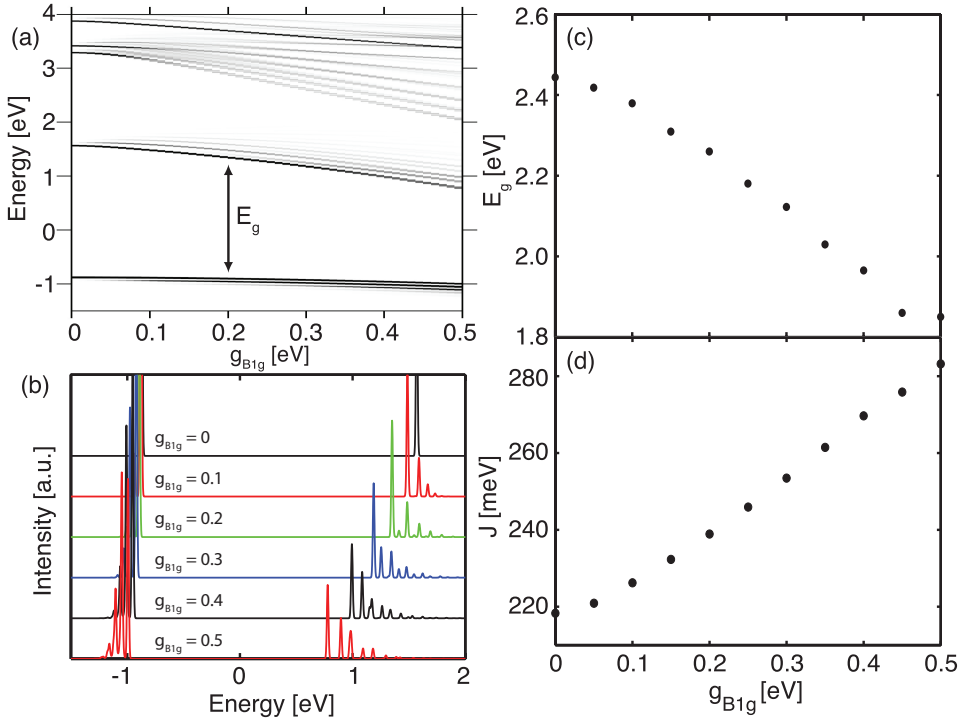

Figure 7.4: (a) The electron addition and removal spectra obtained from Cu_2O_7 clusters coupled to c-axis oxygen vibrations as a function of el-ph coupling strength g_{B1g}. The energy gap E_g is indicated. (b) The electron addition (positive energy) and removal (negative energy) spectra as a function of energy for selected coupling strengths. (c, d) E_g, J as a function of el-ph coupling, respectively.

the spectral weight is gradually transferred into phonon side bands giving broader and suppressed spectral peaks. The corresponding energy gap E_g between the first removal and addition states *decreases* with increasing g_{B1g} (fig. 7.4c) as the effective charge transfer energy is reduced by the gain in lattice energy. As a consequence, the value of J (correspondingly determined from two-hole Cu_2O_7 clusters with phonons) increases substantially with increasing g_{B1g}, as shown in fig. 7.4d. The decrease of E_g and increase of J due to local phonons will overwhelm the countering effects from purely electrostatic considerations as the coupling to the lattice increases.

In order to estimate the size of the effect for Bi-2212, $E_{plane} = 1.16$ eV for the undoped lattice yields $g_{B1g} \sim 0.073$ eV, well into the large polaron regime where side bands are weak. Near the dopant, however, g_{B1g} is enhances to ~ 0.2 eV, where side bands begin to develop spectral weight in the removal/addition spectra and the charge gap is reduced (fig. 7.4a-c). At the same time, for this parameter regime, which is characteristic of multi-

layer cuprates, J is increased by 20 meV. This is much greater than the small reduction determined from electrostatic effects alone. Thus for realistic parameter regimes, c-axis phonons act in concert with strong spatial variations of Madelung energies giving an increase in J as well. The dopant may then provide two coupled channels for d-wave pair enhancement, while causing suppressed spectral features as a consequence of strong local el-ph coupling. This is qualitatively what has been observed in the experiments [24]. Such synergy among phonons, polarons and antiferromagnetism has already been noticed in cluster quantum Monte Carlo studies [207].

7.5 Summary

In this chapter we have examined electrostatic modulations of the local Madelung energies arising from the presence of a dopant Oxygen atom in Bi-2212 unit cells. While eV changes are found for the Madelung energies for copper and oxygen, these changes largely cancel for the charge transfer energy and give a small local suppression to J. However, the strong local variations in Madelung energies are manifest in order-1 changes in el-ph coupling for c-axis oxygen modes. Using cluster studies, it was found that in combination, electrostatic modifications and coupling to the lattice yield broadened spectral features, reduced charge gap energies E_g and caused a sizeable local increase of J, implying a strong local interplay between antiferromagnetism, polarons and superconducting pairing. The amount of variation of the local charge gap can thus serve as an important diagnostic for determining lattice coupling, electrostatic effects and pairing. However, at this time, it is an open question whether a link between these quantities can be made experimentally.

Chapter 8

Determinant Quantum Monte Carlo

The analytical techniques employed in the previous chapters have been successful in accounting for many of the electron-phonon (el-ph) signatures in the optimal and overdoped regions of the phase diagram where the cuprates are more metallic. The natural extension to this is to begin examining the underdoped side of the phase diagram. However, in this region the electron-electron (el-el) interaction becomes important, and in order to proceed one requires a method for handling the el-el interaction non-perturbatively. Furthermore, it is desirable to have a means for treating el-el and el-ph interactions on an equal footing. Monte Carlo methods provide a natural way to do this. In this work the method of choice will be Determinant Quantum Monte Carlo, which allows for treatments of the full many-body problem with strong el-el and el-ph interactions. In this chapter the framework of Determinant Quantum Monte Carlo (DQMC) is laid out and in the following chapter the general results for the DQMC treatment of Hubbard and Hubbard-Holstein models are given.

8.1 The General Methodology

DQMC is an auxiliary-field imaginary-time Monte Carlo method for simulating interacting systems of particles in the grand canonical ensemble [208, 209, 210]. The goal is to calculate the single-particle Green's function at finite temperature

$$G(\tau,\tau')_{ij} = \langle T[c_{i,\sigma}(\tau)c^{\dagger}_{j,\sigma}(\tau)]\rangle, \tag{8.1}$$

by stochastically evaluating the finite temperature expectation value. The Green's function is important since, in general, any single or multi-particle correlation function can expressed in terms of $G(\tau,\tau')$ through the application of Wick's theorem [9].

The thermodynamic expectation value of any observable $\hat{O}$ at finite temperatures is defined as

$$\langle \hat{O} \rangle = \frac{\mathrm{Tr}(\hat{O} e^{-\beta \hat{H}})}{\mathrm{Tr}(e^{-\beta \hat{H}})}. \tag{8.2}$$

In order to outline the method, consider the evaluation of the partition function $Z = \mathrm{Tr} e^{-\beta \hat{H}}$ (the generalization to evaluating the numerator is then straightforward), evaluated for the single-band Hubbard model

$$H = -\sum_{i,j,\sigma} t_{i,j} [c^{\dagger}_{i,\sigma} c_{j,\sigma} + c^{\dagger}_{j,\sigma} c_{i,\sigma}] - \mu \sum_{i,\sigma} \hat{n}_{i,\sigma} + U \sum_{i} \left(\hat{n}_{i,\uparrow} - \frac{1}{2} \right) \left(\hat{n}_{j,\downarrow} - \frac{1}{2} \right). \tag{8.3}$$

Here, $\hat{n}_{i,\sigma} = c^{\dagger}_{i,\sigma} c_{i,\sigma}$ is the usual number operator for site i and spin σ, $t_{i,j}$ is the matrix element for hopping from site i to site j, U is the on-site Coulomb interaction[1] and μ is the chemical potential which is adjusted to maintain the desired filling.

To evaluate the partition function in imaginary time one divides the interval $[0, \beta]$ into L discrete time slices $\Delta\tau = \beta / L$ in length. The partition function can then be written as:

$$Z = Tr[e^{-\beta H}] = \mathrm{Tr}[e^{-\Delta\tau L H}] \sim \mathrm{Tr}[(e^{-\Delta\tau K} e^{-\Delta\tau V})^{L}] \tag{8.4}$$

where K is the solvable non-interacting portion of (8.3) and V contains the remaining interaction term. (In the treatment of the Hubbard-Holstien model V also contains the el-ph interaction terms.) In the last step the Trotter approximation has been used where the fact that K and V do not commute is neglected. This approximation introduces a systematic error on the order of $(\Delta\tau)^2$ to measured quantities and is therefore a controlled approximation [210, 211, 212, 213].

The interaction term, involving four fermion operators, is further reduced to a set of quadratic terms through the introduction of an auxiliary field $s_{i,l} = \pm 1$ at each site and time slice and applying a discrete Hubbard-Stratonovich transform [214]

$$e^{-\Delta\tau U (\hat{n}_{i,\uparrow} - 1/2)(\hat{n}_{i,\downarrow} - 1/2)} = \frac{1}{2} e^{-\Delta\tau U / 4} \sum_{s_{i,l} = \pm 1} e^{-\Delta\tau s_{i,l} \lambda (\hat{n}_{i,\uparrow} - \hat{n}_{i,\downarrow})}. \tag{8.5}$$

where λ is defined by the relation $\cosh(\Delta\tau\lambda) = \exp(\Delta\tau U/2)$. At this stage, all terms involving fermion operators have been made quadratic through the introduction of the auxiliary field. The trace over the fermion degrees of freedom can now be explicitly performed for a given configuration $\{s_{i,l}\}$ [208, 210, 215] (For a formal derivation please refer to Appendix C) leaving

$$Z = \sum_{s_{i,l} = \pm 1} \det(M^{\uparrow}) \det(M^{\downarrow}) \tag{8.6}$$

[1]Here the interaction term has been written such that $\mu = 0$ corresponds to the half-filled case with $< n >= 1$ by absorbing an additional term into the definition of μ.

where

$$M^{\sigma} = I + B_L^{\sigma} B_{L-1}^{\sigma} ... B_1^{\sigma}. \tag{8.7}$$

and I is the identity matrix. The B_l matrices are defined as

$$B_l^{\pm} = e^{\mp \Delta\tau \lambda v(l)} e^{-\Delta\tau K}. \tag{8.8}$$

Here, $v(l)$ denotes a diagonal matrix who's i-th element is the field value $s_{i,l}$. All that remains is to evaluate the sum over field configurations appearing in equation 8.6.

For reasonably large lattice problems the number of possible configurations for the Hubbard-Stratonovich field is prohibitively large. Therefore, one must resort to Monte Carlo methods to evaluate the sum over $\{s_{i,l}\}$. To do this one generates a sequence of spin configurations, distributed with probability $Z^{-1} \mathrm{det} M^{\uparrow} \mathrm{det} M^{\downarrow}$, to be sampled. Generally, the sum over $\{s_{i,l}\}$ is dominated by a subset of configurations. Therefore, if the generated sequence is primarily drawn from this subset then accurate measures of the properties of the system can be obtained. This is accomplished by using an importance sampling algorithm which will be discussed in the following section.

Finally, for an electron propagating through a given field configuration $s_{i,l}$, the equal-time Green's function $G^{\sigma}(l)$ at discrete time $\tau = l\Delta\tau$ is given by [210]

$$G^{\sigma}(l)_{ij} = \langle T[c_{i,\sigma}(\tau) c_{j,\sigma}^{\dagger}(\tau)] \rangle = [I + B_l^{\sigma} ... B_1^{\sigma} B_L^{\sigma} ... B_{l+1}^{\sigma}]_{ij}^{-1}. \tag{8.9}$$

and the determinant M^{σ} is related to the Green's function by

$$\mathrm{det} M^{\sigma} = \mathrm{det} G^{-1}(l) = \mathrm{det}[I + A^{\sigma}(l)] \tag{8.10}$$

where $A^{\sigma}(l)$ is shorthand for the product $B_l^{\sigma} ... B_L^{\sigma} B_1^{\sigma} ... B_{l+1}^{\sigma}$. In general, the largest and smallest eigenvalues of B_l scale as $\exp(\beta E)$ and $\exp(-\beta E)$, where E represents the energy scale of the problem (for the non-interacting limit $E \sim 4t$). Clearly, as the temperature is lowered these eigenvalues become well separated and B_l matrices become stiff. As a result, the product defining $A^{\sigma}(l)$ is numerically unstable as round-off errors become larger than the smaller eigenvalues. In order to evaluate this product a stable matrix product routine must be used which makes use of UDR-decompositions. The details of this procedure can be found in appendix D as well as references [210, 216, 217].

8.1.1 Sampling the Hubbard-Stratonovich Fields

In order to sample the Hubbard-Stratonovich (HS) fields an importance sampling algorithm commonly referred to as the *Metropolis algorithm* is employed. One begins by using Eq. 8.9 to calculate $G(\tau)$ on a particular time slice for some initial (usually random) configuration of $s_{i,l}$. Once $G(\tau)$ has been calculated, a loop through the sites is carried

out and a flip of the field $s_{i,l} \rightarrow s'_{i,l}$ is proposed at each site. The probability of accepting such an update is given by the ratio R of the determinants before and after the change in $s_{i,l}$

$$R = R^{\uparrow} R^{\downarrow} = \frac{\mathrm{det}M^{\uparrow\prime}\mathrm{det}M^{\downarrow\prime}}{\mathrm{det}M^{\uparrow}\mathrm{det}M^{\downarrow}}. \tag{8.11}$$

An efficient algorithm for calculating the ratio can be obtained by noting that for a change $s_{i,l} \rightarrow -s_{i,l}$ the resulting change in the matrix product $A^{\sigma}(l)$ is

$$A^{\sigma}(l) \rightarrow A^{\sigma\prime}(l) = [I + \Delta^{\sigma}(i,l)]A^{\sigma}(l) \tag{8.12}$$

where the matrix $\Delta^{\uparrow,\downarrow}(i,l)_{j,k} = \delta_{j,i}\delta_{k,i}[\exp(\pm 2\Delta\tau s_{i,l}) - 1]$ has a single non-zero element [210]. Therefore, the ratio of the determinants before and after the update is then given by

$$R^{\sigma} = \frac{\mathrm{det}M^{\sigma\prime}}{\mathrm{det}M^{\sigma}} = \frac{\mathrm{det}G^{\sigma}(l)}{\mathrm{det}G^{\sigma\prime}(l)} = 1 + [1 - G^{\sigma}(l)_{ii}]\Delta^{\sigma}(i,l)_i i \tag{8.13}$$

and the ratio for accepting a proposed change $R = R^{\uparrow}R^{\downarrow}$ can be calculated from the Green's function for the current configuration. Therefore, all that is needed at a given step in the Monte Carlo sweeps is the Green's function at the current imaginary time slice.

If the change is accepted then the Green's function is updated accordingly $G(l) \rightarrow G'(l)$. Computing $G^{\sigma}(l)$ by evaluating equation 8.9 is costly since it involves multiplying a sequence of L $N \times N$ matrices, which scales as LN^3, where N is the total number of sites in the lattice. One can gain a significant performance increase by using a "Sherman-Morrison" updating scheme which exploits the fact that only a single row and column of $G^{\sigma}(l)$ are affected by a single flip of $s_{i,l}$. The updated Green's function can then be computed by from the current Green's function [210, 216, 217]

$$G^{\sigma\prime}(l) = G^{\sigma}(l) - \frac{G^{\sigma}(l)\Delta^{\sigma}(i,l)[I - G^{\sigma}(l)]}{1 + [1 - G^{\sigma}_{ii}(l)\Delta^{\sigma}_{ii}(i,l)} \tag{8.14}$$

and since $\Delta^{\sigma}(i,l)$ has a single non-zero element no matrix multiplications are needed to perform the update. The cost of updating in this manner is reduced to N^2 operations.

Finally, once changes have been proposed for each site on a given time slice, and the appropriate updates have been made, $G^{\sigma}(l)$ is advanced to the next time slice and the process is repeated. The advancement to the next time slice is done by a simple left and right matrix multiplication

$$G^{\sigma}(l+1) = B^{\sigma}_{l+1} G^{\sigma}(l) (B^{\sigma}_{l+1})^{-1}. \tag{8.15}$$

This process is repeated several thousand times and the quantities of interest are "measured" periodically by calculating their current value at a given Monte Carlo step. These measurements are then averaged together to produce a final estimate for the quantities of interest.

8.1.2 Unequal Time Green's Function

At any given step in a sequence of field configurations (generally referred to as a Markov chain) one has the equal-time Green's function on a given time slice. However, in order to measure dynamic quantities, one needs to measure the full time-dependent Green's function $G(\tau, \tau') = G(\tau - \tau')$. This can be constructed from the inverse of the $NL \times NL$ matrix [208]

$$O = \begin{bmatrix} I & 0 & 0 & ... & 0 & B_1 \\ -B_2 & I & 0 & ... & 0 & 0 \\ 0 & -B_3 & I & ... & 0 & 0 \\ . & . & . & . & . & . \\ . & . & . & . & . & . \\ . & . & . & . & . & . \\ 0 & 0 & 0 & ... & -B_L & I \end{bmatrix} \tag{8.16}$$

where the B_l matrices are defined as before and I is the identity matrix. The full time-dependent Green's function is then given by the inverse of O

$$G(\tau, \tau') = e^{\Delta\tau K/2} O^{-1} e^{-\Delta\tau K/2}. \tag{8.17}$$

The $N \times N$ Green's function $G(\tau)$ at time $\tau = (i - j)\Delta\tau$ is then given by the (i,j) block of the larger $NL \times NL$ matrix. Evaluating the inverse of O scales as $(NL)^3$ and is therefore computationally intensive for large clusters and low temperatures, even if efficient numerical routines are used. A significant improvement can be made by exploiting the fact that the matrix O is a sparse block matrix. By requiring that $OO^{-1} = I$ one then obtains

$$\begin{aligned} G_{ii} &= [I + B_{i-1} \dots B_1 B_L \dots B_i]^{-1} \\ G_{ij} &= G_{jj}[B_{i-1} \dots B_j] \qquad (i > j) \\ G_{ij} &= -G_{jj}[B_{i-1} \dots B_1 B_L \dots B_j] \qquad (i < j). \end{aligned} \tag{8.18}$$

The first expression is simply the equal time Green's function and the remaining two are the $\tau - \tau' > 0$ and $\tau - \tau' < 0$ unequal time Green's functions. Evaluating G_{ii} requires order N^2 operations to compute while the unequal time Green's functions G_{ij} requires $2N^2$ operations.

8.2 The Fermion Sign Problem

In general, the factor $\det(M^\uparrow)\det(M^\downarrow)$ is not positive definite, and therefore the sampling procedure just outlined occurs over an unrenormalized probability distribution which

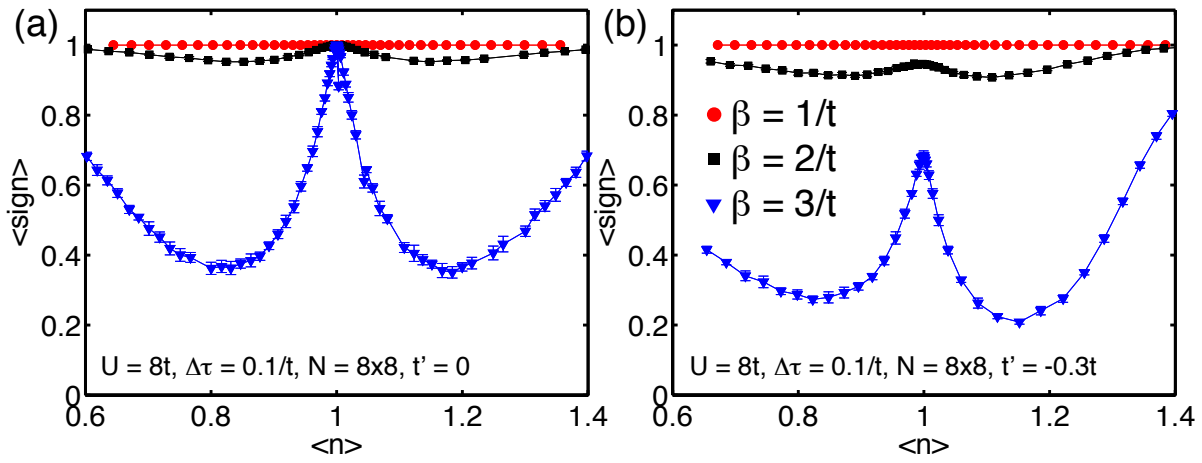

Figure 8.1: Plots of the average fermion sign as a function of filling on an 8×8 Hubbard model cluster with $U = 8t$ with (a) $t' = 0$ and $t' = -0.3t$.

is not positive definite. To overcome this problem the absolute value of the product $|\det(M^{\uparrow})\det(M^{\downarrow})|$ is used and the expectation value of an observable must be augmented

$$\langle O \rangle = \frac{\langle O P_s \rangle}{\langle P_s \rangle} \tag{8.19}$$

where P_s denotes the sign of the product $\det(M^{\uparrow})\det(M^{\downarrow})$ and $\langle\rangle$ denotes the same averaging procedure outlined above.

The physical origin for the sign problem is Fermi statistics. The DQMC formalism calculates expectation values in the grand canonical ensemble and at any point in the simulation the method has no information regarding the many-body wavefunction. Formally, the electron configuration at a given step in the simulation is determined by the current HS-field configuration and characterized by a set of creation operators $\{c^{\dagger}_{i,\sigma}\}$. However, the simulation does not have knowledge of the order in which the $c^{\dagger}_{i,\sigma}$ were applied to the vacuum state in order to produce the various sampled states. Therefore there can be an overall -1 phase factor associated with interchanges of the fermion operators. If the wavefunction were known, such as in the case of exact diagonalization, then the fermion operators are normal-ordered and the phase factor is explicitly taken into account. However, since DQMC does not calculate wavefunctions explicitly, the phase factor remains unknown. This affects the calculation of expectation values and is reflected in the negative values of the product $\det(M^{\uparrow})\det(M^{\downarrow})$.

At low temperatures, the quantum statistics of the problem become increasingly important and the average sign of the product $< P_s >$ tends towards zero. This places a severe limitation on the range of parameters accessible to the simulation, especially with

respect to the temperatures that can be reached. Furthermore, the average sign depends on a number of factors including the size of the system, the overall filling, the strength of the interaction U, and inverse temperature β. In figure 8.1 the average sign is plotted as a function of filling for $U = 8t$ and $\beta = 1/t$, $2/t$ and $3/t$. The remainder of the parameters used in the simulation are listed in the figure. Figure 8.1a plots the average sign without next nearest neighbour hopping t', and 8.1b is for the case of $t' = -0.3t$. At half-filling, when $t' = 0$, the sign is identically 1 due to particle-hole symmetry which ensures that the product of determinants is positive [210]. When t' is non-zero this symmetry is removed and a fermion sign develops even at half-filling. As the system is doped away from half-filling the sign problem becomes more severe and the average sign takes its lowest values around fillings of 0.8 and 1.2.

8.3 The Hubbard-Holstein Model

The goal in the next chapter is to study el-ph coupling in the presence of strong el-el interactions. To this end, the Hubbard-Holstein (HH) model is examined, which is the simplest model which includes both of these interactions. In the HH model phonons are included as independent harmonic oscillators, characterized by a frequency Ω, on each site. The el-ph interaction is included as a local coupling similar to the coupling mechanism discussed in chapter 3 for the c-axis modes. The Hamiltonian is given by $H = H_{\text{hub}} + H_{\text{lat}} + H_{\text{el-ph}}$ where H_{hub} is the Hubbard Hamiltonian defined by equation 8.3,

$$H_{\text{lat}} = \sum_i \frac{1}{2} M\Omega^2 \hat{X}_{i,l}^2 + \frac{1}{2M}\hat{P}_{i,l}^2 \tag{8.20}$$

and

$$H_{\text{el-ph}} = \sum_{i,\sigma} g_0 \hat{n}_{i,\sigma} \hat{X}_{i,\sigma}. \tag{8.21}$$

Here, $\hat{X}_{i,l}$, $\hat{P}_{i,l}$ are the position and momentum operators for the oscillator at site i, and g_0 characterizes the strength of the el-ph interaction. In order to handle the lattice degrees of freedom the operator $\hat{X}_{i,l}$ is replaced with a continuous variable $X_{i,l}$ and the momentum operator $\hat{P}_{i,l}$ is replaced with a discrete forward difference on the imaginary time grid

$$P_{i,l} = \frac{X_{i,l+1} - X_{i,l}}{\Delta\tau}. \tag{8.22}$$

The interaction terms are handled as they were for the Hubbard model but with a simple modification to the matrices B_l

$$B_l^{\pm} = e^{\mp\Delta\tau\lambda v(l) - \Delta\tau g X(l)} e^{-\Delta\tau K}. \tag{8.23}$$

Here, $X(l)$ is shorthand for the diagonal matrix whose ith diagonal element is the value of the lattice displacement $X_{i,l}$.

It is useful to define a dimensionless el-ph coupling strength λ which is the ratio of the lattice deformation energy $E_p = g_0^2/(2M\Omega^2)$ to half of the electronic bandwidth $W/2 = 4t$: $\lambda = g_0^2/M\Omega^2 W$. As previously discussed, $\lambda = 1$ divides the boundary between the weak and strong coupling limit and, for $\lambda > 1$, a crossover to a polaron system is expected to occur. This crossover is typically marked by a sudden drop in the quasiparticle weight Z at the Fermi level, as the local lattice distortions tend to bind the electron and increase its overall effective mass m^*.

The lattice degrees of freedom also contribute to Hamiltonian and therefore the probability of accepting any update must also be augmented with the change in the energy associated with the change in the phonon field. The new ratio for accepting an update to the fields $s_{i,l}$ and $X_{i,l}$ must be amended to be $R = R^{\uparrow}R^{\downarrow}\exp(g_0\Delta\tau\Delta E)$ where R^{α} is the usual ratio of the determinants and ΔE is the total change in kinetic and potential energy of the phonon fields associated with the update.

8.4 Phonon Field Updates

8.4.1 Single Site Updates

In addition to the HS fields, the phonon displacement fields $X_{i,l}$ must now also be sampled. There are a number of ways of doing this, and in general a minimum of two classes of updating schemes are required to ensure that the phonon fields satisfy Bose statistics at low temperature. The first class of updates are single-site updates where the displacement field is sampled by proposing changes to the displacement field $X_{i,l} \rightarrow X_{i,l} + \Delta x$ on a site by site basis. In this case, Δx is drawn from a uniform probability distribution centered at zero while the width of the distribution is adjusted during runtime in order to maintain a desired acceptance rate for the phonon fields. For single site updates the Sherman-Morrison updating scheme can still be used for fast updates of the equal-time Green's function.

8.4.2 Block Updates

The second class of updates required are block updates, where an entire set of displacements along a block of imaginary times slices are updated simultaneously. For the calculations presented in the next chapter, a uniform block update is implemented where a lattice site is selected at random and the displacement for that site is shifted by a uniform

amount for all time slices. As with the single site updates, the size of the uniform shift is drawn from a uniform distribution centered at zero and the width of this distribution is adjusted at run time in order to maintain a specified block update acceptance rate. In principle, the length of the block in imaginary time can be variable; however, tests conducted here indicate that updating all $\tau \in [0, \beta]$ is sufficient to recover the Bose statistics. The main drawback of the block updating scheme is that the Sherman-Morrison updating scheme cannot be used and the full Green's function must be recomputed from scratch.

Block updates are required due to a slowing of the rate of acceptance of single-site updates at low temperature. For large values of β the total expectation value of the phonon momentum is small and the DQMC algorithm will tend to reject large changes of a single $X_{i,l}$ since they will produce large changes in momentum. As a result, phonon configurations can be frozen in and a large number of small phonon updates are required in order to move such a configuration to another statistically independent configuration. The introduction of the block updates allows for large changes in $X_{i,l}$ for a whole set of sites while maintaining a fixed or small change in kinetic energy. Therefore, the algorithm can efficiently escape from frozen configurations and a proper sampling of the phonon fields can occur.

8.5 Measurements

Estimates for the statistical error in measured quantities are obtained through a straightforward binning procedure. The N_{sweep} measurement sweeps are divided into N_{Bin} intervals and each bin is assigned a measurement value obtained from averaging the individual measurements performed over that interval. After N_{sweep} measurements are performed, N_{bin} measurements are obtained for each quantity of interest. The binned measurements are then treated as statistically independent measurements and a sample mean

$$\bar{x} = \frac{1}{N} \sum_{i=1}^{N_{bin}} x_i \tag{8.24}$$

is taken as the final measurement value while the error estimate is given by the sample variance

$$\sigma_x^2 = \frac{1}{N-1} \sum_{i=1}^{N_{bin}} (x_i - \bar{x})^2. \tag{8.25}$$

Throughout this work, all error values quoted are $1\sigma_x$ for an overall confidence interval of 67.3%. The definitions of individual quantities of interest will be given in the following chapter as the results are discussed.

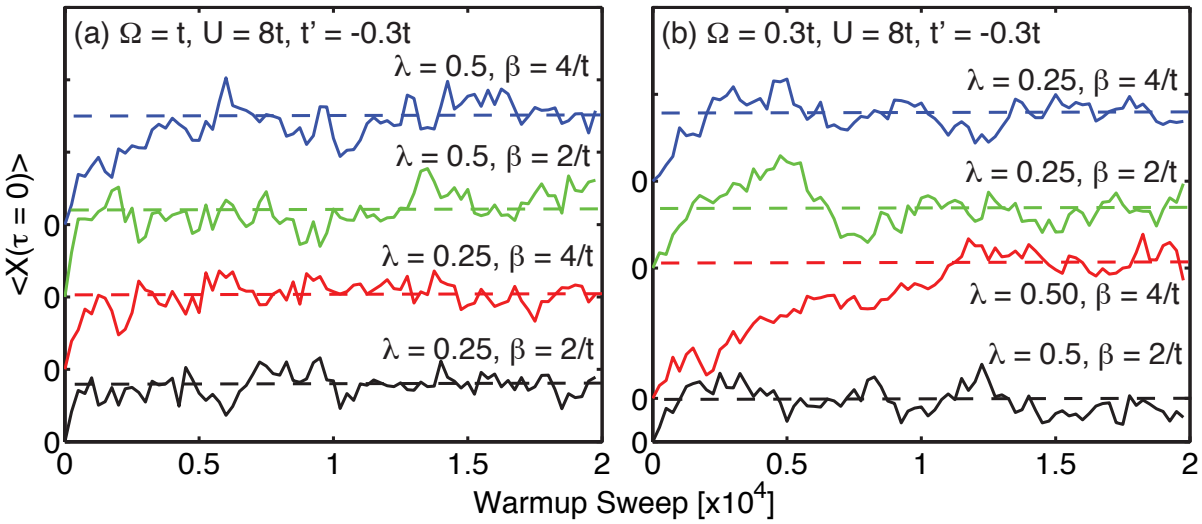

Figure 8.2: Average lattice displacement at $\tau = 0$ for an 8×8 lattice as a function of the warm-up sweep number.

8.5.1 Autocorrelation and Equilibration Times

The autocorrelation and equilibration times are two important quantities in Monte Carlo simulations. For the Hubbard-Holstein model, especially at low temperatures, the phonon fields are the bottleneck in terms of autocorrelations and warmup due to the lower rate of acceptance of phonon updates [218]. Therefore, the equilibration and autocorrelation times for the phonon field at $\tau = 0$ are considered here.

8.5.2 Equilibration Time

The equilibration time is defined as the number of warmup sweeps one must perform before the system reaches thermal equilibrium and measurements can begin. If measurements begin prior to this time then the Markov chain will be biased by the initial field configuration and the measured quantities will not be accurate. In figure 8.2 the average value of the phonon displacement field $\langle X_i(\tau = 0)\rangle$, averaged over all sites in an 8×8 lattice, is plotted for the cases of a high ($\Omega = t$) and low ($\Omega = 0.3t$) frequency phonon as a function of warmup sweep number. In all cases the phonon field was initialized to zero and, as the warmup sweeps accumulate, the average phonon displacement rises until reaching the equilibrium position indicated by the dashed lines. The longest warmup times occur for the low-temperature cases with larger el-ph coupling constants. This is due to the lower acceptance rates for phonon updates at low temperature and the increased offset in the lattice equilibrium position with larger coupling. However, in all

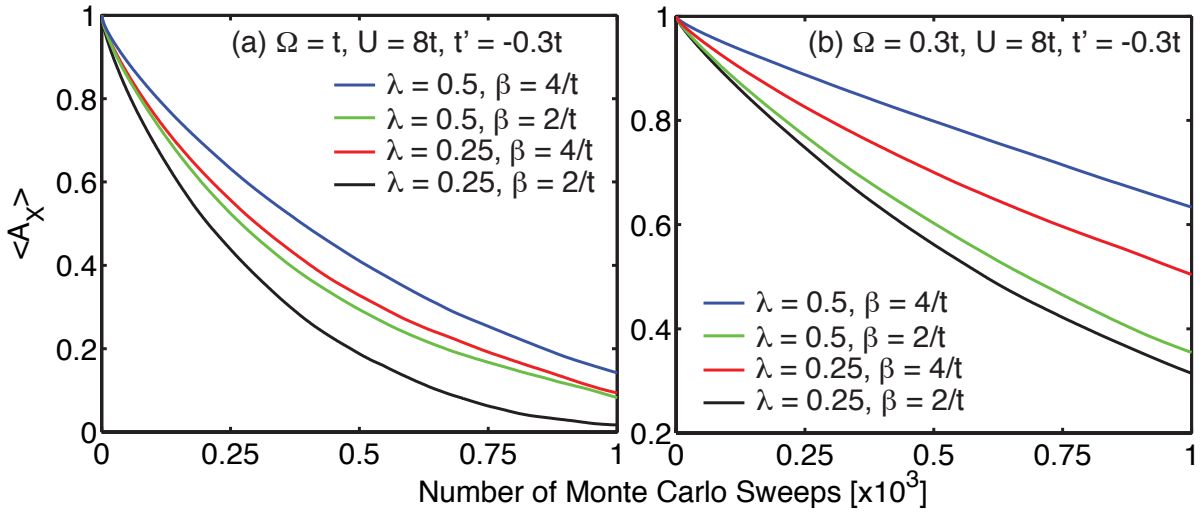

Figure 8.3: Sample autocorrelation functions for the phonon displacement field for the same parameter set shown in figure 8.2. In all cases $\Delta\tau = 0.1/t$.

cases equilibrium is reached in approximately 1×10^4 sweeps (or less). In the remainder of this work the number of warmup sweeps is set to 2×10^4 to 5×10^4 in order to ensure a properly equilibrated field configuration prior to measurement sweeps.

8.5.3 Autocorrelation Time

The autocorrelation time is a measure of the amount of time one must wait between measurements in order to ensure that the measurements are drawn from statistically independent field configurations. The autocorrelation time can be estimated by examining the autocorrelation function for various quantities. The autocorrelation function A_l for a quantity X_i is defined as [216]

$$A_l = \frac{\langle X_{n+l} X_n \rangle - \langle X_n \rangle^2}{\langle X_n^2 \rangle - \langle X_n \rangle^2} \tag{8.26}$$

where the subscripts l denotes the Monte Carlo sweep number and $\langle X_n X_{n+l} \rangle = \frac{1}{M} \sum_{n=1}^{M} X_n X_{l+n}$.

The autocorrelation function is plotted in figure 8.3 for the same parameter sets used in figure 8.2. In general, the autocorrelation time scales as $\propto 1/(\Delta\tau\Omega)$ [218]. This is apparent in fig. 8.3, as the autocorrelation times for the $\Omega = 0.3t$ case are substantially longer that the $\Omega = t$ case.

The autocorrelation time also increases with the strength of the el-ph coupling. For large values of λ at low temperature, the autocorrelation time becomes prohibitively long

and using a single Markov chain becomes impractical. There are a number of methods for decreasing the autocorrelation time such as parallel tempering [216], running multiple Markov chains in parallel while defining fewer bins per chain, or by performing a principle coordinate transform such as that recently proposed by Hohenadler *et al.* [218]. However, the principle coordinate transform comes at a price of introducing a momentum field and complex hopping terms to the Hamiltonian, which removes the ability to perform the Sherman-Morrison updates. This is not an issue for the Holstein model since the loss of performance would be recovered by the reduction in autocorrelation time. However, in treating the Hubbard-Holstein model, no such compensation occurs for sampling the HS fields. In the case of parallel tempering multiple Markov chains at different temperatures are run in parallel. Periodically, the field configurations are switched between the chains allowing for a frozen phonon configuration to "unfreeze" at the higher simulation temperatures. However, in the DQMC simulations, the current value of the Green's function $G^{\sigma}(l)$ is defined for a given instance of the fields. Therefore, after the field configurations are swapped, additional warmup sweeps must be made in order to equilibrate the swapped fields to the temperature of new chain. Therefore, in order to maintain the ability to perform the fast Sherman-Morrision updates, and to avoid the costs associated with parallel tempering, the method of parallel markov chains is used in this work to overcome long autocorrelation times.

8.6 Analytic Continuation: The Method of Maximum Entropy

Since DQMC is an imaginary time formalism it provides information about the imaginary time Green's function. However, one is often interested in dynamical properties of the system and in order to calculate them, the imaginary time Green's function to be Wick rotated to the real frequency axis. Formally, the Wick rotation is performed by analytically continuing the Matsubara Green's function $G(i\omega_n)$ to the real axis $G(\omega)$ by setting $i\omega_n \rightarrow \omega + i\delta$, where δ is an infinitesimal positive real number. However, since the DQMC method does not produce an analytical form for G this procedure must be performed numerically.

In general, one is interested in calculating the single-particle spectral function $A(\omega) = \mathrm{Im}G(\omega)$ which is related to $G(\tau)$ by the integral equation

$$G(\tau) = \int d\omega \frac{A(\omega)e^{-\tau\omega}}{1 \pm e^{-\beta\omega}} \tag{8.27}$$

with the +ve (-ve) sign for fermion (boson) problems. Obtaining $A(\omega)$ from inverting equation 8.27 is known to be an ill-posed problem, especially when $G(\tau)$ contains noise

and is only known up to some statistical error. This is due to the fact that the kernel $\exp(-\tau\omega)/[1 \pm \exp(-\beta\omega)]$ is small for $|\omega| \to \infty$ and $A(\omega)$ is therefore very sensitive to small changes in $G(\tau)$. However, the opposite problem of generating $G(\tau)$ given $A(\omega)$ is well defined and a number of numerical procedures exploit this fact to determine $A(\omega)$ for a given $G(\tau)$. One such method is the Method of Maximum Entropy (MaxEnt) [219], which is the method that will be used in this work to perform the analytic continuation of the Green's function produced in the DQMC simulations.

From the DQMC simulation it is assumed that k independent measurements of the Green's function at time τ_i have been obtained which are denoted as $G_i^{(j)}$. For a sufficiently large number of measurements, $G_i^{(j)}$ are normally distributed with a sample mean of $\bar{G}_i$. For a given trial $A(\omega)$ a proposed G_i is then obtained from equation 8.27. The $A(\omega)$ which is best represented by the data is the one which maximizes the probability that the data set $\bar{G}_i$ would be drawn from the (unknown) parent population. This probability depends on $A(\omega)$ and is denoted by the conditional probability $\Pr[G|A]$. Using Bayesian inference and the principle of maximum likelihood this probability can be shown to be proportional to e^{-Q} [219], where

$$Q = \alpha S - \frac{1}{2}\chi^2 \tag{8.28}$$

and S is a Shannon Entropy

$$S = \int_{-\infty}^{\infty} d\omega A(\omega) - M(\omega) - A(\omega) \log\left[\frac{A(\omega)}{M(\omega)}\right], \tag{8.29}$$

and $M(\omega)$ is a default model. The default model incorporates information about the solution $A(\omega)$ which is known from physical arguments. This includes properties such as the fact that $A(\omega) \geq 0$ for fermions or $A(\omega) \to 0$ as $|\omega| \to 0$. The parameter α controls how closely the solution should conform to the default model. In equation 8.29 the χ^2 metric is defined as

$$\chi^2 = \sum_{ij} (\bar{G}_i - G_i)[C^{-1}]_{ij}(\bar{G}_j - G_j) \tag{8.30}$$

with covariance matrix

$$C_{ij} = \frac{1}{M(M-1)} \sum_{k=1}^{M} (\bar{G}_i - G_i^k)(\bar{G}_j - G^{(k)_j}). \tag{8.31}$$

Note that the above expressions for χ^2 and the covariance matrix depend on the fact that the data $\bar{G}_i$ is normally distributed. This can be assured by appealing to the Central Limit Theorem and generating a large number of measurements $G_i^{(j)}$. The quality of the data set can be estimated by testing the statistical moments of the measurements to ensure that they conform to the expectation of normally distributed data.

To find the optimal $A(\omega)$, which minimizes Q, a stochastic optimization procedure is applied. $A(\omega)$ is defined on a discrete grid ω_i and changes to $A_i = A(\omega_i)$ are proposed until Q is minimized. In general, the solution should be insensitive to the choice in default model and one method for verifying the solution is to check that it holds for different choices for the default model or α.

8.7 Summary

In this chapter the details of the Determinant Quantum Monte Carlo method have been laid out for both the Hubbard and Hubbard-Holstein models. The advantage of this method is that one can treat both models in their strong coupling limits and, in the case of the Hubbard-Holstein model, both the el-ph and el-el interactions can be treated on equal footing. DQMC also has the advantage of treating the full many-body problem, which contrasts with methods like diagrammatic quantum Monte Carlo. In the next chapter DQMC will be applied to the Hubbard and Hubbard-Holstein models in the vicinity of half-filling, where the analytical treatments of the previous chapters break down. In doing so, one hopes to gain insight into the role of el-ph coupling in the underdoped region of the cuprate phase diagram where strong el-ph coupling may lead to interesting physics.

Chapter 9

DQMC Results for the Hubbard and Hubbard-Holstein Models

The treatment of the electron-phonon (el-ph) interaction up to this point (with the exception of the small cluster calculations discussed in chapter 7) has neglected the role of electronic correlations. The details of the el-ph interaction in the presence of strong electron-electron (el-el) interactions is a topic of great interest, not only in the context of the cuprates but also in the colossal magnetoresistive manganites [220, 221] and the fullerenes [222, 223]. In this chapter the results for the DQMC treatment of the single-band Hubbard and Hubbard-Holstein models will be presented. In the case of the Hubbard model, attention will be focused on the spectral function in order to determine the role of correlations in forming the high-energy anomaly discussed in chapter 2. In the case of the Hubbard-Holstein model a number of quantities will be examined in order to study the el-ph interaction in the presence of strong correlations.

9.1 Electron-Phonon Coupling in Strongly Correlated Systems

A great deal of effort has been expended on understanding el-ph coupling in strongly correlated systems. Before turning to the results of the two models it is therefore useful to review some of the salient results arising from these efforts. Much theoretical work has focused models which incorporate the el-ph interaction into t-J [45, 224, 225, 226, 227, 228, 229, 230, 231, 232, 233, 234, 235, 236, 237, 238, 239] and single-band Hubbard [240, 241, 242, 243, 244, 245, 207, 246, 47, 247, 248, 249, 250, 251] Hamiltonians, although some work has also been done on multi-band models [160, 252, 253, 254, 255, 256, 257, 258]. Analytical solutions to the Hubbard model are lacking and the addition of the el-ph

interaction further complicates the problem. Progress in this area has also been somewhat hindered by the fact that the energy scales of the two interactions are quite different. Furthermore, it is desirable to treat both interactions equally in order to address any interplay that may occur between them. For these reasons, much of the work has focused on numerical treatments of these models and a wide range of results has been obtained depending on the methodology used.

There are two effects expected on general grounds for el-ph coupling in strongly correlated systems [259]. The first is the attractive interaction between electrons mediated by the el-ph interaction which is expected to counteract the strength of the repulsive Coulomb interaction. For a Holstein phonon in a single-band model, the el-ph coupling term is given by equation 8.21,

$$H_{el-ph} = g_0 \sum_{i,\sigma} \hat{n}_{i,\sigma} \hat{X}_i = g \sum_{i,\sigma} \hat{n}_{i,\sigma} (b_i^\dagger + b_i) \tag{9.1}$$

where $g = g_0\sqrt{\hbar/2M\Omega}$, Ω is the phonon frequency, M is the ion mass, g_0 is the el-ph coupling strength and b_i ($b_i^\dagger$) creates (annihilates) a phonon quanta at site i. This interaction can be transformed into a negative-U Hubbard interaction with a dynamical (retarded) attractive interaction between electrons of different spins $U = -\frac{2g^2\Omega}{\Omega^2-\omega^2}$ [9, 244]. As a result, one might expect the low-energy physics of the Hubbard-Holstein model to map onto an effective Hubbard model with a dynamical U_{eff} defined as

$$U_{\text{eff}} = U - \frac{2g^2\Omega}{\Omega^2 - \omega^2}. \tag{9.2}$$

In the antiadiabatic limit $\Omega \to \infty$ this reduces to a frequency-independent effective Hubbard model with $U_{\text{eff}} = U - 2g^2/\Omega - \lambda W$, where $W = 8t$ is the total bandwidth of the non-interacting system and $\lambda = g^2/4t\Omega$ is the dimensionless el-ph coupling strength. Therefore, in the limit of large phonon frequencies it is expected that the el-ph interaction will simply act to reduce the effects of the on-site Coulomb interaction.

The second effect expected from the el-ph interaction is the additional dressing of carriers by phonon scattering processes, thus reducing the total quasiparticle weight Z. In the limit of large el-ph coupling this can lead to polaron formation as the effective mass of the carriers becomes large due to the presence of the local lattice distortions dressing the carriers. However, in a correlated system these carriers are already dressed by correlation effects. Therefore, there are two competing effects: one which reduces carrier mobility via el-ph scattering and one which increases it through an effective reduction in the Coulomb interaction. The resulting behaviour is difficult to predict on intuitive grounds and in many cases it will depend on the values of parameters such as the phonon frequency Ω, Coulomb repulsion U, hopping parameters t, the el-ph coupling g, or alternatively λ [244, 259].

A full solution to the two-site Hubbard-Holstein model [258] has been obtained by treating the phonon degrees of freedom within the momentum average approximation [260, 261]. For the half-filled case it was observed that for small λ the ground state consists of the two-site singlet with phonons tied to the electrons on each site. For large λ a crossover to a bipolaron state occurs where one site is doubly occupied with an associated large number of phonon quanta. The value of λ at which this crossover occurred was set by a balance between the energy cost of the double occupation and the energy gain associated with coupling to the lattice and the kinetic energy gain from virtual hopping to the other site. As a consequence of this, larger values of the Coulomb repulsion produced crossovers between the two ground states at higher values of λ.

Work carried out on the t-J-Holstein model has focused on a single hole doped in the antiferromagnetic background. Mishchenko and Nagaosa [229] have examined the spectral properties of the hole in the intermediate to strong el-ph coupling regime using Diagrammatic Monte Carlo (DMC) for the el-ph interaction while treating the magnetic excitations within the standard spin-wave approximation [262]. Above a critical el-ph coupling λ_c this model exhibited small polaron formation with a spectral function displaying a vanishing weight in the quasiparticle peak and a broad Frank-Conden shake-off band at higher binding energy which inherited the dispersion of the hole in the t-J model without phonons. These spectral features were found to be in good agreement with recent ARPES measurements on the parent compound $Ca_2CuO_2Cl_2$ [51, 263]. This study also observed that the value of λ_c was significantly reduced from the value obtained form the pure Holstein model with the same value of nearest-neighbour hopping t. This was attributed to the additional dressing provided by the magnetic excitations, which reduced the mobility of the carriers thus making them easier to localize once the coupling to the lattice is included. Similar results have been obtained using the spin-wave approximation in conjunction with the a variant of the momentum average approximation for the phonon degrees of freedom [226], and in exact diagonalization (ED) treatments with a reduced Hilbert space [225]. This work has also been extended to the extended range t-t'-t''-Holstein model as well as models with non-local el-ph couplings using Lanczos ED and the coherent state basis approach [227]. In general the results are similar to the t-J approaches however, the extended range hopping produces stronger polaronic behaviour in the antinodal region while the non-local el-ph interaction produces an enhanced suppression of Z for $\lambda < \lambda_c$ and a reduced suppression for $\lambda > \lambda_c$. Finally, ED studies of the t-J which include the in-plane full- and half-breathing modes [238] have demonstrated that the t-J model is capable of capturing the anomalous softening [96] of these modes. This calculation provides an alternative proposal to the charge-fluctation models touched upon in chapter 6 [190, 191, 192, 193].

Within dynamical mean field theory (DMFT) the effects of el-ph interactions have produced mixed results, depending on the underlying phase assumed for the calculation. Single-site paramagnetic DMFT (P-DMFT) calculations for the half-filled single-band

Hubbard-Holstein model, carried out by Sangiovanni *et al.* [244], predicted that the the el-ph interaction is strongly suppressed by the Coulomb interaction. It was also demonstrated that the low-energy spectral properties of the Hubbard-Holstein model could be accurately reproduced by the Hubbard model with an effective U. However, discrepancies between the two models were observed in the spectral functions at higher energies. It was therefore concluded that the primary effect of the el-ph interaction was to renormalize U but with additional important effects due to retardation at higher energy. Later DMFT work by the same group [245] considered an antiferromagnetic (AF-DMFT) solution to the single-band Hubbard-Holstein model. In this case the el-ph interaction suppressed much less as a function of U in comparison to the P-DMFT results but the value of λ_c for the polaron crossover was found to *increase* from its value in $U = 0$ limit. With progressive doping away from half-filling, λ_c was observed to further increase. This indicates that, although λ_c in correlated systems is larger than its value in the non-correlated system in DMFT, AFM does play a role in reducing λ_c. Barone *el al.* have also examined the single-band Hubbard-Holstein model, performing a variational Lang-Firsov transformation for the lattice degrees of freedom and treating the resulting Hamiltonian with the Kotliar-Ruckenstein slave-boson technique [240]. Within this approach the Coulomb repulsion was reduced by the el-ph interaction, in agreement with the DMFT results [244].

A third DMFT study was conducted by Werner *et al.* who took yet another approach to the single-band Hubbard-Holstein model by applying a Lang-Firsov transformation to the phonon coordinates [242]. For small λ the half-filled case was found to be a Mott insulator which gave way to a metallic state once the system was doped away from half-filling. However, for large λ the system underwent a phase transition to a bipolaronic insulating phase for all values of doping. These results are in contradiction to reference [247], which found that the el-ph interaction stabilized the AFM phase against doping. The difference between the two was attributed to the fact that reference [247] coupled the phonons to the total density $\hat{n}$ while reference [242] coupled to $\hat{n} - 1$. This choice results in different chemical potential renormalizations which may change the filling of the system. Results similar to reference [242] have been obtained at half-filling using numerical renormalization group approaches [264, 265].

There are also indications that correlations may induce a momentum-dependent renormalization to local Holstein couplings. For finite values of Ω, away from the antiadiabatic limit, there are indications that the retarded nature of the el-ph interaction remains important and a non-trivial renormalization of the el-ph vertex occurs. For example, Huang *et al.* extracted the renormalized el-ph vertex from Quantum Monte Carlo data obtained for the single-band Hubbard model and found a suppression of the el-ph vertex for small U and a strong enhancement of the forward scattering peak, with no substantial suppression of the total el-ph vertex at large U [47]. As already noted, such an enhancement of the vertex at small $\mathbf{q}$ is beneficial to d-wave pairing. As such, strong correlations may

renormalize the el-ph vertex in favour of d-wave pairing in a manner similar to the effects of poor screening. Slave-boson approaches on the t-J model have produced a similar d-wave enhancement of the el-ph vertex [45, 232, 233]. In contrast to this, slave-boson studies of the single-band Hubbard model with phonons has found no such enhancement of forward scattering and an overall suppression in the el-ph vertex for all $\mathbf{q}$ at low temperature [243]. However, this approach does produce an enhancement of the el-ph vertex at small $\mathbf{q}$ at high temperature ($\beta \sim t$-$2t$) and this behaviour was attributed to a tendency towards phase separation. Cumulant expansion techniques on the same model have also observed an enhancement of the el-ph vertex with accompanying evidence for phase separation [241].

Using the dynamical cluster approximation (DCA), an extension of DMFT, examinations of the el-ph interaction within small Hubbard clusters [207, 246] find an overall suppression of the d-wave superconducting T_c with increasing el-ph coupling. This occurs despite an increase in the apparent pairing correlations in the $d_{x^2-y^2}$ channel. The reduction in T_c was attributed to polaron formation, which reduces quasi-particle weight at the Fermi level, suppressing T_c through the loss of carrier mobility. The enhancement of pairing correlations reported in references [207, 246] indicates that bare el-ph vertex has been renormalized in favour of d-wave pairing, consistent with the observations of reference [47]. Furthermore, exact diagonalization (ED) studies on the t-J model, which include coupling to buckling and breathing vibrations, show that the former enhance d-wave pairing while the latter suppress it [234].

A number of the correlated el-ph models have also been applied to understanding the optical conductivity $\sigma(\omega)$ of a hole doped into the AFM background [266, 267, 268, 231, 228]. DMC approaches show that both the t-J model and Holstein models predict sharp peaks in $\sigma(\omega)$ at energies below the midinfrared peak observed experimentally [231] and these predicted peaks have no corresponding feature in the data. The t-J-Holstein model is able to reproduce the qualitative features of the data in the strong el-ph coupling regime and it was concluded that both the magnon and polaron physics are essential for understanding $\sigma(\omega)$ in the underdoped cuprates. Similar conclusions have been reached in ED studies on the breathing phonon in the t-J model [228].

From the variety of results it is clear that there is no definitive interpretation of the effect of el-ph coupling in strongly correlated systems. It is therefore advantageous to bring as many methods as possible to bear on the problem in order to gain further insight.

9.2 Spectral Properties of the Hubbard Model

Before discussing the results for the Hubbard-Holstein model a brief examination of the single-band Hubbard model will be presented in order to obtain a point of comparison

for the calculations with finite λ. Here, focus placed on the spectral properties of the Hubbard model with the aim of addressing the role of strong correlations in the formation of the high-energy anomaly (HEA) discussed in chapter 2. It will be demonstrated that the HEA is the result of the strong el-el interactions and can be captured by the physics of the Hubbard model. Although matrix elements may dress the aesthetics of these band renormalizations, the presence of such a feature in the single-band Hubbard model indicates that it is a genuine phenomena of the strong el-el interaction in the hole- and electron-doped cuprates. The results of this section have appeared in references [126, 269].

In what follows, the single-particle green's function $G(\tau, \tau')$ is calculated using DQMC and the analytic continuation is performed using the method of maximum entropy (MaxEnt), as described in the previous chapter. The calculations are performed on an $N = 8 \times 8$ cluster, in the strong el-el coupling limit with $U = 8t$. In order to capture the proper shape of the Fermi surface, a next-nearest neighbour hopping is included with $t' = -0.3t$ in the hole-doped system and $t' = -0.2t$ in the electron doped system. Finally, $t = 1$ and $a = 1$ set the units of energy and length throughout this chapter.

Because of the finite size cluster is used in these calculations $A(\mathbf{k}, \omega)$ is defined on a discrete momentum grid $\mathbf{k} \in \mathbf{K}$. In order to determine the spectral function at $\mathbf{k}$ points lying off of this grid, an interpolation routine is used. First, Dyson's equation is used to extract the self-energy $\Sigma(\mathbf{K}, \omega)$ from the analytically continued Green's function. Then, assuming a weak momentum dependence for the self-energy, $\Sigma(\mathbf{k}, \omega)$ is obtained by interpolating $\Sigma(\mathbf{K}, \omega)$ in momentum space. Dyson's equation is then reapplied to obtain $A(\mathbf{k}, \omega)$ at an arbitrary point in $\mathbf{k}$.

9.2.1 The Undoped Parent System

The spectral function $A(\mathbf{k}, \omega)$ of the half-filled Hubbard model ($t' = -0.3t$) is shown in figure 9.1 for a cut taken along the nodal direction $(0, 0)$ - (π, π) and at an inverse temperature $\beta = 3/t$. As expected, the lower and upper Hubbard bands (LHB,UHB) are clearly resolved and a Mott gap exists at the chemical potential ($\mu = 0$). Furthermore, in the vicinity of $\mathbf{k} = (\pi/2, \pi/2)$ a weak satellite band is formed in each of the Hubbard bands, in agreement with previous works [270, 271]. These satellite structures of the LHB and UHB resemble low energy features observed in ARPES experiments on the parent insulator [125] and serve as precursors to the quasiparticle band (QBP) which forms as the system is doped.

9.2.2 Electron- and Hole-doped systems

Having established $A(\mathbf{k}, \omega)$ for the parent insulator, this calculation is then repeated for 14% hole- and 16% electron-doping. The results are shown in figure 9.2. Figures 9.2a

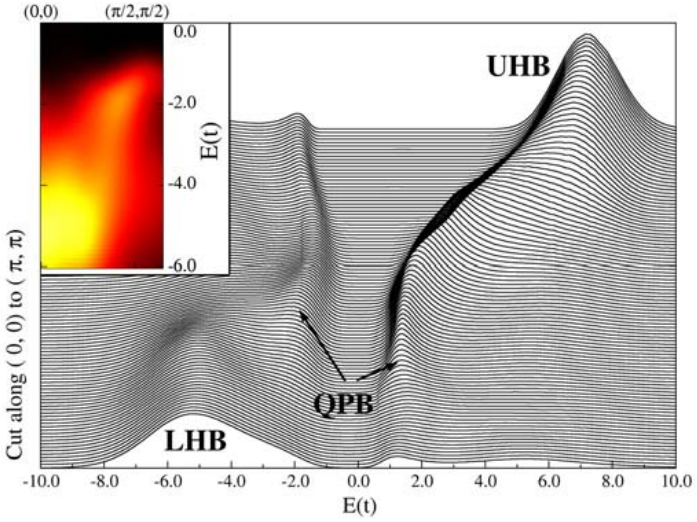

Figure 9.1: The single-particle spectral function $A(\mathbf{k}, \omega)$ for the Hubbard model at half-filling along the nodal cut (0,0) - (π,π). Here, $t' = -0.3t$,$\beta = 3/t$, $\Delta\tau = 1/16t$ and $U = 8t$. The inset shows a false colour plot of the spectra below the Fermi level. The labels denote the LHB, UHB and the precursor structure to the QPB bands which form and cross E_F with hole or electron doping.

and 9.2c show the evolution of $A(\mathbf{k}, \omega)$ along high symmetry cuts of the first Brillouin zone for the hole- and electron-doped cases, respectively. Despite the fact that both the tightbinding parameters and Fermi surfaces are similar for both the electron and hole doped systems it is clear from figure 9.2 that the two spectra are not related by a simple particle-hole transformation.

For the hole-doped system, the LHB is localized to the Γ-point $(0, 0)$ with trailing intensity weakly dispersing towards $(\pi, 0)$ and (π,π). The point in $\mathbf{k}$-space where the suppression of the spectral weight in the incoherent LHB occurs coincides approximately with the location of the HEA observed experimentally. A sharp dispersive QPB has also formed in the Mott gap from the precursor structures shown in figure 9.1, with spectral weight transferred from the UHB to the QPB with hole doping [272, 273]. Along the nodal cut, the QPB is highly dispersive and crosses the Fermi level near (π/2,π/2). However, near (π/4,π/4) the spectral weight of the QPB begins to drop and is nearly completely suppressed at the Γ-point. As a result, the HEA appears as a crossover from this coherent QPB to the incoherent UHB at an energy $\sim -0.5t$ to $-0.75t$. While the spectral intensity decreases in the QPB as the Γ-point is approached, there is a significant range of $\mathbf{k}$-space where the QPB and LHB co-exist in support of the cross-over scenario [126].

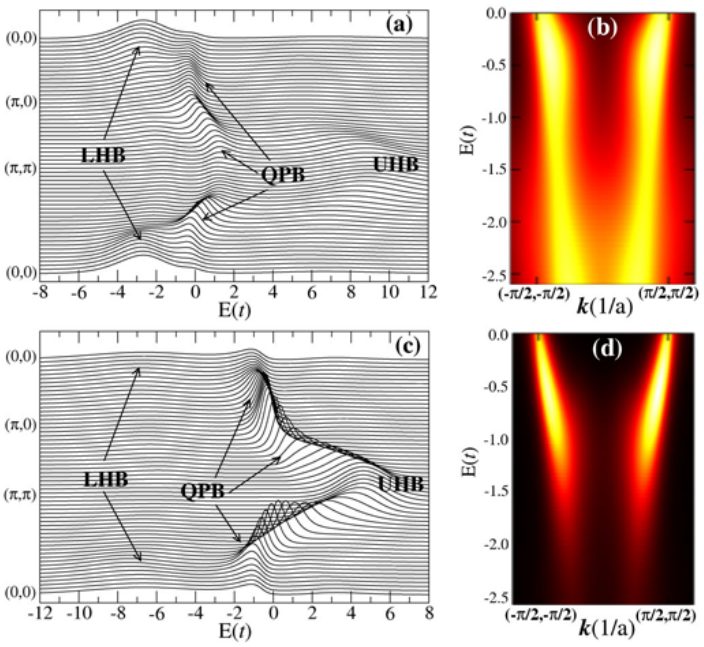

Figure 9.2: Calculated single-particle spectral functions $A(\mathbf{k}, \omega)$ for (a),(b) 14% hole-doping ($\mu = -2.5t$, $t' = -0.3t$) and (c),(d) 16% electron-doping ($\mu = 2.25t$, $t' = -0.2t$). Panels (a) and (c) trace the path cuts of high symmetry in the first Brillouin zone. Panels (b) and (d) show false colour spectra along the cut $(-\pi/2a,-\pi/2a)$ - $(\pi/2a,\pi/2a)$, where representative photoelectric matrix elements have been used to show the effect of matrix elements in determining the HEA.

Turning now to the electron-doped system, the dispersive QPB shown in figure 9.2c disperses further below the Fermi level than in its hole-doped counter part. In this case, the cross-over occurs at an energy $\sim -t$ to $-1.5t$ or twice that of the hole-doped case. This difference in energy scales is also in agreement with experiments discussed in chapter 2 (see for example figure 2.10). More importantly, in this case the QPB forms from the precursor of the UHB in the undoped system [270, 271], in contrast to the spectral weight forming the QPB of the hole-doped system.

The dichotomy between hole- and electron-doped systems is apparent in the relative spectral weight of the LHB and UHB. Upon hole doping the chemical potential shifts from the Mott gap into the LHB, and spectral weight is transferred from the UHB, increasing weight near the Fermi level and forming the QPB. This is in contrast to electron doping, where the chemical potential shifts into the UHB and spectral weight is transferred primarily from the LHB to higher energy to form the QPB. These chemical potential shifts and spectral weight transfers with doping are consistent with the results of reference [272]. It should also be noted that in both cases the Mott gap does not

collapse with doping but is instead shifted in energy. With electron doping the gap becomes the intermediate energy region just below the HEA energy scale while with hole doping the gap is pushed above the Fermi level.

The appearance of the HEA as a "waterfall" may be highlighted by multiplying $A(\mathbf{k}, \omega)$ by photoelectric matrix elements, as shown in figures 9.2b and 9.2d for the hole- and electron-doped systems, respectively. The values of the matrix elements are taken to be representative of the experimentally derived values along the nodal cut [126, 136]. In both cases, and particularly for the hole-doped system, this leads to the appearance of the HEA as a "waterfall" as intensity is suppressed in the QPB and LHB near the the Γ-point. In the case of the electron-doped system, the lack of weight in the LHB results in a simple suppression of intensity near the Γ-point and no significant overlap between the LHB and the QPB occurs. These results could change in a multi-band model calculation with the inclusion of additional valence bands.

These calculations support the conclusion that strong correlations play an important role in the formation of the HEA. They also demonstrate that the HEA is expected to occur both in hole- and electron-doped systems, in agreement with experiment. Furthermore, the energy scale of the HEA is not simply related to the antiferromagnetic exchange energy J, as proposed by some, since this energy scale should be similar in both the electron and hole doped systems. Finally, the DQMC treatment of the single-band Hubbard model captures the physics of all of the renormalization pathways in order to produce the crossover behaviour from the coherent QPB to the incoherent LHB. This behaviour is consistent with experiments and is not captured by weak coupling theories that produce kink-like dispersions analogous to the el-ph features [130, 129, 131]. Similar conclusions were reached in reference [123] however, the results presented here highlight the interplay between doping, spectral weight transfer and band renormalizations in producing the HEA, all of which are beyond examinations based on simple tightbinding analysis with straightforward chemical potential shifts.

9.3 Results for the Hubbard-Holstein Model

9.3.1 The Fermion Sign

The average value of the fermion sign for the Hubbard-Holstein model is plotted in figure 9.3 as a function of filling and λ. These simulations were carried out in the strong coupling limit $U = 8t$ with a phonon frequency $\Omega = 0.3t$. Results are presented both with and without next-nearest neighbour hopping t' and the inverse temperature has been set to $\beta = 3/t$. For small values of λ the average sign follows the trends obtained for the Hubbard model (see figure 8.1). For increasing λ the average sign is suppressed

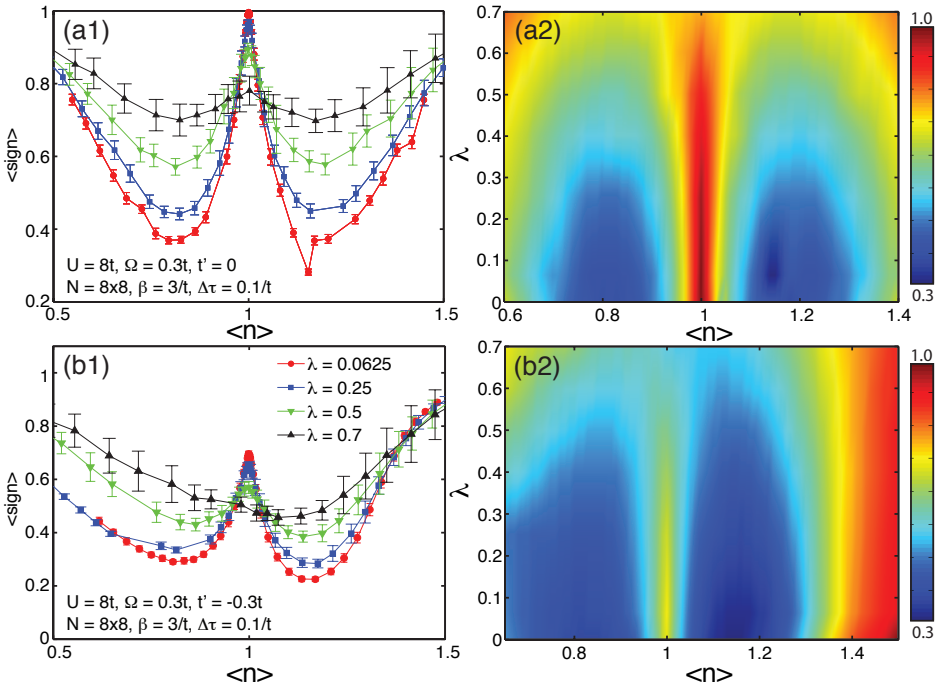

Figure 9.3: The average value of the Fermion sign for the Hubbard-Holstein model as a function of the el-ph coupling strength λ. (a1), (b1) The average sign as a function of filling for selected values of λ for $t' = 0$ and $t' = -0.3t$, respectively. The legend in panel (b1) applies to both panels. (a2), (b2) A false colour plot of the average sign as a function of $\langle n \rangle$ and λ for the corresponding value of t'. The remaining parameters of the simulation are given in panel (b1).

at half-filling. This occurs even when $t' = 0$, where the sign is protected by particle-hole symmetry when $\lambda = 0$. This is due to the fact that individual phonon field configurations break particle-hole symmetry and can therefore induce a sign problem when $t' = 0$ or exacerbate one when $t' \neq 0$.

Away from half-filling the average sign is improved, due to the effective attractive el-el interaction mediated by the phonons; the el-ph interaction term of the Hamiltonian provides an energy gain by doubly occupying a given site which offsets the overall energy cost of the Hubbard repulsion. This results in a renormalized effective Coulomb interaction U_{eff} which improves the average value of the sign with increasing values of λ. A similar reduction in the Coulomb interaction has been reported in DMFT calculations [242, 244, 245, 251].

Despite the improvement in the Fermion sign problem, DQMC simulations of the Hubbard-Holstein model are still limited in terms of temperature and the average sign is

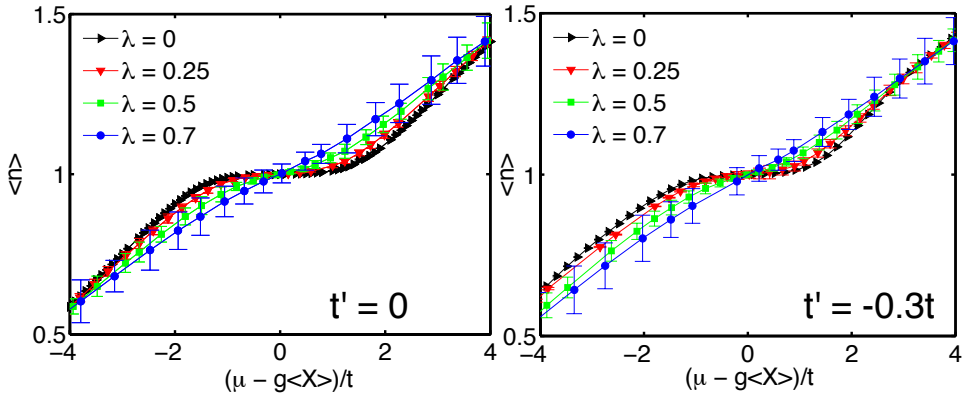

Figure 9.4: The average filling $\langle n \rangle$ as a function of μ for the strongly correlated Hubbard-Holstein model ($U = 8t$, $\Omega = 0.3t$) with (a) $t' = 0$ and (b) $t' = -0.3t$. An overall chemical potential shift $g\langle X_i \rangle$, due to a uniform shift in the lattice's equilibrium position, has been subtracted. The remaining parameters are $\beta = 3/t$, $\Delta\tau = 0.1$, $N = 8 \times 8$.

exponential suppressed with increasing β as is the case with the Hubbard model [210]. As a result, simulations are still restricted to $\beta \sim 3/t$ - $4/t$ for arbitrary fillings however, lower temperatures can be reached at half-filling.

9.3.2 Filling vs Chemical Potential

The average filling $\langle n \rangle$ as a function of chemical potential μ is plotted in figure 9.4a and 9.4b for the cases $t' = 0$ and $t' = -0.3t$, respectively. The remaining parameters are identical to those used in figure 9.3. In figure 9.4, a uniform shift $\Delta\mu = g\langle X_i \rangle$ has been subtracted from the chemical potential μ in order to account for the shift in the lattice's equilibrium position with the inclusion of a non-zero coupling λ.

For $\lambda = 0$ (black triangles) the filling recovers the result for the Hubbard model in the strong coupling limit and the Mott gap is clearly resolved as a flattening of $\langle n \rangle$ versus μ centred at $\mu = 0$. However, as the value of λ is increased, the width of this flattened region begins to narrow signifying a reduction in the size of the Mott gap. For $\lambda = 0.7$ it appears that the Mott gap has closed and the filling nearly varies linearly with μ. This is a reflection of the reduction in U produced by the attractive phonon-mediated interaction and it is the same phenomenon responsible for the improvement of the average sign noted earlier. Although it appears that the Mott gap has collapsed for $\lambda \sim 0.7$, it should be noted that the temperature $\beta = 3/t$ used in figure 9.4 is still relatively high and a small Mott gap may still be present but obscured by thermal broadening.

The results shown in figure 9.4 show no indication of phase separation in the form of a negative $d\langle n\rangle/d\mu$, in contradiction to the results obtained using slave-boson techniques at similar temperatures [243]. However, for increasing λ the error bars for each data point begin to grow signaling large variations in the measured fillings. This behaviour has been generically observed in all simulations performed at half-filling, regardless of the value of Ω or U. Furthermore, when $\lambda > 1$ these error bars become quite large and the results obtained from the simulation have been generally found to be unreliable. There are two possible sources for this instability. The first is that the increased error could reflect a tendency for the system to phase separate. This would produce hole-rich and hole-depleted regions in multiple Markov chains which, when averaged together, would produce large errors in the estimated filling. The second possibility is that the growing error bars reflect increased fluctuations due to a competition between the AFM-ordered state at low λ and a charge-density-wave state at large λ. If the effective value of U is lowered below the critical $U_c = 4t$ for the Hubbard model's metal-insulator transition then the CDW correlations would be expected to become increasingly important as the Fermi surface re-forms and nesting conditions are reinstated. In order to address this possibility a careful examination of the susceptibilities is required and this is the topic of the following section.

9.3.3 Susceptibilities for the Half-Filled Model

The results for the average sign and filling indicate that there may be a competition between the attractive interaction mediated by the phonons and the repulsive Coulomb interaction. Therefore, attention is now turned to an examination of the various susceptibilities relevant to the Hubbard-Holstein model. This will provide further insight into any competition that may be occurring between the various possible ordered states.

It is well known that the Holstein model exhibits an instability to a Peierls charge-density-wave (CDW) phase at a wave-vector set by Fermi surface nesting conditions [274, 171]. A measure of the Peierls correlations can be obtained by calculating the density-density correlation function

$$\chi_{CDW}(\mathbf{q}) = \frac{1}{N}\int_0^\beta d\tau \langle \rho_{\mathbf{q}}(\tau)\rho_{\mathbf{q}}^\dagger(0)\rangle \qquad \rho_{\mathbf{q}}^\dagger = \sum_{\mathbf{n},\sigma} e^{i\mathbf{q}\cdot\mathbf{n}}\hat{n}_{\mathbf{n},\sigma}. \tag{9.3}$$

In the half-filled Holstein model, with $t' = 0$, the CDW correlations are dominated by the $\mathbf{q} = (\pi, \pi)$ nesting condition [171]. When extended range hopping are included the nesting condition may shift depending on the topology of the Fermi surface. However, for the limited cluster sizes used here, the peak in χ_{CDW} will remain at $\mathbf{q} = (\pi, \pi)$ for finite t' and near half-filling. Focus is therefore placed on $\chi_{CDW}(\pi, \pi)$ in what follows.

Near half-filling the Hubbard model has an instability towards an AFM ordered state with wavevector $\mathbf{q} = (\pi, \pi)$ [210, 214]. A measure of the magnetic correlations is given by [214]

$$\chi_{ZZ}(\mathbf{q}) = \frac{1}{N} \sum_{i,j} e^{i\mathbf{q}(R_i - R_j)} \int_0^\beta d\tau \langle [\hat{n}_{i,\uparrow}(\tau) - \hat{n}_{i,\downarrow}(\tau)][\hat{n}_{j,\uparrow}(0) - \hat{n}_{j,\downarrow}(0)] \rangle \tag{9.4}$$

where R_i denotes the position of lattice site i and the AFM correlations relevant to the half-filled Hubbard model are characterized by $\chi_{ZZ}(\pi, \pi)$. The competition between the el-ph driven bipolaron or CDW phase and the el-el driven antiferromagnetic phase will be evident in χ_{CDW} and χ_{ZZ}. (Since attention is now restricted to specific ordering wave vectors the $\mathbf{q}$ vector will be suppressed in order to simplify the notation.) For completeness, the s- and d-wave pair-field susceptibilities are also examined in order to provide a measure of the superconducting correlations. The pair-field susceptibility is given by [210, 274]

$$\chi_{SC} = \frac{1}{N} \int_0^\beta d\tau \langle \Delta(\tau) \Delta^\dagger(0) \rangle \tag{9.5}$$

where

$$\Delta^\dagger = \sum_i c^\dagger_{i,\uparrow} c^\dagger_{i,\downarrow} \tag{9.6}$$

for an s-wave gap symmetry and

$$\Delta^\dagger = \frac{1}{2} \sum_{i,\delta} P_\delta c^\dagger_{i,\uparrow} c^\dagger_{i+\delta,\downarrow} \tag{9.7}$$

for a d-wave gap symmetry. Here, δ is an index that runs over the nearest neighbours of the site i and the phase factor P_δ alternates in sign with $P_{\pm\hat{x}} = 1 = -P_{\pm\hat{y}}$. To distinguish between the two gap symmetries the pair-field susceptibilities will be denoted χ_s and χ_d for the s- and d-wave cases, respectively.

In figure 9.5 the results for the four susceptibilities obtained for the half-filled Hubbard-Holstein model are plotted as a function of λ. Three cases are shown, corresponding to $U = 6t$ (blue), $8t$ (black) and $10t$ (red). In this case, a phonon frequency $\Omega = t$ has been used in order to allow $\lambda = 1$ to be reached at an inverse temperature $\beta = 4/t$. For lower values of Ω, the sign problem becomes problematic for $\lambda > 0.7$. From figure 9.5 it is clear that at half-filling the system is dominated by χ_{CDW} and χ_{ZZ}. For small λ, the AFM correlations dominate for all three values of U. As λ is initially increased from zero, χ_{ZZ} is slowly suppressed and finally gives way to a more rapid suppression at larger λ. Once the AFM correlations are driven low enough, the CDW correlations begin to rise signaling the onset of the CDW. The point at which the increased rate of suppression in χ_{ZZ} (and subsequent rise in χ_{CDW}) occurs is dependent on the value of U with the

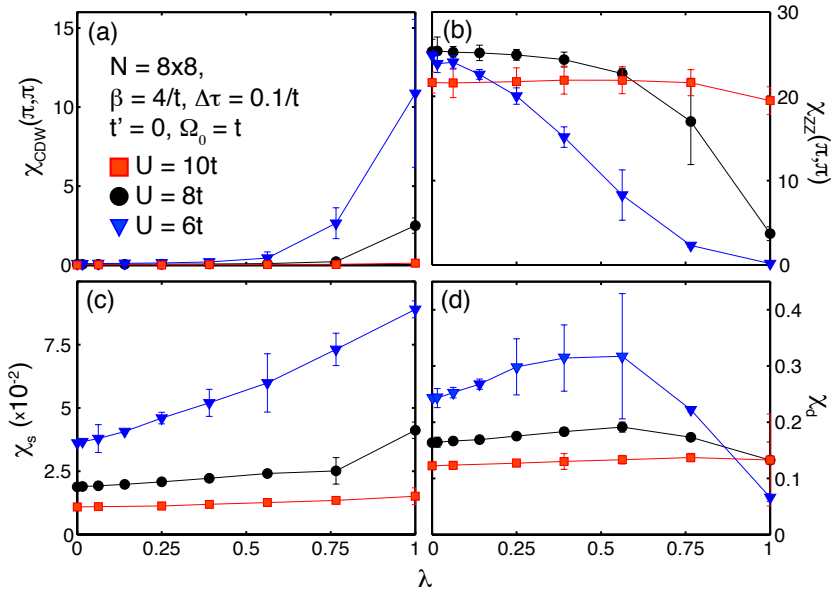

Figure 9.5: A summary of the (a) (π, π) CDW, (b) AFM, (c) s-wave pair-field and (d) d-wave pair-field susceptibilities for the Hubbard-Holstein model at half-filling and $\beta = 4/t$. The parameters used in the DQMC simulations are given in panel (a).

larger values of U maintaining the AFM correlations out to larger values of λ. For the $U = 10t$ case, only at $\lambda = 1$ does χ_{ZZ} begin to decrease.

The superconducting susceptibilities also exhibit behaviour reflecting the AFM/CDW competition. At $\lambda = 0$ the on-site s-wave susceptibility is suppressed by the Coulomb repulsion. As λ increases this suppression is relieved as U is renormalized by the el-ph interaction and χ_s increases as a function of λ, essentially in line with the suppression of χ_{ZZ}. In the case of the d-wave susceptibility similar behaviour is observed however, for $U = 6t$, there is a marked decline in χ_d for $\lambda > 0.5$, precisely where the CDW correlations begin to dominate. This is not surprising given that the CDW ordering tends to doubly occupy sites in a checkerboard pattern which is detrimental to the pair field defined in equation 9.7.

The trade off between χ_{ZZ} and χ_{CDW} at large λ is consistent with a competition between the AFM and CDW ordered states. In this scenario, the first order effect of the el-ph interaction is to renormalize the Hubbard U. This behaviour was reflected in both the average Fermion sign as well as $\langle n \rangle$ versus μ and it is now appearing in the AFM and CDW susceptibilities. Therefore, the increased error bars shown in the previous sections are likely due to fluctuations associated with the phase transition from the AFM to CDW ordered states which would occur at lower temperature.

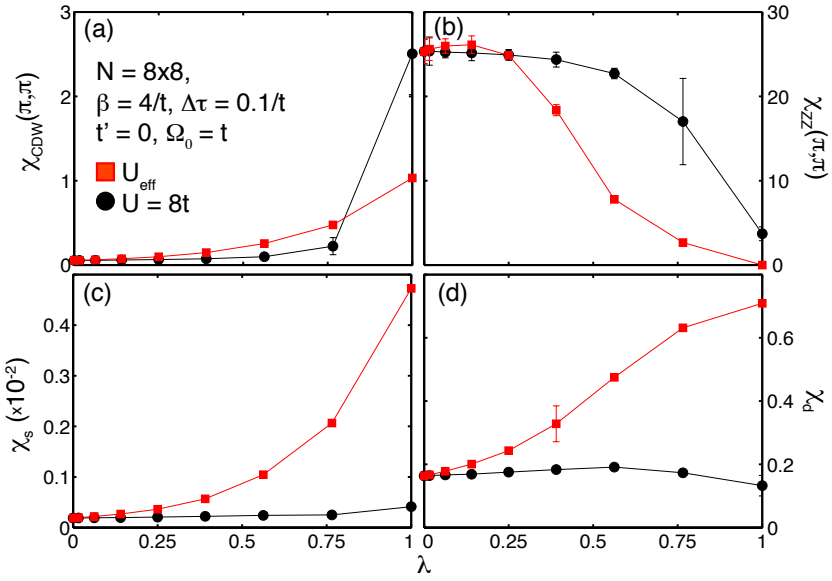

Figure 9.6: The susceptibilities of the Hubbard-Holstein model compared to an effective Hubbard model with $U_{\text{eff}} = U - 2g^2/\Omega = U - \lambda W$, where $W = 8t$ is the bandwidth of the non-interacting system.

Given that the first order effect of the el-ph interaction is to renormalize the Coulomb interaction it is tempting to try to describe the physics of the Hubbard-Holstein model with an effective-U Hubbard model. The P-DMFT calculations of reference [244] have shown that the low-energy physics of the Hubbard-Holstein model can be accurately reproduced with such an approach. In figure 9.6 a comparison is made between the $U = 8t$ results of figure 9.5 and an effective Hubbard model with U_{eff} given by the antiadiabatic limit of equation 9.2, $U_{\text{eff}} = U - 2g^2/\Omega = U - \lambda W$. For small λ the two models give relatively good agreement however, as λ is increased the results begin to diverge rapidly, demonstrating the importance of retardation effects even for $\Omega = t$. For the CDW correlations, the Hubbard-Holstein model produces a smaller χ_{CDW} up until the point at which the CDW correlations become dominant and beyond this point the Hubbard-Holstein model overtakes the values of the U_{eff} model. This highlights the importance of the retarded nature of the el-ph interaction and the softening of the phonon in establishing the CDW. Similarly, the AFM correlations are suppressed at a much faster rate for the U_{eff} model. In the case of superconductivity, the Hubbard-Holstein model predicts that χ_s and χ_d remain suppressed for all λ while for the U_{eff} model they are monotonically rising as $U_{\text{eff}} \to 0$ ($\lambda = 1$). Previous DQMC calculations for the Hubbard model have shown that χ_s and χ_d are smaller than the values one obtains from the non-interacting system [210, 275]. Therefore, the rise in the superconducting

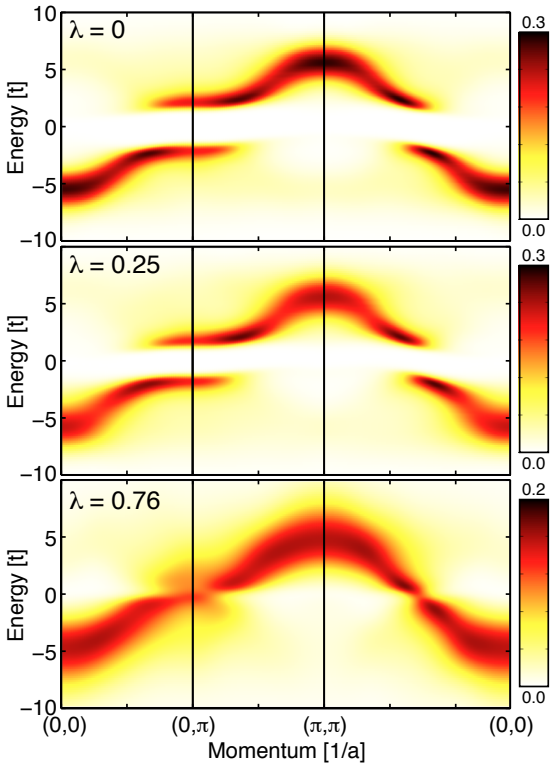

Figure 9.7: The single-particle spectral function $A(\mathbf{k}, \omega)$ for the Hubbard-Holstein model for $\lambda = 0$, 0.25 and 0.76 along the directions of high-symmetry in the BZ. The remaining parameters are $\Omega = t$, $\beta = 4/t$, $\Delta\tau = 1/10t$, $t' = 0$. All spectra have been plotted using the same colour scale.

correlations for the U_{eff} model represents the recovery of the results in the non-interacting limit as $U_{\text{eff}} \to 0$. These results confirm the results of reference [244] in that they show the importance of the retarded el-ph interaction which manifests at higher energy and therefore in dynamic quantities such as the susceptibilities.

9.4 Spectral Properties of Hubbard-Holstein Model

Attention is now turned to the spectral properties of the Hubbard-Holstein model. Here, $A(\mathbf{k}, \omega)$ is obtained using the interpolation scheme outlined above for the Hubbard model calculations. Selected spectral functions for the half-filled Hubbard-Holstein model with $\Omega = t$, $t' = 0$ and $U = 8t$ are presented in figure 9.7 for the inverse temperature $\beta = 4/t$.

For $\lambda = 0$, $A(\mathbf{k}, \omega)$ recovers the result for the Hubbard model, similar to those shown in figure 9.1 but with minor changes in the dispersion due to the lack of next-nearest-neighbour hopping. A clear Mott gap $\sim 2t$ is observed with precursor structures in the LHB and UHB. As the value of λ is increased, the effect of the el-ph attraction begins to grow and even for $\lambda = 0.25$ the Mott gap begins to visibly narrow. In addition, $A(\mathbf{k}, \omega)$ broadens due to self-energy effects from el-ph scattering processes. These trends continue

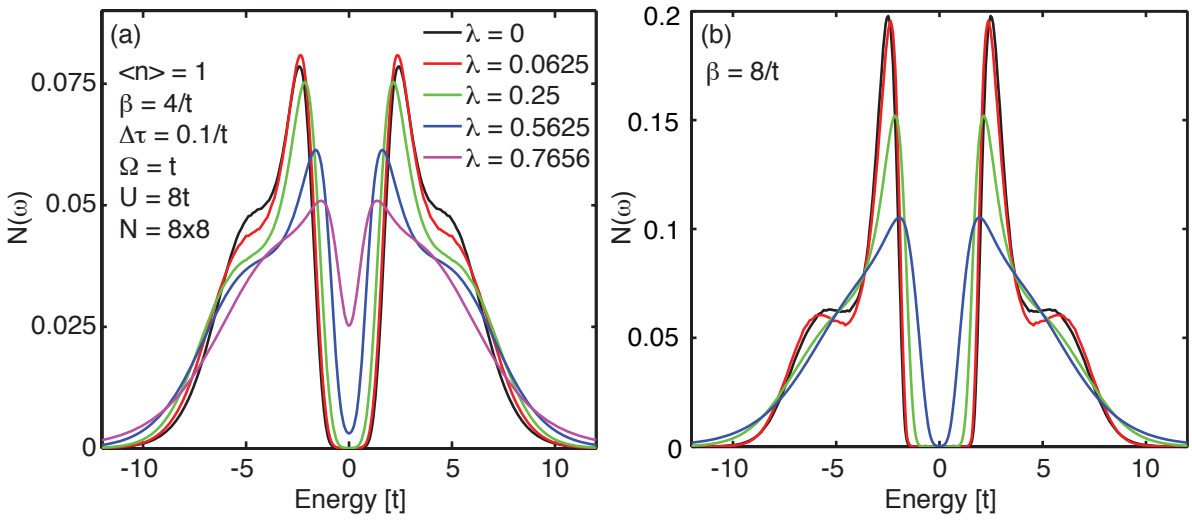

Figure 9.8: The density of states for the half-filled Hubbard-Holstein model as a function of the strength of the el-ph interaction at (a) $\beta = 4/t$ and (b) $\beta = 8/t$. The parameters used in this simulation are the same as those used in figure 9.7 and are indicated in panel (a).

as λ is further increased and for $\lambda = 0.76$ the Mott gap has narrowed considerably with thermal broadening filling in the weight across the chemical potential. As a result, a suppressed but non-zero spectral weight is present at the Fermi level. These results mirror the susceptibility results of the previous section and indicate that the el-ph interaction is renormalizing the Coulomb interaction and destabilizing the AFM order.

The competition between the two interactions is also present in the single-particle density of states $N(\omega) = \sum_{\mathbf{k}} A(\mathbf{k}, \omega)$, which is plotted in figure 9.8a for $\beta = 4/t$. As with the spectral function, for $\lambda = 0$ the Mott gap is clearly present. As the value of λ is increased the gap begins to close and the peaks associated with the QPB precursor begin to shift towards the chemical potential and broaden, again due to the el-ph scattering. The structure in the DOS associated with the incoherent portions of the UHB and LHB, located at $\omega \sim \pm 5t$ for $\lambda = 0$, also broaden and shift somewhat to lower energies. For larger values of λ the Mott gap has become small enough that thermal broadening produces finite weight in the DOS at the chemical potential, echoing the behaviour observed for $A(\mathbf{k}, \omega)$. The degree of thermal broadening can be assessed by examining figure 9.8b, which shows $N(\omega)$ at a lower temperature $\beta = 8/t$. For small λ the structures associate with the QPB precursor and Hubbard bands are clearly resolved, while with increasing λ the DOS follows the trends of the $\beta = 4/t$ data. (In this case the $\lambda = 0.7656$ data is not present due to the significant sign problem for this temperature and el-ph coupling strength.)

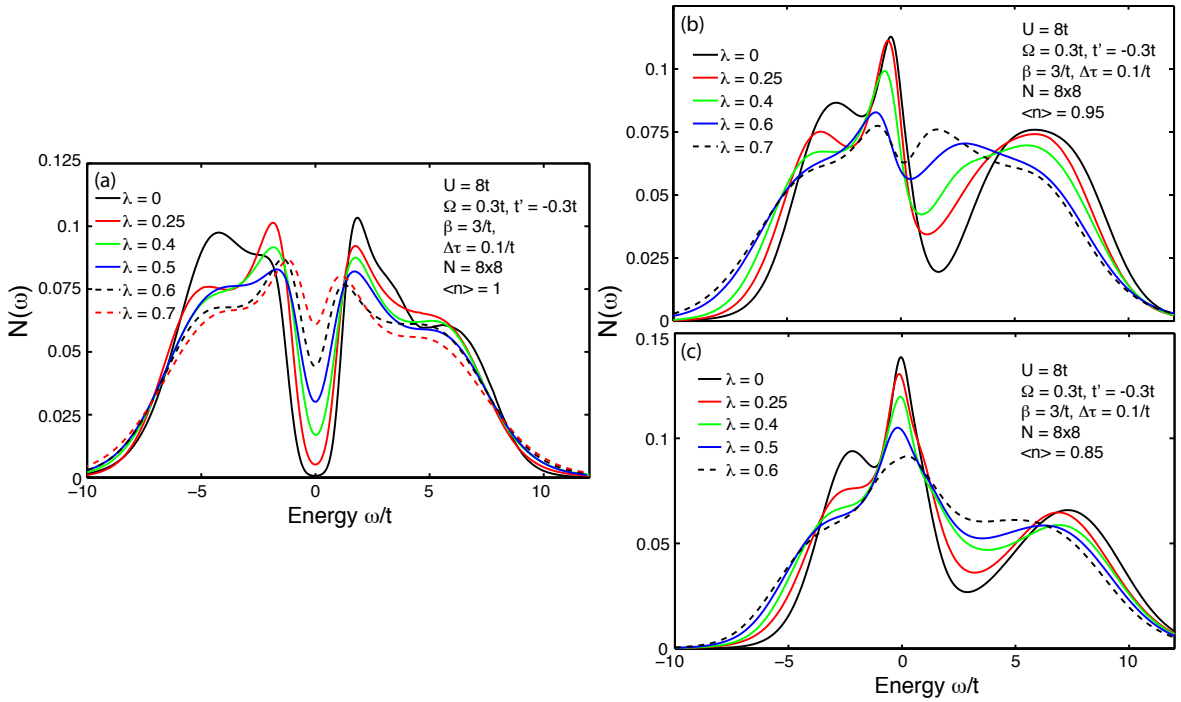

Figure 9.9: $N(\omega)$ for the Hubbard-Holstein model with parameters appropriate for the high-T_c cuprates. (a) $N(\omega)$ at half-filling, (b) 5% hole doping, and (c) 15% hole doping.

Turning now to finite doping, figure 9.9 presents the DOS for $\Omega = 0.3t$, $t' = -0.3t$ and $U = 8t$ for $\langle n \rangle = 1$ (Fig. 9.9a), 0.95 (9.9b) and 0.85 (9.9c) at an inverse temperature $\beta = 3/t$. The lower value of the phonon frequency is more appropriate for the cuprates and this parameter set is identical to those used in references [207] and [246]. At half-filling the results are similar to those shown in figure 9.8; for increasing λ the peaks associated with the quasi-particle precursor bands are reduced in intensity and begin to disperse to lower energy while spectral weight begins to rise inside Mott gap. These results indicate that the apparent collapse of the Mott gap occurs even for smaller values of Ω, at least for temperatures as low as $t/3$.

At finite doping, in the absence of el-ph coupling (solid black), the spectra exhibit structures consistent with the results of section 9.2. The quasiparticle band has formed, appearing as a peak in $N(\omega)$ at the chemical potential, and the LHB and UHB manifest as the peaks located at $\omega = -2.5t$ to $-3t$ and $\omega = 6t$ - $8t$, respectively. The spectral weight transfer from the UHB is also evident in the reduced weight of the UHB relative relative to the half-filled case. For increasing values of λ the spectra display behaviour similar to that of the half-filled case. Both the intensity and peak-to-peak distance between the Hubbard bands are reduced, while the spectral weight increases in the remnant of the

Mott gap, which has been pushed above the Fermi level.

Results for $N(\omega)$ in the 5% hole-doped system, obtained using the dynamical cluster approximation on a 2×2 cluster have also been reported for the single-band Hubbard-Holstein model [207]. The gross feature of the LHB and UHB shown in figure 9.9b are in agreement with these results in that with increasing λ the quasiparticle peak is suppressed and the UHB disperses to lower energy while broadening somewhat. However, at the Fermi level the DCA results showed a suppression spectral weight with increasing λ. This behaviour was interpreted as a reflection of the formation of polarons, which reduce carrier mobility and therefore lower the quasiparticle weight at the Fermi level. The results obtained here using DQMC are clearly in conflict with this picture. There are a two obvious possible sources for the discrepancy in the two sets of results. First, and most likely, is the difference in temperature between the two calculations. The DCA calculations were performed at a much lower temperature ($\beta = 11.5/t$) than the DQMC calculations shown in figure 9.9 and the changes in the spectra at $\omega = 0$ presented here may be masked by thermal broadening effects or the fact that coherent phonon effects are not expected for $\beta \leq \Omega$. Another possible source is the differences in cluster size. The 2×2 cluster contains only three unique momentum points, $(0, 0)$, $(0, \pi)$, $(\pi, 0)$and (π, π). Therefore, $N(\omega)$ obtained from such a cluster will oversample the anti-nodal region whereas the DQMC spectra are obtained from a cluster with 16 unique momentum points. In order to address this issue, a systematic study of the spectra with cluster size should be carried out.

9.4.1 Discussion

The results presented in the previous sections indicate a suppression of the AFM order and the subsequent collapse of the Mott gap with increasing el-ph coupling. It is important to note that this transition is driven not by polaron formation but rather a renormalization of the Hubbard interaction. As the value of the Hubbard U is renormalized, the Fermi surface is restored by the loss of magnetic order and the $\mathbf{q} = (\pi, \pi)$ nesting condition can again be satisfied allowing the CDW to begin to form. Therefore, the DQMC treatment predicts that near half-filling the physics of the Hubbard-Holstein model is dominated by competition between AFM and el-ph driven charge ordering. Similar behaviour is also observed in the spectral function and density of states at finite filling however, it should be reiterated that this statement can only be made at high temperature $\beta \leq 3/t$ due to the sign problem at these fillings. However, at half-filling this behaviour extends to lower temperatures ($\beta = 8/t$).

The competition outlined here has also been observed in various DMFT calculations [244, 242]. These results are also in direct contrast to results obtained from the t-J model [229, 225], which show an increased tendency towards polaron formation for a

doped hole in an antiferromagnetic background. In t-J model based approaches the hole is dressed by AFM fluctuations which increases its effective mass and makes it easier to self-trap via coupling to the lattice. Thus the AFM background plays an important role in reducing the value of λ needed for the crossover to small polarons [229, 225, 245]. The discrepancy between the t-J-Holstein results and the DQMC results presented here can be understood in terms of the robust AFM state imposed by the t-J model (which is itself the $U \rightarrow \infty$ limit of the Hubbard model). As a result of the infinitely large Coulomb interaction, the AFM order present in the t-J model cannot be destabilized, regardless of the strength of any competing interaction, and any magnetic excitations which dress the carriers will always be present. This is not the case with the DQMC treatment of the single-band Hubbard model with finite U where the AFM order can be lost as the strength of the el-ph interaction is increased. Indeed, as the value of U is increased in the DQMC calculations presented here (see Fig. 9.5), the point at which the CDW correlations become important is pushed to larger values of λ. Therefore, for sufficiently large U it is expected that the el-ph interaction will reach the polaron crossover before the Hubbard U is renormalized sufficiently enough to allow for the formation of a CDW order.

9.5 Summary

In this chapter the Hubbard and Hubbard-Holstein models have been examined using DQMC, with particular focus placed on the spectral properties of each model. First, $A(\mathbf{k}, \omega)$ of the half-filled and doped cases of the Hubbard model were examined and found to qualitatively reproduce the HEA observed in the electron- and hole-doped cuprates. In this case, the HEA arose from a crossover between the coherent quasiparticle band formed in the doping process and the incoherent UHB and LHB for the electron- and hole-doped cases respectively. Although matrix elements may dress the aesthetics of this feature, the calculations presented here demonstrate that the HEA is captured by the physics of the Hubbard model and it represents a genuine renormalization arising from correlated many-body effects in the cuprates. Furthermore, this calculation correctly captures the dichotomy of the energy scales appearing in the electron- and hole-doped cuprates. This aspect of the physics is not captured in models based on electron-boson coupling to electronic excitations analogous to the low-energy kinks produced by el-ph coupling.

Next, the various properties of the Hubbard-Holstein model were presented. In this case, a number of metrics including the Fermion sign, $\langle n \rangle$, susceptibilities, $A(\mathbf{k}, \omega)$, and the density of states, all revealed evidence for a competition between antiferromagnetism and the $\mathbf{q} = (\pi, \pi)$ charge-density-wave. This competition was not only present at half-filling but also at finite doping. These findings are in contrast to studies on the t-J model,

as well as DCA calculations on the single-band Hubbard models with phonons, which find that antiferromagnetism dresses the carriers to such an extent that polaron formation occurs at weaker couplings. These findings suggest the physics of el-ph coupling in correlated models may depend critically on the robustness of any magnetic order present in these systems. This is a topic which deserves attention in future works.

Chapter 10

Conclusions

Over the last two decades significant progress has been made towards understanding the cuprate family of high-temperature superconductors. Although it has generally been accepted that planar models for the CuO_2 plane capture the relevant low-energy physics of the cuprates, there are increasing indications of a need to extend our thinking beyond intrinsically planar models. Perhaps the most compelling example of this fact is the large variation in T_c observed across the cuprates, which is difficult to account for without involving the material-specific chemical environment of the CuO_2 plane. Further evidence for the importance of off-plane structures and other c-axis effects has come from the growing body of experimental evidence for strong coupling to the lattice. As was reviewed in chapter 2, angle-resolved photoemission spectroscopy (ARPES) has revealed spectra with polaronic features in some parent compounds, and ubiquitous dispersion renormalizations in the doped systems which have been interpreted in terms of coupling to a spectrum of oxygen phonon modes. Similar signs of electron-phonon (el-ph) coupling have appeared in scanning tunneling microscopy (STM) experiments as well as Raman, IR, and neutron spectroscopies. The collective evidence provided by the various probes points to the presence of a significant el-ph interaction in these systems and this interaction requires extensions of the canonical strongly correlated models. With these observations the challenge is then to determine to what extent the el-ph interactions are playing a role in high-temperature superconductivity. Attempting to address this question was the primary goals of this work.

The scenario that emerged from modelling the ARPES and STM data is that of a two-channel model in which the phonons act in conjunction with an underlying dominant pairing mechanism. (At present this second mechanism is unknown but antiferromagnetic spin fluctuations appear to be a promising candidate.) This model was motivated largely by observations made while examining the el-ph coupling in both ARPES and STM. In terms of the band renormalizations observed by ARPES it was found that relatively small

values for the total coupling $\lambda_z \sim 0.2$-0.5 were required in order to obtain quantitative agreement with the experimental data. Such a small value of λ_z ($\lambda_\phi < \lambda_z$) is far too small to account for high-temperature superconductivity and therefore, in modelling the ARPES data, the superconducting gap had to be introduced by hand. This fact is consistent with the idea that the phonons are modulating over an existing pairing interaction. In studying the signatures of el-boson coupling in the context of the STM experiments this proposal was placed on firmer ground. Here it was found that the qualitative signature of a boson that contributes heavily to pairing is quite different than one that renormalizes over the dominant interaction. It was then argued that the scenario most consistent with the STM data is the latter. Following this observation, the el-ph model used to account for the ARPES data was then applied to understanding the STM data and it was demonstrated that this model is sufficient to reproduce the features observed experimentally.

The two-channel model can not only account for the data observed in various probes but also provides a natural framework for understanding the materials dependence of T_c. As was shown in chapter 4, changes in the chemical composition and structure of the unit cell are reflected in the orbital character of the band at the Fermi level, the strength of the local electric fields arising from structural-induced symmetry breaking, doping-dependent changes in the underlying band structure, and the ionicity of the crystal governing the material's ability to screen c-axis perturbations. Given the sensitivity of T_c to the structural details of the crystal, it is clear that the underling mechanism(s) for high-temperature superconductivity must address these factors. In this work it was demonstrated that the overall coupling to the c-axis phonon modes is quite sensitive to these factors and therefore the inclusion of the el-ph coupling provides a means of linking the electronic properties of the CuO_2 plane to the structural elements of the material as well as carrier concentration. In chapter 4 these details were systematically examined and the resulting variation in the coupling to the B_{1g} mode was found to be correlated with the material's T_c at optimal doping. Furthermore, the T_c considerations presented in chapter 6 showed that moderate values of $\lambda_{z,\phi}$, comparable to those required to reproduce the ARPES and STM data, are capable of producing sizeable enhancements in T_c within the Eliashberg formalism.

The theory of el-ph coupling in the cuprates was then extended to include the effects of screening in these systems. Due to the quasi-2D nature of the cuprates, with poor conductivity along the c-axis, it was found that a window of small $\mathbf{q}$ opens in which screening is inoperable. This results in an overall enhancement of the d-wave projected coupling, enhancing the phonon's ability to mediate d-wave pairing. With progressive doping, the total phonon contribution to λ_ϕ was enhanced while the total contribution to λ_z, which suppresses d-wave pairing, was screened away. As a result, doping the system away from half-filling resulted in an increased contribution to d-wave superconductivity mediated by el-ph coupling. This may help to explain the doping-dependence of T_c

however, until the doping dependence of the dominant mechanism is understood this remains an open question.

Up until this point, this work has focused on the doped-cuprates where Migdal-Eliashberg theory appears to capture much of the experimental details. In an effort to extend this analysis to the underdoped region of the phase diagram, where strong correlations become increasingly important and experiments indicate the presence of polaronic behaviour, numerical work was then undertaken. Here, the interplay between strong correlations and the el-ph interaction was examined using determinant quantum Monte Carlo (DQMC) and small-cluster exact diagonalization calculations.

The exact diagonalization calculations were performed in the context of an oxygen dopant in an otherwise idealized lattice of $Bi_2Sr_2CaCu_2O_8$. In this case, the Madelung energies of the CuO_2 plane were modified by the dopant on an eV scale but, due to the relative sign of Madelung energy on each site, these changes largely cancelled producing only minor modifications to the local electronic properties if the el-ph interaction was neglected. However, the dopant oxygen also produced sizeable enhancements to the local el-ph coupling λ which in turn produced a reduced charge gap, broadened spectral features, and a sizeable local increase of J. All of these observations imply a strong interplay between antiferromagnetism, polarons and superconductivity beyond the simple T_c enhancement predicted by Eliashberg theory. The DQMC results obtained for the single-band Hubbard-Holstein model produced a somewhat different picture. In this case, evidence for a competition between the correlation-driven antiferromagnetism and phonon-driven charge-density-wave was observed in multiple measurements. Here, the antiferromagnetic correlations were suppressed not by the formation of polarons but rather by a renormalization of the Hubbard U. These results are in contrast with results obtained from t-J-Holstein model calculations, which observe an increased tendency towards polaron formation for doped holes dressed by antiferromagnetic fluctuations.

From the high-temperature DQMC results it is clear that there are a number of open questions regarding el-ph coupling in a correlated system. The obvious next step is to revisit the destabilization of the antiferromagnetic order at lower temperatures. Recently, a variant of the DQMC algorithm has been developed which imbeds the cluster into a mean-field bath. This procedure allows inverse temperatures on the order of $\beta \sim 10/t$ to be reached at optimal doping [276]. Implementing the Holstein phonon into this approach should allow future simulations to reach much lower temperatures where phonon coherence effects can occur. This could remedy the inconsistency between the t-J model results and those presented here. There is also the possibility that since the antiferromagentic is impossible to destabilize in the t-J model that the Hubbard model with phonons will display qualitatively different physics, even at low temperatures.

Future work can also be carried out in considering different forms for the el-ph coupling or by examining phonons in multi-band Hubbard models. In a three-band Hubbard

model with c-axis oxygen phonons there is a clear partition between the lattice degrees of freedom located on the oxygen sites and the largest Hubbard U term located on the copper sites. Such a separation may help to counteract any competition between the two interactions and could produce results more in-line with those of the t-J model. The possible role of extended range el-ph coupling in polaron formation is also worth exploring since such coupling would dress the carrier with extended lattice deformations and allow for overlap between neighbouring large polarons. Finally, the role of bond phonons in forming stripes presents another potential area of research.

Throughout this work a number of aspects of el-ph coupling in the cuprates have been examined, reiterating the importance of this interaction in the physics of high-temperature superconductivity. Within the traditional Migdal-Eliashberg framework, phonons can provide substantial variations in T_c and are likely required in order to understand the material-specific properties of the cuprates. This behaviour stems in part from the quasi-two-dimensional nature of the cuprates and would be absent in good three-dimensional metals. Because of this, many of the results obtained here - particularly the poor screening results - may be generalized to other layered systems with large transport anisotropies. In extending the theory to the half-filled systems and therefore moving beyond conventional Migdal-Eliashberg theory, numerical evidence pointing towards competition and entanglement of antiferromagnetism, el-ph coupling, and superconductivity was uncovered. This evidence further points to the potential for el-ph coupling to play a complicated role in the cuprates, extending far beyond the validity of conventional el-ph theory. This research highlights the importance for continued research in this area.

Appendix A

Kramers-Kronig Relations for the Self-Energy

Let $f(x) = f_1(x) + if_2(x)$ for $x \in R$, where $f_1(x)$ and $f_2(x)$ are real-valued functions. If a describes a physical quantity governed by causality then the real and imaginary parts are related by the Kramers-Kronig relations

$$f_1(x) = \frac{1}{\pi} P \int_{-\infty}^{\infty} dx' \frac{f_2(x')}{x' - x} \qquad f_2(x) = -\frac{1}{\pi} P \int_{-\infty}^{\infty} dx' \frac{f_1(x')}{x' - x} \tag{A.1}$$

where P denotes the principle part of the integral. The imaginary parts of the electron-phonon self-energies $\chi_2(\mathbf{k}, \omega)$ and $\phi_2(\mathbf{k}, \omega)$ are odd with respect to ω. Using this symmetry one can the show that the real parts are given by

$$\chi_1(\mathbf{k}, \omega) = \frac{2}{\pi} P \int_0^{\infty} \frac{\omega' \chi_2(\mathbf{k}, \omega)}{\omega'^2 - \omega^2} d\omega' \tag{A.2}$$

and

$$\phi_1(\mathbf{k}, \omega) = \frac{2}{\pi} P \int_0^{\infty} \frac{\omega' \phi_2(\mathbf{k}, \omega)}{\omega'^2 - \omega^2} d\omega'. \tag{A.3}$$

The renormalization parameter $Z_2(\mathbf{k}, \omega)$ also has odd parity; however it is the quantity $\omega[1 - Z(\mathbf{k}, \omega)]$ which is governed by causality and $Z_1(\mathbf{k}, \omega)$ is given by

$$Z_1(\mathbf{k}, \omega) = 1 + \frac{2}{\pi} P \int_0^{\infty} \frac{\omega' Z_2(\mathbf{k}, \omega')}{\omega'^2 - \omega^2}. \tag{A.4}$$

Appendix B

The Eliashberg Equations

The starting point for deriving the Eliashberg equations is the electron-boson self-energy, calculated within the Migdal approximation. The diagrams included are shown in figure 3.4. Here, contributions from multiple bosonic modes are allowed for. Each mode indexed by μ, modelled as an Einstein mode of frequency Ω_μ and assigned coupling constants $g_\mu(\mathbf{k},\mathbf{q})$. Using the Nambu notation, the self-energy is then:

$$\hat{\Sigma}(\mathbf{k},i\omega_n) = -\frac{1}{N\beta}\sum_{\mu,m,\mathbf{q}} |g(\mathbf{k},\mathbf{q})|^2 D_\mu(\mathbf{q},i\omega_m)\hat{\tau}_3\hat{G}(\mathbf{p},i\omega_n - i\omega_m)\hat{\tau}_3 \tag{B.1}$$

where $\mathbf{p} = \mathbf{k} - \mathbf{q}$ and $D(\mathbf{q},i\omega_m)$, $G(\mathbf{k},i\omega_n)$ are the phonon and electron propagators, respectively.

One now introduces the spectral representation for the propagators

$$D(\mathbf{q},i\omega_m) = \int_0^\infty dx \frac{2xB_\nu(x)}{(i\omega_m)^2 - x^2} \qquad G(\mathbf{k},i\omega_n) = \int_{-\infty}^\infty \frac{dz}{\pi}\frac{\hat{G}''(\mathbf{p},z)}{z - i\omega_n} \tag{B.2}$$

where $B_\mu(x) = -D''_\mu(x)/\pi = \delta(x - \Omega_\mu)$ for an Einstein mode. Substituting Eq. B.2 into Eq. B.1 and carrying out the Matsubara sum over bosonic frequencies yields

$$\hat{\Sigma}(\mathbf{k},i\omega_n) = \frac{1}{N}\sum_{\mu,\mathbf{p}} |g_\mu(\mathbf{k},\mathbf{q})|^2 \int_{-\infty}^\infty dz \hat{\tau}_3\hat{G}(\mathbf{p},z)\hat{\tau}_3 A(z,\Omega_\mu,i\omega_n) \tag{B.3}$$

with

$$A(z,\Omega,i\omega_n) = \left[\frac{n_b(\Omega) + n_f(z)}{z - \Omega - i\omega_n} + \frac{n_b(\Omega) + n_f(-z)}{z + \Omega - i\omega_n}\right] \tag{B.4}$$

where n_f and n_b are the Fermi and Bose occupation numbers. The el-boson self-energy can also be written in the phenomenological form [65]:

$$\hat{\Sigma}(\mathbf{k},i\omega_n) = i\omega_n[1 - Z(\mathbf{k},i\omega_n)]\hat{\tau}_0 + \chi(\mathbf{k},i\omega_n)\hat{\tau}_3 + \phi(\mathbf{k},i\omega_n)\hat{\tau}_1 \tag{B.5}$$

where $\omega(1-Z)$, χ are the odd and even components of the normal state self-energy, respectively, and ϕ is the anomalous self-energy. With this division of the self-energies, the electron propagator is given by

$$\hat{G}(\mathbf{k},z) = \frac{zZ(\mathbf{k},z)\hat{\tau}_0 + [\epsilon_{\mathbf{k}} + \chi(\mathbf{k},z)]^2\hat{\tau}_3 + \phi(\mathbf{k},z)\hat{\tau}_1}{[zZ(\mathbf{k},z)]^2 - [\epsilon_{\mathbf{k}} + \chi(\mathbf{k},z)]^2 - \phi^2(\mathbf{k},z)}. \tag{B.6}$$

For a d-wave superconductor, one now assumes that the el-boson coupling constant can be separated $|g(\mathbf{k},\mathbf{q})|^2 = g_{z,\mu}^2 + g_{\phi,\mu}^2 d_{\mathbf{k}} d_{\mathbf{p}}$, with contributions to the self-energy in the s-(g_z) and d-wave channels (g_ϕ). Here, $d_{\mathbf{k}} = [\cos(k_x a/2) - \cos(k_y a/2)]/2$ is the usual d-wave form factor. If one only admits a d-wave solution for the gap function $\Delta(\mathbf{k},\omega) = \Delta(\omega)d_{\mathbf{k}}$ then Z and χ are momentum independent and the momentum and frequency dependence of the anomalous self-energy can be separated $\phi(\mathbf{p}, i\omega_n) = \phi(i\omega_n)d_{\mathbf{p}}$. This simplifies the expressions for the three self-energy components

$$i\omega_n[1 - Z(i\omega_n)] = \frac{1}{N\pi}\sum_{\mathbf{p},\mu} g_{z,\mu}^2 \int_{-\infty}^{\infty} dz \mathrm{Im}\left[\frac{zZ(z)}{z^2Z^2(z) - (\epsilon_{\mathbf{p}} + \chi_{\mathbf{p}})^2 - \phi_{\mathbf{p}}^2 d_{\mathbf{p}}^2}\right] A(z, \Omega_\mu, i\omega_n)$$

$$\chi(i\omega_n) = \frac{1}{N\pi}\sum_{\mathbf{p},\mu} g_{z,\mu}^2 \int_{-\infty}^{\infty} dz \mathrm{Im}\left[\frac{\epsilon_{\mathbf{p}} + \chi_{\mathbf{p}}(z)}{z^2Z^2(z) - (\epsilon_{\mathbf{p}} + \chi_{\mathbf{p}})^2 - \phi_{\mathbf{p}}^2 d_{\mathbf{p}}^2}\right] A(z, \Omega_\mu, i\omega_n)$$

$$\phi(i\omega_n) = -\frac{1}{N\pi}\sum_{\mathbf{p},\mu} g_{\phi,\mu}^2 \int_{-\infty}^{\infty} dz \mathrm{Im}\left[\frac{\phi_{\mathbf{p}} d_{\mathbf{p}}^2}{z^2Z^2(z) - (\epsilon_{\mathbf{p}} + \chi_{\mathbf{p}})^2 - \phi_{\mathbf{p}}^2 d_{\mathbf{p}}^2}\right] A(z, \Omega_\mu, i\omega_n).$$

A set of standard approximations are now made [181, 183]. First, a cylindrical Fermi surface is assumed and the d-wave gap is replaced with its θ-representation $d_{\mathbf{k}} \to \cos(2\theta)$. Second, the sum over momenta is replaced with an integral over the density of states $N(\epsilon)$ and the density of states is replaced by its value at the Fermi level N_f.

$$\frac{1}{N}\sum_{\mathbf{p}} A_{\mathbf{p}}(\epsilon_p) = N_f \int_{-\infty}^{\infty} d\epsilon \langle A_{\mathbf{p}}(\epsilon)\rangle$$

where $\langle \dots \rangle$ denotes an average over $\theta = [0, 2\pi]$. Once these approximations are made, the integral over ϵ can now be explicitly carried out by extending the integral to the complex plane [9]. In this case, the energy integral for χ vanishes

$$\int_{-\infty}^{\infty} d\epsilon \left\langle \frac{\epsilon + \chi(z)}{z^2Z^2(z) - (\epsilon + \chi(x))^2 - \phi(z)^2\cos^2(2\theta)} \right\rangle = 0.$$

Note that if the sum over momenta is evaluated explicitly then χ will need to be retained. For the remaining self-energies the ϵ integrals are

$$\int_{-\infty}^{\infty} d\epsilon \left\langle \frac{zZ(z)}{z^2Z^2(z) - \epsilon^2 - \phi(z)^2\cos^2(2\theta)} \right\rangle = -\pi i \left\langle \frac{z\,\mathrm{sgn}(z)}{\sqrt{z^2 - \Delta^2(z)\cos^2(2\theta)}} \right\rangle$$

$$\int_{-\infty}^{\infty} d\epsilon \left\langle \frac{\phi(z)\cos^2(2\theta)}{z^2 Z^2(z) - \epsilon^2 - \phi(z)^2\cos^2(2\theta)} \right\rangle = -\pi i \left\langle \frac{\Delta(z)\cos^2(2\theta)\mathrm{sgn}(z)}{\sqrt{z^2 - \Delta^2(z)\cos^2(2\theta)}} \right\rangle$$

where the gap function $\Delta(\omega)\cos(2\theta) = \phi(\omega)\cos(2\theta)/Z(\omega)$ has been introduced and $\mathrm{sgn}(z)$ denotes the sign of z. The expressions for the self-energy are then

$$\begin{aligned} \Delta(\omega)Z(\omega) &= \sum_{\mu} \lambda_{\phi,\mu} \frac{\Omega_\mu}{2} \int_0^{\infty} dz Re \left\langle \frac{\Delta(\omega)\cos^2(\theta)}{\sqrt{z^2 - \Delta^2(\omega)\cos^2(\theta)}} \right\rangle K_-(\omega, z, \Omega_\nu) \\ \omega[1 - Z(\omega)] &= \sum_{\mu} \lambda_{z,\mu} \frac{\Omega_\mu}{2} \int_0^{\infty} dz Re \left\langle \frac{z}{\sqrt{z^2 - \Delta^2(\omega)\cos^2(\theta)}} \right\rangle K_+(\omega, z, \Omega_\mu) \end{aligned} \tag{B.7}$$

with kernels

$$\begin{aligned} K_{\pm}(\omega, z, \Omega) &= [n_b(\Omega) + n_f(-z)] \left[\frac{1}{\omega + \Omega + z + i\delta} \pm \frac{1}{\omega - \Omega - z + i\delta} \right] \\ &+ [n_b(\Omega) + n_f(z)] \left[\frac{1}{\omega - \Omega + z + i\delta} \pm \frac{1}{\omega + \Omega - z + i\delta} \right]. \end{aligned}$$

In the final step the integral over z has been rewritten over the range $[0, \infty)$, $\lambda_{(z,\phi)\mu} = 2N_f |g_{(z,\phi)\mu}|^2/\Omega_\nu$ has been introduced and the analytic continuation $i\omega_n \to \omega + i\delta$ has been explicitly performed.

Appendix C

Evaluation of the Trace over Fermion Degrees of Freedom

In deriving the DQMC methodology the trace over the Fermion degrees of freedom was performed through the use of the identity

$$\mathrm{Tr}\left(e^{c^\dagger T_1 c} e^{c^\dagger T_2 c} ... e^{c^\dagger T_n c}\right) = \det(I + e^{T_1} e^{T_2} \dots e^{T_n}). \tag{C.1}$$

A formal proof of this identity is presented here using Slater determinants [1].

First, consider a Hamiltonian $\hat{H} = \sum_{i,j} c_j^\dagger H_{i,j} c_i$, which is bilinear in creation and annihilation operators. The $N \times N$ matrix H is hermitian and therefore an orthogonal transformation U exists such that $U^\dagger H U = D$ where D is diagonal. The fermion operators in the diagonal basis are given by

$$\gamma_i = \sum_j U_{ij}^\dagger c_j \qquad \gamma_i^\dagger = \sum_j c_j^\dagger U_{ji} \tag{C.2}$$

and an arbitrary p-particle state is given by

$$\gamma_{\alpha_1}^\dagger \gamma_{\alpha_2}^\dagger \dots \gamma_{\alpha_p}^\dagger |0\rangle = \prod_{n=1}^{p} \left(\sum_j c_j^\dagger U_{j,\alpha_n} \right) |0\rangle = \prod_{n=1}^{p} \left(c^\dagger P\right)_n |0\rangle. \tag{C.3}$$

where $|0\rangle$ denotes the vacuum state, $c^\dagger = [c_1^\dagger, c_2^\dagger, \dots, c_n^\dagger]$ is a row vector and $(AP)_n$ denotes that the matrix product AP be evaluated using only the n-th column of the rectangular $N \times p$ matrix P. The state $\prod_n (c^\dagger P)_n |0\rangle$ is a Slater determinant and it is the solution to

[1] The treatment here is an expanded treatment of that given in reference [215], and corrects a few typographical errors which occur therein.

the bilinear Hamiltonian [215]. In order to prove the relation C.1 it first useful to derive two lemmas regarding Slater determinants.

Lemma 1: For a hermitian matrix T

$$e^{c^\dagger T c}\prod_{n=1}^{p}(c^\dagger P)_n|0\rangle = \prod_{n=1}^{p}(c^\dagger e^T P)_n|0\rangle. \tag{C.4}$$

In other words, when a Slater determinant is multiplied by the operator $\exp(c^\dagger T c)$ the result is itself a Slater determinant.

Proof. It is convenient to first diagonalize $U^\dagger T U = \lambda$ yielding

$$\begin{aligned} e^{c^\dagger T c}\prod_{n=1}^{p}(c^\dagger P)_n|0\rangle &= e^{\gamma^\dagger\lambda\gamma}\prod_{n=1}^{p}(\gamma^\dagger U^\dagger P)_n|0\rangle \\ &= e^{\gamma^\dagger\lambda\gamma}\left(\gamma^\dagger U^\dagger P\right)_{\alpha_1}\left(\gamma^\dagger U^\dagger P\right)_{\alpha_2}\ldots\left(\gamma^\dagger U^\dagger P\right)_{\alpha_p}|0\rangle. \end{aligned} \tag{C.5}$$

Each of the terms appearing in the brackets is simply a sum over the Fermion operators $\gamma^\dagger$. Explicitly writing out these sums yields

$$\begin{aligned} e^{c^\dagger T c}\prod_{n=1}^{p}(c^\dagger P)_n|0\rangle = e^{\gamma^\dagger\lambda\gamma} \times & \left[\gamma_1^\dagger(U^\dagger P)_{\alpha_1,1}+\ldots+\gamma_N^\dagger(U^\dagger P)_{\alpha_1,N}\right]\times \\ & \left[\gamma_1^\dagger(U^\dagger P)_{\alpha_2,1}+\ldots+\gamma_N^\dagger(U^\dagger P)_{\alpha_2,N}\right]\times\ldots \\ & \left[\gamma_1^\dagger(U^\dagger P)_{\alpha_p,1}+\ldots+\gamma_N^\dagger(U^\dagger P)_{\alpha_p,N}\right]|0\rangle \end{aligned} \tag{C.6}$$

Here, $(U^\dagger P)_{\alpha,i}$ denotes the i-th row of the column vector produced by multiplying the $N\times N$ matrix $U^\dagger$ with the α column of the rectangular matrix P. Expanding the products in Eq. C.6 will produce a sum of terms which are proportional to products of N fermion creation operators. Any term which has a particular operator $\gamma_i^\dagger$ appearing more than once is identically zero once it acts upon the vacuum state $|0\rangle$. Therefore, all that remains is a sum of terms in which each of the $\gamma_i^\dagger$'s appear only once and Eq. C.6 can be reduced to a sum over all permutations of of the product $\gamma_1^\dagger\ldots\gamma_N^\dagger$

$$\begin{aligned} e^{c^\dagger T c}\prod_{n=1}^{p}(c^\dagger P)_n|0\rangle &= \sum_{\{\gamma_i\}} e^{\gamma^\dagger\lambda\gamma}\gamma_1^\dagger\gamma_2^\dagger\ldots\gamma_N^\dagger|0\rangle(U^\dagger P)_{\alpha_1,1}\ldots(U^\dagger P)_{\alpha_p,p} \\ &= \sum_{\{\gamma_i\}} \gamma_1^\dagger e^{\lambda_{1,1}\gamma_1^\dagger\gamma_1}\gamma_2^\dagger e^{\lambda_{2,2}\gamma_2^\dagger\gamma_2}\ldots\gamma_N^\dagger e^{\lambda_{N,N}\gamma_N^\dagger\gamma_N}|0\rangle(U^\dagger P)_{\alpha_1,1}\ldots(U^\dagger P)_{\alpha_p,p} \\ &= \sum_{\gamma_i} \gamma_1^\dagger e^{\lambda_{1,1}}\gamma_2^\dagger e^{\lambda_{2,2}}\ldots\gamma_N^\dagger e^{\lambda_{N,N}}|0\rangle(U^\dagger P)_{\alpha_1,1}\ldots(U^\dagger P)_{\alpha_p,p} \\ &= \prod_{n=1}^{p}(\gamma^\dagger e^\lambda U^\dagger P)_n|0\rangle. \end{aligned}$$

In the final step the sum has been recombined into a product, undoing the expansion which was performed in equation C.6. Transforming back to the original basis then gives

$$e^{c^\dagger T c}\prod_{n=1}^{p}(c^\dagger P)_n|0\rangle = \prod_{n=1}^{p}(\gamma^\dagger e^\lambda U^\dagger P)_n|0\rangle = \prod_{n=1}^{p}(c^\dagger U e^\lambda U^\dagger P)_n|0\rangle = \prod_{n=1}^{p}(c^\dagger e^T P)_n|0\rangle. \quad \text{(C.7)}$$

□

Lemma 2: The overlap of two p-particle Slater determinants $|\psi\rangle = \prod_{n=1}^{p}(c^\dagger P)|0\rangle$ and $|\tilde{\psi}\rangle = \prod_{\tilde{n}=1}^{p}(c^\dagger \tilde{P})|0\rangle$ is

$$\langle\psi|\tilde{\psi}\rangle = \det[P^\dagger \tilde{P}]. \quad \text{(C.8)}$$

Proof.

$$\begin{aligned}\langle\psi|\tilde{\psi}\rangle &= \langle 0|\prod_{n=1}^{p}(P^\dagger c)_n \prod_{\tilde{n}=1}^{p}(c^\dagger P)_{\tilde{n}}|0\rangle \\ &= \sum_{\{c_\alpha\}}\sum_{\{c_\beta\}}(P^\dagger)_{\alpha_p,p}\ldots(P^\dagger)_{\alpha_1,1}(\tilde{P})_{\beta_1,1}\ldots(\tilde{P})_{\beta_p,p}\times\langle 0|c^\dagger_{\alpha_p}\ldots c^\dagger_{\alpha_1}c_{\beta_1}\ldots c_{\beta_p}|0\rangle\end{aligned}$$

In the second step the products have been expanded as before. The product of fermion creation operators is zero unless for every creation operator $c^\dagger_{\alpha_i}$ there is a corresponding annihilation operator c_{β_j} and each set of operators appears only once. The product of fermion operators is now reordered such that

$$\langle\psi|\tilde{\psi}\rangle = \sum_{\{c_\alpha\}}|c_{\alpha_1}c_{\alpha_2}\ldots c_{\alpha_p}|0\rangle|^2\times\sum_{\pi}(-1)^\pi P^\dagger_{\alpha_p,p}\ldots P^\dagger_{\alpha_1,1}\tilde{P}_{\pi(\alpha_1),1}\ldots\tilde{P}_{\pi(\alpha_p),p}$$

where $\pi(\alpha_i)=\beta_j$ is the permutation required to produce this ordering. The factor $(-1)^\pi$ is the sign induced by reordering the Fermion operators.

$$\begin{aligned}\langle\psi|\tilde{\psi}\rangle &= \sum_{\{c_\alpha\}}\sum_{\pi}(-1)^\pi P^\dagger_{\alpha_p,p}\ldots P^\dagger_{\alpha_1,1}\tilde{P}_{\alpha_1,\pi^{-1}(1)}\ldots\tilde{P}_{\alpha_p,\pi^{-1}(p)} \\ &= \sum_{\pi}(-1)^{\pi^{-1}}(P^\dagger\tilde{P})_{1,\pi^{-1}(1)}\ldots(P^\dagger\tilde{P})_{p,\pi^{-1}(p)}\end{aligned}$$

The final line is the Leibniz formula for the determinant $\mathrm{Det}(P^\dagger P)$. □

All of the ingredients are now in place to prove the identity

$$\mathrm{Tr}[e^{c^\dagger T_1 c}e^{c^\dagger T_2 c}\ldots e^{c^\dagger T_N c}] = \det(I + e^{T_1}e^{T_2}\ldots e^{T_N}) \quad \text{(C.9)}$$

where I is the identity matrix. Let $B = \exp(T_1)\ldots\exp(T_N)$ and $U = \exp(c^\dagger T_1 c)\ldots\exp(c^\dagger T_N c)$ and write out the right hand side of Eq. C.9 using the Leibniz formula for the determinant. (Let S_n denote the set of permutations of the matrix indicies of B.)

$$\begin{aligned}
\det(I+B) &= \sum_{\pi\in S_n}(-1)^\pi (I+B)_{\pi(1),1}\ldots(I+B)_{\pi(N),N} \\
&= \sum_{\pi\in S_n}(-1)^\pi (\delta_{\pi(1),1}+B_{\pi(1),1})\ldots(\delta_{\pi(N_s),N}+B_{\pi(N),N}) \\
&= \sum_{\pi\in S_n}(-1)^\pi \delta_{\pi(1),1}\delta_{\pi(2),2}\ldots\delta_{\pi(N),N} \\
&+ \sum_i\sum_{\pi\in S_n}(-1)^\pi B_{\pi(i),i}\delta_{\pi(1),1}\ldots\bar{\delta}_{\pi(i),i}\ldots\delta_{\pi(N),N} \\
&+ \sum_{j>i}\sum_{\pi\in S_n}(-1)^\pi B_{\pi(i),i}B_{\pi(j),j}\delta_{\pi(1),1}\ldots\bar{\delta}_{\pi(i),i}\ldots\bar{\delta}_{\pi(j),j}\ldots\delta_{\pi(N),N}+\ldots
\end{aligned}$$

where $\bar{\delta}_{\pi(i),i}$ indicates that this term is omitted from the product. Consider now the second term of the expansion in greater detail. The permutation operator $i=\pi(j)$ performs a one-to-one mapping of the set of indices onto themselves. Therefore, the second term will vanish for all permutations apart from the identity permutation ($\pi(i)=i$, $\pi(j)=j$) and the transposition permutation ($\pi(i)=j$, $\pi(j)=i$). This set of permutations can be represented by a $N\times 2$ rectangular matrix P where the j-th row of the i-th column is set to 1 and the remaining elements are zero. The second term can therefore be writen as

$$\sum_{j>i} B_{i,i}B_{j,j}\delta_{\pi(i),i}\delta_{\pi(j),j} - B_{i,j}B_{j,i}\delta_{\pi(j),i}\delta_{\pi(i),j} = \sum_{j>i}\det(P^\dagger BP). \tag{C.10}$$

Equations C.4 and C.8 can now be applied to express this result in terms of fermion operators

$$\mathrm{Det}(P^\dagger BP) = \mathrm{Det}P^\dagger\tilde{P} = \langle P|\tilde{P}\rangle = \langle P|U|P\rangle = \langle 0|c_i c_j U c_j^\dagger c_i^\dagger|0\rangle. \tag{C.11}$$

The same argument can then be applied to the higher order terms. Therefore,

$$\det(I+e^T) = \langle 0|0\rangle + \sum_i\langle 0|c_i U c_i^\dagger|0\rangle + \sum_{j>i}\langle 0|c_i c_j U c_j^\dagger c_i^\dagger|0\rangle + \sum_{k>j>i}\langle 0|c_i c_j c_k U c_k^\dagger c_j^\dagger c_i^\dagger|0\rangle + \ldots$$

which is the definition of $\mathrm{Tr}(U)$ evaluated in Fock space.

Appendix D

UDR Decomposition

In the DQMC formalism, the electron Green's function $G_\sigma(l)$ for propagation through the auxiliary field $\{s_{i,l}\}$ at imaginary time slice l is given by the matrix product

$$G_\sigma^{-1} = I + B_l^\sigma \dots B_1^\sigma B_L^\sigma \dots B_{l+1}^\sigma, \tag{D.1}$$

where the matrix B_l is defined as $B_l^{\uparrow,\downarrow} = \exp(\mp\Delta\tau\lambda v(l))\exp(-\Delta\tau K)$. Here K is an $N \times N$ hermitian matrix representing the kinetic and onsite terms of the Hamiltonian and $v(l)$ is an $N \times N$ identity matrix whose diagonal elements are $v_{i,i}(l) = s_{i,l}$ (please refer to chapter 7 for further details).

In general, the B_l matrices are stiff with eigenvalues that scale as $\exp(-\beta E)$ and $\exp(\beta E)$, where E is some energy scale in the problem. Therefore, as the temperature is lowered, the matrix product

$$A^\sigma(l) = B_l^\sigma \dots B_1^\sigma B_L^\sigma \dots B_{l+1}^\sigma \tag{D.2}$$

is numerically ill-defined. In order to circumvent this issue, the product must be evaluated using matrix factorization methods. These methods are standard linear procedures and are commonly referred to as UDR or QR decompositions and are included in most numerical linear algebra libraries such as LaPack or Matlab [217]. The stabilization procedure is as follows. Suppose that the first m right matrix multiplications in Eq. D.2 can be evaluated without producing a numerical instability (from here on the σ subscript is suppressed in order to tidy the notation)

$$A(l) = B_l \dots B_1 B_L \dots B_{l+1+m} A_1 \qquad A_1 = B_{l+m} \dots B_{l+1}. \tag{D.3}$$

The matrix A_1 is then factored using a UDR-decomposition $A_1 = U_1 D_1 R_1$, where U_1 is an orthogonal matrix, D_1 is a diagonal matrix and R_1 is an upper triangular matrix with ones along the diagonal. The diagonal elements of D_1 contain the large variations associated

with the eigenvalues of the original matrix product while U_1 and R_1 are generally well behaved for numerical work. Once this decomposition has been completed, D_1 and R_1 are set aside in storage and U_1 is carried forward and the next m right matrix multiplications are performed

$$A(l) = B_l \dots B_{l+1+2m} A_2 D_1 R_1 \qquad A_2 = B_{l+2m} \dots B_{l+m+1} U_1. \tag{D.4}$$

The matrix A_2 is then multiplied on the right by D_1. This operation only rescales the columns of A_2 and is numerically stable. Then, a second UDR decomposition is performed $A_2 = U_2 D_2 R_2$ to obtain

$$A(l) = B_l \dots B_{l+1+2m} U_2 D_2 R_2 R_1 = B_l \dots B_{l+1+2m} U_2 D_2 R_2' \tag{D.5}$$

where in the last step $R_2' = R_2 R_1$. Again, the product of the right triangular matrices is generally numerically stable due to the fact their diagonal elements are one by construction. This procedure is then iterated until the complete product has been evaluated leaving $A(l) = U_{L/m} D_{L/m} R_{L/m}$. The electron Green's function is then given by

$$\begin{aligned} G^{-1}(l) &= I + U_{L/m} D_{L/m} R_{L/m} \\ &= U_{L/m} (U_{L/m}^{-1} R_{L/m}^{-1} + D_{L/m}) R_{L/m} \\ &= U_{L/m} (U' D' R') R_{L/m} \qquad (U_{L/m}^{-1} R_{L/m}^{-1} + D_{L/m} = U' D' R') \\ &= UDR \end{aligned}$$

In the last step, a final UDR decomposition has been performed in the result from the previous line. The final inversion required to obtain the Green's function stable since the problematic pieces are contained within the diagonal elements of D. It should also be noted that the number of matrix multiplications m that can be performed between the factoring procedure is variable and will decrease as the temperature is lowered. For a Hubbard interaction strength $U \sim 8t$ and $\beta \sim 3 - 4$, m should be set to 4-6.

Bibliography

[1] J. G. Bednorz and K. A. Müller, "Possible high-T_c superconductivity in the Ba-La-Cu-O system," *Zeitschrift für Physik B Condensed Matter*, vol. 64, p. 189, 1986. 1, 7

[2] L. N. Cooper, "Bound electron pairs in a degenerate fermi gas," *Physical Review*, vol. 104, p. 1189, 1956. 1, 101

[3] J. Bardeen, L. N. Cooper, and J. R. Schrieffer, "Theory of superconductivity," *Physical Review*, vol. 108, p. 1175, 1957. 1, 101

[4] J. Bardeen, L. N. Cooper, and J. R. Schrieffer, "Microscopic theory of superconductivity," *Physical Review*, vol. 106, p. 162, 1957. 1, 101

[5] P. A. Lee, N. Nagaosa, and X.-G. Wen, "Doping a mott insulator: Physics of high-temperature superconductivity," *Reviews of Modern Physics*, vol. 78, p. 17, 2006. 2, 6, 7

[6] W. S. Lee, I. M. Vishik, K. Tanaka, D. H. Lu, T. Sasagawa, N. Nagaosa, T. P. Devereaux, Z. Hussain, and Z.-X. Shen, "Abrupt onset of a second energy gap at the superconducting transition of underdoped Bi2212," *Nature*, vol. 450, p. 81, 2007. 2, 11

[7] K. Tanaka, W. S. Lee, D. H. Lu, A. Fujimori, T. Fujii, Risdiana, I. Teraskai, D. J. Scalapino, T. P. Devereaux, Z. Hussain, and Z.-X. Shen, "Distinct fermi-momentum-dependent energy gaps in deeply underdoped Bi2212," *Science*, vol. 314, p. 1910, 2006. 2, 11

[8] A. Mourachkine, *High-Temperature Superconductivity in Cuprates - The Nonlinear Mechanism and Tunneling Measurements*. Kluwer Academic Publshers, 1st ed., 2002. 2

[9] G. D. Mahan, *Many-Particle Physics*. Plenum Press, 2nd ed., 1990. 2, 13, 29, 36, 46, 48, 51, 54, 89, 90, 101, 115, 130, 158

[10] N. W. Ashcroft and N. D. Mermin, *Solid State Physics*. Nelson Thomson Learning, 1st ed., 1976. 2

[11] S. Maekawa, T. Tohyama, S. E. Barnes, S. Ishihara, W. Koshibae, and G. Khaliullin, *Physics of Transition Metal Oxides*, vol. 144. Springer Series in Solid-State Science, 2004. 3

[12] A. J. Leggett, "Towards a complete theory of high-T_c," *Nature Physics*, vol. 2, p. 134, 2006. 3

[13] W. E. Pickett, "Electronic structure of the high-T_c oxides," *Reviews of Modern Physics*, vol. 61, p. 433, 1989. 4, 5

[14] F. C. Zhang and T. M. Rice, "Effective hamiltonian for the superconducting Cu oxides," *Physical Review B*, vol. 37, p. 3759, 1988. 6

[15] K. Fujita, T. Noda, K. M. Kojima, H. Eisaki, and S. Uchida, "Effect of disorder outside the CuO_2 planes on T_c of copper oxide superconductors," *Physical Review Letters*, vol. 95, p. 097006, 2005. 6

[16] H. Eisaki, N. Kaneko, D. L. Feng, A. Damascelli, P. K. Mang, K. M. Shen, Z.-X. Shen, and M. Greven, "Effect of chemical inhomogeneity in bismuth-based copper oxide superconductors," *Physics Review B*, vol. 69, p. 064512, 2004. 6, 105

[17] S. Graser, P. J. Hirschfeld, L.-Y. Zhu, and T. Dahm, "T_c suppression and resistivity in cuprates with out of plane defects," *Physical Review B*, vol. 76, p. 054516, 2007. 6

[18] Y. Ohta, T. Tohyama, and S. Maekawa, "Apex oxygen and critical temperature in copper oxide superconductors: Universal correlation with the stability of local singlets," *Physics Review B*, vol. 43, p. 2968, 1991. 7, 46, 70, 105, 107

[19] A. Iyo, Y. Tanaka, M. Tokumoto, and H. Ihara, "High-pressure synthesis and properties of $Ba_2Ca_{n-1}Cu_nO_{2n}(O,F)_2$ ($n = 2 - 5$) superconductors," *Physica C*, vol. 366, p. 43, 2001. 7

[20] Y. Chen, A. Iyo, W. Yang, X. Zhou, D. Lu, H. Eisaki, T. P. Devereaux, Z. Hussain, and Z.-X. Shen, "Anomalous fermi-surface dependent pairing in a self-doped high-T_c superconductor," *Physical Review Letters*, vol. 97, p. 236401, 2006. 7

[21] Y. Chen, A. Iyo, W. Yang, A. Ino, M. Arita, S. Johnston, H. Eisaki, H. Namatame, M. Taniguchi, T. P. Devereaux, Z. Hussain, and Z.-X. Shen, "Unusual layer-dependent charge distribution, collective mode coupling, and superconductivity in multilayer cuprate $Ba_2Ca_3Cu_4O_8F_2$," *Physical Review Letters*, vol. 103, p. 036403, 2009. 7, 11, 15, 16, 17

[22] E. Pavarini, I. Dasgupta, T. Saha-Dasgupta, O. Jepsen, and O. K. Andersen, "Band-structure trend in hole-doped cuprates and correlation with $T_{c,max}$," *Physical Review Letters*, vol. 87, p. 047003, 2001. 7, 105

[23] S. Johnston, "Anisotropic electron-phonon coupling in cuprate families of high-temperature superconductors," Master's thesis, University of Waterloo, Canada, 2006. 7, 22, 33, 36, 37, 38, 39, 40, 42, 45, 47, 50, 51, 55, 59, 68, 69, 70, 71, 77

[24] K. McElroy, J. Lee, J. A. Slezak, D.-H. Lee, H. Eisaki, S. Uchida, and J. C. Davis, "Atomic-scale sources and mechanism of nanoscale electronic disorder in $Bi_2Sr_2CaCu_2O_{8+\delta}$," *Science*, vol. 309, p. 1048, 2005. 7, 29, 30, 85, 106, 114

[25] T. S. Nunner, B. M. Andersen, A. Melikyan, and P. J. Hirschfeld, "Dopant-modulated pair interaction in cuprate superconductors," *Physical Review Letters*, vol. 95, p. 177003, 2005. 7, 106, 111

[26] T. S. Nunner, W. Chen, B. M. Andersen, A. Melikyan, and P. J. Hirschfeld, "Fourier transform spectroscopy of d-wave quasiparticles in the presence of atomic scale pairing disorder," *Physical Review B*, vol. 73, p. 104511, 2006. 7

[27] J.-X. Zhu, K. McElroy, J. Lee, T. P. Devereaux, Q. Si, J. C. Davis, and A. V. Balatsky, "Effects of pairing potential scattering on fourier-transformed inelastic tunneling spectra of high-T_c cuprate superconductors with bosonic modes," *Physical Review Letters*, vol. 97, p. 177001, 2006. 7, 111

[28] R. Jamei, J. Robertson, E.-A. Kim, A. Fang, A. Kapitulnik, and S. A. Kivelson, "Inferring effective interactions from the local density of states: Application to STM data from $Bi_2Sr_2CaCu_2O_{8+\delta}$," *Physical Review B*, vol. 74, p. 174521, 2006. 7

[29] B. M. Andersen, P. H. Hirschfeld, and J. A. Slezak, "Superconducting gap variations induced by structural supermodulation in $Bi_2Sr_2CaCu_2O_8$," *Physical Review B*, vol. 76, p. 020507, 2007. 7, 106

[30] T. P. Devereaux, T. Cuk, Z.-X. Shen, and N. Nagaosa, "Anisotropic electron-phonon interaction in the cuprates," *Physical Review Letters*, vol. 93, p. 117004, 2004. 7, 8, 15, 19, 21, 22, 33, 36, 37, 38, 40, 45, 47, 48, 55, 59, 60, 72, 76, 77, 83, 84

[31] T. Cuk, F. Baumberger, D. H. Lu, N. Ingle, X. J. Zhou, H. Eisaki, N. Kaneko, Z. Hussain, T. P. Devereaux, N. Nagaosa, and Z.-X. Shen, "Coupling of the B_{1g} phonon to the antinodal electronic states of $Bi_2Sr_2Ca_{0.92}Y_{0.08}Cu_2O_{8+\delta}$," *Physical Review Letters*, vol. 93, p. 117003, 2004. 7, 11, 15, 16, 17, 18, 19, 20, 21, 22, 56, 61, 65, 72, 76

[32] Z. J. Zhou, T. Cuk, T. P. Devereaux, N. Nagaosa, and Z.-X. Shen, "Angle-resolved photoemission spectroscopy on electronic structure and electron-phonon coupling in cuprate superconductors," in *Handbook of High-Temperature SUperconductivity: Theory and Experiment* (J. R. Schrieffer, ed.), ch. 3, p. 87, Springer, 2007. 7, 12, 102

[33] S. Johnston, W. S. Lee, Y. Chen, E. A. Nowadnick, B. Moritz, Z.-X. Shen, and T. P. Devereaux, "Material and doping dependence of the nodal and anti-nodal dispersion renormalizations in single- and multilayer cuprates," *Advances in Condensed Matter Physics*, vol. 2010, p. 968304, 2010. 7, 15, 16, 17, 18, 19, 21, 22, 33, 36, 59, 69

[34] T. Dahm, V. Hinkov, S. V. Borisenko, A. A. Kordyuk, V. B. Zabolotnyy, J. Fink, B. Büchner, D. J. Scalapino, W. Hanke, and B. Keimer, "Strength of the spin-fluctuation-mediated pairing interaction in a high-temperature superconductor," *Nature Physics*, vol. 5, p. 217, 2009. 7, 15, 21

[35] D. J. Scalapino, "Numerical studies of the 2D Hubbard model," in *Handbook of High-Temperature Superconductivity: Theory and Experiment* (J. R. Schrieffer, ed.), ch. 13, p. 495, Springer, 2007. 7

[36] P. W. Anderson, "Is there glue in cuprate superconductors?," *Science*, vol. 316, p. 1705, 2007. 7, 21

[37] B. Batlogg, R. J. Cava, A. Jayaraman, R. B. van Dover, G. A. Kourouklis, S. Sunshine, D. W. Murphy, L. W. Rupp, H. S. Chen, A. White, K. T. Short, A. M. Mujsce, and E. A. Rietman, "Isotope effect in the high-T_c superconductors $Ba_2YCu_3O_7$ and $Ba_2EuCu_3O_7$," *Physical Review Letters*, vol. 58, p. 2333, 1987. 7, 102

[38] L. C. Bourne, M. F. Crommie, A. Zettl, H.-C. zur Loye, S. W. Keller, K. L. Leary, A. M. Stacy, K. J. Chang, M. L. Cohen, and D. E. Morris, "Search for isotope effect in superconducting Y-Ba-Cu-O," *Physical Review Letters*, vol. 58, p. 2337, 1987. 7, 102

[39] P. J. Yvon, R. B. Schwarz, C. B. Pierce, L. Bernardez, A. Conner, and R. Meisenheimer, "Oxygen isotope effect in $YBa_2Cu_3O_7$ prepared by burning YBa_2Cu_3 in ^{16}O and ^{18}O," *Physical Review B*, vol. 39, p. 6690, 1989. 7

[40] M. Gurvitch and A. T. Fiory, "Resistivity of $La_{1.825}Sr_{0.175}CuO_4$ and $YBa_2Cu_3O_7$ to 1100 K: Absence of saturation and its implications," *Physical Review Letters*, vol. 59, p. 1337, 1987. 8

[41] S. Martin, A. T. Fiory, R. M. Fleming, L. F. Schneemeyer, and J. V. Waszczak, "Normal-state transport properties of $Bi_{2+x}Sr_{2-y}CuO_{6+\delta}$," *Physical Review B*, vol. 41, p. 846, 1990. 8

[42] M. K. Crawford, M. N. Kunchur, W. E. Farneth, E. M. McCarron, and S. J. Poon, "Anomalous oxygen isotope effect in $La_{2-x}Sr_xCuO_4$," *Physical Review B*, vol. 41, p. 282, 1990. 8

[43] T. Schneider and H. Keller, "Isotope effects in underdoped cuprate superconductors: A quantum critical phenomenon," *Physical Review Letters*, vol. 86, p. 4899, 2001. 8

[44] T. P. Devereaux, A. Virosztek, and A. Zawadowski, "Neutron scattering and the B_{1g} phonon in the cuprates," *Physical Review B*, vol. 59, p. 14618, 1999. 8, 22, 23, 35, 36, 37, 40, 111

[45] R. Zeyher and M. L. Kulić, "Renormalization of the electron-phonon interaction by strong electronic correlations in high-T_c superconductors," *Physical Review B*, vol. 53, p. 2850, 1996. 8, 94, 129, 133

[46] N. Bulut and D. J. Scalapino, "$d_{x^2-y^2}$ symmetry and the pairing mechanism," *Physical Review B*, vol. 54, p. 14971, 1996. 8

[47] Z. B. Huang, W. Hanke, E. Arrigoni, and D. J. Scalapino, "Electron-phonon vertex in the two-dimensional one-band Hubbard model," *Physical Review B*, vol. 68, p. 220507(R), 2003. 8, 94, 129, 132, 133

[48] W. McMillan and J. Rowell, "Tunneling and strong-coupling superconductivity," in *Superconductivity* (R. D. Parks, ed.), ch. 11, p. 561, Marcel Dekker, Inc., 1969. 8, 21, 30, 75, 76, 79, 101

[49] J. M. Rowell and W. L. McMillan, "Electron interference in a normal metal induced by superconducting contacts," *Physical Review Letters*, vol. 16, p. 453, 1966. 8, 75, 76

[50] W. L. McMillan and J. M. Rowell, "Lead phonon spectrum calculated from superconducting density of states," *Physical Review Letters*, vol. 14, p. 108, 1965. 8, 75, 76

[51] K. M. Shen, F. Ronning, W. Meevasana, D. H. Lu, N. J. C. Ingle, F. Baumberger, W. S. Lee, L. L. Miller, Y. Kohsaka, M. Azuma, M. Takano, H. Takagi, and Z.-X. Shen, "Angle-resolved photoemission studies of lattice polaron formation in the cuprate $Ca_2CuO_2Cl_2$," *Physical Review B*, vol. 75, p. 075115, 2007. 8, 131

[52] A. Damascelli, Z. Hussain, and Z.-X. Shen, "Angle-resolved photoemission studies of the cuprate superconductors," *Reviews of Modern Physics*, vol. 75, p. 473, 2003. 11, 12, 15

[53] C. G. Olson, R. Liu, A.-B. Yang, D. W. Lynch, A. J. Arko, R. S. List, B. W. Veal, Y. C. Chang, P. Z. Jiang, and A. P. Paulikas, "Superconducting gap in Bi-Sr-Ca-Cu-O by high-resolution angle-resolved photoelectron spectroscopy," *Science*, vol. 245, p. 731, 1989. 11

[54] Z.-X. Shen, D. S. Dessau, B. O. Wells, D. M. King, W. E. Spicer, A. J. Arko, D. Marshall, L. W. Lombardo, A. Kapitulnik, P. Dickinson, S. Doniach, J. DiCarlo, T. Loeser, and C. H. Park, "Anomalously large gap anisotropy in the a-b plane of $Bi_2Sr_2CaCu_2O_{8+\delta}$," *Physical Review Letters*, vol. 70, p. 1553, 1993. 11

[55] H. Ding, T. Yokoya, J. C. Campuzano, T. Takahashi, M. Randeria, M. R. Norman, T. Mochiku, K. Kadowaki, and J. Giapintzakis, "Spectroscopic evidence for a pseudogap in the normal state of underdoped high-T_c superconductors," *Nature*, vol. 382, p. 51, 1996. 11

[56] D. S. Dessau, B. O. Wells, Z.-X. Shen, W. E. Spicer, A. J. Arko, R. S. List, D. B. Mitzi, and A. Kapitulnik, "Anomalous spectral weight transfer at the superconducting transition of $Bi_2Sr_2CaCu_2O_{8+\delta}$," *Physical Review Letters*, vol. 66, p. 2160, 1991. 11, 15, 18

[57] T. Valla, A. V. Fedorov, P. D. Johnson, B. O. Wells, S. L. Hulbert, Q. Li, G. D. Gu, and N. Koshizuka, "Evidence for quantum critical behavior in the optimally doped cuprate $Bi_2Sr_2CaCu_2O_{8+\delta}$," *Science*, vol. 285, p. 2110, 1999. 11, 15, 16

[58] P. V. Bogdanov, A. Lanzara, S. A. Kellar, X. J. Zhou, E. D. Lu, W. J. Zheng, G. Gu, J.-I. Shimoyama, K. Kishio, H. Ikeda, R. Yoshizaki, Z. Hussain, and Z.-X. Shen, "Evidence for an energy scale for quasiparticle dispersion in $Bi_2Sr_2CaCu_2O_8$," *Physical Review Letters*, vol. 85, p. 2581, 2000. 11, 15, 16, 17

[59] P. D. Johnson, T. Valla, A. V. Fedorov, Z. Yusof, B. O. Wells, Q. Li, A. R. Moodenbaugh, G. D. Gu, N. Koshizuka, C. Kendziora, S. Jian, and D. G. Hinks, "Doping and temperature dependence of the mass enhancement observed in the cuprate $Bi_2Sr_2CaCu_2O_{8+\delta}$," *Physical Review Letters*, vol. 87, p. 177007, 2001. 11, 15, 21

[60] A. Kaminski, M. Randeria, J. C. Campuzano, M. R. Norman, H. Fretwell, J. Mesot, T. Sato, T. Takahashi, and K. Kadowaki, "Renormalization of spectral line shape and dispersion below T_c in $Bi_2Sr_2CaCu_2O_{8+\delta}$," *Physical Review Letters*, vol. 86, p. 1070, 2001. 11, 15, 17, 19, 20, 21, 59, 61

[61] A. Lanzara, P. V. Bogdanov, X. J. Zhou, S. A. Kellar, D. L. Feng, E. D. Lu, T. Yoshida, H. Eisaki, A. Fujimori, K. Kishio, J.-I. Shimoyama, T. Noda, S. Uchida, Z. Hussain, and Z.-X. Shen, "Evidence for ubiquitous strong electron-phonon coupling in high-temperature superconductors," *Nature*, vol. 412, p. 510, 2001. 11, 15, 16, 17, 21, 22, 72

[62] X. J. Zhou, T. Yoshida, A. Lanzara, P. V. Bogdanov, S. A. Kellar, K. M. Shen, W. L. Yang, F. Ronning, T. Sasagawa, T. Kakeshita, T. Noda, H. Eisaki, S. Uchida, C. T. Lin, F. Zhou, J. W. Xiong, W. X. Ti, Z. X. Zhao, A. Fujimori, Z. Hussain, and Z.-X. Shen, "High-temperature superconductors: Universal nodal fermi velocity," *Nature*, vol. 423, p. 398, 2003. 11, 15, 16, 17

[63] A. D. Gromko, A. V. Fedorov, Y.-D. Chuang, J. D. Koralek, Y. Aiura, Y. Yamaguchi, K. Oka, Y. Ando, and D. S. Dessau, "Mass-renormalized electronic excitations at (π,0) in the superconducting state of $Bi_2Sr_2CaCu_2O_{8+\delta}$," *Physical Review B*, vol. 68, p. 174520, 2003. 11, 15, 20, 21, 22

[64] J. D. Koralek, J. F. Douglas, N. C. Plumb, Z. Sun, A. V. Fedorov, M. M. Murnane, H. C. Kapteyn, S. T. Cundiff, Y. Aiura, K. Oka, H. Eisaki, and D. S. Dessau, "Laser based angle-resolved photoemission, the sudden approximation and quasiparticle-like spectral peaks in $Bi_2Sr_2CaCu_2O_{8+\delta}$," *Physical Review Letters*, vol. 96, p. 017005, 2006. 11, 15, 16

[65] D. J. Scalapino, "The electron-phonon interaction and strong-coupling superconductors," in *Superconductivity* (R. D. Parks, ed.), ch. 10, p. 449, Marcel Dekker, Inc., 1969. 13, 21, 30, 49, 75, 76, 78, 79, 157

[66] M. R. Norman, H. Ding, J. C. Campuzano, T. Takeuchi, M. Randeria, T. Yokoya, T. Takahashi, T. Mochiku, and K. Kadowaki, "Unusual dispersion and line shape of the superconducting state spectra of $Bi_2Sr_2CaCu_2O_{8+\delta}$," *Physical Review Letters*, vol. 79, p. 3506, 1997. 15, 59, 60

[67] S. V. Borisenko, A. A. Kordyuk, V. Zabolotnyy, J. Geck, D. Inosov, A. Koitzsch, J. Fink, M. Knupher, B. Büchner, V. Hinkov, C. T. Lin, B. Keimer, T. Wolf, S. G. Chiuzbv̆ain, L. Patthey, and R. Follath, "Kinks, nodal bilayer splitting and interband scattering in $YBa_2Cu_3O_{6+x}$," *Physical Review Letters*, vol. 96, p. 117004, 2006. 15, 16, 21, 68

[68] T. K. Kim, A. A. Kordyuk, S. V. Borisenko, A. Koitzsch, M. Knupfer, H. Berger, and J. Fink, "Doping dependence of the mass enhancement in $(Pb,Bi)_2Sr_2CaCu_2O_8$ at the antinodal point in the superconducting and normal states," *Physical Review Letters*, vol. 91, p. 167002, 2003. 15, 21, 59

[69] T. Cuk, D. H. Lu, X. J. Zhou, Z.-X. Shen, T. P. Devereaux, and N. Nagaosa, "A review of electron-phonon coupling seen in the high-t_c superconductors by angle-resolved photoemission studies (ARPES)," *Physica Status Solidi (b)*, vol. 242, p. 11, 2005. 15, 19, 22

[70] T. Sato, H. Matsui, T. Takahaski, H. Ding, H.-B. Yang, S.-C. Wang, T. Fujii, T. Watanabe, A. Matsuda, T. Terashima, and K. Kadowaki, "Observation of band renormalization effects in hole-doped high-T_c superconductors," *Physica Review Letters*, vol. 91, p. 157003, 2003. 15, 59, 61

[71] W. S. Lee, W. Meevasana, S. Johnston, D. H. Lu, I. M. Vishik, R. G. Moore, H. Eisaki, N. Kaneko, T. P. Devereaux, and Z. X. Shen, "Superconductivity-induced self-energy evolution of the nodal electron of optimally doped $Bi_2Sr_2Ca_{0.92}Y_{0.08}Cu_2O_{8+\delta}$," *Physical Review B*, vol. 77, p. 140504(R), 2008. 15, 17, 21, 22, 25, 33, 56, 59, 62

[72] W. S. Lee, S. Johnston, T. P. Devereaux, and Z.-X. Shen, "Aspects of electron-phonon self-energy revealed from angle-resolved photoemission spectroscopy," *Physical Review B*, vol. 75, p. 195116, 2007. 15, 17, 21, 22, 33, 51, 59, 72, 83, 85

[73] X. J. Zhou, J. Shi, T. Yoshida, T. Cuk, W. L. Yang, V. Brouet, J. Nakamura, N. Mannella, S. Komiya, Y. Ando, F. Zhou, W. X. Ti, J. W. Xiong, Z. X. Zhao, T. Sasagawa, T. Kakeshita, H. Eisaki, S. Uchida, A. Fujimori, Z. Zhang, E. W. Plummer, R. B. Laughlin, and Z.-X. Shen, "Multiple bosonic mode coupling in the electron self-energy of $(La_{2-x}Sr_x)CuO_4$," *Physical Review Letters*, vol. 95, p. 117001, 2005. 15, 25, 26, 32, 60, 65, 66

[74] W. Meevasana, N. J. C. Ingle, D. H. Lu, J. R. Shi, F. Baumberger, K. M. Shen, W. S. Lee, T. Cuk, H. Eisaki, T. P. Devereaux, N. Nagaosa, J. Zaanen, and Z.-X. Shen, "Doping dependence of the coupling of electrons to bosonic modes in the single-layer high-temperature $Bi_2Sr_2CuO_6$ superconductor," *Physical Review Letters*, vol. X, p. 157003, 2006. 15, 16, 21, 22, 25, 27, 60, 66

[75] A. A. Kordyuk, S. V. Borisenko, V. B. Zabolotnyy, J. Geck, M. Knupfer, J. Fink, B. Bückner, C. T. Lin, B. Keimer, H. Berger, A. V. Pan, S. Komiya, and Y. Ando, "Constituents of the quasiparticle spectrum along the nodal direction of high-T_c cuprates," *Physical Review Letters*, vol. 97, p. 017002, 2006. 15, 68

[76] S. V. Borisenko, A. A. Kordyuk, A. Koitzsch, J. Fink, J. Geck, V. Zabolotnyy, M. Knupfer, B. Büchner, H. Berger, M. Falub, M. Shi, J. Krempasky, and L. Patthey, "Parity of the pairing bosons in a high-temperature Pb-$Bi_2Sr_2CaCu_2O_8$

bilayer superconductor by angle-resolved photoemission spectroscopy," *Physical Review Letters*, vol. 96, p. 067001, 2006. 15

[77] W. S. Lee, K. Tanaka, I. M. Vishik, D. H. Lu, R. G. Moore, H. Eisaki, A. Iyo, T. P. Devereaux, and Z.-X. Shen, "Dependence of band-renormalization effects on the number of copper oxide layers in Tl-based copper oxide superconductors revealed by angle-resolved photoemission spectroscopy," *Physical Review Letters*, vol. 103, p. 067003, 2009. 15, 16, 18, 19, 22

[78] T. Valla, T. E. Kidd, J. D. Rameau, H.-J. Noh, G. D. Gu, P. D. Johnson, H.-B. Yang, and H. Ding, "Fine details of the nodal electronic excitations in $Bi_2Sr_2CaCu_2O_{8+\delta}$," *Physical Review B*, vol. 73, p. 184518, 2006. 15

[79] K. Byczuk, M. Kollar, K. Held, Y.-F. Yang, I. A. Nekrasov, Th. Pruschke, and D. Vollhardt, "Kinks in the dispersion of strongly correlated electrons," *Nature Physics*, vol. 3, p. 168, 2007. 15, 24, 27, 61

[80] S. Engelsberg and J. R. Schrieffer, "Coupled electron-phonon system," *Physics Review*, vol. 131, p. 993, 1963. 15, 18

[81] W. S. Lee, T. Cuk, W. Meevasana, D. H. Lu, K. M. Shen, Z.-X. Shen, W. L. Yang, X. J. Zhou, Z. Hussain, C. T. Lin, J.-I. Shimoyama, and T. P. Devereaux, "Band renormalization effect in $Bi_2Se_2Ca_2Cu_3O_{10+\delta}$," in *High-$T_c$ Superconductors and Related Transition Metal Oxides* (A. Bussmann-Holder and H. Keller, eds.), ch. 20, p. 227, Springer-verlag, Berlin Heidelberg, 2007. 16, 60, 61

[82] N. C. Plumb, T. J. Reber, J. D. Koralek, Z. Sun, J. F. Douglas, Y. Aiura, K. Oka, E. Eisaki, and D. S. Dessau, "Low-energy ($<$ 10 mev) feature in the nodal electron self-energy and strong temperature dependence of the fermi velocity in $Bi_2Sr_2CaCu_2O_{8+\delta}$," *arXiv:0903.4900*, 2009. 16

[83] G.-H. Gweon, S. Y. Zhou, and A. Lanzara, "Strong influence of phonons on the electron dynamics of $Bi_2Sr_2CaCu_2O_{8+\delta}$," *Journal of Physics and Chemistry of Solids*, vol. 65, p. 1397, 2004. 17

[84] M. R. Norman, M. Eschrig, A. Kaminski, and J. C. Campuzano, "Momentum distribution curves in the superconducting state," *Physical Review B*, vol. 64, p. 184508, 2001. 18, 28

[85] M. Eschrig and M. R. Norman, "Neutron resonance: Modeling photoemission and tunneling data in the superconducting state of $Bi_2Sr_2CaCu_2O_{8+\delta}$," *Physical Review Letters*, vol. 85, p. 3261, 2000. 18, 21

[86] D. C. Peets, J. D. F. Mottershead, B. Wu, I. S. Elfimov, R. Liang, W. N. Hardy, D. A. Bonn, M. Raudsepp, N. J. C. Ingle, and A. Damascelli, "$Tl_2Ba_2CuO_{6+\delta}$ brings spectroscopic probes deep into the overdoped regime of the high-T_c cuprates," *New Journal of Physics*, vol. 9, p. 28, 2007. 18

[87] T. Sato, K. Terashima, K. Nakayama, T. Takahashi, K. Kadowaki, M. Kofu, and K. Hirota, "Bogliubov quasiparticle and low-energy dispersion kink in the superconducting state of $La_{1.85}Sr_{0.15}CuO_4$," *Physica C*, vol. 460, p. 864, 2007. 18

[88] M. Shi, J. Chang, S. Pailhés, M. R. Norman, J. C. Campuzano, M. Månsson, T. Claesson, O. Tjernberg, A. Bendounan, L. Patthey, M. Momono, M. Oda, M. Ido, C. Mudrey, and J. Mesot, "Coherent d-wave superconducting gap in underdoped $La_{2-x}Sr_xCuO_4$ by angle-resolved photoemission spectroscopy," *Physical Review Letters*, vol. 101, p. 047002, 2008. 18

[89] A. W. Sandvik, D. J. Scalapino, and N. E. Bickers, "Effect of an electron-phonon interaction on the one-electron spectral weight of a d-wave superconductor," *Physics Review B*, vol. 69, p. 094523, 2004. 19, 55, 81, 85

[90] J. Rossat-Mignod, L. P. Regnault, C. Vettier, P. Bourges, P. Burlet, J. Bossy, J. Y. Hengy, and G. Lapertot, "Neutron scattering study of the $YBa_2Cu_3O_{6+x}$ system," *Physica C*, vol. 185, p. 86, 1991. 21

[91] M. Eschrig and M. R. Norman, "Effect of the magnetic resonance on the electronic spectra of high-T_c superconductors," *Physical Review B*, vol. 67, p. 144503, 2003. 21

[92] H. A. Mook, M. Mostoller, J. A. Harvey, N. W. Hill, B. C. Chakoumakos, and B. C. Sales, "Observation of phonon softening at the superconducting transition in $Bi_2Sr_2CaCu_2O_8$," *Physical Review Letters*, vol. 65, p. 2712, 1990. 21, 22, 35

[93] H. A. Mook, M. Yethiraj, G. Aeppli, T. E. Mason, and T. Armstrong, "Polarized neutron determination of the magnetic excitation in $YBa_2Cu_3O_7$," *Physical Review Letters*, vol. 70, p. 3490, 1993. 21

[94] N. Pyka, W. Reichardt, L. Pintschovius, G. Engel, J. Rossat-Mignod, and J. Y. Henry, "Superconductivity-induced phonon softening in $YBa_2Cu_3O_7$ observed by inelastic neutron scattering," *Physical Review Letters*, vol. 70, p. 1457, 1993. 21, 22, 35

[95] H. He, P. Bourges, Y. Sidis, C. Ulrich, L. P. Regnault, S. Paihès, N. S. Berzigiarova, N. N. Kolesnikov, and B. Keimer, "Magnetic resonant mode in the single-layer high-temperature superconductor $Tl_2Ba_2CuO_{6+\delta}$," *Science*, vol. 295, p. 1045, 2002. 21, 22, 57

[96] L. Pintschovius, "Electron-phonon coupling effects explored by inelastic neutron scattering," *Physica Status Solidi (b)*, vol. 242, p. 30, 2005. 22, 32, 35, 65, 131

[97] N. N. Kovaleva, A. V. Boris, T. Holden, C. Ulrich, B. Liang, C. T. Lin, B. Keimer, C. Bernhard, J. L. Tallon, D. Munzar, and A. M. Stoneham, "c-axis lattice dynamics in Bi-based cuprate superconductors," *Physical Review B*, vol. 69, p. 054511, 2004. 22, 35, 92, 107

[98] T. P. Devereaux, A. Virosztek, and A. Zawadowski, "Charge-transfer fluctuation, d-wave superconductivity, and the B_{1g} raman phonon in cuprates," *Physical Review B*, vol. 51, p. 505, 1995. 22, 23, 35, 36

[99] B. Friedl, C. Thomsen, and M. Cardona, "Determination of the superconducting gap in $RBa_2Cu_3O_{7-\delta}$," *Physical Review Letters*, vol. 65, p. 915, 1990. 22, 32, 35

[100] E. Altendorf, X. K. Chen, J. C. Irwin, R. Liang, and W. N. Hardy, "Temperature dependences of the 340-, 400-, and 500-cm^{-1} raman modes of $YBa_2Cu_3O_y$ for 6.7 $\leq y \leq$ 7.0," *Physical Review B*, vol. 47, p. 8140, 1993. 22, 32, 35, 65

[101] J. Li and J. Ladik, "The electric field strength at the sites of O(2) and O(3) in the high-T_c superconductor '123' system and its dependence on the surface structure," *Solid State Communications*, vol. 95, p. 35, 1995. 23

[102] T. P. Devereaux, A. Virosztek, A. Zawadowski, M. Opel, P. F. Müller, C. Hoffmann, R. Philipp, R. Nemetschek, R. Hackl, A. Erb, E. Walker, H. Berger, and L. Forró, "Enhanced electron-phonon coupling and its irrelevance to high T_c superconductivity," *Solid State Communications*, vol. 108, p. 407, 1998. 23, 36, 37

[103] M. Opel, R. Hackl, T. P. Devereaux, A. Virosztek, A. Zawadowski, A. Erb, E. Walker, H. Berger, and L. Forró, "Physical origin of buckling in CuO_2: Electron-phonon coupling and raman spectra," *Physical Review B*, vol. 60, p. 9836, 1999. 23, 36, 65

[104] K.-P. Bohnen, R. Heid, and M. Krauss, "Phonon dispersion and electron-phonon interaction for $YBa_2Cu_3O_7$ from first-principles calculations," *Europhysics Letters*, vol. 64, p. 104, 2003. 24, 44, 47

[105] R. Heid, K.-P. Bohnen, R. Zeyher, and D. Manske, "Momentum dependence of the electron-phonon coupling and self-energy effects in superconducting $YBa_2Cu_3O_7$ within the local density approximation," *Physical Review Letters*, vol. 100, p. 137001, 2008. 24, 42, 44, 47

[106] F. Giustino, M. L. Cohen, and S. G. Louie, "Small phonon contribution to the photoemission kink in the copper oxide superconductors," *Nature*, vol. 452, p. 975, 2008. 24, 47

[107] R. Heid, R. Zeyher, D. Manske, and K.-P. Bohnen, "Phonon-induced pairing interaction in $YBa_2Cu_3O_7$ within the local-density approximation," *Physical Review B*, vol. 80, p. 024507, 2009. 24

[108] D. Reznik, G. Sangiovanni, O. Gunnarsson, and T. P. Devereaux, "Photoemission kinks and phonons in the cuprates," *Nature*, vol. 455, p. E6, 2008. 24, 32, 44

[109] R. S. Markiewicz, S. Sahrakorpi, M. Londroos, H. Lin, and A. Bansil, "One-band tight-binding model parametrization of the high-T_c cuprates including the effect of k_z dispersion," *Physical Review B*, vol. 72, p. 054519, 2005. 24, 28, 44, 47

[110] G.-H. Gweon, T. Sawagawa, S. Y. Zhou, J. Graf, H. Takagi, D.-H. Lee, and A. Lanzara, "An unusual isotope effect in a high-temperature superconductor," *Nature*, vol. 430, p. 187, 2004. 27

[111] J. F. Douglas, H. Iwasawa, Z. Sun, A. V. Fedorov, M. Ishikado, T. Saitoh, H. Eisaki, H. Bando, T. Iwase, A. Ino, M. Arita, K. Shimada, H. Namatame, M. Taniguchi, T. Masui, S. Tajima, K. Fujita, S. Ushida, Y. Aiura, and D. S. Dessau, "Unusual oxygen isotope effects in cuprates," *Nature*, vol. 446, p. E5, 2007. 27

[112] H. Iwasawa, Y. Aiura, T. Saitoh, H. Eisaki, H. Bando, A. Ino, M. Arita, K. Shimada, H. Namatame, M. Taniguchi, T. Masui, S. Tajima, M. Ishikado, K. Kujita, S. Ushida, J. F. Douglas, Z. Sun, and D. S. Dessau, "A re-examination of the oxygen isotope effect in ARPES spectra of Bi-2212," *Physica C*, vol. 52, p. 463, 2007. 27

[113] H. Iwasawa, J. F. Douglas, K. Sato, T. Masui, Y. Yoshida, Z. Sun, H. Eisaki, H. Bando, A. Ino, M. Arita, K. Shimada, H. Namatame, M. Taniguchi, S. Tajima, S. Uchida, T. Saitoh, D. S. Dessau, and Y. Aiura, "Isotopic fingerprint of electron-phonon coupling in high-T_c cuprates," *Physical Review Letters*, vol. 101, p. 157005, 2008. 27

[114] E. Schachinger, J. P. Carbotte, and T. Timusk, "Characteristics of oxygen isotope substitutions in the quasiparticle spectrum of $Bi_2Sr_2CaCu_2O_{8+\delta}$," *Europhysics Letters*, vol. 86, p. 67003, 200. 27, 78

[115] J. Graf, G.-H. Gweon, K. McElroy, S. Y. Zhou, C. Jozwiak, E. Rotenberg, A. Bill, T. Sasagawa, H. Eisaki, S. Uchida, H. Takagi, D.-H. Lee, and A. Lanzara, "Universal high energy anomaly in the angle-resolved photoemission spectra of high temperature superconductors: Possible evidence of spinon and holon branches," *Physical Review Letters*, vol. 98, p. 067004, 2007. 27

[116] W. Meevasana, X. J. Zhou, S. Sahrakorpi, W. S. Lee, W. L. Yang, K. Tanaka, N. Mannella, T. Yoshida, D. H. Lu, Y. L. Chen, R. H. He, H. Lin, S. Komiya, Y. Ando, F. Zhou, W. X. Ti, J. W. Xiong, Z. X. Zhao, T. Sasagawa, T. Kakeshita, K. Fujita, S. Uchida, H. Eisaki, A. Fujimori, Z. Hussain, R. S. Markiewicz, A. Bansil, N. Nagaosa, J. Zannen, T. P. Devereaux, and Z.-X. Shen, "Hierarchy of multiple many-body interaction scales in high-temperature superconductors," *Physical Review B*, vol. 75, p. 174506, 2007. 27, 28

[117] B. P. Xie, K. Yang, D. W. Shen, J. F. Zhao, H. W. Ou, J. Wei, S. Y. Gu, M. Arita, S. Qiao, H. Namatame, M. Taniguchi, N. Kaneko, H. Eisaki, K. D. Tsuei, C. N. Cheng, I. Vobornik, J. Fujii, G. Rossi, Z. Q. Yang, and D. L. Feng, "High-energy scale revival and giant kink in the dispersion of a cuprate superconductor," *Physical Review Letters*, vol. 98, p. 147001, 2007. 27

[118] T. Valla, T. E. Kidd, W.-G. Yin, G. D. Gu, P. D. Johnson, Z.-H. Pan, and A. V. Fedorov, "High-energy kink observed in the electron dispersion of high- temperature cuprate superconductors," *Physical Review Letters*, vol. 98, p. 167003, 2007. 27

[119] J. Chang, S. Pailhés, M. Shi, M. Månsson, T. Claesson, O. Tjernberg, J. Voigt, V. Perez, L. Patthey, N. Momono, M. Oda, M. Ido, A. Schnyder, C. Mudry, and J. Mesot, "When low- and high-energy electronic responses meet in cuprate superconductors," *Physical Review B*, vol. 75, p. 224508, 2007. 27

[120] D. S. Inosov, J. Fink, A. A. Kordyuk, S. V. Borisenko, V. B. Zabolotnyy, R. Schuster, M. Knupfer, B. Büchner, R. Follath, H. A. Dürr, W. Eberhardt, V. Hinkov, B. Keimer, and H. Berger, "Momentum and energy dependence of the anomalous high-energy dispersion in the electronic structure of high temperature superconductors," *Physical Review Letters*, vol. 99, p. 237002, 2007. 27, 28

[121] W. Zhang, G. Liu, J. Meng, L. Zhao, H. Liu, X. Dong, W. Lu, J. S. Wen, Z. J. Zu, G. D. Gu, T. Sasagawa, G. Wang, Y. Zhu, H. Zhang, Y. Zhou, X. Wang, Z. Zhao, C. Chen, Z. Xu, and X. J. Zhou, "High energy dispersion relations for the high temperature $Bi_2Sr_2CaCu_2O_8$ superconductor from laser-based angle-resolved photoemission spectroscopy," *Physical Review Letters*, vol. 101, p. 017002, 2008. 27, 29

[122] S. R. Park, C. S. Leem, Y. S. Roh, K. J. Choi, J. H. Kim, B. J. Kim, H. Koh, H. Eisaki, D. H. Lu, Z.-X. Shen, N. P. Armitage, and C. Kim, "Rare earth ion effects on the pseudo-gap in electron-doped superconductors and possible nodeless *d*-wave gap," *Journal of Physics and Chemistry of Solids*, vol. 69, p. 2939, 2008. 27

[123] M. Ikeda, T. Yoshida, A. Fujimori, M. Kubota, K. Ono, Y. Kaga, T. Sasagawa, and H. Takagi, "Differences in the high-energy kink between hole- and electron-doped high-T_c superconductors," *Physical Review B*, vol. 80, p. 184506, 2009. 27, 29, 137

[124] Z.-H. Pan, P. Richard, Y.-M. Xu, M. Neupane, P. Bishay, A. V. Fedorov, H. Luo, L. Fang, H.-H. Wen, Z. Wang, and H. Ding, "Evolution of fermi surface and normal-state gap in the chemically substituted cuprates $Bi_2Sr_{2-x}Bi_xCuO_{6+\delta}$," *Physical Review B*, vol. 79, p. 092507, 2009. 27

[125] F. Ronning, K. M. Shen, N. P. Armitage, A. Damascelli, D. H. Lu, Z.-X. Shen, L. L. Miller, and C. Kim, "Anomalous high-energy dispersion in angle-resolved photoemission spectra from the insulating cuprate $Ca_2CuO_2Cl_2$," *Physical Review B*, vol. 71, p. 094518, 2005. 27, 134

[126] B. Moritz, F. Schmitt, W. Meevasana, S. Johnston, E. M. Motoyama, M. Greven, D. H. Lu, C. Kim, R. T. Scalettar, Z.-X. Shen, and T. P. Devereaux, "Effect of strong correlations on the high energy anomaly in hole- and electron-doped high-T_c superconductors," *New Journal of Physics*, vol. 11, p. 093020, 2009. 27, 28, 29, 134, 135, 137

[127] E. Manousakis, "String excitations of a hole in a quantum antiferromagnet and photoelectron spectroscopy," *Physical Review B*, vol. 75, p. 035106, 2007. 27

[128] A. S. Alexandrov and K. Reynolds, "Angle-resolved photoemission spectroscopy of band tails in lightly doped cuprates," *Physical Review B*, vol. 76, p. 132506, 2007. 27

[129] R. S. Markiewicz, S. Sahrakorpi, and A. Bansil, "Paramagnon-induced dispersion anomalies in the cuprates," *Physical Review B*, vol. 76, p. 174514, 2007. 27, 137

[130] A. Macridin, M. Jarrell, T. Maier, and D. J. Scalapino, "High-energy kink in the single-particle spectra of the two-dimensional hubbard model," *Physical Review Letters*, vol. 99, p. 237001, 2007. 27, 137

[131] S. Basak, T. Das, H. Lin, J. Nieminen, M. Lindroos, R. S. Markiewicz, and A. Bansil, "Origin of the high-energy kink or the waterfall effect in the photoemission spectrum of the $Bi_2Sr_2CaCu_2O_8$ high-temperature superconductor," *arXiv:cond-mat:0904.1749v1*, 2009. 27, 137

[132] F. Tan, Y. Wan, and Q.-H. Wang, "Theory of high-energy features in single-particle spectra of hole-doped cuprates," *Physical Review B*, vol. 76, p. 054505, 2007. 27

[133] M. M. Zemljič, P. Prelovšek, and T. Tohyama, "Temperature and doping dependence of the high-energy kink in cuprates," *Physical Review Letters*, vol. 100, p. 036402, 2008. 27

[134] C. Weber, K. Haule, and G. Kotliar, "Optical weights and waterfalls in doped charge-transfer insulators: A local density approximation and dynamical mean-field theory study of $La_{2-x}Sr_xCuO_4$," *Physical Review B*, vol. 78, p. 134519, 2008. 27

[135] A. F. Santander-Syro, T. Kondo, J. Chang, A. Kaminski, S. Pailhes, M. Shi, L. Patthey, A. Zimmers, B. Liang, P. Li, and R. L. Greene, "Anisotropic dressing of charge-carriers in the electron-doped cuprate superconductor $Sm_{1.85}Ce_{0.15}CuO_4$ from angle-resolved photoemission measurements," *arXiv:cond-mat:0903.3413v1*, 2009. 27

[136] W. Meevasana, F. Baumberger, K. Tanaka, F. Schmitt, W. R. Dunkel, D. H. Lu, S.-K. Mo, H. Eisaki, and Z.-X. Shen, "Extracting the spectral function of the cuprates by a full two- dimensional analysis: Angle-resolved photoemission spectra of $Bi_2Sr_2CuO_6$," *Physical Review B*, vol. 77, p. 104506, 2008. 28, 137

[137] M. Kugler, Ø. Fischer, C. Renner, S. Ono, and Y. Ando, "Scanning tunneling spectroscopy of $Bi_2Sr_2CuO_{O+\delta}$: New evidence for the common origin of pseudogap and superconductivity," *Physical Review Letters*, vol. 86, p. 4911, 2001. 29, 30

[138] M. C. Boyer, W. D. Wise, K. Chatterjee, M. Yi, T. Kondo, T. Takeuchi, H. Ikuta, and E. W. Hudson, "Imaging the two gaps of the high-temperature superconductor $Bi_2Sr_2CuO_{6+x}$," *Nature Physics*, vol. 3, p. 802, 2007. 29, 30

[139] K. M. Lang, V. Madhavan, J. E. Hoffman, E. W. Hudson, H. Eisaki, S. Uchida, and J. C. Davis, "Imaging the granular structure of high-T_c superconductivity in underdoped $Bi_2Sr_2CaCu_2O_{8+\delta}$," *Nature*, vol. 415, p. 412, 2002. 29

[140] S. H. Pan, J. P. O'Neal, R. L. Badzey, C. Chamon, H. Ding, J. R. Engelbrecht, Z. Wang, H. Eisaki, S. Uchida, A. K. Gupta, K.-W. Ng, E. W. Hudson, K. M. Lang, and J. C. Davis, "Microscopic electronic inhomogeneity in the high-T_c superconductor $Bi_2Sr_2CaCu_2O_{8+x}$," *Nature*, vol. 413, p. 282, 2001. 29

[141] K. McElroy, D.-H. Lee, J. Hoffman, K. M. Lang, J. Lee, E. W. Hudson, H. Eisaki, S. Uchida, and J. C. Davis, "Coincidence of checkerboard charge order and antinodal state decoherence in strongly underdoped superconducting $Bi_2Sr_2CaCu_2O_{8+\delta}$," *Physical Review Letters*, vol. 94, p. 197005, 2005. 29

[142] J. W. Alldredge, J. Lee, K. McElroy, M. Wang, K. Fujita, Y. Kohsaka, C. Taylor, H. Eisaki, S. Uchida, P. J. Hirschfeld, and J. C. Davis, "Evolution of the electronic excitation spectrum with strongly diminished hole density in superconducting $Bi_2Sr_2CaCu_2O_{8+\delta}$," *Nature Physics*, vol. 4, p. 319, 2008. 29

[143] N. Jenkins, Y. Fasano, C. Berthod, I. Maggio-Aprile, A. Piriou, E. Giannini, B. W. Hoogenboom, C. Hess, T. Cren, and Ø. Fischer, "Imaging the essential role of spin fluctuations in high-T_c superconductivity," *Physical Review Letters*, vol. 103, p. 227001, 2009. 30, 31, 75, 76, 81, 84, 88

[144] J. Lee, K. Kujita, K. McElroy, J. A. Slezak, M. Wang, Y. Aiura, H. Bando, M. Ishikado, T. Masui, J.-X. Zhu, A. V. Balatsky, H. Eisaki, S. Uchida, and J. C. Davis, "Interplay of electron-lattice interactions and superconductivity in $Bi_2Sr_2CaCu_2O_{8+\delta}$," *Nature*, vol. 442, p. 546, 2006. 30, 31, 75, 76, 81, 84, 88, 111

[145] A. N. Pasupathy, A. Pushp, K. K. Gomes, C. V. Parker, J. Wen, Z. Xu, G. Gu, S. Ono, Y. Ando, and A. Yazdani, "Electronic origin of the inhomogeneous pairing interaction in the high-T_c superconductor $Bi_2Sr_2CaCu_2O_{8+\delta}$," *Science*, vol. 320, p. 196, 2008. 31, 75, 76, 81, 84, 88

[146] J. Lambe and R. C. Jaklevic, "Molecular vibration spectra by inelastic electron tunneling," *Physical Review*, vol. 165, p. 821, 1968. 32, 77

[147] S. Pilgram, T. M. Rice, and M. Sigrist, "Role of inelastic tunneling through the insulating barrier in scanning-tunneling- microscope experiments on cuprate superconductors," *Physical Review Letters*, vol. 97, p. 117003, 2006. 32, 77

[148] H. Shim, P. Chaudhari, G. Logvenov, and I. Bozovic, "Electron-phonon interactions in superconducting $La_{1.84}Sr_{0.16}CuO_4$ films," *Physical Review Letters*, vol. 101, p. 247004, 2008. 32, 75, 76

[149] G.-M. Zhao, "Strong coupling to multiple phonon modes in high-temperature superconductors," *Physical Review B*, vol. 75, p. 214507, 2007. 32, 75, 76

[150] G.-M. Zhao, "Fine structure in the tunneling spectra of electron-doped cuprates: No coupling to the magnetic resonance mode," *Physical Review Letters*, vol. 103, p. 236403, 2009. 32, 75, 76

[151] T. P. Devereaux and R. Hackl, "Inelastic light scattering from correlated electrons," *Reviews of Modern Physics*, vol. 79, p. 175, 2007. 32, 107

[152] R. J. McQueeney, Y. Petrov, T. Egami, M. Yethiraj, G. Shirane, and Y. Endoh, "Anomalous dispersion of lo phonons in $La_{1.85}Sr_{0.15}CuO_4$ at low temperature," *Physical Review Letters*, vol. 82, p. 628, 1998. 32

[153] D. Reznik, B. Keimer, F. Dogan, and I. A. Aksay, "q-dependence of self-energy effects of the plane oxygen vibration in $YaBa_2Cu_3O_7$," *Physical Review Letters*, vol. 75, p. 2396, 1995. 32

[154] C. Thomsen, M. Cardona, B. Gegenheimer, R. Liu, and A. Simon, "Untwinned single crystals of $YBa_2Cu_3O_{7-\delta}$: An optical investigation of the $a-b$ anisotropy," *Physical Review B.* 32

[155] M. C. Krantz, C. Thomsen, H. Mattausch, and M. Cardona, "Raman-active phonons and mode softening in superconducting $HgBa_2CuO_{8+\delta}$," *Physical Review B*, vol. 50, p. 1165, 1994. 32, 35

[156] X. Zhou, M. Cardona, D. Colson, and V. Viallet, "Plane oxygen vibrations and their temperature dependence in $HgBa_2Cu_3O_{8+\delta}$ single crystals," *Physical Review B*, vol. 55, p. 12770, 1997. 32

[157] V. G. Hadjiev, X. Zhou, T. Strohm, M. Cardona, Q. M. Lin, and C. W. Chu, "Strong superconductivity-induced phonon self-energy effects in $HgBa_2Ca_3Cu_4O_{10+\delta}$," *Physical Review B*, vol. 58, p. 1043, 1998. 32, 35

[158] M. Limonov, S. Lee, S. Tajima, and A. Yamanaka, "Superconductivity-induced resonant raman scattering in multilayer high-T_c superconductors," *Physical Review B*, vol. 66, p. 054509, 2002. 32, 35

[159] I.-S. Yang, H.-G. Lee, N. H. Nur, and J. Yu, "Raman modes of the apical oxygen in mercury-based superconductors," *Physical Review B*, vol. 52, p. 15078, 1995. 35

[160] O. Rösch and O. Gunnarsson, "Electron-phonon interaction in the three-band model," *Physical Review B*, vol. 70, p. 224518, 2004. 36, 43, 70, 92, 129

[161] O. K. Andersen, S. Y. Savrasov, O. Jepsen, and A. I. Liechtenstein, "Out-of-plane instability and electron-phonon contribution to s- and d-wave pairing in high-temperature superconductors: LDA linear-response calculation for doped $CaCuO_2$ and a generic tight-binding model.," *Journal of Low Temperature Physics*, vol. 105, p. 285, 1996. 36, 42, 46, 69

[162] B. S. Shastry, "t-J model and nuclear magnetic relaxation in high-T_c materials," *Physical Review Letters*, vol. 63, p. 1288, 1989. 38

[163] P.-O. Löwdin, "A note on the quantum-mechanical perturbation theory," *The Journal of Chemical Physics*, vol. 19, p. 1396, 1951. 41

[164] T. Xiang and J. M. Whealthy, "c axis superfluid response of copper oxide superconductors," *Physical Review Letters*, vol. 77, p. 4632, 1996. 41

[165] W. A. Harrison, *Elementry Electronic Structure.* World Scientific, 2004. 42, 70, 110

[166] S. Y. Savrasov and O. K. Andersen, "Linear-response calculation of the electron-phonon coupling in doped $CaCuO_2$," *Physical Review Letters*, vol. 77, p. 4430, 1996. 44, 47

[167] S. Y. Savrasov, D. Y. Savrasov, and O. K. Andersen, "Linear-response calculations of electron-phonon interactions," *Physical Review Letters*, vol. 72, p. 372, 1994. 44, 47

[168] M. R. Norman, M. Randeria, H. Ding, and J. C. Campuzano, "Phenomenological models for the gap anisotropy of $Bi_2Sr_2CaCu_2O_8$ as measured by angle-resolved photoemission spectroscopy," *Physical Review B*, vol. 52, p. 615, 1995. 44, 82, 85, 92

[169] A. B. Migdal, "Interaction between electrons and lattice vibrations in a normal metal," *Soviet Physics JETP*, vol. 11, p. 696, 1960. 48

[170] G. M. Eliashberg, "Interactions between electrons and lattice vibrations in a superconductor," *Soviet Physics JETP*, vol. 11, p. 696, 1960. 48

[171] F. Marsiglio, "Pairing and charge-density-wave correlations in the Holstein model at half-filling," *Physical Review B*, vol. 42, p. 2416, 1990. 48, 50, 140

[172] F. Marsiglio, M. Schossmann, and J. P. Carbotte, "Iterative analytic continuation of the electron self-energy to the real axis," *Physics Review B*, vol. 37, p. 4965, 1988. 50, 78

[173] D. Reznik, L. Pintschovius, M. Ito, S. Iikubo, M. Sato, H. Goka, M. Fujita, K. Yamada, G. D. Gu, and J. M. Tranquada, "Electron-phonon coupling reflecting dynamic charge inhomogeneity in copper oxide superconductors," *Nature*, vol. 440, p. 1170, 2006. 65

[174] C. Bernhard, D. Munzar, A. Golnik, C. T. Lin, A. Wittlin, J. Humlíček, and M. Cardona, "Anomaly of oxygen bond-bending mode at 320 cm^{-1} and additional absorption peak in the c-axis infrared conductivity of underdoped $YBa_2Cu_3O_{7-\delta}$ single crystals revisited with ellipsometric measurements," *Physical Review B*, vol. 61, p. 618, 2000. 65

[175] K. C. Hewitt, X. K. Chen, C. Roch, J. Chrzanowski, J. C. Irwin, E. H. Altendorf, R. Liang, D. Bonn, and W. N. Hardy, "Hole concentrations and phonon renormalization of the 340-cm^{-1} B_{1g} mode in 2% Ca-doped $YBa_2Cu_3O_y$ ($6.76 \leq y \leq 7.00$)," *Physical Review B*, vol. 69, p. 064514, 2004. 65

[176] W. Meevasana, T. P. Devereaux, N. Nagaosa, Z.-X. Shen, and J. Zaanen, "Calculation of overdamped c-axis charge dynamics and the coupling to polar phonons in cuprate superconductors," *Physical Review B*, vol. 74, p. 174524, 2006. 66, 67

[177] P. P. Ewald, "Evaluation of optical and electrostatic lattice potentials," *Annals of Physics*, vol. 369, p. 253, 1921. 68, 107

[178] T. S. Nunner, J. Schmalian, and K. H. Bennemann, "Influence of electron-phonon interaction on spin-fluctuation-induced superconductivity," *Physical Review B*, vol. 59, p. 8859, 1999. 71, 101

[179] Y. Bang, "Effects of phonon interactions on pairing in high-T_c superconductors," *Physical Review B*, vol. 78, p. 075116, 2008. 71, 101

[180] S. Johnston and T. P. Devereaux, "Density of states modulations from oxygen phonons in d-wave superconductors: Reconciling angle-resolved photoemission spectroscopy and scanning tunneling microscopy," *Physical Review B*, vol. 81, p. 214512, 2010. 75

[181] J. P. Carbotte, "Properties of boson-exchange superconductors," *Reviews of Modern Physics*, vol. 62, p. 1027, 1990. 76, 78, 79, 99, 101, 158

[182] A. V. Balatsky and J.-X. Zhu, "Local strong-coupling paring in d-wave superconductors with inhomogeneous bosonic modes," vol. 74, p. 094517, 2006. 77, 111

[183] P. B. Allen and B. Mitrović, "Theory of superconducting T_c," *Solid State Physics*, vol. 37, p. 1, 1982. 78, 100, 101, 158

[184] C. Jiang, E. Schachinger, J. P. Carbotte, D. Basov, and T. Timusk, "Imaginary part of the infrared conductivity of a $d_{x^2-y^2}$ superconductor," *Physical Review B*, vol. 54, p. 1264, 1998. 78

[185] J. P. Carbotte, E. Schachinger, and J. Hwang, "Boson structures in the relation between optical conductivity and quasiparticle dynamics," *Physical Review B*, vol. 71, p. 054506, 2005. 78

[186] E. Schachinger and J. P. Carbotte, "Oxygen isotope effect on quasiparticle and optical properties in cuprates," *Physical Review B*, vol. 81, p. 014519, 2010. 78

[187] T. A. Maier, D. Poilblanc, and D. J. Scalapino, "Dynamics of the pairing interaction in the Hubbard and t-J models of high-temperature superconductors," *Physical Review Letters*, vol. 100, p. 237001, 2008. 81

[188] J. M. Ziman, *Electrons and Phonons*. Oxford Classic Series, 2001. 89

[189] S. Komiya, Y. Ando, X. F. Sun, and A. N. Lavrov, "c-axis transport and resistivity of lightly to moderately doped La_{2-x} Sr_xCuO_4 single crystals: Implications on the charge transport mechanism.," *Physical Review B*, vol. 65, p. 214535, 2002. 89

[190] C. Falter, K. Klenner, and Q. Chen, "Role of bonding, reduced screening, and structure in the high-temperature superconductors," 89, 131

[191] C. Falter, M. Klenner, G. A. Hoffmann, and Q. Chen, "Origin of phonon anomalies in La_2CuO_4," *Physical Review B*, vol. 55, p. 3308, 1997. 89, 131

[192] C. Falter, M. Klenner, and G. A. Hoffmann, "Anisotropy dependence of the c-axis phonon dispersion in the high-temperature superconductors," *Physical Review B*, vol. 57, p. 14444, 1998. 89, 131

[193] T. Bauer and C. Falter, "Impact of dynamical screening on the phonon dynamics of metallic La_2CuO_4," *Physical Review B*, vol. 80, p. 094525, 2009. 89, 131

[194] A. A. Abrikosov and V. M. Genkin, "On the theory of raman scattering of light in superconductors," *Soviet Physics JETP*, vol. 38, p. 417, 1974. 90

[195] A. L. Fetter, "Electrodynamics of a layered electron gas. II. periodic array," *Annals of Physics*, vol. 88, p. 1, 1974. 92

[196] D. N. Aristov and G. Khaliullin, "Charge susceptibility in the t-J model," *Physical Review B*, vol. 74, p. 045124, 2006. 92

[197] M. A. Quijada, D. B. Tanner, R. J. Kelley, M. Onellion, H. Berger, and G. Margaritondo, "Anisotropy in the ab-plane optical properties of $Bi_2Sr_2CaCu_2O_8$ single-domain crystals," *Physical Review B*, vol. 60, p. 14917, 1999. 92

[198] S. Johnston, F. Vernay, and T. P. Devereaux, "The impact of an oxygen dopant in $Bi_2Sr_2CaCu_2O_{8+\delta}$," *Europhysics Letters*, vol. 86, p. 37007, 2009. 105

[199] J. A. Slezak, J. Lee, M. Wang, K. McElroy, K. Fujita, B. M. Andersen, P. J. Hirschfeld, H. Eisaki, S. Uchida, and J. C. Davis, "Imaging the impact on cuprate superconductivity of varying the interatomic distances within individual crystal unit cells," *Proceedings of the National Academy of Sciences of the United States of America*, vol. 105, p. 3203, 2008. 106

[200] M. Mori, G. Khaliullin, T. Tohyama, and S. Maekawa, "Origin of spatial variation of pairing gap in Bi-based high-T_c cuprates," *Physical Review Letters*, vol. 101, p. 247003, 2008. 106, 111

[201] J.-X. Zhu, "Dopant-induced local pairing inhomogeneity in $Bi_2Sr_2CaCu_2O_{8+\delta}$," *arXiv:cond-mat/0508646*, 2005. 106, 110

[202] M. M. Maśka, Żaneta Śledź, K. Czajka, and M. Mierzejewski, "Inhomogeneity-induced enhancement of the pairing interaction in cuprate superconductors," *Physical Review Letters*, vol. 99, p. 147006, 2007. 106, 110

[203] H. Eskes and J. H. Jefferson, "Superexchange in the cuprates," *Physical Review B*, vol. 48, p. 9788, 1993. 107, 109

[204] Y. He, T. S. Nunner, P. J. Hirschfeld, and H.-P. Cheng, "Local electronic structure of $Bi_2Sr_2CaCu_2O_{8+\delta}$ near oxygen dopants: A window on the high-T_c pairing mechanism," *Physical Review Letters*, p. 197002, 2006. 108, 110

[205] K. Foyevtsova, R. Valentí, and P. J. Hirschfeld, "Effect of dopant atoms on local superexchange in cuprate superconductors: A perturbative treatment," *Physical Review B*, vol. 79, p. 144424, 2009. 110

[206] J.-X. Zhu, A. V. Balatsky, T. P. Devereaux, Q. Si, J. Lee, K. McElroy, and J. C. Davis, "Fourier transformed local density of states and tunneling into a d-wave superconductor with bosonic modes," *Physical Review B*, vol. 73, p. 014511, 2006. 111

[207] A. Macridin, B. Moritz, M. Jarrell, and T. Maier, "Synergistic polaron formation in the Hubbard-Holstein model at small doping," *Physical Review Letters*, vol. 97, p. 056402, 2006. 114, 129, 133, 146, 147

[208] R. Blankenbecler, D. J. Scalapino, and R. L. Sugar, "Monte carlo calculations of coupled boson-fermion systems. I," *Physical Review D*, vol. 24, p. 2278, 1981. 115, 116, 119

[209] R. T. Scalettar, D. J. Scalapino, and R. L. Sugar, "New algorithm for the numerical simulation of fermions," *Physical Review B*, vol. 34, p. 7911, 1986. 115

[210] S. R. White, D. J. Scalapino, R. L. Sugar, E. Y. Loh, J. E. Gubernatis, and R. T. Scalettar, "Numerical study of the two-dimensional Hubbard model," *Physical Review B*, vol. 40, p. 506, 1989. 115, 116, 117, 118, 121, 138, 141, 143

[211] M. Suzuki, "Relationship between d-dimensional quantal spin systems and $(d+1)$-dimensional Ising systems," *Progress of Theoretical Physics*, vol. 56, p. 1454, 1976. 116

[212] R. M. Fye, "New results on Trotter-like approximations," *Physical Review B*, vol. 33, p. 6271, 1986. 116

[213] R. M. Fye and R. T. Scalettar, "Calculation of specific heat and susceptibilities with the use of the Trotter approximation," *Physical Review B*, vol. 36, p. 3833, 1987. 116

[214] J. E. Hirsch, "Two-dimensional hubbard model: Numerical simulation study," *Physical Review B*, vol. 31, p. 4403, 1985. 116, 141

[215] F. F. Assaad and H. G. Evertz, *Computational Many-Particle Physics*. 2008. 116, 161, 162

[216] T. Pang, *An Introduction to Computational Physics*. Cambridge, 2006. 117, 118, 125, 126

[217] W. H. Press, S. A. Teuklsky, W. T. Vetterling, and B. P. Flannery, *Numerical Recipies in Fortran 77*. Cambridge University Press, 1982. 117, 118, 165

[218] M. Hohenadler, H. G. Evertz, and W. von der Linden, "Quantum monte carlo and variational approaches to the Holstein model," *Physical Review B*, vol. 69, p. 024301, 2004. 124, 125, 126

[219] M. Jarrell and J. E. Gubernatis, "Bayesian inference and the analytic continuation of imaginary-time quantum monte carlo data," *Physics Reports*, vol. 269, p. 133, 1996. 127

[220] A. J. Millis, R. Mueller, and B. I. Shraiman, "Fermi-liquid-to-polaron crossover. II. double exchange and the physics of colossal magnetoresistance," *Physical Review B*, vol. 54, p. 5405, 1996. 129

[221] N. Mannella, W. L. Yang, K. Tanaka, X. J. Zhou, H. Zheng, J. F. Mitchell, J. Zaanen, T. P. Devereaux, N. Nagaosa, Z. Hussain, and Z.-X. Shen, "Polaron coherence condensation as the mechanism for colossal magnetoresistance in layered manganites," *Physical Review B*, vol. 76, p. 233102, 2007. 129

[222] O. Gunnarsson, "Superconductivity in fullerides," *Reviews of Modern Physics*, vol. 69, p. 575, 1997. 129

[223] J. E. Han, O. Gunnarsson, and V. H. Crespi, "Strong superconductivity with local Jahn-Teller phonons in C_{60} solids," *Physical Review Letters*, vol. 90, p. 167006, 2003. 129

[224] A. Ramšak, P. Horsch, and P. Fulde, "Effective mass of quasiparticle in a t-J model with electron-phonon interactions," *Physical Review B*, vol. 46, p. 14305, 1992. 129

[225] J. Bonča, S. Maekawa, T. Tohyama, and P. Prelovšek, "Spectral properties of a hole coupled to optical phonons in a generalized t-J model," *Physical Review B*, vol. 77, p. 054519, 2008. 129, 131, 147, 148

[226] V. Cataudella, G. De Filippis, A. S. Mishchenko, and N. Nagaosa, "Temperature dependence of the angle resolved photoemission spectra in the underdoped cuprates: self-consistent approach to the t-J Holstein model," *Physical Review Letters*, vol. 99, p. 226402, 2007. 129, 131

[227] G. De Filippis, V. Cataudella, A. S. Mishchenko, and N. Nagaosa, "Nonlocal composite spin-lattice polarons in high temperature superconductors," *Physical Review Letters*, vol. 99, p. 146405, 2007. 129, 131

[228] G. De Filippis, V. Cataudella, A. S. Mishchenko, C. A. Perroni, and N. Nagaosa, "Optical conductivity of a doped mott insulator: The interplay between correlation and electron-phonon interaction," *Physical Review B*, vol. 80, p. 195104, 2009. 129, 133

[229] A. S. Mishchenko and N. Nagaosa, "Electron-phonon coupling and a polaron in the t-J model: From the weak to the strong coupling regime," *Physical Review Letters*, vol. 93, p. 036402, 2004. 129, 131, 147, 148

[230] A. S. Mishchenko and N. Nagaosa, "Numerical study of the isotope effect in underdoped high-temperature superconductors: Calculation of the angle-resolved photoemission spectra," *Physical Review B*, vol. 73, p. 092502, 2006. 129

[231] A. S. Mishchenko, N. Nagaosa, Z.-X. Shen, G. D. Filippis, V. Cataudella, T. P. Devereaux, C. Bernhard, K. W. Kim, and J. Zaanen, "Charge dynamics of doped holes in high T_c cuprate superconductors: A clue from optical conductivity," *Physical Review Letters*, vol. 100, p. 166401, 2008. 129, 133

[232] S. Ishihara and N. Nagaosa, "Interplay of electron-phonon interaction and electron correlation in high-temperature superconductivity," *Physical Review B*, vol. 69, p. 144520, 2004. 129, 133

[233] M. K. Kulić and R. Zeyher, "Influence of strong electron correlations on the electron-phonon coupling in high-T_c oxides," *Physical Review B*, vol. 49, p. 4395, 1994. 129, 133

[234] T. Sakai, D. Poilblanc, and D. J. Scalapino, "Hole pairing and phonon dynamics in generalized two-dimensional t-J Holstein models," *Physical Review B*, vol. 55, p. 8445, 1997. 129, 133

[235] O. Gunnarsson and O. Rösch, "Electron-phonon coupling in the self-consistent Born approximation of the t-J model," *Physical Review B*, vol. 73, p. 174521, 2006. 129

[236] P. Prelovšek, R. Zeyher, and P. Horsch, "Self-localization of composite spin-lattice polarons," *Physical Review Letters*, vol. 96, p. 086402, 2006. 129

[237] A. S. Mishchenko, "Manifestations of the electron-phonon coupling in the spectroscopy of high-temperature superconductors," *Advances in Condensed Matter Physics*, vol. 2010, p. 206106, 2010. 129

[238] O. Rösch and O. Gunnarsson, "Electron-phoon interaction in the t-J model," *Physical Review Letters*, vol. 92, p. 146403, 2004. 129, 131

[239] V. N. Kostur and P. B. Allen, "Polaron and bipolaron formation in a cubic perovskite lattice," *Physical Review B*, vol. 56, p. 3105, 1997. 129

[240] P. Barone, R. Raimondi, M. Capone, and C. Castellani, "Effective electron-phonon coupling and polaronic transition in the presence of strong correlation," *Physical Review B*, vol. 73, p. 085120, 2006. 129, 132

[241] R. Citro, S. Cojocaru, and M. Marinaro, "Renormalization of the electron-phonon interaction in presence of charge fluctuations," *Physical Review B*, vol. 72, p. 115108, 2005. 129, 133

[242] P. Werner and A. J. Millis, "Efficient dynamical mean field simulation of the Holstein-Hubbard model," *Physical Review Letters*, vol. 99, p. 146404, 2007. 129, 132, 138, 147

[243] E. Koch and R. Zeyher, "Renormalization of the electron-phonon coupling in the one-band Hubbard model," *Physical Review B*, vol. 70, p. 094510, 2004. 129, 133, 140

[244] G. Sangiovanni, M. Capone, C. Castellani, and M. Grilli, "Electron-phonon interaction close to a mott transition," *Physical Review Letters*, vol. 94, p. 026401, 2005. 129, 130, 132, 138, 143, 147

[245] G. Sangiovanni, O. Gunnarsson, E. Koch, C. Castellani, and M. Capone, "Electron-phonon interaction and antiferromagnetic correlations," *Physical Review Letters*, vol. 97, p. 046404, 2006. 129, 132, 138, 148

[246] A. Macridin, B. Moritz, M. Jarrell, and T. Maier, "Suppression of superconductivity in the Hubbard model by buckling and breathing phonons," *arXiv:cond-mat/0611067*, 2006. 129, 133, 146

[247] M. Capone, G. Sangiovanni, C. Castellani, C. D. Castro, and M. Grilli, "Phase separation close to the density-driven mott transition in the Hubbard-Holstein model," *Physical Review Letters*, vol. 92, p. 106401, 2004. 129, 132

[248] E. Cappelluti, B. Cerruti, and L. Pietronero, "Charge fluctuations and electron-phonon interaction in the finite-U Hubbard model," *Physical Review B*, vol. 69, p. 161101(R), 2004. 129

[249] B. J. Alder, K. J. Runge, and R. T. Scalettar, "Variational monte carlo study of an interaction electron-phonon model," *Physical Review Letters*, vol. 79, p. 3022, 1997. 129

[250] A. Macridin and M. Jarrell, "Isotope effect in the Hubbard model with local phonons," *Physical Review B*, vol. 79, p. 104517, 2009. 129

[251] J. Bauer and A. C. Hewson, "The competition between antiferromagnetic and charge order in the hubbard-holstein model," *arXiv:1004.3677v1*, 2010. 129, 138

[252] Y. Petrov and T. Egami, "Exact-diagonalization study of the electron-lattice coupling in the effective two-band t-J model," *Physical Review B*, vol. 58, p. 9485, 1998. 129

[253] S. Koikegami and Y. Aiura, "Kink structure in the electronic dispersion of high-T_c superconductors from the electron-phonon interaction," *Physical Review B*, vol. 77, p. 184519, 2008. 129

[254] Z. G. Yu, J. Zang, J. T. Gammel, and A. R. Bishop, "Charge localization and stripes in a two-dimensional three-band Peierls-Hubbard model," *Physical Review B*, vol. 57, p. 3241(R), 1998. 129

[255] M. Grilli and C. Castellani, "Electron-phonon interaction in the presense of strong correlations," *Physical Review B*, vol. 50, p. 16880, 1994. 129

[256] K. Yonemitsu, A. R. Bishop, and J. Lorenzana, "Doping staes in the two-dimensional three-band Peierls-Hubbard model," *Physical Review B*, vol. 47, p. 12059, 1993. 129

[257] Z. B. Huang, H. Q. Lin, and E. Arrigoni, "Strong enhancment of the d-wave superconducting state in the three-band Hubbard model coupled to an apical oxygen phonon," *arXiv:1004.2740v1*, 2010. 129

[258] M. Berciu, "Exact Green's functions for the two-site Hubbard-Holstein Hamiltonian," *Physical Review B*, vol. 75, p. 081101(R), 2007. 129, 131

[259] M. Capone, C. Castellani, and M. Grilli, "Electron-phonon coupling in strongly correlated systems," *arXiv:1003.1042v1*, 2010. 130

[260] G. L. Goodvin, M. Berciu, and G. A. Sawatzky, "Green's function of the Holstein polaron," *Physical Review B*, vol. 74, p. 245104, 2006. 131

[261] M. Berciu and G. L. Goodvin, "Systematic improvement of the momentum average approximation for the Green's function of a Holstein polaron," *Physical Review B*, vol. 76, p. 165109, 2007. 131

[262] Z. Liu and E. Manousakis, "Dynamical properties of a hole in a heisenberg antiferromagnet," *Physical Review B*, vol. 45, p. 2425, 1992. 131

[263] K. M. Shen, F. Ronning, D. H. Lu, W. S. Lee, N. J. C. Ingle, W. Meevasana, F. Baumberger, A. Damascelli, N. P. Armitage, L. L. Miller, Y. Kohsaka, M. Azuma, M. Takano, H. Takagi, and Z.-X. Shen, "Missing quasiparticles and the chemical potential puzzle in the doping evolution of the cuprate superconductors," *Physical Review Letters*, vol. 93, p. 267002, 2004. 131

[264] W. Koller, A. C. Hewson, and D. M. Edwards, "Polaronic quasiparticles in a strongly correlated electron band," *Physical Review Letters*, vol. 95, p. 256401, 2005. 132

[265] W. Koller, D. Meyer, Y. Ono, and A. C. Hewson, "First- and second-order phase transitions in the Holstein-Hubbard model," vol. 66, p. 559, 2004. 132

[266] B. Kyung, S. I. Mukhin, V. N. Kostur, and R. A. Ferrell, "Spectral properties of the t-J model in the presence of hole-phonon interaction," *Physical Review B*, vol. 54, p. 13167, 1996. 133

[267] A. S. Mishchenko, N. V. Prekof'ev, A. Sakamoto, and B. V. Svistunov, "Diagrammatic quantum monte carlo study of the frölich polaron," *Physical Review B*, vol. 62, p. 6317, 2000. 133

[268] E. Cappelluti, S. Ciuchi, and S. Fratini, "Polaronic features in the optical properties of the Holstein t-J model," *Physical Review B*, vol. 76, p. 125111, 2007. 133

[269] B. Moritz, S. Johnston, and T. P. Devereaux, "Insights on the cuprate high energy anomaly observed in ARPES," *arXiv:1004.4685*, 2010. 134

[270] R. Preuss, W. Hanke, and W. von der Linden, "Quasiparticle dispersion of the 2D Hubbard model: From an insulator to a metal," *Physical Review Letters*, vol. 75, p. 1344, 1995. 134, 136

[271] C. Gröber, R. Eder, and W. Hanke, "Anomalous low-doping phase of the Hubbard model," *Physical Review B*, vol. 62, p. 4336, 2000. 134, 136

[272] H. Eskes, M. B. J. Meinders, and G. A. Sawatzky, "Anomalous transfer of spectral weight in doped strongly correlated systems," *Physical Review Letters*, vol. 67, p. 1035, 1991. 135, 136

[273] P. G. Steeneken, L. H. Tjeng, G. A. Sawatzky, A. Tanaka, O. Tjernberg, G. Ghiringhelli, N. B. Brookes, A. A. Nugroho, and A. A. Menovsky, "Crossing the gap from p- to n-type doping: Nature of the states near the chemical potential in $La_{2-x}Sr_xCuO_4$ and $Nd_{2-x}Ce_xCuO_{4-\delta}$," *Physical Review Letters*, vol. 90, p. 247005, 2003. 135

[274] R. T. Scalettar, N. E. Bickers, and D. J. Scalapino, "Competition of pairing and peierls -charge-density-wave correlations in a two-dimensional electron-phonon model," *Physical Review B*, vol. 40, p. 197, 1989. 140, 141

[275] S. R. White, D. J. Scalapino, R. L. Sugar, N. E. Bickers, and R. T. Scalettar, "Attractive and repulsive pairing interaction vertices for the two-dimensional Hubbard model," *Physical Review B*, vol. 39, p. 839, 1989. 143

[276] E. Khatami, C. R. Lee, Z. J. Bai, R. T. Scalettar, and M. Jarrell, "Dynamical mean field theory cluster solver with linear scaling in inverse temperature," *arXiv:0904.1239*, 2009. 153